Multiscale Structures and Mechanics of Biomineralized Lattices in Hexactinellid sponges and Echinoderms

Hongshun Chen

Dissertation to the Faculty of the
Virginia Polytechnic Institute and State University
in partial fulfillment of the requirements for the degree of

Doctor of Philosophy
In
Mechanical Engineering

Ling Li, Chair
Bahareh Behkam
Jake Socha
Pinar Acar

April 28th, 2023
Blacksburg, Virginia

Keywords: Multiscale structure, Biomineralized cellular lattice, Mechanical properties, Hexactinellid sponge, Echinoderm, Bio-inspiration

Copyright 2023, Hongshun Chen

Multiscale Structures and Mechanics of Biomineralized Lattices in Hexactinellid sponge and Echinoderms

Hongshun Chen

ABSTRACT

Biomineralized lattice materials with have high mineral contents (~ 99 wt%), usually "conceal" multiscale structural arrangements for unique mechanical or functional performance, such as the remarkable damage tolerance despite of the brittle nature of the constituents (e.g., biogenic silica and calcite). However, the quantitative explorations of the structure-mechanics relationships in multiscale of biomineralized lattices remain insufficient and hence hinder the leverage of the functional benefits to design architected cellular materials. In this dissertation, I selected two groups of marine animals (i.e., Hexactinellid sponges and Echinoderms) for systematic structural-mechanical study. Their biomineralized lattice skeletons exhibit three representative types of multiscale structures: 1) multiscale hierarchical structure: skeleton of Hexactinellid sponge such as *Euplectella aspergillum*; 2) multiscale functionally graded structure: spine of sea urchin *Heterocentrotus mammillatus*; and 3) dual-scale (atomic and microlattice scales) periodic structure: ossicle of starfish *Protoreaster nodosus*. This dissertation develops quantitatively the structural-mechanical/functional correlations in biomineralized cellular materials for bio-inspired material design.

Four different species of Hexactinellid sponges have been studied with particular focus on the species *E. aspergillum*. As an example of the multiscale hierarchical biomineralized lattice, the extremely lightweight skeleton (~99% porosity) of *E. aspergillum* exhibits 1) amorphous nanoparticular biogenic silica; 2) micron-sized fibrous

spicule with cylindrically laminated silica layers separated by organic interfaces; 3) spicule bundles where the individual spicules merged by secondary silica deposition; 4) a centimeter-sized Voronoi-like cellular dome known as sieve plate; and 5) a centimeter-sized cylindrically arranged rectangular lattice with double-diagonal reinforcement and external helical ridge. Here, we discovered a series of mechanical or functional properties or formation process of structures in different length scales: 1) for the biogenic silica in three different species of Hexactinellid sponge, consistent modulus and hardness of the biogenic silica throughout the cross section of the spicule are found via substantial correlation between the measured values and locations; 2) for the sieve plate, the Voronoi-like cellular dome constructed by porous branch with increased height achieves balance between improved mechanical stiffness and large pore opening for sponge's current pumping mechanism; 3) via microstructural study, the formation process of the sieve plate is proposed; and 4) for the cylindrical skeletal body, the double-diagonal configuration and the ridge structure are found to provide tendency to optimize torsional rigidity, and enhanced radial stiffening and improved permeability, respectively.

The cellular structure in the spine of the *H. mammillatus* (i.e., stereom) made of ~99wt% of single-crystalline calcite shows a multiscale functionally graded structure. We developed and optimized a cellular network analysis workflow on the large-volume 3D lattice structure obtained from the synchrotron-based micro-Computed Tomography scan. The analysis provides quantitative descriptions of the branch, ring structure, and septum which reveals a functionally graded structure in multiscale from the center region to the edge region of the spine: 1) in microscale, the branch thickness and length increases, resulting in a significantly decreased porosity; and 2) in macroscale, the center region of

the spine with galleried stereom of highly aligned branches transits to the edge region with laminar stereom of radially arranged septa and interconnecting branches. The multiscale structural variations lead to the mechanical variations the increased elastic modulus and mechanical isotropy from the center to the edge of the spine. This provides a biological pathway for designing the lightweight, strong, and tough beam with multiscale structural gradient.

In previous work, we discovered that ossicle in starfish *P. nodosus* possesses a unique dual-scale periodic lattice structure, which means periodic single crystal calcite in nanoscale and diamond triply periodic minimal surface (diamond-TPMS) lattice in microscale. It has three unique structural features: 1) microlattice dislocations in ossicles similar to those found in crystals with diamond cubic lattice; 2) a diamond-TPMS microlattice with ca. 50% relative density; and 3) dual-scale crystallographic coalignment between c-axis of the single-crystalline constituent calcite and the [111] direction of the diamond-TPMS microlattice. Based on this work, this dissertation mainly reveals: 1) unique type and core structures of the dislocations in the ossicle for stiffness, strength, and toughness; 2) the 3D property compensation of dual-scale crystallographic coalignment for improved mechanical isotropy; and 3) mechanical benefits (improved mechanical isotropy and effective fragment jamming) and morphological benefits (minimal surface and highest surface area to volume ratio) for 50% relative density.

Multiscale Structures and Mechanics of Biomineralized Lattices in Hexactinellid sponge and Echinoderms

Hongshun Chen

GENERAL AUDIENCE ABSTRACT

Architected lattice materials, featured by their tailorable 3D multiscale architectures, achieve unique mechanical properties such as breaking the trade-off between strength and toughness, and mechanical isotropy reaching theoretical limit. In nature, as a result of evolutionary driving force, the biomineralized skeletons of the animals such as sea sponge, sea urchin, and starfish usually delicately control the architectural arrangements in different length scales and provide excellent templates for the design of architected lattices with desirable properties. Quantitative understanding of the 3D multiscale structures and mechanics of these natural biomineralized lattices allows the development of bio-inspired materials that are, for example, simultaneously stiff, strong, and tough.

This dissertation establishes the quantitative structural-mechanical/functional relationships in multiscale of three biomineralized lattices with high mineral contents (~99 wt%) and a wide range of porosity (50~99 vol%) in Hexactinellid sponges with main emphasis on species (*Euplectella aspergillum*), sea urchin *Heterocentrotus mammillatus*, and starfish *Protoreaster nodosus*. They are selected for their representative multiscale structures, i.e., multiscale hierarchical structure, multiscale functionally graded structure, and dual-scale (i.e., atomic and microlattice scales) periodic structure, respectively. Study of these biomineralized lattices significantly improve our understanding of the biological strategies in structural arrangement and pave the way towards bio-inspired modeling to leverage the mechanical benefits.

To my families

ACKNOWLEDGMENTS

I am deeply grateful for the support and assistance I have received during the writing of my dissertation. I am especially fortunate to have Dr. Ling Li as my advisor. Dr. Li's humble and patient approach had a significant impact not only on my research but also on my life. He provided beneficial guidance and insightful feedback that pushed me to sharpen my thoughts and bring my research to a higher level. Dr. Li understood my strengths and weaknesses as a researcher, and he always encouraged me to work harder and more efficiently. His passion, profoundness, and attention to detail are a great role model for my future career.

I would also like to thank my committee members, Dr. Pinar Acar, Dr. Jake Socha, and Dr. Bahareh Behkam. They provide their insightful knowledge in different fields of studies to further improve the thoroughness and depth of my research.

I am also grateful to my colleagues and friends in the Laboratory of Biological and Bio-inspired Materials for their assistance in every aspect of my research. Dr. Ting Yang, Dr. Zhifei Deng, and Chenhao Hu helped me with nanoindentation, μ-CT scan, and structural analysis of the cellular network. Dr. Zian Jia provided valuable feedback and discussions, while Shahbaz Khan, Yang Geng, and Liuni Chen always raised good questions and offered valuable suggestions.

I also want to give thanks to Dr. Xianghui Xiao from Brookhaven National Laboratory, Dr. Pavel D. Shevchenko and Dr. Francesco De Carlo from the Argonne National Laboratory for their help on the experiments at the Argonne National Laboratory, Dr. James C. Weaver from the Harvard University for providing important

suggestions on the glass sponge research, and Dr. Hermann Ehrlich from the TU Bergakademie Freiberg for providing spicule samples of three Hexactinellid species and the collaboration on the biogenic silica project.

I am grateful to the Air Force Office of Scientific Research, National Science Foundation, and Argonne National Laboratory for providing funding for my research.

Last but not least, I would like to give my special thanks to my families and best friend. My parents and grandparents give me endless love and supports. We always video chat and they always resolve any concerns in my heard. I also thank my dearest friend, Mr. Zhiren Li, for all the warm-hearted talking, playing, and sharing, and mutual giving about our lives. I want to give my special thanks to my kind, wise, and gorgeous wife, Dr. Wanlu Gu. Our love and marriage are destined. She is very supportive and understanding as we are tightly bonded.

TABLE OF CONTENTS

ACKNOWLEDGMENTS vii
TABLE OF CONTENTS ix
Chapter 1 Introduction 1
Chapter 2 Background 8
2.1. Architected cellular lattices 9
2.1.1. Multiscale structures 9
2.1.2. Mechanical designs of multiscale cellular lattices 12
2.2. Fundamentals of Hexactinellid sponge 16
2.2.1. Introduction to Hexactinellid sponges 16
2.2.2. Structure, formation, and mechanics of biogenic silica 20
2.2.3. Structure, formation, and mechanics of spicule 26
2.2.4. Macroscale structures of *Euplectella aspergillum*: structure, formation, and functions 30
2.2.5. Current knowledge gaps 33
2.3. Fundaments of echinoderms: Sea urchin and starfish 34
2.3.1. Introduction to echinoderms 34
2.3.2. Structure and mechanics of sea urchin spines 36
2.3.3. Structure and mechanics of the starfish ossicle 39
2.3.4. Current knowledge gaps 41
2.4. Motivations and challenges 43
Chapter 3 Compositional and mechanical analysis of biogenic silica in three species of Hexactinellid sponges 46
3.1. Introduction 48
3.2. Materials and Methods 50
3.3. Results 55
3.3.1. Structures of the anchoring spicules and their biogenic silica 55
3.3.2. Modulus and hardness of the biogenic silica 60
3.3.3. Fracture of the monolithic and laminated biogenic silica 66
3.3.4. Element and chemical bond distributions 68
3.4. Discussions and conclusions 80
Chapter 4 The structural-mechanical understanding of cellular dome in the sieve plate of glass sponge *Eupletella aspergillum* 82
4.1. Introduction 84

4.2 Materials and Methods 86
4.3. Results 96
4.3.1. Introduction to the sieve plate 96
4.3.2. Structural quantification of sieve plate 97
4.3.3. Effect of the cellular dome structure on the stiffness 107
4.3.4. Effect of the porous branch with increased height on the stiffness 111
4.4. Discussions 114
4.5. Conclusions 117
Chapter 5 Microstructure-based study of the formation of the sieve plate in glass sponge *Euplectella aspergillum* 118
5.1. Introduction 119
5.2. Materials and Methods 122
5.3. Results and discussions 123
5.3.1. Microstructural observations for sieve plate's cellular pattern formation 123
5.3.2. Characteristics and growth of individual spicules 132
5.3.3. Formation process of the sieve plate 138
5.4. Discussions 141
5.5. Conclusions 142
Chapter 6 Multifunctional properties of the lightweight lattice-based skeleton of the sponge *Euplectella aspergillum* 144
6.1. Introduction 146
6.2. Materials and Methods 150
6.3. Results 163
6.3.1. Skeletal lattice structure of *E. aspergillum* 163
6.3.2. Modeling and simulations of bioinspired lattices 165
6.3.3. Parametric modeling and simulations of the bioinspired lattices 169
6.3.4. Structure and mechanics of the ridge structure 172
6.3.5. Fluid-mechanical behaviors of the ridge structure 178
6.4. Discussions and conclusions 187
Chapter 7 Multiscale functionally graded lattice and mechanics of the sea urchin spine of *Heterocentrotus mammillatus* 193
7.1. Introduction 195
7.2. Materials and Methods 197
7.3. Results 206
7.3.1. Structural overview of the analyzed volume 206

7.3.2. Characteristics of nodes 208
7.3.3. Characteristics of branches 212
7.3.4. Characteristics of ring structure 222
7.3.5. Structure of septum 226
7.3.6. Variation of mechanical properties 230
7.4. Discussions 232
7.4.1. Nodal configurations for lightweight and robust cellular structure 232
7.4.2. Galleried stereom in the center region and laminar stereom in the edge region 234
7.4.3. Structure-mechanics interplay for *H. mammillatus* spines 235
7.4.4. Local structural modifications 236
7.4.5. Limitations of current work 237
7.5. Conclusions 238
Chapter 8 Dislocation engineering in the biomineralized microlattice of the ossicle of starfish *Protoreaster nodosus* 241
8.1. Introduction 242
8.2. Materials and Methods 245
8.3. Results 249
8.3.1. Dislocation structures in the starfish ossicles 249
8.3.2. Core structures of 60° dislocation in ossicle 252
8.3.3. Core structures in the screw dislocation 257
8.4. Discussions 265
8.5. Conclusions 267
Chapter 9 Mechanical properties of dual-scale crystallographic coalignment in starfish's ossicle stereom 269
9.1. Introduction 270
9.2. Methods 272
9.3. Results 280
9.3.1. Dual-scale diamond-TPMS microlattice in ossicles 280
9.3.2. 3D elastic properties 282
9.3.3. Effect of relative density 295
9.3.4. Effect of dual-scale coalignment 300
9.4. Discussions 311
9.5. Conclusions 314
Chapter 10 Summary and future directions 316

10.1. Summary 316
10.2. Future directions 327
REFERENCES 330

Chapter 1 Introduction

Lattice materials are of importance for their tailorable 3D architectures and properties and for their wide ranges of applications in, for instances, packaging, thermal insulation, tissue scaffold, etc. By introducing multiscale hierarchical structures, these architected lattices are able to control the deformation mechanisms in multiscale and achieve high stiffness and strength as well as recoverable properties despite the brittle ceramic constituent. The multiscale structure scheme is also ubiquitously found in organisms with biomineralized skeletons, including sea sponge[1], sea urchin[2], diatom[3], and starfish[4], which possess lightweight, stiff, strong, and damage-tolerant properties desirable for engineering materials. Therefore, learning the lessons of structural-functional properties and formation from the natural biomineralized lattices may provide lucrative strategies towards bio-inspired lattice designs with desired mechanical or functional performance.

In this dissertation, three representative models of biomineralized lattices were selected for their most unique multiscale structures, i.e., the multiscale hierarchical structure in the skeleton of the Hexactinellid sponges (or commonly known as glass sponge), especially the species of *Euplectella aspergillum*, the multiscale functionally graded structure in the stereom of the spine of sea urchin, *Heterocentrotus mammillatus*, and the dual-scale periodic lattice with microlattice dislocations in the ossicle of starfish *Protoreaster nodosus*, respectively. Through experiments, simulations, and theoretical development, this dissertation quantitatively describes the 3D multiscale structures and their correlations with the mechanical/functional performances, which leads to bio-inspired modeling.

Chapter 2 provides a summary of the fundamentals and backgrounds related to architected lattice materials, Hexactinellid sponges, and Echinoderms. At first, the basic structural motifs of multiscale structures are summarized in the context of this dissertation, which is followed by the review of micromechanical theory describing the mechanical properties (i.e., stiffness, strength, fracture behavior) of the current multiscale lattice materials. Secondly, the fundamentals of the Hexactinellid sponges are introduced and reviewed in details. This review includes i) a brief introduction of the Hexactinellid sponges; ii) formation, structures and mechanics of their multiscale structural features; and iii) the current knowledge gaps that inspire the research on glass sponges in this dissertation. Thirdly, the fundamentals and knowledge gaps related to the Echinoderms, specifically the sea urchin spine of *H. mammillatus* and starfish ossicles *P. nodosus*, are introduced and discussed. Fourthly, current challenges in studying the 3D multiscale structures and their mechanical performances are presented. Finally, the motivation of this dissertation is discussed. The model systems used in this dissertation and perspectives in the bio-inspiration from the structure-mechanics correlations in this work are briefly introduced.

Chapter 3 to 9 provide the detailed multiscale structural, mechanical, functional, or formation analyses of three selected model systems of the biomineralized lattices. Specifically, for the multiscale hierarchical structures in the Hexactinellid sponges, I divided this work into four chapters (3~6) to introduce the structures and mechanics from constituent-level to lattice-level.

Chapter 3 studied the nanoscale compsitions and mechanics of the biogenic silica from the Hexactinellid sponges. As significant amount of structural and mechanical

studies for biogenic silica in *E. aspergillum* and *Monorhaphis chuni* has been carried out[5,6], here, three different species of class Hexactinellida are selected, which are *Corynonema populiferum*, *Hyalonema sieboldin*, and *Sericolophus hawaiicus*, respectively, for the investigation of biogenic silica,. The modulus, hardness and fracture toughness of the nanoscale biogenic silica from three species were probed and analyzed. Similar to the previous work, the biogenic silica exhibits lower modulus and hardness compared to the synthetic glass due to the hydration and organics. Our results show nearly consistent modulus and hardness throughout the cross sections of the spicules, which is explained by the consistent element distribution and hydration and organics distributions within the biogenic silica, except for the organic interfaces. In addition, the fracture toughness, obtained from cube-corner indentation experiments, was found lower of the monolithic biogenic silica and higher of the layering structure than the synthetic silica, respectively. Finally, the mechanical results obtained from the nanoindentation under 90% humidity condition are closely similar to those obtained under ambient condition which could be a result of already saturated biogenic silica or thin layer of altered surface structure compared to indentation depth.

Chapter 4 explores one of the structural components in the skeletal body of glass sponge *E. aspergillum*—sieve plate. Our structural analysis demonstrates its dome shape of elliptical paraboloid and the Voronoi cellular structure of 0.4~0.6 regularity with anisotropic pore alignments. In addition, the sieve plate branch is porous and has increased height which is ca. 3 times of the width. 2D and 3D mechanical investigations are performed which reveals that the sieve plate with irregular cellular structure provides stiffness and hence mechanical protection to the osculum similar to the corresponding

regular honeycomb structure. The porous sieve plate branch with increased height provides improved stiffness while maintaining the large pore opening for current pumping. Further in-depth exploration of the microstructures may provide better understanding and hence mechanical modeling of the sieve plate.

Chapter 5 focuses on the understanding of the formation process of sieve plate based on the microstructural study. Assumptions are made for the formation of sieve plate based on previous literatures regarding the spicule and skeletal formation of Hexactinellid sponges. Next, based on the microscale observation, sieve plate is found to be a continuation of cylindrical skeleton. Also, the bridging sieve plate branches are observed which form the final Voronoi-like tessellation of sieve plate based on the initial cellular tessellation of sieve plate. Furthermore, the excessive amount of hexactine concentrated at the growing tips of the sieve plate branch implies that they assist the anchoring of the tissue and hence the silica deposition. Moreover, individual spicules are traced, which reveals various classes of the spicules based on their location and morphology. Quantitative analysis of the individual spicules show that the radius is ca. 15 μm except for the curved spicules located at the outer surface of the sieve plate nodes of ca. 10 μm. Long spicules spanning more than 12 nodes are also found, demonstrating the capability of sponge to grow long spicules in sieve plate. With these microstructural understanding, formation process and hypothetical driving forces are proposed.

Chapter 6 studies the structure and multi-functions (i.e., fluidic and mechanical functions) of the cylindrical skeleton of the *E. aspergillum*. The cylindrical lattice of the *E. aspergillum*, known as double-diagonally reinforcement rectangular lattice in cylindrical shape, is quantitatively described which enables the parametric mechanical

analysis. Through parametric modeling and simulations, the skeletal lattice exhibits tendency to optimize torsional resistance. In addition, the double-diagonal configuration of the bio-inspired lattice has no effect on the linear mechanical properties compared to other diagonal configurations and, thus, leave freedoms to hole opening for fluid transport inside the sponge. Furthermore, the ridge structure that helically spirals along the cylindrical lattice is also found to provide multifunctionality such as radial stiffening and enhanced fluid permeability, despite its inefficient contribution to the other stiffness of the entire cylindrical body.

Chapter 7 moves the focus to the biomineralized lattice with multiscale functionally graded structure in the sea urchin spine, *H. mammillatus*. We developed and optimized the script for quantitative cellular network analysis that is suitable for studying a large volume from the stereom of sea urchin spine. Then the quantitative analysis characterizes the stereom at multiscale: individual node and branch (~10 μm), local ring structure (~100 μm), septum structure (~2 mm), and the entire center and edge region (~6 mm). The large volume extended from the core to the edge region is analyzed which shows structural variations in two scales: i) in millimiter-scale, a galleried stereom at the center and a laminar stereom at the edge; and ii) in microscale, the increase of branch thickness from core to edge regions. The significant long-range structural variation is correlated with the mechanical variations, exhibiting a beam design with increasing stiffness from the core to periphery that may improve overall effective stiffness.

Finally, Chapter 8 and 9 study the dual-scale biomineralized microlattice recently discovered in the ossicle of starfish *P. nodosus*, which is the diamond triply periodic

minimal surface lattice with dual-scale single-crystalline crystallographic coalignment (dual-scale diamond-TPMS).

Firstly, in ossicle, the dislocations in the lattice-scale were found to provide crack deviation mechanisms and hence improved damage tolerance. Therefore, Chapter 8 studies the structure of the dislocations in the diamond-TPMS micro-lattice of ossicle with emphasis on the unique structural features dissimilar to those found in crystals with diamond cubic lattices (i.e., diamond and silicon). Secondly, the design strategies learnt from the microlattice dislocations in starfish is proposed and how starfish confines the structural effect around the dislocation cores is discussed. Finally, how to leverage the structural features in the biological microlattice dislocations and corresponding mechanical benefits in architected lattice is discussed via bio-inspired modeling of the dislocations in lattice design.

Subsequently in Chapter 9, the mechanical properties of the dual-scale single-crystalline coalignment, a unique structure found in ossicle, are studied. A combined theoretical and computational method is proposed to predict the 3D elasticity surfaces of the microlattice with dual-scale coalignment. Our results of 3D elastic properties reveal that the ossicle's dual-scale coalignment provides improved mechanical isotropy despite the calcite's high mechanical anisotropy. Yet, further structural analysis shows that the ossicle with ~50% relative density achieves a trade-off between unmaximized mechanical isotropy and morphological requirements (e.g., maximized surface-to-volume ratio and minimal surface curvature). In addition, ossicle's dual-scale coalignment provides a minimal strength compared to other surveyed coalignments, which guides the design of dual-scale lattices. This work not only provides understanding to the mechanical

properties of echinoderm's stereom with similar structural concept, but also an unprecedented design strategy for multiscale hierarchical architected lattices with desired mechanical isotropy and structural symmetry.

Chapter 2 Background

This chapter introduces the background knowledge for this dissertation. Enabled by the state-of-the-art manufacturing techniques (e.g., high-resolution additive manufacturing), multiscale hierarchical architected lattices[7], demonstrate their capabilities in unique properties such as improved damage tolerance of the ceramic lattices and careful control of multiscale deformation mechanisms. Nature has also evolved biomineralized lattices with multiscale hierarchical structures due to evolutionary driving forces, which usually provides a different pathway to expand our knowledge and material design space. Therefore, understanding the multiscale design strategies hidden in the natural biomineralized lattices becomes significantly important for developing bio-inspired lattices with desirable or optimal mechanical performance. However, it is challenging to explore the 3D structures and mechanics of these biomineralized lattices with architectures typically from nanoscale (atomic-scale arrangements) to macroscale (up to centimeter-scale arrangements). Through the use of multiscale structural-mechanical characterization methods, such as synchrotron-based micro-computed tomography (μ-CT), nanoindentation, and Instron mechanical testing, the 3D multiscale architectures as well as the mechanical/functional performances become accessible and quantifiable. Furthermore, the bio-inspired modeling in this dissertation not only assists our understanding of the unique structures in the biomineralized lattices, but also leverages the mechanical/functional benefits.

In this chapter, section 2.1 first introduces the structures, manufacturing, and mechanics of the artificial architected lattices and their current limitations. In section 2.2, the multiscale hierarchical structures, formation, and mechanics of the Hexactinellid

sponges are summarized in detailed, which leads to the current knowledge gaps that inspire the research in this dissertation. In section 2.3, I introduce other types of multiscale biomineralized lattices in echinoderms that possess unique structural organizations, specifically the species of *H. mammillatus* and *P. nodosus*. In section 2.4, current challenges in accessing the 3D multiscale architectures, understanding structure-mechanics correlation, and generating bio-inspirations are discussed which leads to the motivation of this study. In addition, the model systems in this dissertation are briefly introduced.

2.1. Architected cellular lattices

2.1.1. Multiscale structures

Architected lattice, an important group of cellular solids, architects themselves via controlling alignments and connections of branches. Some of cellular lattices, especially the so-called lattice-based metamaterial with periodic architectures, enables the explicit theoretical prediction of properties like modulus and strength, and, therefore, allows the design of unique combinations of mechanical properties that are unprecedented in naturally occurring materials[7–11]. Further introduction of multiscale hierarchical structures significantly expands the lattice design space and enable the tuning of deformation modes in distinct length-scales to achieve improved stiffness and strength[7,11,12].

The unbounded architectural designs and various types of amorphous or polycrystalline materials, including polymer, metals, and ceramics, as constituent materials, cellular lattices significantly expand the design space of materials[8]. The

ceramic cellular lattice is of high interest among all types of cellular lattices for providing a novel pathway to resolve the limitation of the brittleness of ceramics which are usually lightweight, strong, erosion-resistant and high-temperature resistant compared to metals and polymers. Previous works successfully demonstrated that various types of ceramics such as Al_2O_3, glass (SiO_2), carbon, SiCO, and etc. are able to form cellular lattices which exhibit improved toughness, recoverability, and damage-tolerant with further reduction of weight (**Fig. 2.1.1 and 2.1.2**)[7,9,13,14]. Currently, the main structural strategies to overcome the brittleness of the ceramics are: i) extremely low-density using core-shell structure or simply ceramics hollow tubes as construction units; and ii) multiscale hierarchical architecture to bring about the nanoscale size effect (**Fig. 2.1.1**)[7,9,15]. However, unlike biomineralized lattices, achieving such enhanced mechanical properties for high-density ceramic cellular lattice suitable for real-world large-scale structural supports is challenging.

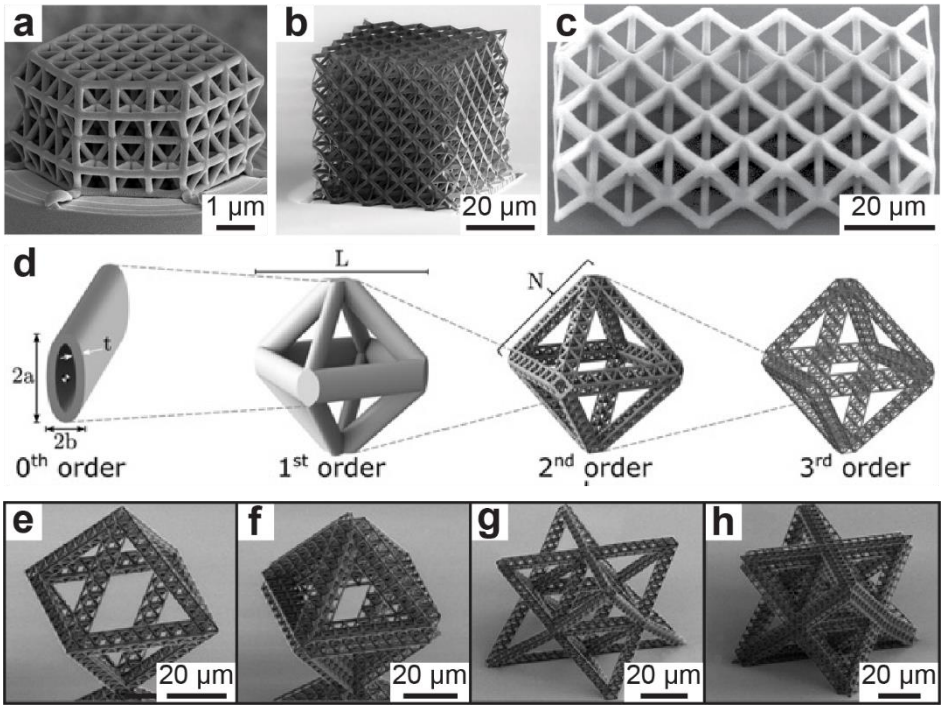


Figure 2.1.1. Architected ceramic lattices and multiscale hierarchical structures. (**a-c**) Ceramic lattices with single level of structural hierarchy made of (**a**) Carbon, (**b**) Al_2O3, and (**c**) silica. (**d**) Example of structural hierarchy in multiscale from beam's morphology to lattice with three levels of structural hierarchy. (**e-h**) Architected lattices with multiscale hierarchy of (**e**) an octahedron constructed by octahedra beams, (**f**) a octahedron constructed by octet beams, (**g**) a octet constructed by octahedra beams, and (**h**) a octet constructed by octet beams. Adapted and modified from[7,8,13,16].

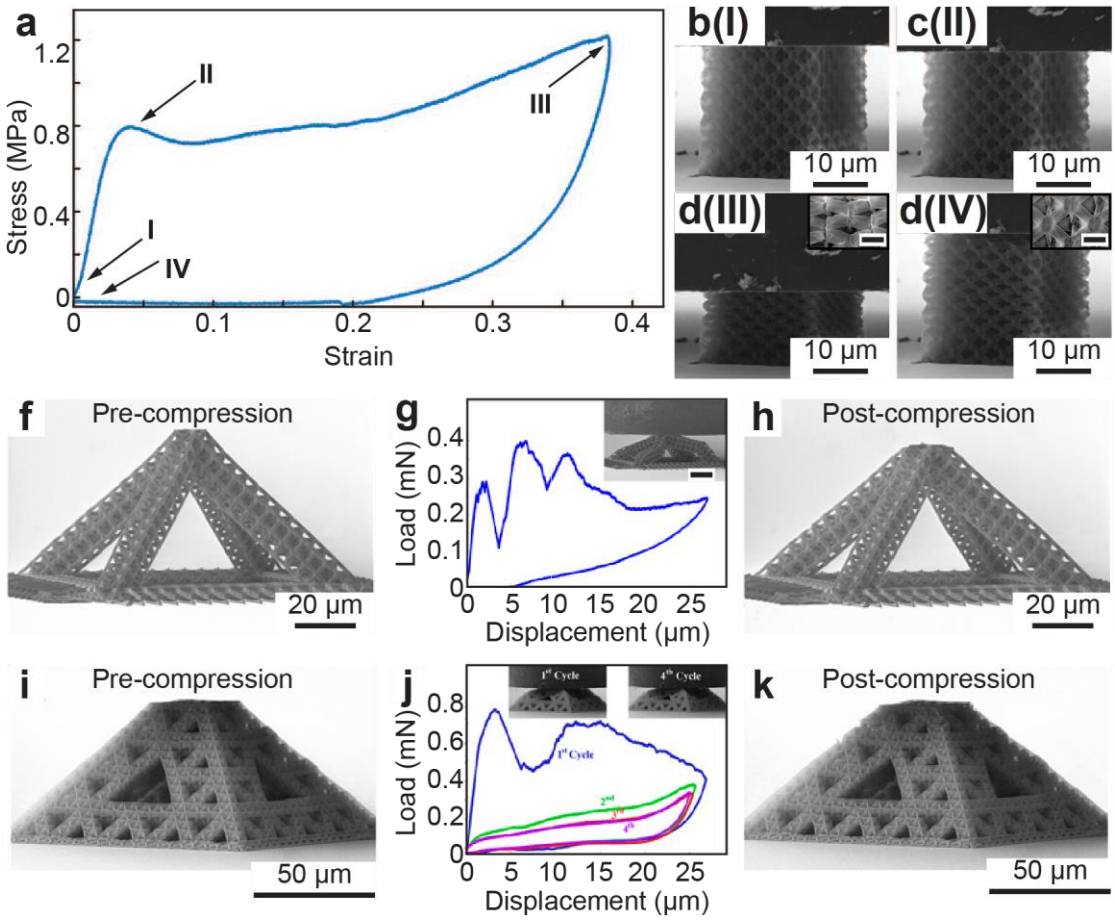


Figure 2.1.2. Mechanical performance of architected ceramic lattices. (**a-d**) Mechanical performance of architected alumina lattices with single level of structural hierarchy and hollow beams of 10 nm. (**f-k**) Mechanical performance of multiscale hierarchical alumina lattices with (**f-h**) 2nd order hierarchy and (**i-k**) 3rd order hierarchy. Adapted and modified from[7,9].

2.1.2. Mechanical designs of multiscale cellular lattices

The most important structural parameters, which control the architectures and mechanics of the cellular lattices, are the relative density ρ/ρ_s (or porosity as a counterpart), aspect ratio of branch t/l, and average connectivity of nodes Z. The relative density ρ/ρ_s, which is a function of the aspect ratio of branch t/l, has direct effect on the

mechanical properties as shown in the classic scaling law in Eq. 2.1.1 for cellular lattices: the higher the relative density, the higher the modulus and strength.

$$\frac{P_{eff}}{P_S} = C \cdot \left(\frac{\rho_{eff}}{\rho_S}\right)^n \quad (2.1.1),$$

where P_{eff} is the effective modulus (E_{eff}) or strength (σ_{eff}) of the cellular lattice, P_S is the modulus (E_S) or strength (σ_S) of the constituent material, ρ_{eff} is the effective density of the lattice, ρ_S is the density of the constituent material, *C* and *n* are the geometric constant and scaling factor, respectively. The modulus and strength predictions (Eq. 2.1.2-2.1.4) for octet-truss lattice is taken as an example to write the Eq. 2.1.1 in terms of branch's aspect ratio (**Fig. 2.1.3a**).

$$\frac{E_{eff}}{E_S} = \frac{2\sqrt{2}}{3} \cdot \left(\frac{t}{l}\right)^2 \quad (2.1.2),$$

$$\frac{\sigma_{eff,tension}}{\sigma_S} = 2\sqrt{2} \cdot \left(\frac{t}{l}\right)^2 \quad (2.1.3),$$

$$\frac{\sigma_{eff,bucking}}{E_S} = \frac{\sqrt{2}\pi^2}{6} \cdot \left(\frac{t}{l}\right)^4 \quad (2.1.4),$$

where $\sigma_{eff,tension}$ and $\sigma_{eff,bucking}$ are the effective strength of lattice with failure mode of beam fracture and buckling, respectively.

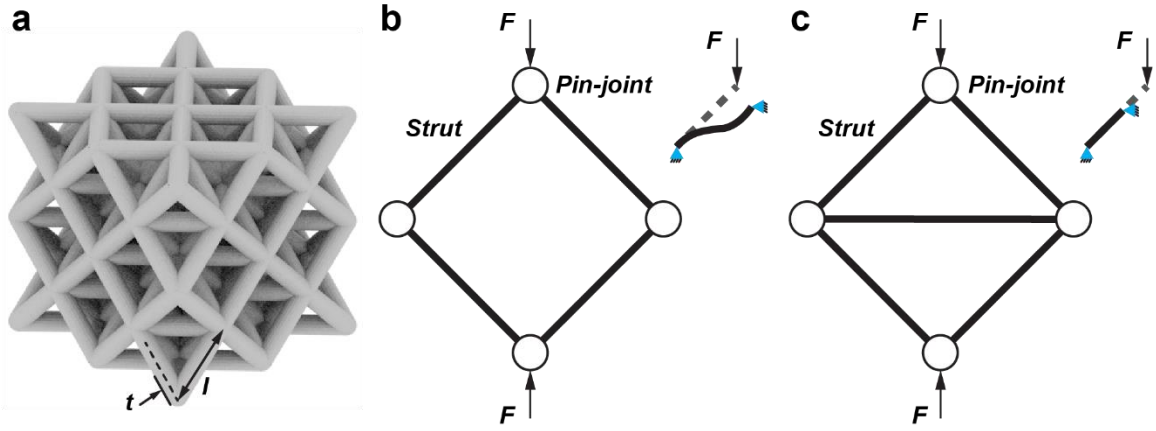


Figure 2.1.3. Stretching and bending -dominated lattices. (**a**) Octet truss lattice as an example of stretching-dominated lattice. (**b**) Non-rigid lattice structure with pin-joint (inset: dominant deformation mode for non-rigid lattice with welding joint). (**c**) Rigid lattice structure with pin-joint (inset: dominant deformation mode for rigid lattice with welding joint).

According to Eq. 2.1.1 to 2.1.4, the geometric constants (C) and the scaling factor (n) which are mainly affected by the aspect ratio of branch t/l and the average connectivity Z also play determining roles in the mechanical properties. The Maxwell's criterion provides a necessary yet insufficient relationship between numbers of struts and joints to determine whether a 2D (Eq. 2.1.5) or 3D (Eq. 2.1.6) framework is rigid (**Fig. 2.1.3b,c**).

$$b = 2j - 3 \qquad (2.1.5),$$

$$b = 3j - 6 \qquad (2.1.6),$$

where b is the number of strut and j is the number of joint. For an infinite 3D lattice framework with an average connectivity Z and j joints, the number of struts $b \approx Zj/2$, leading to the necessary average connectivity Z of 6. Yet, to achieve a necessary and sufficient condition, 3D lattice is required to have $Z = 12$[17]. For cellular lattices with

rigid joints instead of pin joints, this criterion differentiates the lattices by the dominant deformation modes of the branch: bending or stretching, resulting in two categories of lattices: stretching and bending -dominated lattices (**Fig. 2.1.3b,c**). Table 2.1.1 summarizes the scaling factors of relative modulus and strength for stretching and bending -dominated lattices. Despite it is a convenient theory, two things are important to note:

- This is not entirely applicable for cellular lattices with high relative density as the decrease of slenderness of branch (reversely related to *t/l*) alters the dominant deformation mode to a mixture of bending and stretching modes[18];
- For cellular lattices without definite periodicity such as stochastic foam, the explicit relationship is not able to obtain definitely. However, Eq. 2.1.1 is still able to generally describe the mechanical performance[19].

Table 2.1.1. Scaling factors (*n*) of relative modulus and strength for stretching and bending -dominated lattices.

	Relative modulus	Relative strength	
	(E_{eff}/E_S)	Fracture (σ_{eff}/σ_S)	Buckling (σ_{eff}/E_S)
Stretching	1	1	1
Bending	2	1.5	1.5

This theory can be further extended to describe cellular lattices with multiscale hierarchical structures by substituting the scaling relationship of the architectural design in lower length-scale[11,20]. Importantly, this is generally applicable for lattice structures

with atomic-scale architectures such as constituent materials with anisotropic mechanical properties which have never been considered. This is significantly important for biomineralized lattices as organisms usually have controls over the architectures for constituent materials such as laminated composites in spicule of Hexactinellid sponge[21] and single-crystalline minerals in Echinoderms[4].

Bearing these fundamental knowledges about the structures and mechanics of cellular lattices, we may use similar strategies to understand some aspects of the multiscale structures and mechanics of biomineralized lattices such as variation of porosity and branch's slenderness.

2.2. Fundamentals of Hexactinellid sponge

2.2.1. Introduction to Hexactinellid sponges

The sea sponges (phylum: *Porifera*) represent one of the most ancient heritage of metazoans and possess less physiological complexity, which are of significant importance in various fields of research, including Ecology, Evolutionary biology, Nanotechnology, Structural engineering, and etc[1,21–25]. One of the classes of sponges, the Hexactinellid sponges, named by Schmidt, or most commonly known as glass sponge, construct their bodies with hydrated silica, the second most abundant mineral formed by organisms on Earth[22,23,26,27]. Although Hexactinellid sponges' fossil record can be dated back to about half of a billion year, nowadays they still largely distribute in all oceans on Earth from shallow water of tens of meters to deep water of thousands of meters[1,22,28].

Hexactinellid sponges distinguish themselves from others (e.g., demosponge) by their unique organization of syncytial tissue and triaxonal spicules (i.e., biogenic silica fibers)

which build a massive variety of body morphologies[22,23,27]. These silica spicules in the sponges' body can be a few tens of microns to meters long, resulting in various spicule forms of microscleres (small spicule of ca. 10 μm in size) and megascleres (large spicule of at least hundreds of microns in size), complex spicule frameworks forming the body skeleton, and long bundles of spicules anchored in the sediment (**Fig. 2.2.1a-c**)[22,29–31]. In addition, spicules usually composed of concentric layers of hydrated and consolidated silica nanoparticles separated by organic interlayers and an axial filament with squared cross section[22,29] (**Fig. 2.2.1d-g**). Moreover, the spicules are usually classified into three categories depending on their locations: (1) dermalia, atrialia, and etc.: spicules closed to the surface membranes; (2) parenchymalia: the spicules distributed within the tissue; (3) prostalia: spicules extended outside the body such as the basalia (or the anchoring spicules) (**Fig. 2.2.1h**)[22,27]. Within the group of parentchymalia, further classification can be made based on whether the spicules fused together by additional deposition of hydrated silica or not: (1) lyssacine skeleton with typically unfused spicules; and (2) dictyonine skeleton with fused spicules, forming relatively regular arrangement of skeletal framework (**Fig. 2.2.1c**)[22,23,27].

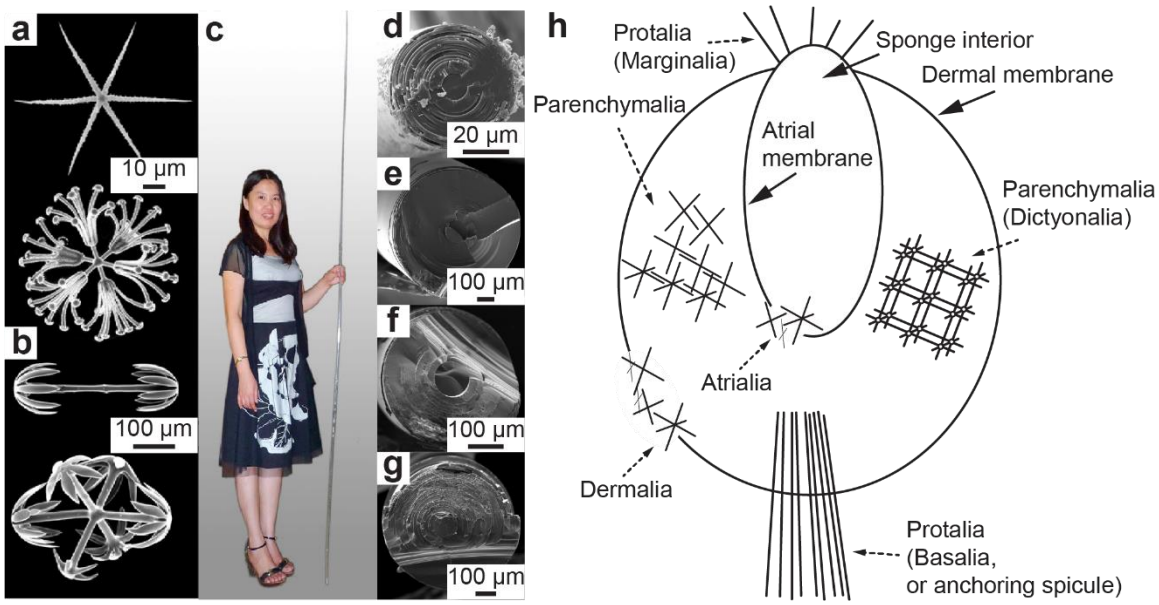


Figure 2.2.1. Multiscale hierarchical structures of the biogenic silica skeleton of Hexactinellid sponges. (**a-b**) Spicule (microscleres) of (**a**) a few tens or (**b**) a few hundreds of microns. (**c**) Giant spicule of a few meters of length and a few centimeters of diameter. (**d-g**) Fracture surfaces of anchoring spicules from various species: (**d**) *E. aspergillum*, (**e**) *C. populiferum*, (**f**) *H. sieboldin*, (**g**) *S. hawaiicus*. (**h**) Classification of the spicule types. Adapted or modified from[22,29].

It is clear, from the schematics (**Fig. 2.2.1**), that the skeleton of Hexactinellid sponges exhibit multiscale hierarchical structures from nanoscale silica nanoparticles to the macroscale spicule-based skeleton. The skeleton of a model system, *E. aspergillum*, is presented in **Fig. 2.2.2** to provide a typical example and visualization of the multiscale structural hierarchy of Hexactinellid sponges. These multiscale arrangements of silica spicules imply a precious template to be explored for nano-synthesis and ceramic lattices with multiscale architectural controls[7,21,32]. In addition, as filtering feeders, their body plans with spicule-based frameworks and tissue organizations may significantly impact

the multifunctionality of glass sponges, for example, their feeding efficiency, prevention of sediment blockages, and mechanics of the spicule skeleton[30,33–35]. Yet, these types of research remain largely unexplored considering a large group of discovered glass sponge species, as it is challenging to access the deep sea and keep glass sponges alive in laboratory and museum[22]. With the recent advances in submersibles and remote operated vehicles, researchers expect to greatly expand the knowledge of deep-sea glass sponges in terms of biosilification, filtering feeding mechanisms, growth, and reproduction[22,32–34,36,37].

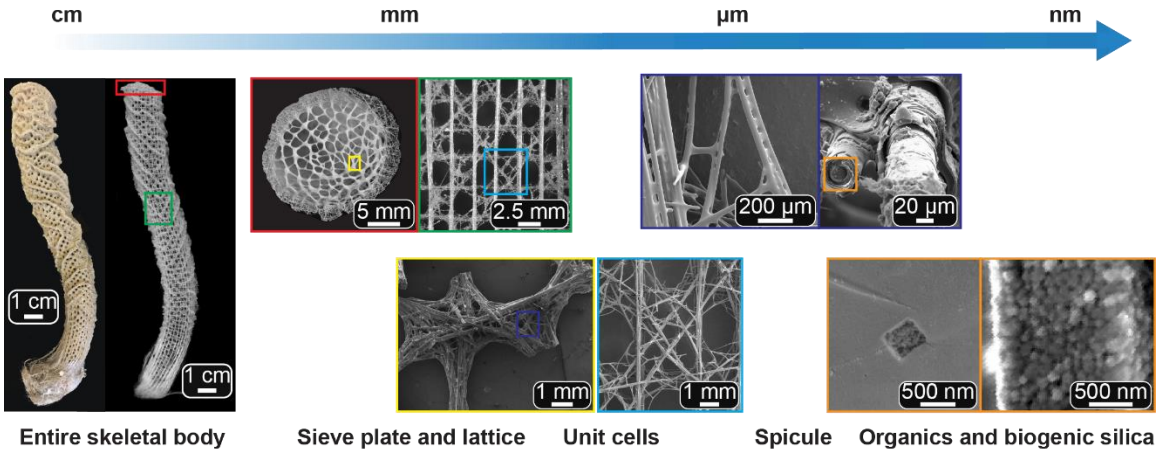


Figure 2.2.2. Multiscale hierarchical structures of the of *E. aspergillum* sponges from the entire macroscale skeletal body to the nanoscale biogenic silica particles. Adapted or modified from[21,30].

Therefore, I selected four Hexactinellid sponges, for which the names and taxonomy are summarized in **Table 2.2.1**, to study the multiscale structures and mechanics of biomineralized lattices. The structural features and corresponding mechanics in multiscale are reviewed in details in the following subsections.

Table 2.2.1 Names and taxonomy of the glass sponges in this dissertation (NA: Not applicable).

	Corynonema populiferum	***Hyalonema sieboldii***	***Sericolophus hawaiicus***	***Euplectella aspergillum***
Kingdom	Animalia			
Phylum	Porifera			
Class	Hexactinellida			
Subclass	Amphidiscophora			Hexasterophora
Order	Amphidiscosida			Lyssacinosida
Family	Hyalonematidae		Pheronematidae	Euplectellidae
Subfamily	(NA)		(NA)	Euplectellinae
Genus	*Hyalonema*		*Sericolophus*	*Euplectella*
Subgenus	*Hyalonema (Corynonema)*	*Hyalonema (Hyalonema)*	(NA)	(NA)
Species	*Hyalonema (Corynonema) populiferum*	*Hyalonema (Hyalonema) sieboldii*	*Sericolophus hawaiicus*	*Euplectella aspergillum*
Abbreviation	*C. populiferum*	*H. sieboldii*	*S. hawaiicus*	*E. aspergillum*

2.2.2. Structure, formation, and mechanics of biogenic silica

The formation of biogenic hydrated silica in glass sponges (i.e., biosilification) and its structural aspect are of great interests. Modern techniques, such as Small-angle X-ray diffraction (SAXS), X-ray diffraction (XRD), Raman spectroscopy (Raman), Infrared spectroscopy (IR), Solid-State ^{29}Si Nuclear Magnetic Resonance (NMR), and etc., demonstrate their capabilities to provide in-depth understanding of the nanostructures of biogenic silica[6,38–41]. However, the biosilification process in living glass sponges is challenging to observe and study and hence remains indirectly surveyed[22,42–44]. Despite this, the study on the as-obtained spicules from dead glass sponges using advanced silica etching techniques, composition characterization, and *in vitro* polymerization still

provide insights into the organics-involved biosilification process and novel pathways towards nanofabrication and nanotechnology[25,31,32,44–46].

The basic structure of biogenic silica in glass sponge is hydrated nanoparticulate ($SiO_2 \cdot nH_2O$) with a size of 50-200 nm in diameter for *E. aspergillum* (**Fig. 2.2.3**)[21,30]. According to the SAXS and XRS analysis, while the silica nanoparticle is amorphous (lack of long-range crystallinity), the silica nanoparticle itself may compose of particles smaller than 3 nm in diameter[6]. In the spicule of *E. aspergillum*, a size gradient of the silica nanoparticles from the periphery to the core of the spicule has also been found under Scanning Electronic Microscope (SEM): the mean particle size gradually decreases from the periphery (187 ± 34 nm) to the core (48 ± 9 nm)[21]. Whether this size gradient of silica nanoparticles is true universally for Hexactinellid sponges is unknown yet important for their mechanical properties. Neilson et al. have proposed that, based on the results of the etched spicule with nanoparticles and NMR measurements, the spicule's silica layer is a condensed silica nanoparticle (Q^4) reinforced hydrated silica matrix, while the condensed silica nanoparticles are surrounded by a thin shell of Q^3 species of silica[38]. As the hydrated silica is less condensed than the un-hydrated silica, this provides insight that the variation of the nanoparticle size and hence hydration content may result in a mechanical gradient in the spicule[38,39].

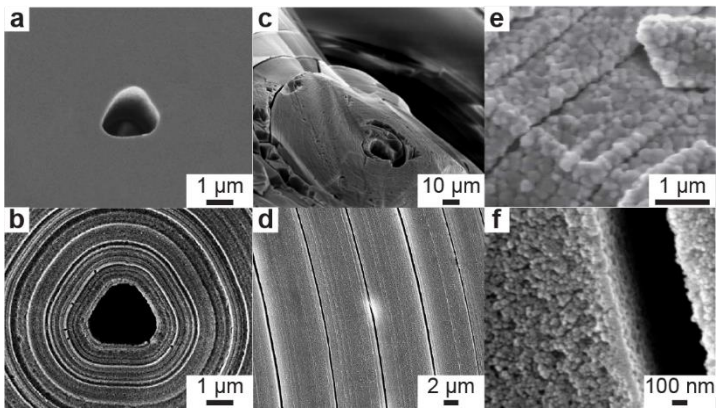


Figure 2.2.3. Microstructure of spicule and spicule bundle. (**a-b**) Unetched and etched cross section of the anchoring spicule from demosponge *Tethya aurantia*. (**c-d**) Etched cross section of the anchoring spicule from Hexactinellid sponge *S. hawaiicus*. (**e-f**) Silica nanoparticles of the anchoring spicules from *E. aspergillum* and *S. hawaiicus*. (**a,b,e**) are adapted or modified from[6,39].

EDS measurements performed on the biogenic silica reveal various elements such as Silicon (Si), Oxygen (O), Carbon (C), Sodium (Na), and Potassium (K)[44,46–50]. Surprisingly, the element contents at different locations of the spicule's cross section may not be consistent. Kul'chin et al. showed a gradient of various elements using EDS measurement on the spicule of *H. sieboldii*, where the atomic content of Si and K decreases from the core to the periphery, while the atomic contents of Na and O do not vary significantly[48]. However, due to the increased amount of Si towards the core, the weight contents of Na and O decreases. The authors stated arguably that the occurrence of Na and K indicate various degree of Si condensation or density as well as hydration which may affect the mechanical properties. Specifically, in another word, the density of the biogenic silica varies and it is more condensed in the core region due to relatively low

contents of Na (or -OH functional group) and K ions. Yet, the increased content of Si may also contribute to the increased density at the core region, as higher the hydration, less condensed the biogenic silica[38,39]. In addition, it is indeed that the Na affects the mechanics of the silica glass where the increased amount of Na decreases the Young's modulus of the silica glass. However, the contents of Na and K are extremely small (~1%) in biogenic silica which may not effectively contribute to the mechanical properties. Nevertheless, one limitation in the above measurements is that the measured results are not carefully correlated to the measured locations (i.e., biogenic silica or interlayer organics).

Furthermore, various types of chemical bonding in the spicule of Hexactinellid sponges, such as silica, hydrated silica, and organics, have been investigated via Raman measurement. Similar to the synthetic silica glass, a symmetric Si-O-Si bending mode at Raman shift (ν) of 450 cm^{-1} and D_1 band at ν = 480~490 cm^{-1} have been observed[6,40]. It is worth to note that this is only a relatively simple description of the peaks and bands as the Raman spectrum analysis of amorphous silica is much more complicated. A band may be a mixture of multiple vibration mode and the separation of each mode needs to be extremely careful. Different from the synthetic silica glass, the peak at ν = 960 cm^{-1} corresponding to the Q^3 silanol (i.e., symmetric Si-O-H stretching mode), has only been observed for glass spicule and silica gel with hydrated silica. In addition, the peak for amide at ν = ~1655 cm^{-1} has been observed, demonstrating the existence of organics. In the higher Raman shift, a small peak at ν = ~2900 cm^{-1} and a large band at ν = 3000~3800 cm^{-1} have also been observed for spicule and silica gel for C-H stretching and water molecule, respectively. Apart from the point measurements, Raman image scan

shows the distribution of different types of chemical bonds in the spicule's cross section which enables the visualization of hydration content obtained from the comparison between intensity peaks as previously obtained for *Monorhaphis chuni*[6]. Unlike the previously found element distribution gradients for *H. sieboldii* using EDS, the Raman measurements so far did not find any organics or hydration gradients in biogenic silica for Hexactinellid sponges. Other types of measurements such as Thermogravimetric analysis (TGA) and Solid-State ^{29}Si NMR are also able to quantitatively characterize the content of different constituents[40]. However, their particle-based samples only allow the overall measurement of the spicule and limit the detailed understanding of the element or chemical bonds' distribution. Therefore, EDS and Raman measurements, especially the large area image scans, provide better gateways to correlate the local nanoscale compositions with the local mechanics.

The formation of the biogenic silica has been investigated. In the class of demospongiae (another class of Porifera with silica spicule), silicatein, discovered in the axial filament, plays a key role to catalyze the formation, polymerization, and condensation of silica nanoparticles from the environmental silicon compounds (e.g., silicic acid ($Si(OH)_4$), silicates) with the assistance of other organics such as F-actin[25,43,51–53]. The silicatein has also been found in Hexactinellid *Crateromorpha meyeri* and *Monorhaphis chuni*, which is believed to also enzymatically assist the formation of biogenic silica[31,54,55]. Beside the silicatein, studies show that proteins such as collagen-like fibrillar protein and hydroxylated collagen in Hexactinellid play a critical role in templating the formation of biogenic silica[31,56].

It is in recent decades that the mechanical properties of biogenic silica in Hexactinellid sponges, mainly limited to *E. aspergillum*, *M. chuni*, and *H. sieboldii*, become easily accessible due to the advance in nanoindentation technique[5,6,57]. The mechanical information of modulus, hardness, and fracture toughness can be obtained from nanoindentation using various types of indenter tips[5,6,57]. Generally, the modulus of the biogenic silica is approximately half of that of the synthetic silica glass (~40 GPa v.s. ~75 GPa) while the hardness is ~1/3 of that of the synthetic glass (~3 GPa v.s. ~10 GPa), which is a result of organic composition and hydration[5,6]. For *M. chuni*'s giant spicule, the linear fracture toughness of the monolithic biogenic silica is smaller than that of the monolithic synthetic silica which may be a result of decreased modulus and hardness (0.35 $MPa\sqrt{m}$ v.s. 0.53 $MPa\sqrt{m}$)[5]. Yet, the fracture toughness of the laminated biogenic silica is 1.4 folds of that of the monolithic biogenic silica (0.84 $MPa\sqrt{m}$ v.s. 0.35 $MPa\sqrt{m}$) and the threshold load of crack initiation is improved by ~100 fold (5 mN v.s. 500 mN) compared to the monolithic biogenic silica[5]. In addition, as previously found for the *H. sieboldii*'s spicule, the modulus (39 GPa to 33 GPa) and hardness (2 GPa to 1.6 GPa) values of biogenic silica decrease from the core to the periphery region[57]. This result of mechanical gradient was attributed by the authors to the decreasing silica layer thickness and hence increasing content of organics. However, to provide substantial evidence for the question whether mechanical gradients exist throughout the spicules, careful correlation between measured mechanical values and measured locations should be conducted.

Therefore, this dissertation explores this in details via a variety of multiscale structural and mechanical characterization methods, which expands our understanding of compositional and mechanical properties in various Hexactinellid sponges.

2.2.3. Structure, formation, and mechanics of spicule

Spicule, or silica rod, is the basic microscale building block of the skeleton of Hexactinellid sponge[21]. The spicules investigated mostly are individual spicules from the basalia spicules or more commonly known as anchoring spicules.

For a single anchoring spicule in Hexactinellid sponge, its structure usually exhibits a cylindrically laminated structure where a central solid cylinder with squared axial proteinaceous filament is surrounded by a number of hydrated silica rings separated by organic interface (**Fig. 2.2.3**). These spicules could be as small as a few tens of microns (e.g., *E. aspergillum*) or as large as a few centimeters (e.g., *M. chuni*) in diameter which varies from species to species. Currently, comprehensive statistical measurements on the silica layer thickness have only been performed on the spicules from *M. chuni* and *E. aspergillum* which demonstrate a decreasing layer thickness from the core to the periphery of the spicule[5,6,58]. However, this trend is not consistently obeyed by the giant spicules of *M. chuni*[59].

The formation mechanism of the multilayered spicules has been studied based on the observations of the basal spicule's architecture and morphogenesis. As most of the studied is based on the species of *M. chuni*, the formation of spicule is discussed based on this species[59–61]. At the beginning, the axial filament and the first layer of biogenic silica (or the cylindrical core layer) are believed to form intracellularly in the sclerocytes. The

silicasome is hypothesized to be the vesicle to transport precursor such as silicic acid which is further enzymatically polymerized to form amorphous and hydrated silica by the proteins such as silicatein. In the meantime, the galectin forms the network for the silica deposition to grow the silica core of the spicule around the axial filament. Later, as *M. chuni* has giant spicule with diameter of more than a centimeter, the spicule growth become extracellular. However, this may not be true for spicules with micrometer diameters such as the anchoring spicules of *E. aspergillum*, for which the entire growth process could be intracellular. Furthermore, the spicule is grown in longitudinal direction via the extension of the axial filament and deposition of silica at the tip which is supported by the high concentration of silicatein around the tip of spicule[59]. Thirdly, it is postulated that a cylindrical cage is first formed by the silicatein and lectin molecules to deposit silica layers around the core, which grows the spicule in the diametric direction. These multilayers are initially thin and then merge into one silica layer through a bio-sintering process which can be demonstrated by the observation of the spicule at different stage and supported by the traces within each lamellae due to the easily-etched area with higher hydration (**Fig. 2.2.3**)[62]. Finally, how these cages are formed is also of interest. Initially, the cage is believed to start forming at the tip of spicule and grow downward along the previous layer, which repeats to form multiple silica layers[59]. However, recent investigation found structural characteristics, including step surface, patches of silica, and thinner tip than other part of the spicule, which demonstrate that the new layers can be deposited anywhere and grow towards the tip and end of the spicule[61].

Through theoretical and experimental explorations, this cylindrically laminated structure is proved to provide enhanced mechanical performance such as improved

flexibility, bending strength, and fracture toughness[5,49,58,63–65]. Specifically, by allowing the sliding between weak organic interfaces, the anchoring spicule of *E. aspergillum* has ~140% improvement (0.0377 v.s. 0.0158) of the bending strain prior to failure compared to the spicule with monolithic biogenic silica from demosponge *Tethya auratia*[65]. In addition, a theoretical optimization process of layer thickness in terms of bending strength show that the layer thickness gradient found in *E. asperigllum*'s anchoring spicule represents an optimal stress redistribution and hence bending strength[58]. In specific, the peak stress of each silica layer equals to the failure strength of biogenic silica at the onset of spicule failure, meaning that the cylindrical layers and core cylinder start to break all at once. The strength increases with increasing layers compared to the monolithic spicule (up to 25% not considering the cylindrical core), while, compared to other thickness gradient, this enhancement becomes marginal (<1%) as the number of layers exceed 30[58]. With such advantage, the motivation of constructing a large cylindrical core in the spicule may not be explained from a mechanical point of view but the optical ones: the core provides efficient light transmission within the spicule and hence bioluminescent effect[47,57]. Furthermore, whether spicules in Hexactinellid sponges generally utilize such strategy of decreasing layer thickness gradient for enhanced mechanical performance is largely unknown due to the lack of systematic and comprehensive structural measurements of other sponges.

The fracture toughness is found to be increased for the spicule with multilayered structures compared to monolithic spicule or glass rod[5,63,64]. However, recent investigation argued that the cylindrically laminated structure may not be an efficient template for enhancing fracture toughness (2-fold increase) compared to the planar

laminated structure in Nacre (1000-fold increase)[64]. This is because the cylindrical laminated structure suppresses the intrinsic toughening mechanisms such as crack arrestment by the interface and crack re-nucleation[64,66]. Moreover, since the proposed mechanism is computation-based, the visualization of deformation and fracture process of the spicule is still required to confirm whether the Cook-Gordon mechanism is absent[66]. Recent in-situ SEM tensile experiments have been performed on the anchoring spicule of *E. aspergillum*, which found crack arrestment mechanism. Yet, the contribution of this mechanism to the material toughness has not been quantitatively understood[67]. One may argue that the conclusion of suppression of Cook-Gordon mechanism is due to their boundary conditions used in experiments and simulations where both ends of the spicule are completely fixed. But Kochiyama and Fang et al. recently published follow-up papers and demonstrated that the this is a reasonable BC to use compared to the condition where both ends are simply supported[68,69]. The previously observed sawtooth behavior in the load-deflection curves for the bending of laminated spicules is correlated with the slipping between the sample surface and support, instead of the successive layer-by-layer fracture behavior. The kinetic energy due to slipping cannot be accounted as a part of the material toughness, and thus, the bending with both ends fixed provides a valid way of observing the existence of Cook-Gordon mechanism for laminated structure. This series of work alarms us about the conditions we used in the bending experiments on the spicules to obtain the accurate properties.

2.2.4. Macroscale structures of *Euplectella aspergillum*: structure, formation, and functions

As shown in **Fig. 2.2.2**, the macroscale skeletal lattice and sieve plate in *E. aspergillum* show delicately 3D architectures of lattice structures. While current knowledge on the dictyonine skeleton in other Hexactinellid sponges is limited, the cylindrical skeleton of *E. aspergillum* has been investigated in terms of its architecture, mechanical and hydrodynamic performances. Here, two components of the skeleton of the *E. aspergillum* are discussed: i) the cylindrical lattice which is a rectangular lattice with double-diagonal arrangement with helical ridge structure, and ii) the sieve plate which is a spicule-based Voronoi-like cellular lattice covering the osculum of *E. aspergillum*, as shown in **Fig. 2.2.2**[21].

The cylindrical skeleton is usually considered as a rectangular lattice with a special double-diagonal reinforcement and a helical strake-like ridge surrounding the cylindrical lattice[21,30,70]. First of all, the rectangular lattice has longer branch in the longitudinal direction of the cylindrical skeleton than the circumferential branch[71]. The size and aspect ratio of the rectangular lattice remain nearly consistent throughout the entire skeleton and among different individuals[71]. The number of rectangular cells slowly increases from the bottom to the top of sponge by splitting the longitudinal branches, which results in the relatively consistent size and aspect ratio of the rectangular lattice[71,72]. Secondly, the double-diagonal reinforcement presents at every two rectangular lattices in both longitudinal and circumferential directions of the cylindrical skeleton, leaving a large opening every two rectangular lattices[21,70,71,73]. This diagonal configuration may provide opening hole for fluid transport from the exterior to interior of the sponge for its filtering

feeding. Thirdly, the ridge structure spirals around the cylindrical skeleton and positions at every 4 rectangular lattices[21,71]. The ridge usually spirals in either one direction or in opposite directions, while the distribution of ridge shows a checkerboard-like system[71,73].

Limited studies have been carried out to explore the formation of skeletal framework, as in-situ observation and laboratory cultivation of the growth of many deep-sea sponges are challenging. This skeletal framework is a result of branching of axial filament due to the structural protein F-actin as recently demonstrated[53]. Furthermore, based on observations of sponges at different growth stages, researchers have found that the young skeleton with soft tissue scaffold and small silica spicules is first grown. Subsequently, the sponge continues to grow in its longitudinal direction until its final height while spicule-based skeleton at the bottom part continues to stiffen via secondary silica deposition to merge multiple small spicules and reach its final skeletal form[21,72]. During this stage, the meshwork of skeleton at the soft part, including the sieve plate at the osculum, allows the symbiotic shrimp to get in and out freely, implying that the pore is large and the soft meshwork can be deformed[72]. Finally, the entire skeleton becomes stiffened and fully grown which encloses the symbiotic shrimps inside.

The mechanics of the cylindrical lattice and the ridge structure have been previously explored. Fernandes *et al.* designed 2D models mimicking the cylindrical lattice and revealed an improved and optimized buckling strength via the use of the unique double-diagonal configuration[70]. In addition, Li *et al.* focused on the three-dimensional (3D) bio-inspired lattice of the sponge skeleton and found that the sponge skeleton with a double-diagonal configuration has a better strength-to-weight ratio compared to the cylindrical honeycomb hollow lattice [74]. However, their bio-inspired design of ridge structure does

not resemble the actual sponge skeleton with ridges, which renders the result incapable of explaining the mechanical function of the ridges in the sponge. In contrast, Fernandes *et al*. provided bio-inspired models of lattice-based ridge structures and demonstrated the ineffective contributions to the mechanical performance yet significant contribution to the hydrodynamics of the sponge[73]. The gap of research about the cylindrical skeleton remains is a systematic and parametric study on the effect of the sponge's skeletal structure on the mechanical properties under various loading.

The glass sponge skeletons not only provide mechanical support, but also have a fluidic function due to the filtering feeding nature of the sponge[34,35,73,75]. Specifically, the ridge structure is found to suppress the vortex shedding that the induced vibration highly unfavorable in engineering[73,75–78]. Moreover, Fernandes *et al*. found that the ridge performs better in a less porous cylinder in suppressing the vortex shedding which is the case of the live sponge with small multiscale holes[73,79]. More importantly, the ridge structures on the cylindrical lattice are optimized for suppressing the vortex shedding in the *E. aspergillum* sponges compared to the ideal biomimetic ridge designs which either spirals along one or opposite directions[73]. However, fluid-structure coupling on the sponge skeleton with ridge structure requires further study to answer how the ridge plays a role in resisting current-induced pressure.

Sieve plate is a unique cellular lattice structure in the Hexactinellid sponge which has only been briefly and qualitatively described (**Fig. 2.2.2**). The osculum of the sponge is to pump out the filtered current water, which makes us question the mechanical or fluidic purpose of the covering this osculum via sieve plate structure. The macroscale Voronoi-like lattice of sieve plate is constructed by a spicule-based spot-soldering fused silica

lattice in microscale which seems to provide smooth transition between the macroscale connections. This multiscale hierarchical structure has never been studied for its detailed structures, mechanical purposes, and formation process. The exploration of this structure may inspire a design of multiscale hierarchical lattice with a unique microscale fiber-based lattice.

2.2.5. Current knowledge gaps

The previous subsections explicitly show the current knowledge gaps for the structural and mechanical research on the multiscale hierarchical structures of the Hexactinellid sponges. Here, these gaps are summarized in different length-scales as follow:

- Nanoscale:
    1. Current technologies limit the direct observation and study of biosilification in Hexactinellid sponges;
    2. Insufficient structural and mechanical explorations on the biogenic silica of Hexactinellid sponge hinder our understanding of the structure-mechanics correlation in nanoscale such as the unconfirmed structural and mechanical gradient.
- Microscale:
    1. The sieve plate's spicule-based structures, including spicule's morphologies, thickness, and distribution, has never been analyzed.
- In macroscale,

1. A parametric and systematic study is still required to complete our understanding of the stiffness properties or potential optimizations of the cylindrical body of *E. aspergillum*;
2. The quantitative structural and mechanical study on the sieve plate's Voronoi-like cellular lattice is null.

Although this dissertation is not able to fully resolve the knowledge gaps above, current knowledge and gaps provide the fundamentals and motivation for this dissertation to study the structure-mechanics relationship in the biomineralized lattice of Hexactinellid sponges with a multiscale hierarchical structure.

2.3. Fundaments of echinoderms: Sea urchin and starfish

2.3.1. Introduction to echinoderms

Echinoderm, a name from Greek word for "spiny skin", is a common name for any member belongs to the phylum Echinodermata, including five main classes: Echinoidea (sea urchins and sand dollar), Asteroidea (starfish), Holothuroidea (sea cucumbers), Ophiuroidea (brittle star), and Crinoidea (sea lilies)[80,81]. The skeletons of these echinoderms (e.g., echinoid test, sea urchin spine, and ossicles in starfish), made of Magnesium-bearing calcium carbonate (Mg-calcite, $(Ca_xMg_{1-x})CO_3$), exhibit biomineralized cellular structures of various types from species to species[2,81–84]. The echinoderm's skeletons have attracted significant attentions to study their structures and mechanics due to the high strength and toughness (see the so-called "graceful failure" in **Fig. 2.3.1**) despite of the brittle constituent (mineral content > 99 wt%). As introduced earlier, achieving high toughness for brittle ceramic lattices is exceptionally challenging

especially in relatively low porosity. Therefore, the exploration of the 3D structures and mechanics in echinoderm's skeletons allow the extraction of biological strategy for the design and fabrication of ceramic lattices with improved strength and toughness.

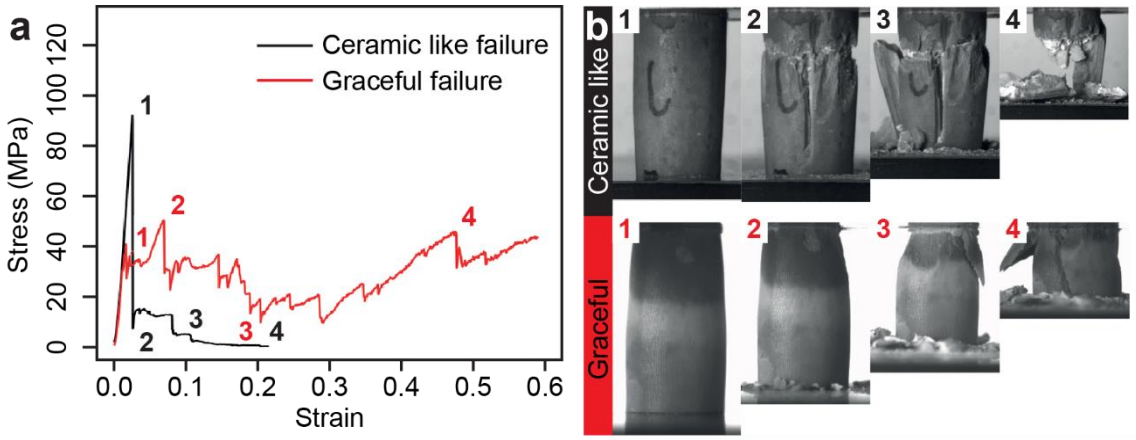


Figure 2.3.1. Mechanical behavior of the sea urchin spine from *H. mammillatus*. (**a**) Stress-strain curves demonstrate the ceramic like failure and the graceful failure. (**b**) The consecutive deformation and fracture process of the sea urchin spine. Adapted from[85].

Unlike the classical multiscale hierarchical structure in the biomineralized lattice of Hexactinellid sponges, the echinoderm's skeletons at least present two distinct categories of multiscale structures: 1) Multiscale functionally graded structure; and 2) Multiscale periodic lattices with atomic-scale architecture and dual-scale crystallographic coalignment[2,4]. Different from the amorphous nature of the biogenic silica in Hexactinellid, the calcite in echinoderm's skeleton, despite the organic occlusions, magnesium doping, and a nanoparticulate ultrastructure termed as meso-crystal, diffracts as a single crystal[6,84,86]. Here, in this dissertation, two species of Echinodermata that possess exoskeletons with multiscale structures as mentioned above (i.e., *Heterocentrotus*

mammillatus and *Protoreaster nodosus*) are selected to study the 3D multiscale structural features and mechanics (**Table 2.3.1**). Prior to in-depth study, the existing research on the skeletons of sea urchin spine and starfish ossicles are reviewed.

Table 2.3.1 Names and taxonomy of the echinoderms in this dissertation.

	Heterocentrotus mammillatus	*Protoreaster nodosus*
Kingdom	Animalia	
Phylum	Echinodermata	
Class	Echinoidea	Asteroidea
Order	Camarodonta	Valvatida
Family	Echinometridae	Oreasteridae
Genus	*Heterocentrotus*	*Protoreaster*
Species	*Heterocentrotus mammillatus*	*Protoreaster nodosus*
Abbreviation	*H. mammillatus*	*P. nodosus*

2.3.2. Structure and mechanics of sea urchin spines

Sea urchins (class Echinoidea) are found to have microscale lattice structures, termed as stereom, in their spines which form the protective system[80,81,87]. The stereom can be classified into ten types, including rectilinear, microperforate, laminar, galleried, labryrinthic, and etc. (**Fig. 2.3.2a**)[87]. While the sea urchin spines show significantly different stereom types in different species, they usually have i) a base and a shaft in the direction of long side; ii) a medulla (central core) surrounded by radiating layers (e.g., septum) with distinct types of stereom; and iii) growth rings (or growth layers) at the radiating layers (**Fig. 2.3.2b**).

Other than the qualitative descriptions, researchers also attempted to quantitatively describe the 3D architectures for different species and at different locations of the spine based on SEM imaging and μ-CT imaging[80,88,89]. However, in the early works, the

structural measurements based on these imaging techniques remain manual and hence provide limited quantitative structural information such as the branch thickness and length as well as porosity[80,88,89]. Still, these measurements are able to show the multiscale structural gradients (e.g., pore size or porosity variations) of the spines from the medulla to the periphery which reveals a multiscale functionally graded lattice structure. Recently, the development of cellular network analysis based on µ-CT imaging enables the extraction of quantitative structural features, including branch thickness, length, orientation, inter-branch angle, porosity, and etc., which capture the 3D internal microstructures. Despite this great step, structural analysis on a large-volume remains challenging due to the significant amount of µ-CT data and limitation of the script, which still hinders the understanding of the structural gradients in the spine[83,90].

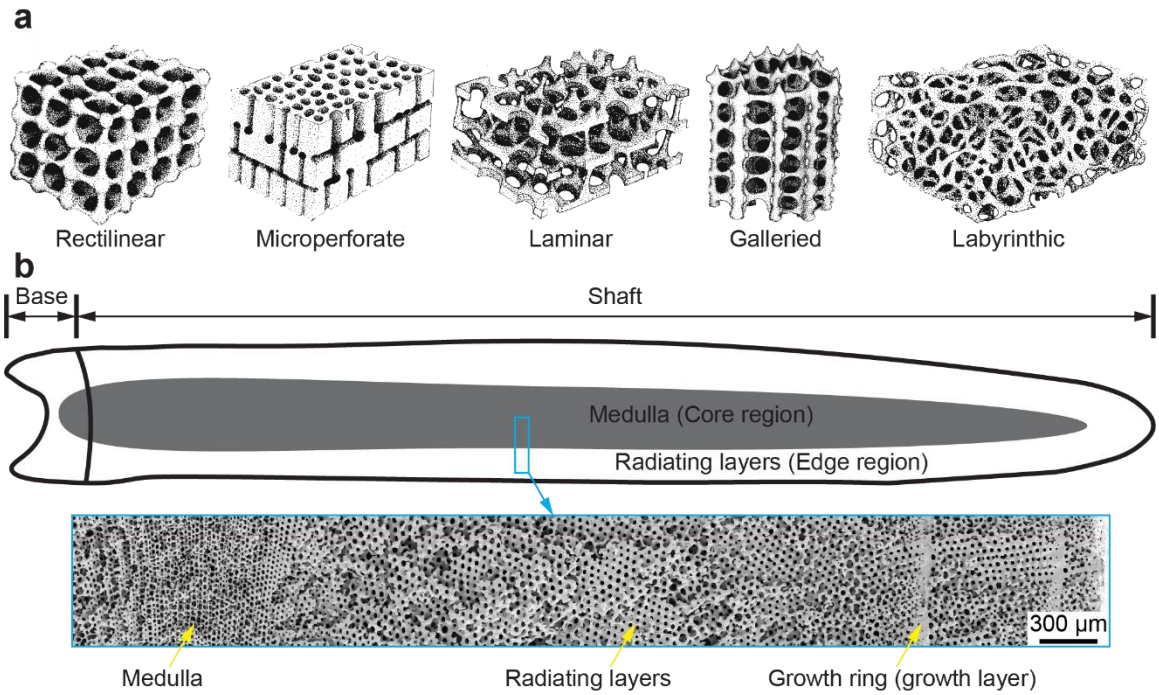


Figure 2.3.2. The multiscale structure of the sea urchin spine. (**a**) A few examples of the microscale stereom meshwork of the sea urchin spine. (**b**) The typical macroscale

arrangement of the sea urchin spine with an example of *H. mammillatus*. Adapted or modified from[87,89].

As shown in **Fig. 2.2.9**, the "graceful failure" with successive crushing and spallation mechanisms attracts much attentions in studying the mechanics and bio-inspiration of the spines. Indeed, the sea urchin spine as a protective mechanism to predators and wedging mechanism into rocks renders the spine's cellular structure an adaptation to the loading environment and, thus, a model template for designing multiscale lattices with improved strength and toughness[80]. So far, nanoindentation, compression, and bending tests have been performed on the spines to obtain the mechanical properties of the Mg-calcite and the spine[91,92]. Firstly, the modulus and hardness of the Mg-calcite in the spines typically range from 50 to 70 GPa and from 3 to 4 GPa, respectively, exhibiting a highly anisotropic and location-dependent behavior due to the single-crystalline nature of Mg-calcite and inhomogeneous distribution of Mg[93,94]. Secondly, compression tests on the sea urchin spines demonstrate strength of up to 120 MPs as well as the "graceful failure" with successive fracture, spallation, and a recently found mechanism called fragment jamming[84,85,95,96]. The strength and toughness of the spine are comparable to or higher than the metal foams considering the average porosity of >50% and brittle constituent[15]. Furthermore, even though the bulk growth ring acts as a mechanism to improve strength and induce the spallation and hence "graceful failure" during compression, the high number of growth rings is not favorable in enhancing the energy absorption efficiency[85,97]. Finally, the strength obtained from bending tests generally agree with that obtained in the compression test, yet the failure of the spine bending is rather catastrophic

as the bending behavior largely depends on the materials and structures away from the neutral axis[80,85,89]. Yet, the porosity which usually decrease from the medulla to the core with dense growth rings at the radiating layers provides a functionally graded beam design to enhance the bending stiffness and strength while maintaining a lightweight design.

These structural features, including stereom meshwork, porosity gradient, and growth rings, inspired works to build structural materials with biomimicry analogs to improve strength and toughness[95]. However, the improvement of toughness is not comparable to the actual sea urchin spine due to the lack of sufficient mimicry of the multiscale structures in the spine. This insufficient bio-inspired design is deemed to the incomprehensive understanding of the 3D internal architectures of the sea urchin spine. Therefore, the spine of *H. mammillatus* with multiscale functional graded lattice structure is selected for a comprehensive and quantitative 3D structural analysis on a large-volume from the spine[83].

2.3.3. Structure and mechanics of the starfish ossicle

The biomineralized lattice in the ossicle, a basic calcareous building block of the skeleton of starfish, represents another type of multiscale structure with atomic-scale and microlattice-scale periodic architectures. Many efforts have been made on i) understanding the microstructures of the ossicles from various species of starfish based on 2D SEM images; ii) studying the arm locomotion and ossicle loading of the starfish; and iii) generating starfish-inspired robot arms[98,99]. However, quantitative structural and mechanical characterization on the ossicles has not been conducted, therefore, the

microstructural or atomic-scale architectures in starfish ossicles and their mechanical implications for potential protective mechanisms show a large knowledge gap.

Recently, our group performed 3D quantitative structural analysis on the ossicles of starfish *P. nodosus* based on μ-CT and made significant structural and mechanical discoveries[4]:

- The ossicle presents a diamond-TPMS micro-lattice structure with approximately 50% relative density;
- Dislocations in the micro-lattice, including 60° dislocation and screw dislocation, are found in the ossicle, which provide crack-deviation mechanism to enhance the damage tolerance;
- The constituent calcite diffracts as a single crystal where the c-axis co-aligned with the [111] direction of the diamond-TPMS micro-lattice (usually the normal direction of the starfish from oral to aboral sides), while the edge formed by any two adjacent $\{10\bar{1}4\}$ cleavage planes is aligned with one of the branches not along the [111] direction of the diamond-TPMS micro-lattice.

Apart from the unique structures, the corresponding mechanical behaviors have been studied[4], which are summarized as follows:

- The ossicle has significant local mechanical variations due to the significant local structural variations (e.g., branch thickness variation of ~3μm in diameter over 6 diamond unit cells);
- Crack deflection occurs due to the dislocations in diamond-TPMS micro-lattice of ossicle;

- The ossicle exhibits stiffness compensation for the relatively weak c-axis of calcite which is crystallographically aligned with the stiff [111] direction of diamond-TPMS lattice.

First of all, the structural gradient structure in ossicles has been ubiquitously found in biomineralized skeleton[2] and artificial architected lattice[100,101], which usually provides enhanced specific stiffness, strength, and toughness. Secondly, the micro-lattice dislocations in ossicles, which provides crack deflection mechanism and hence improves the damage tolerance, has similar mechanical functions of dislocations in crystals that strengthen and toughen the metals or ceramics[102–105]. The strategy that utilize crystallographic defects in architected lattice design, has been employed into multi-grain lattices with boundaries and lattice with precipitation and honeycomb lattice with 5-7 defects which provide strengthening and toughening[106,107]. Finally, the single-crystalline constituent and the corresponding dual-scale crystallographic coalignment found in ossicle have never been considered into the design of multiscale hierarchical architected lattices[7–9,15]. Despite the existing knowledge of the mechanical function of coalignment (i.e., the stiffness compensation), the complete understanding of its mechanical function, such as the 3D dual-scale mechanical synergy, remains an open question.

2.3.4. Current knowledge gaps

Clearly, the knowledge gaps for the skeleton of echinoderms, including the sea urchin spine and starfish ossicle, are generally two-fold: insufficient 3D quantitative structural analysis and multiscale mechanical analysis. To be specific, for sea urchin:

- the cellular structures and types of the stereom in a wide range of sea urchin spines and tests are not understood in 3D;
- further quantitative large-scale volume analysis in 3D on the stereom which reveals the long-range structural variation remains a large knowledge gap;
- and, thus, the 3D local and long-range graded mechanical performances of the stereom in spine have not been sufficiently explored.

While, for starfish ossicle:

- the type and structure of dislocation cores in the micro-lattice, especially those different from the dislocations in ceramics and detailed quantitative structure around the core, are to be explored;
- and how to utilize the dislocation concept into the architected lattice and harness the mechanical benefits remains an open question;
- and, the mechanical function of the unique structural concept of dual-scale crystallographic coalignment has not been completely understood in terms of 3D mechanical properties;
- and, therefore, how this concept can be adopted in the design of dual-scale lattice, a new class of hierarchical lattice for 3D performance is an unanswered question.

In this dissertation, as model systems for multiscale biomineralized lattices other than the Hexactinellid sponges, the structure-mechanics relationships of the sea urchin spine and starfish ossicle as indicated above are explored. In addition, corresponding analysis and modeling techniques are developed.

2.4. Motivations and challenges

Briefly speaking, reviews in the previous sections reveal the insufficiency in understanding the multiscale structures of biomineralized lattice, specifically in the Hexactinellid sponges and echinoderm, which hinders the comprehension of their functions. The unique architectures in biomineralized lattices which are formed driven by the evolutionary forces may inspire novel structural pathways in multiscale for, for examples, improved damage tolerance despite of the high mineral content and nanofabrication of cellular lattices. This motivates this dissertation to study in detailed the multiscale structures and mechanics of biomineralized lattices.

To explore these multiscale structures and mechanics, advanced experimental and computational techniques are significantly important. In nanoscale and microscale, structural analysis techniques such as SEM, EDS, Raman, and etc. are particularly important. These techniques have extensively been utilized in understanding the composition and structures of constituent materials of biomineralized solids, such as biogenic silica[6,38,39], calcite[93,108–110], and aragonite[111–113]. Yet, exploring the 3D architectures and deformation evolution of the biomineralized lattices with high-resolution visualizations is still challenging. In this dissertation, an important technique is utilized, which is in-situ μ-CT mechanical testing (**Fig. 2.4.1**). These techniques not only provide high-resolution structural visualizations, but also characterize the 3D deformation evolution which substantially correlates the mechanical behavior with the 3D structures. Furthermore, computational modeling of each model systems in multiscale need to be developed, which is challenging to incorporate the biological principles, such as the

double-diagonal structure in Hexactinellid sponge, dislocation defects and dual-scale microlattice inspired by starfish ossicle.

This dissertation selects three representative types of biomineralized lattices for studying their multiscale structures and mechanics to provide bio-inspirations of ceramic lattices. They are, as summarized in **Fig. 2.4.2**, **Table 2.2.1** and **Table 2.3.1**, the Hexactinellid sponges (multiscale hierarchical lattice), the sea urchin spine of *H. mammillatus* (multiscale functionally graded lattice), and the ossicle of starfish *P. nodosus* (multiscale hierarchical lattices with atomic-scale architecture and dual-scale crystallographic coalignment).

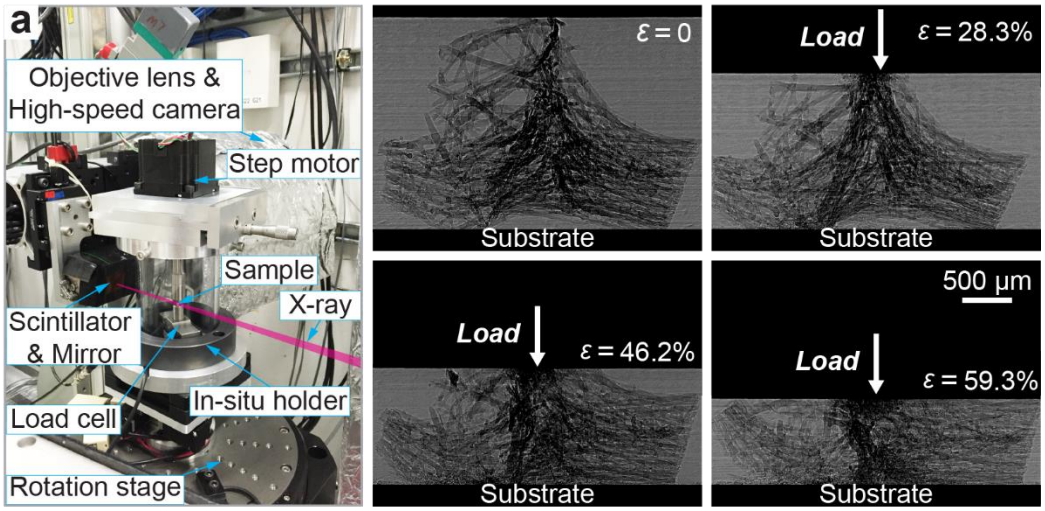


Figure 2.4.1. Synchrotron-based in-situ μ-CT mechanical testing device.

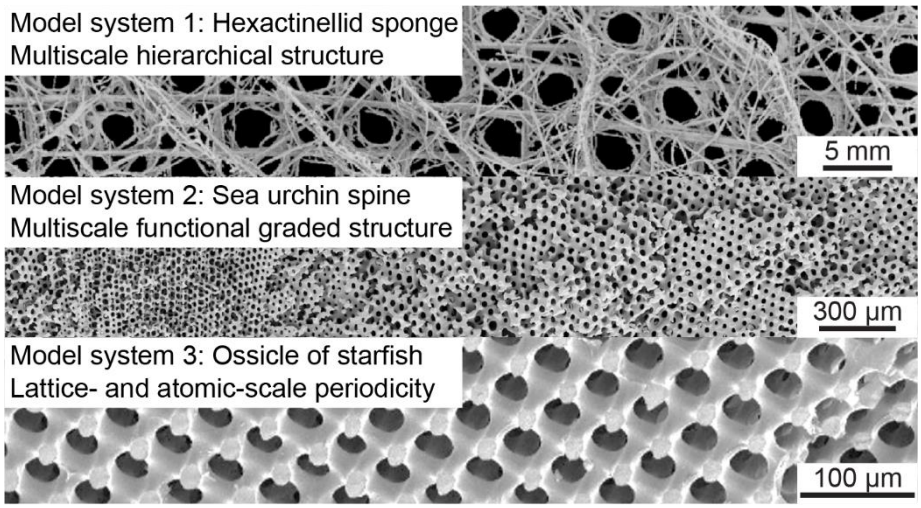


Figure 2.4.2. Three model systems of biomineralized lattices, including the spicule skeleton of Hexactinellid sponge, sea urchin spine of *H. mammillatus*, and ossicle of starfish *P. nodosus*, analyzed in this dissertation which represent three different classifications of multiscale biomineralized lattices: multiscale hierarchical structure, multiscale functional graded structure, and periodic lattice with lattice- and atomic-scale architectures and coalignment.

Chapter 3 Compositional and mechanical analysis of biogenic silica in three species of Hexactinellid sponges

H. Chen, Z. Deng, H. Ehrlich, L. Li, Compositional-mechanical analysis of the biogenic silica in anchoring spicules of three Hexactinellid sponges. In preparation.

Hexactinellid sponges consists primarily of brittle biogenic silica. Existing research on the mechanical and compositional investigations of biogenic silica has been focused on few model systems, while systematic quantitative correlation between the nanoscale compositions and mechanical properties remains limited. Here, this work investigates the nanoscale compositions and mechanics of three species of Hexactinellid sponge, *Corynonema populiferum*, *Hyalonema sieboldii*, and *Sericolophus hawaiicus*, for comparative study. Firstly, observation reveals that the cylindrically laminated silica layers separated by organic interfaces of the cross section of the spicule which show no gradients of the thickness gradient. Next, the nanoindentation reveals consistent modulus and hardness from the core to periphery of the spicules, while the regions containing multiple silica layers in the spicule exhibit higher fracture toughness than the regions containing monolithic biogenic silica. In addition, the humidity condition during the experiments has negligible effect on the modulus, hardness, yet slightly decreases the fracture toughness. Furthermore, Energy dispersive X-ray analysis and Raman spectroscopy analysis show no location-dependent distributions of elements and hydration of the biogenic silica, while the interfaces between silica layers demonstrates improved hydration and organic contents. This supports the nearly consistent modulus and hardness of the cross section of spicules. This work provides not only a substantial

correlation between the measurement locations and the compositional and mechanical results, but also mechanical properties, of the anchoring spicules in three different Hexactinellid sponges.

3.1. Introduction

The multiscale hierarchical structures discovered in Hexactinellid sponges have attracted significant attentions of researchers to study their structure-property correlations[5,6,21,41,58,70]. These glass sponges (class Hexactinellida) typically consist of a skeletal body and anchoring spicule bundles primarily made of brittle biogenic silica[21,41]. The mostly investigated species of glass sponges are *Monorhaphis chuni* and *Euplectella aspergillum*. They exhibit multiscale structures, from the centimeter-scale silica-based skeleton to the microscale cylindrically laminated anchoring spicules, demonstrating lucrative model systems for bioinspired design of lattice materials and composite beam[6,21,58]. Studies of biogenic silica in Hexactinellid sponges and some demosponges, including the nanoscale compositions, mechanics, and biosilification, are of particular interest due to the their nanoparticulate forms with hydration and silica synthesis in ambient conditions[6,21,31,38,39,43,52].

The nanoscale compositions and structure of the biogenic silica of glass sponges has been investigated using various of characterization methods including Scanning Electronic Microscopy (SEM), Small-angle X-ray scattering (SAXS), Raman spectroscopy, Energy-dispersive X-ray spectroscopy (EDS), X-ray diffraction (XRD), and etc[6,21,40,44,48]. The biologically formed silica glass composed of consolidated silica nanospheres with diameter of 50~200nm (measured from SEM images), while the silica nanosphere itself is amorphous (lack of long-range crystallinity) based on SAXS and XRD study[6,40,114]. Furthermore, a size gradient of the silica nanoparticles from the periphery to the core of the spicule of *E. aspergillum* has also been found under SEM[1,6]: the mean particle size gradually decreases from the periphery (187 ±

34 nm) to the core (48 ± 9 nm). Furthermore, through Raman measurements, researchers found that the chemical bonds' vibration modes of biogenic silica generally agree with the those found in the synthetic silica, except for the hydrated silica (Si-O-H) and organics (e.g., Amide, C-H)[6,40,115]. Finally, EDS measurements have also been performed on the biogenic silica and revealed various elements such as Silicon (Si), Oxygen (O), Carbon (C), Sodium (Na), and Potassium (K) which has been confirmed by SIMS measurements [44,46–50]. Among the measurements, Kul'chin et al. have revealed a gradient of various elements from the periphery to the core on the spicule of *H. sieboldin* sponge, which may be correlated to the mechanical gradient found in the same sponge[48,57].

However, careful correlations between compositional or mechanical measurements and location of these measurements are still required to provide substantial evidences to such gradients. Bearing with this motivation, in this work, I systematically study the nanoscale structures and mechanics of the anchoring spicules from three Hexactinellid sponges, *C. populiferum*, *H. sieboldin*, and *S. hawaiicus*. The modulus, hardness, and fracture toughness are measured for the spicules using nanoindentations with Berkovich and cub-corner tips, respectively. These measurements are made under ambient conditions and 90% humidity conditions, respectively. Furthermore, compositional scanning on the entire cross sections of spicules are conducted to correlate with the mechanical properties. Here, the correlation between the measurement locations and results provides unambiguous understanding of the spicule's structural-mechanical properties.

3.2. Materials and Methods

Sample preparation: Anchoring spicules were obtained from three different species of Hexactinellid sponges: *C. populiferum* (COP), *H. sieboldin* (HS), and *S. hawaiicus* (SH) (**Fig. 3.1**). The spicules were cut into segments with length of ~10 mm and then embedded into epoxy. The embedded samples were polished using the MultiPrep^{TM} Precision Polishing System (Allied High Tech Products, Inc., California, USA) with diamond lapping films with decreasing particle sizes (15 µm, 9 µm, 6 µm, and 3 µm) and finally 40 nm colloidal silica suspension on a polishing cloth. The polished samples were subsequently cleaned using micro-organic soap, rinsed using de-ionized water for at least 10 times, and sonicated in de-ionized water for 15 minutes. A set of the embedded spicule samples was immersed in the de-ionized water for a week, which was used in the nanoindentation under 90% humidity condition to study the effect of hydration.

Two types of synthetic glass were prepared for the indentation experiments as control groups: i) microscope glass slides purchased from Ted Pella Inc. (California, USA); and ii) silica glass fabricated using fumed silica nanoparticles purchased from Sigma-Aldrich (MilliporeSigma, Missouri, USA). The fumed silica particles (200g) were first mixed with dissolved Polyvinylpyrrolidone (PVP, 10g) solution (500ml deionized water) which was sonicated for 10 minutes. The mixed solution was then distilled to obtain the hydrated silica-PVP samples. The hydrated samples were first dried under 70°C for 24 hours and, secondly, abraded into powders. The powders were compressed in an oil-pump compressor under 130°C and 40 MPa for 10 minutes. Finally, the compact samples were sintered at approximately 1000°C for 10 minutes to obtain the synthetic fused silica.

Moreover, some samples (not embedded) of anchoring spicules were etched in the NaClO solution (5.25vol%) for examining the silica nanoparticles, location of axial filament, and organic interfaces under SEM.

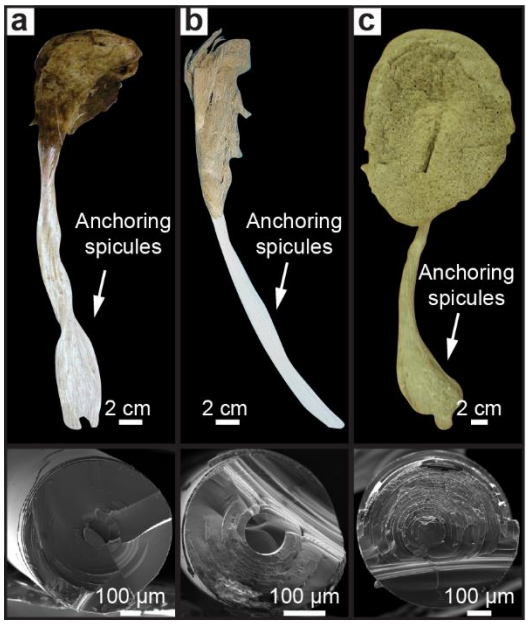


Figure 3.1. Anchoring spicules of three species of Hexactinellid sponges. (**a-c**) Anchoring spicules of (**a**) *C. populiferum*, (**b**) *H. sieboldin*, and (**c**) *S. hawaiicus*, respectively.

Nanoindentation: Instrumented nanoindentation (NanoTest Vantage platform 4, MicroMaterials, Inc., UK) was used to perform nanoindentation experiments on the synthetic and biogenic silica samples which are embedded in epoxy. All samples were mounted onto the indentation stage and under thermal balance for 3 hours prior to testing. The nanoindentation experiments were conducted on the anchoring spicules from COP, HS, and SH sponges as well as the synthetic silica samples. The nanoindentation on biogenic silica from the anchoring spicules were under both ambient and 90% humidity

condition, respectively. The experimental setups for synthetic glass and biogenic glass were summarized in **Table 3.1**. Two types of indenters, including Berkovich tip and cub-corner tip were used to study the mechanical properties of the synthetic and biogenic silica. Berkovich tips was used to measured modulus and hardness under 2 mN load for ambient condition and 90% humidity condition. The samples for nanoindentation under 90% humidity condition were confined in a customized closed , which were immersed in the de-ionized water for a week, space which maintains the humidity throughout the experiments. Line scans were carried out, and each indent was separated by 4 μm to avoid the effect of neighboring indents. For each species, two samples where one with large diameter while another with small diameter, were prepared for Berkovich nanoindentation. In addition, the cube-corner tip was used to measure the indent size and crack size with an increasing load from 1 to 500 mN for calculating fracture toughness under both ambient and 90% humidity conditions. The indentation loads using cube-corner tip were 1~9 mN with 1 mN interval, 10~90 mN with 10 mN interval, 100~500 mN with 100 mN interval.

Table 3.1 Nanoindentation experimental setup for both biogenic and synthetic silica.

Samples		Humidity	Berkovich tip	Cube-corner tip
Biogenic silica	COP spicule	Ambient 90% humidity	1 mN	1-500 mN
	HS spicule	Ambient 90% humidity	1 mN	1-500 mN
	SH spicule	Ambient 90% humidity	1 mN	1-500 mN
Synthetic silica	Microscope glass slide	Ambient 90% humidity	1 mN	1-500 mN
	Fumed silica	Ambient 90% humidity	1 mN	1-500 mN

Calculation of the mechanical properties: Load-depth curves for Berkovich tip indentation were obtained to automatically extract the reduced modulus and hardness values in the nanoindentation system. To convert the reduced modulus into elastic modulus, the following equation was used:

$$\frac{1}{E_r} = \frac{1 - v_{indenter}^2}{E_{indenter}} + \frac{1 - v_{silica}^2}{E_{silica}} \qquad (3.2.1),$$

where E_r is the reduced modulus, $E_{indenter}$ and E_{silica} are elastic modulus of the indenter (diamond, 1141 GPa) and biogenic silica, $v_{indenter}$ and v_{silica} are Poisson's ratio of the diamond indenter (0.07) and silica (0.17).

Calculation of the fracture toughness involves the measurements of the indent size (a) and crack size (c) caused by the cub-corner indentation. The schematic of the indent size and crack size measurements was shown in **Fig. 3.2**. Three different regions of the indentation identified, namely, the core region, lamellae region, and the layering region (**Fig. 3.2**). The equations to calculate the hardness and linear mode-I fracture toughness from the measured indent size and crack size are:

$$\log a = \frac{1}{2}\log(\frac{P}{\alpha H}) = \frac{1}{2}\log(P) + \left[-\frac{1}{2}\log\alpha - \frac{1}{2}\log H\right] \qquad (3.2.2),$$

$$\log c = \frac{2}{3}\log(P) + \left[\frac{2}{3}\log\chi - \frac{2}{3}\log K_{IC} + \frac{1}{3}\log(\frac{E}{H})\right] \qquad (3.2.3),$$

where a and c are the indent size and crack size; P is the indentation load; E and H are the elastic modulus and hardness of the indented material; α and χ are geometrical and nondimensional constants, which are 1.30 and 0.04, respectively, for cube-corner tip indenter. This method is adopted from this reference[5].

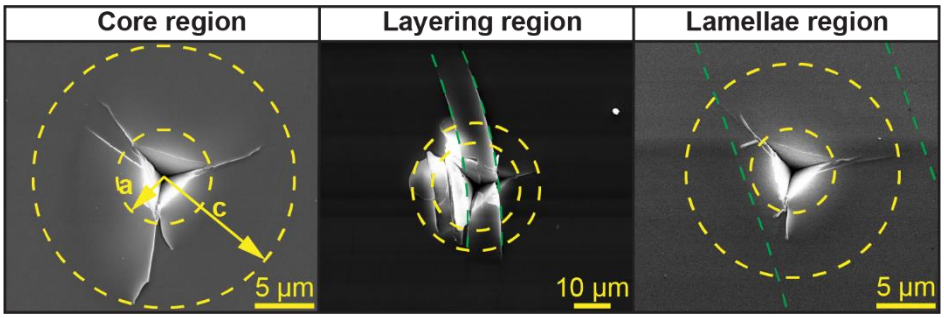


Figure 3.2. Indent locations and definition of the size measurements.

Scanning Electron Microscope: Scanning Electron Microscope (SEM) images on the samples coated with were acquired using FEI Quanta 600 FEG with a working distance of ~12 mm and a voltage of 15 kV. Prior to SEM imaging, the embedded samples of spicules were coated with ~15 nm platinum/palladium. The SEM images were mainly used to capture the cube-corner indents for fracture toughness analysis and the cross section of the spicule samples after etching in the NaClO solution.

Energy-dispersive X-ray spectroscopy: Energy-dispersive X-ray spectroscopy (EDS) data was obtained from a SEM system FEI Quanta 600 FEG in backscatter mode with accelerating voltage of 10 keV. The EDS measurements were acquired with a Bruker QUANTAX 400 with XFlash 4010 silicon drift detector and sufficient acquisition time (60s per measurement) to reach more than 20,000 counts. Bruker Esprit 2.1 software was used to analyze the EDS spectrum to obtain the elemental composition and their respective weight and atomic contents with PB Linemarker-ZAF correction.

Raman spectroscope: The embedded spicule samples were examined under a confocal Raman system (WITec, Ulm, Germany) with a 35 mW Helium-Neon laser of 633nm

(Reo Inc., Colorado, USA). The laser was first focused on the surface of the sample using a 100× (NA = 0.9) objective lens (Olympus Corp., Tokyo, Japan). Then the focus was adjusted to 2.5μm lower than the sample surface to probe the materials inside[6]. The image scans with 1 μm XY resolution were performed on the spicule's cross sections. The as-obtained Raman spectrums were post-processed via cosmic ray removal, background subtraction, and smoothing using a Savitzky-Golay filter. The post-processed data was used to peak fitting and subsequently extract the peak parameters, including peak area, peak centers, and full width at half maximum (FWHM) of the peak, for Si-O-Si symmetric stretching, hydrated silica (Si-O-H symmetric streching), and organics (Amide, C-H streching). Here, the area ratios between two different modes, including Si-O-H/Si-O-Si, C-H/Si-O-Si, and Amide/Si-O-Si, were used to represent the content ratio between the corresponding bonds[6].

3.3. Results

3.3.1. Structures of the anchoring spicules and their biogenic silica

Fig. 3.1 shows the structures of three Hexactinellid sponges COP, HS, and SH, which have distinct body morphologies yet bundles of anchoring spicules to fixate themselves to the sea floor. The SEM images of the cross sections of the spicules from three selected species, which consistently show concentrically laminated structures (**Fig. 3.1**). We measured the silica layer thickness (**Fig. 3.3-3.4**), which reveals that the layer thicknesses are not necessarily decreasing from the core to the periphery as found in *E. aspergillum*[58]. This result actually agrees with the previous finding on the giant anchoring spicule of *Monorhaphis chuni*[59]. As previously demonstrated, the decreasing layer thickness of

spicule provides optimal strength compared to other thickness variations such as the random variation of the layer thickness[58]. However, the improvement in strength seems to be marginal (< 2%) as the number of silica layers is greater than 20. Therefore, we hypothesized that the anchoring spicules with large number of silica layers provides improvement of the strength yet do not necessarily grow for optimal strength due to the marginal improvement.

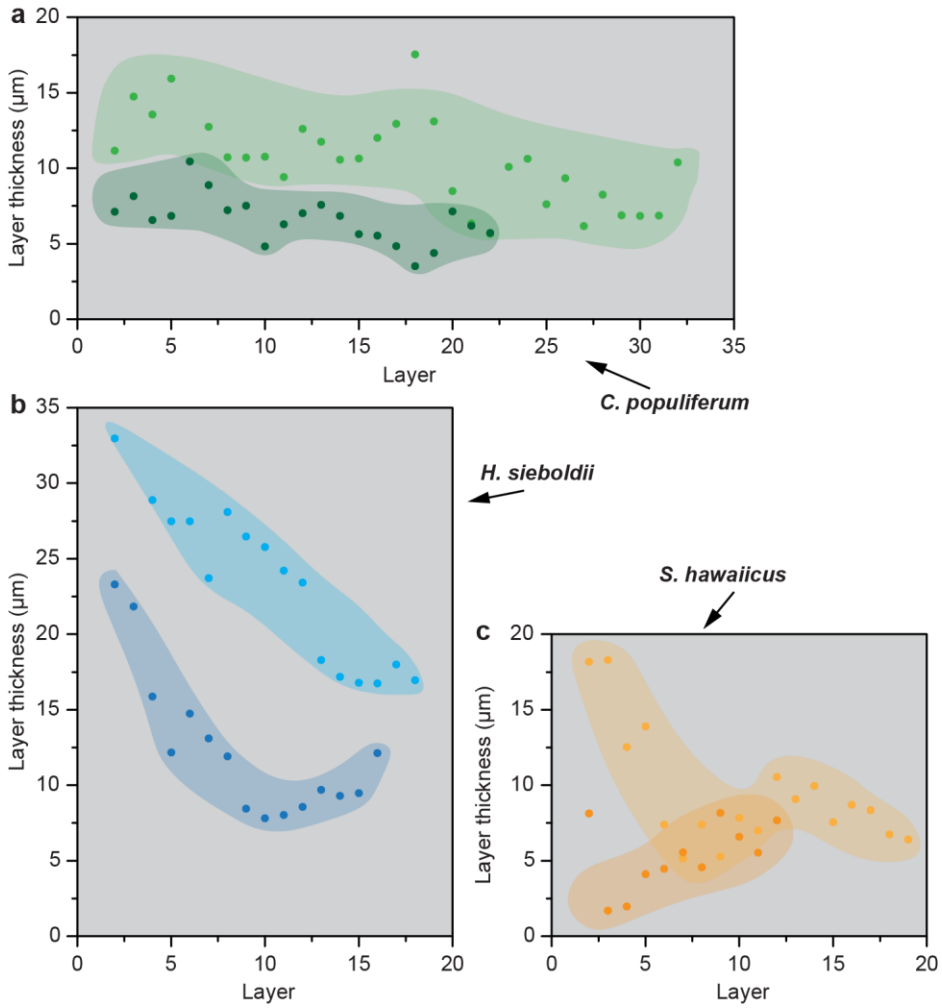


Figure 3.3. Silica layer thickness from the core to periphery of the anchoring spicules of three species of Hexactinellid sponges. (**a-c**) Silica layer thickness of the anchoring spicules of (**a**) COP, (**b**) HS, and (**c**) SH sponges, respectively.

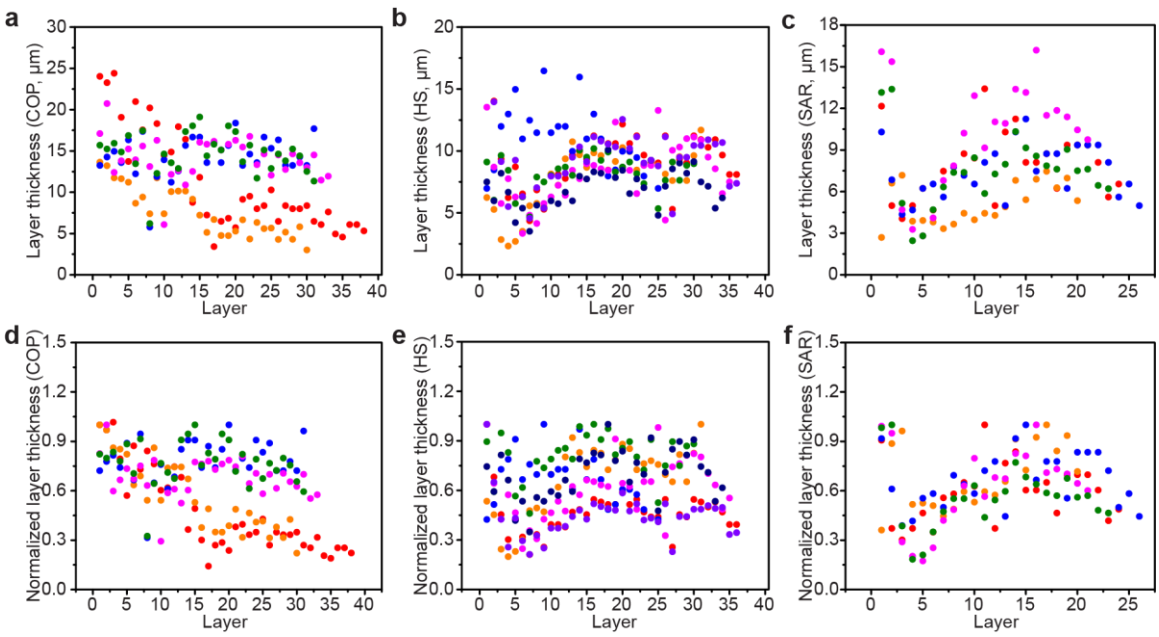


Figure 3.4. More measurements of the silica layer thickness from the core to periphery of the anchoring spicules of three species of Hexactinellid sponges. (**a-c**) Silica layer thickness and (**d-f**) normalized layer thickness by the maximal measured thickness of the anchoring spicules of (**a,d**) COP, (**b,e**) HS, and (**c,f**) SH, respectively.

After removing the interfacial organics via etching, the silica nanoparticles appear, as shown in **Fig. 3.5** as an example for SH spicule. First of all, this silica nanoparticulate structure maintains throughout the entire cross section of the spicule (**Fig. 3.5c-f**). In addition, as previously found, the biogenic silica in spicule are all in the particulate forms in the spicule of other Hexactinellid sponges like *E. aspergillum*[21]. Secondly, concentrically arranged white lines were observed within each silica layer (yellow arrow, **Fig. 3.5e**), which is a typical feature observed in the spicule of demosponges[39,116]. These lines indicate the locations of the highly hydrated silica (Q^3 and Q^2 silica species) which is more sensitive to the etching than the condensed silica (Q^3 silica species)[38,39,116]. For

spicules in class demosponge, these traces have been postulated to correlate with the secondary silica deposition away from the axial filament where the hydrated silica was first deposited followed by later condensation[39,116]. For *M. chuni* in class Hexactinellid, these traces can be considered as the original interfaces separating the silica layers which later consolidate into one layer through a process defined as bio-sintering in ambient environment[62].

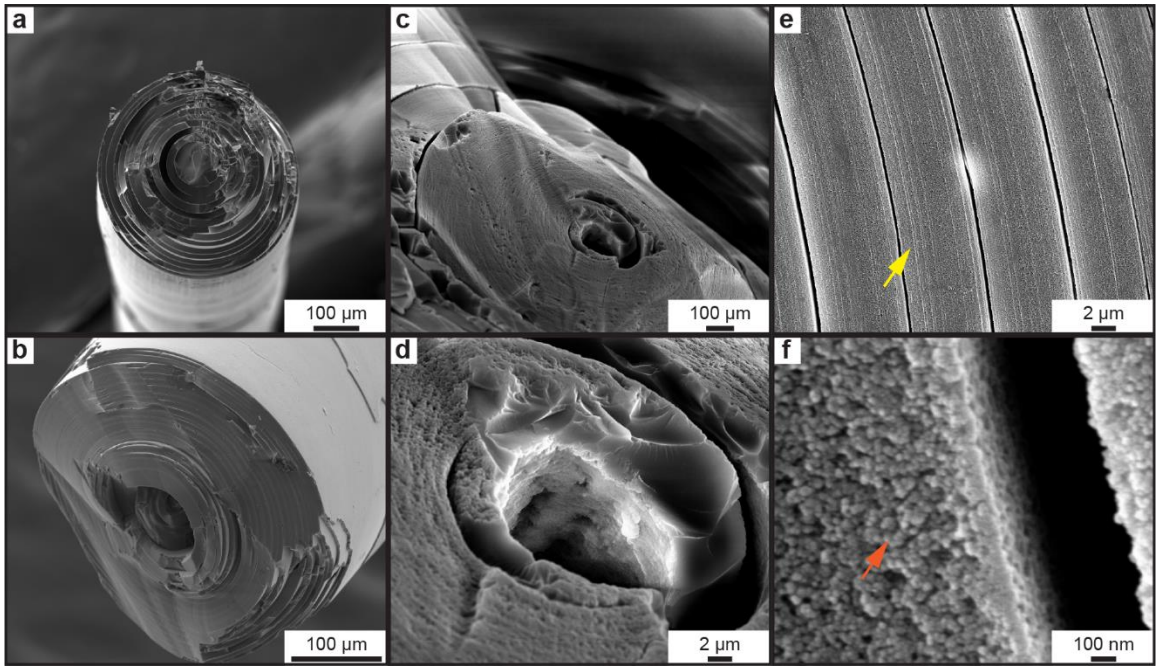


Figure 3.5. SEM images of the etched spicule and silica nanoparticles. (**a**) Unetched SH spicule. (**b**) Etched SH spicule. (**c-d**) The nanoparticulate silica at the core region of the spicule. (**e-f**) The nanoparticulate silica at the laminated region of the spicule (yellow arrow: the trace of the annually arranged etched silica nanoparticles; orange arrow: silica nanoparticles).

3.3.2. Modulus and hardness of the biogenic silica

The elastic modulus and hardness were probed using nanoindentation with a Berkovich tip under ambient and 90% humidity condition, respectively. In addition, the anchoring spicules of three sponges with large and small diameters were selected for comparative studies as they represent older and younger stages of the spicules[61,117].

For spicules from all three Hexactinellid sponges, the modulus and hardness extracted from the nanoindentation line scans from the periphery to the core to the opposite periphery of the selected spicules demonstrate a relatively consistent result for both values (**Fig. 3.6-3.8**, **Table 3.2**). Moreover, no trends of modulus and hardness were observed within the silica layer between two organic interfaces. These results disagree with the previously obtained modulus and hardness gradients in the spicule of *H. sieboldii*[57]. Previous explanation on this gradient is that the increased silica thickness from the periphery to the core implies the increased number of organic interfaces and hence organic content being indented, resulting the modulus and hardness gradient[57]. However, the indentation setup and the correlation between indented locations and measured values were not provided, which renders the gradient results ambiguous. This is also the issue for the nanoscale measurements[48]. In the later section, this mechanical result will be further confirmed from the nanoscale compositional perspective using EDS and Raman measurements.

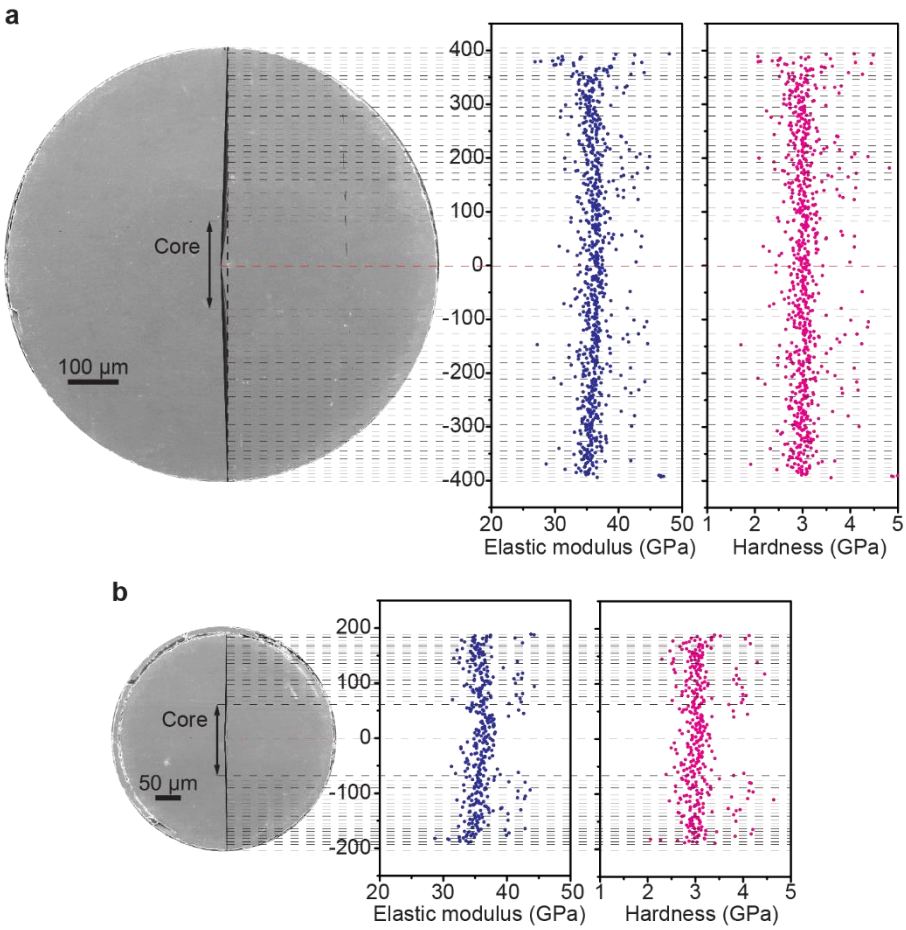


Figure 3.6. Elastic modulus and hardness of the biogenic silica of the large (a) and small (b) COP spicules.

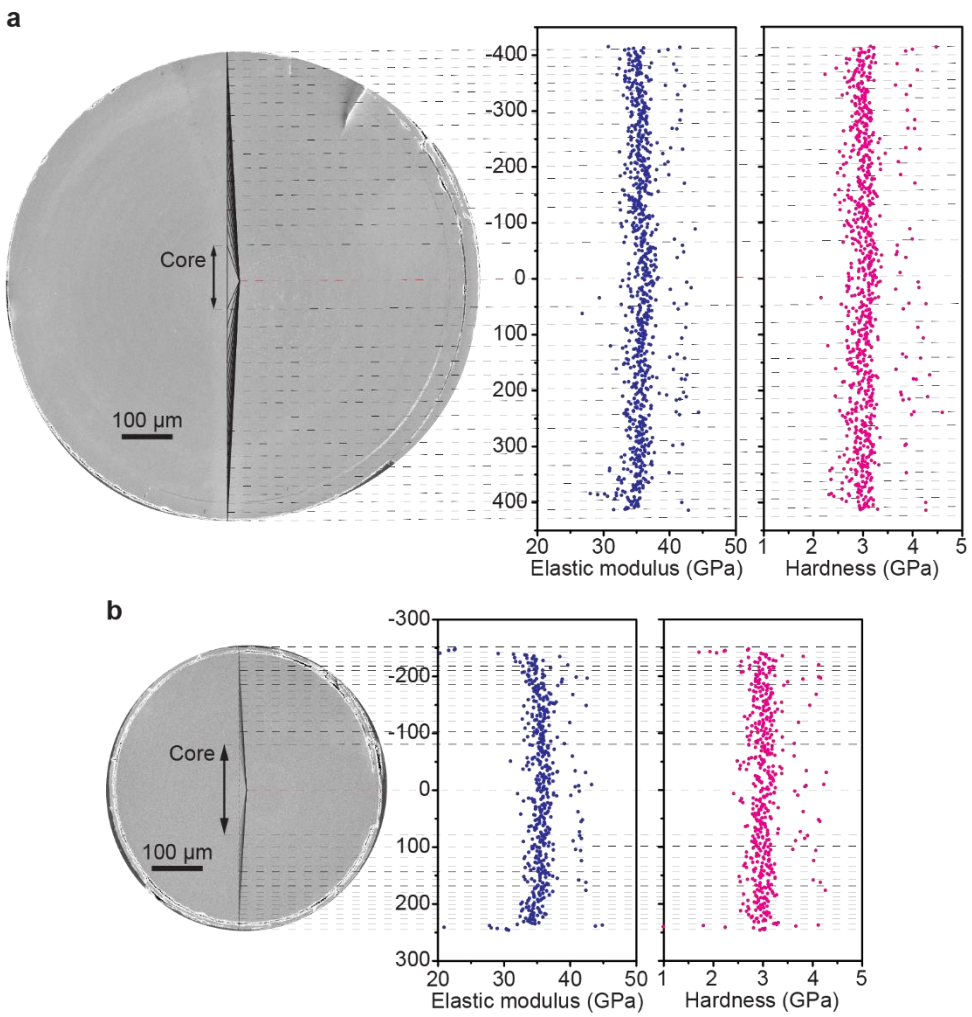


Figure 3.7. Elastic modulus and hardness of the biogenic silica of the large (a) and small (b) HS spicules.

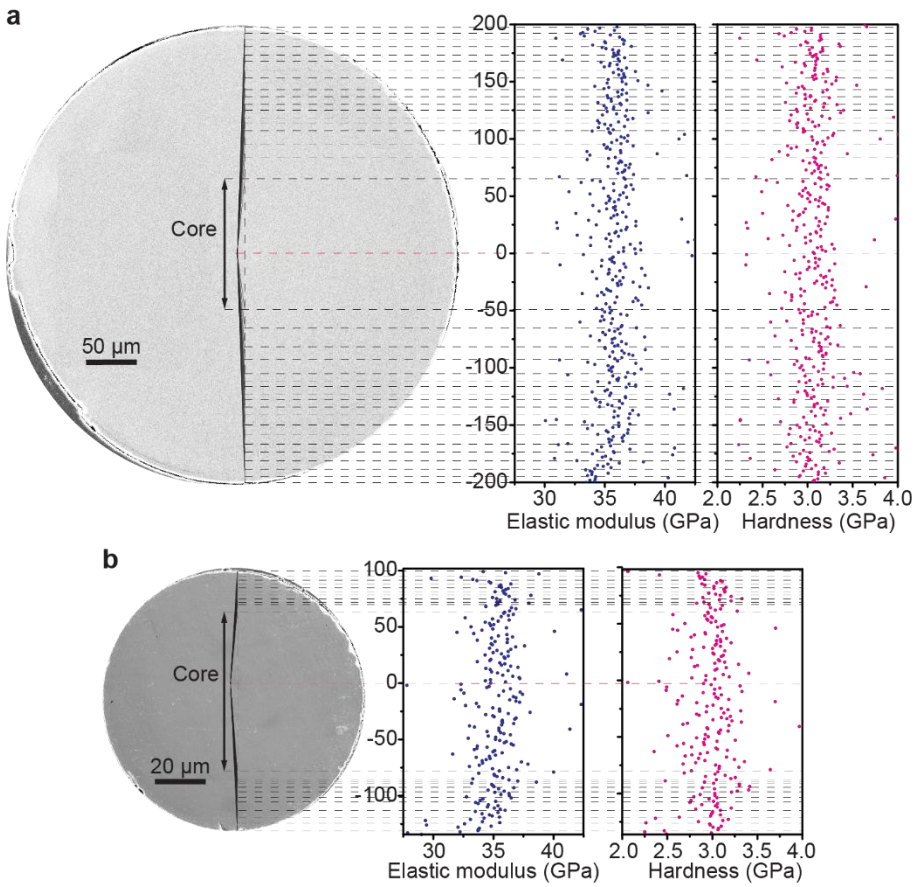


Figure 3.8. Elastic modulus and hardness of the biogenic silica of the large (a) and small (b) SH spicules.

Table 3.2. Summary of reduced modulus, elastic modulus, and hardness of biogenic silica in large and small spicules, respectively, under ambient and 90% humidity conditions, respectively.

Experimental conditions	Sample condition	Samples	Reduced modulus (GPa)	Elastic modulus (GPa)	Hardness (GPa)
Ambient	Large	COP	35.6 ± 1.9	35.7 ± 1.6	3.0 ± 0.2

		HS	35.3 ± 1.6	35.3 ± 1.6	3.0 ± 0.2
		SH	35.5 ± 1.5	35.6 ± 1.5	3.0 ± 0.2
	Small	COP	35.4 ± 1.4	35.5 ± 1.5	3.0 ± 0.2
		HS	34.5 ± 3.5	34.6 ± 3.6	2.9 ± 0.3
		SH	35.0 ± 1.5	35.1 ± 1.5	3.0 ± 0.2
90% humidity	Large	COP	36.1 ± 1.3	36.2 ± 1.4	3.0 ± 0.2
		HS	36.5 ± 1.4	36.6 ± 1.4	3.1 ± 0.2
		SH	34.6 ± 3.6	34.7 ± 3.6	3.0 ± 0.4
	Small	COP	35.1 ± 1.2	35.1 ± 1.3	3.0 ± 0.2
		HS	36.5 ± 1.5	36.6 ± 1.6	3.2 ± 0.2
		SH	35.3 ± 1.3	35.3 ± 1.4	3.1 ± 0.2

The mean values of the reduced modulus, elastic modulus, and hardness of the selected spicules were summarized along with those of the silica glass slice and synthetic silica using fumed silica particles in **Fig. 3.9** and **Table 3.3**. The modulus and hardness show similarity among different types of anchoring spicules yet approximately 50% and 66% reductions, respectively, compared to those of the synthetic silica. This agrees with the previous measurements for the biogenic silica in *M. chuni* and *E. aspergillum*[5,6,57], which was attributed to the hydration state of the silica that soften the biogenic silica. Indentations were also performed on the spicules' cross section under 90% humidity condition, which also show similar values of modulus and hardness (**Fig. 3.9d-f** and **Table 3.3**). This may be a result of three reasons: i) the extremely low content of organics within the silica layers that can

absorb the water molecules; ii) the biogenic silica is already in its hydrated and saturated status to prevent further combination with water; and iii) no living organic matters to assist the further saturation of biogenic silica.

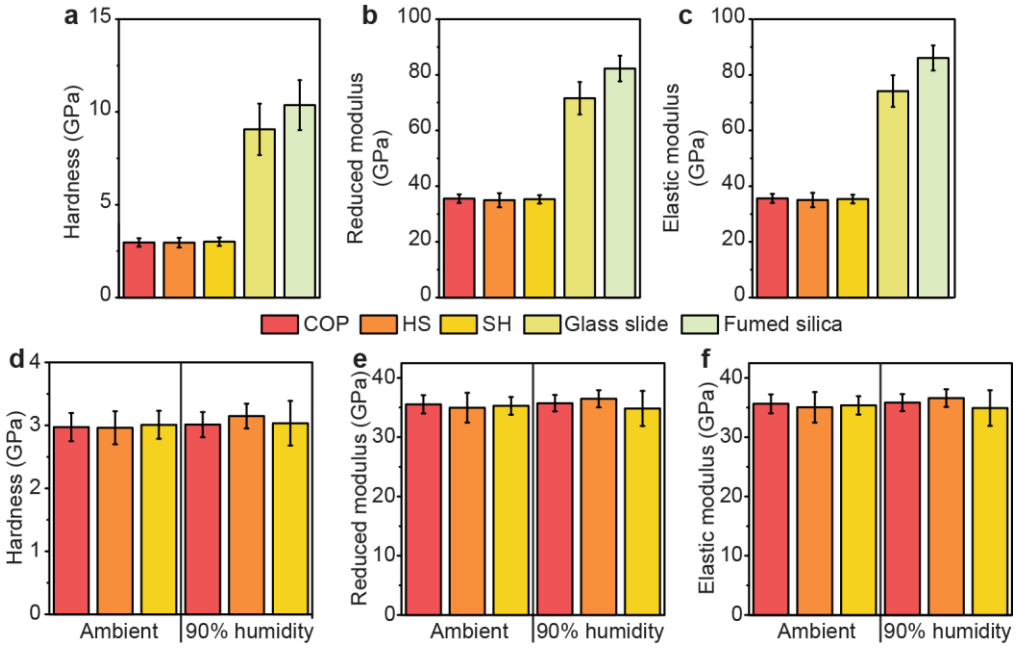


Figure 3.9. Summary of the modulus and hardness of biogenic silica in the selected spicules and the synthetic silica. (**a-c**) Means and standard deviations of the (**a**) hardness, (**b**) reduced modulus, and (**c**) elastic modulus, of the biogenic and synthetic silica, respectively. (**d-f**) Comparison of hardness (**d**), reduced modulus (**e**), and elastic modulus (**f**) of biogenic silica under ambient and 90% humidity conditions, respectively.

Table 3.3. Summary of reduced modulus, elastic modulus, and hardness of biogenic silica in spicules under ambient and 90% humidity conditions, respectively.

Experimental conditions	Samples	Reduced modulus (GPa)	Elastic modulus (GPa)	Hardness (GPa)

Ambient	COP	35.6 ± 1.5	35.6 ± 1.6	3.0 ± 0.2
	HS	35.0 ± 2.5	35.0 ± 2.6	3.0 ± 0.3
	SH	35.3 ± 1.5	35.4 ± 1.6	3.0 ± 0.2
90% humidity	COP	35.8 ± 1.4	35.8 ± 1.4	3.0 ± 0.2
	HS	36.5 ± 1.4	36.6 ± 1.5	3.1 ± 0.2
	SH	34.9 ± 3.0	34.9 ± 2.9	3.0 ± 0.4

3.3.3. Fracture of the monolithic and laminated biogenic silica

The fracture behavior characterized by the fracture toughness is another critical mechanical aspect to consider for the biogenic silica. Previous investigation showed that the laminated silica exhibits improved fracture toughness compared to the monolithic silica[5]. In this study, I also performed nanoindentation using cube-corner tip under ambient and 90% humid conditions to obtain the crack size under different loading forces and calculate the fracture toughness[5]. The measurements of the indent size and crack size were summarized in the logarithmic plots for ambient and 90% humidity conditions as shown in **Fig. 3.10**.

Firstly, the fracture toughness of layering region is usually higher than those measured in lamellae and core regions with monolithic biogenic silica (**Fig. 3.11**). The fracture toughness results of the lamellae region show similarity to that of the core region (**Fig. 3.11**). These values generally agree with the previously obtained values for *M. chuni*'s spicule[5]. Yet, despite the fracture toughness enhancement by layering architecture, the fracture toughness of the monolithic biogenic silica is still lower than that of the fused silica[5]. Secondly, the fracture toughness of the layering region in HS

sponge's spicules show significantly smaller value compared to other species (**Fig. 3.11**). Thirdly, I observed that the fracture toughness of the spicules obtained from the nanoindentation under 90% humidity conditions show relatively small values compared to those obtained in the ambient condition (**Fig. 3.11**).

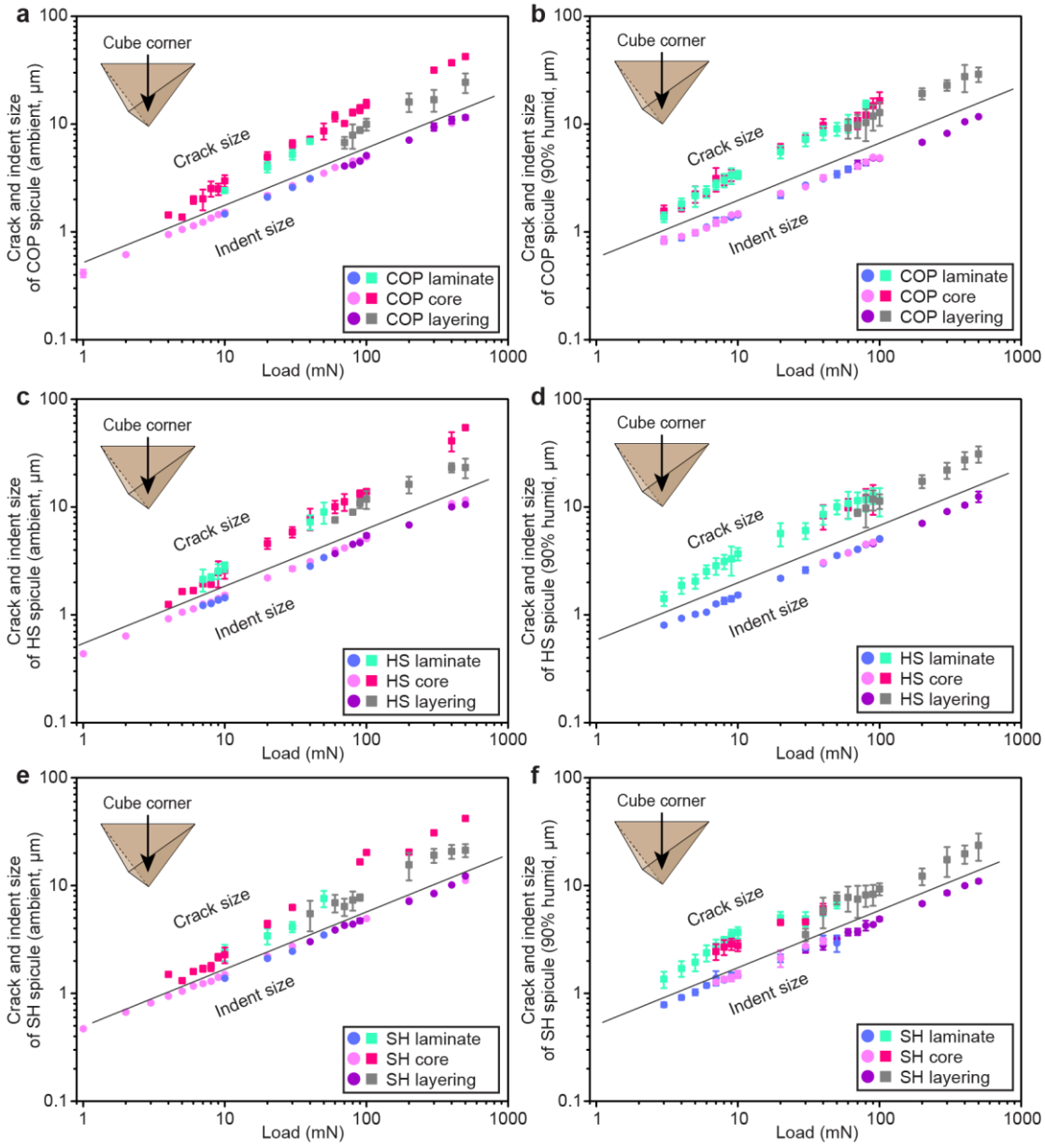


Figure 3.10. Indent and crack sizes after cube-corner indentation. (**a-c**) The measured indent and crack sizes of spicules from (**a**) COP, (**b**) HS, and (**c**) SH, respectively.

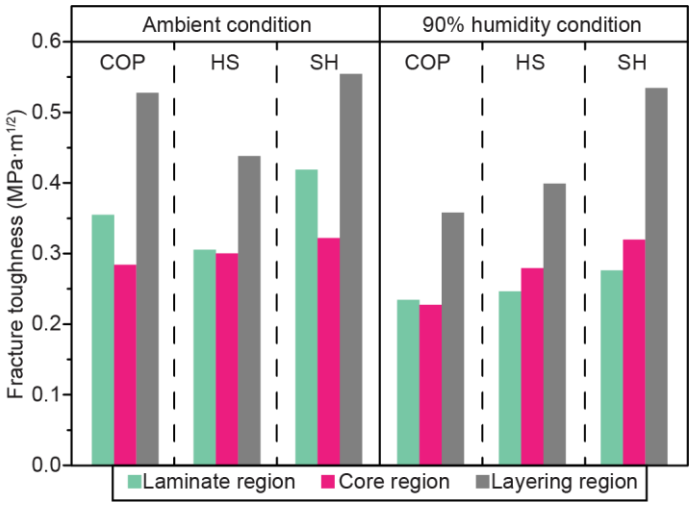


Figure 3.11. Summary of the fracture toughness for each types of the spicule under ambient or 90% humid conditions.

3.3.4. Element and chemical bond distributions

To explain the consistent modulus and hardness throughout the cross section of the spicules, EDS and Raman scans were performed to provide structural evidences.

First of all, point EDS experiments were performed on monolithic biogenic silica and axial organic filament of the anchoring spicules of three sponges, while elemental content of each spicule was obtained from line EDS scanning with 1 μm on the cross section of the spicules (**Fig. 3.12**). The point measurements show that the location where the axial filament resides contains an increased amount of C element and a decreased amount of Si element which is smaller than that in the monolithic biogenic silica at the core region

(**Fig. 3.12a,b,d,e,g,h**). Furthermore, the line EDS scans of the cross section show nearly flat weight percentage of Si, O, and C throughout half of the spicules with some sudden changes (**Fig. 3.12c,f,i**). Those sudden changes may be results of measurements on the organic interfaces. The reason of not observing a lot of significant changes of elemental weight percentage is because the thickness of organic interfaces (ca. 200 nm, **Fig. 3.5**) is much smaller than the 1 μm interval of line scan. Secondly, point EDS measurements on the HS's anchoring spicule were made on the monolithic silica of each laminate away from the organic interfaces, which confirms that the elemental content within the biogenic silica has no noticeable trend throughout the cross section (**Fig. 3.13**). This is different from the previous EDS measurements that show element distribution gradients, which is due to the uncorrelation between measurement results and locations[48]. This demonstrates that the monolithic biogenic silica within different silica layers can be deemed as identical in weight percentage of Si, C, and O elements.

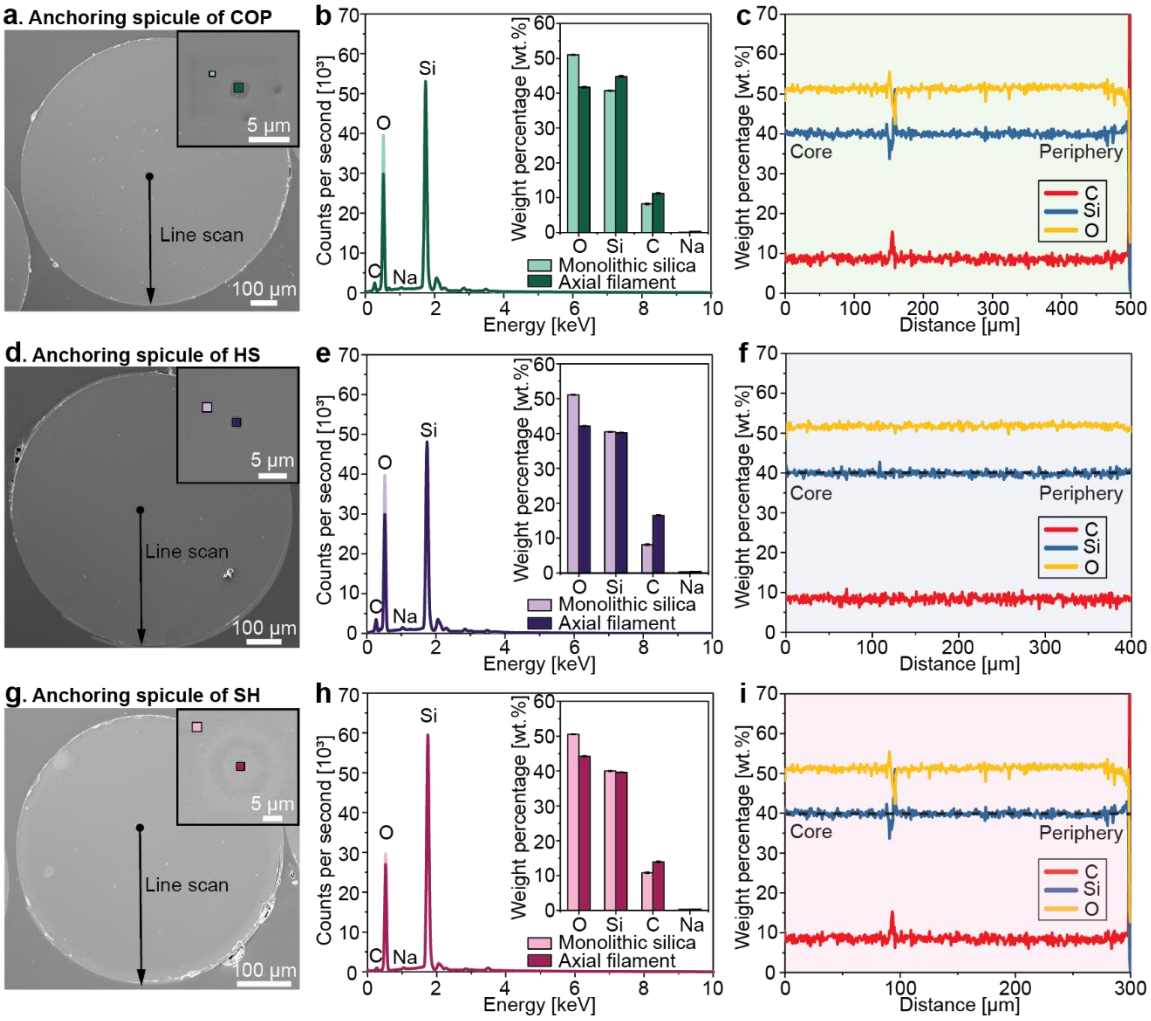


Figure 3.12. Weight contents and atomic contents of Si, O, C, and Na for the HS spicule correlated with the measurement locations.

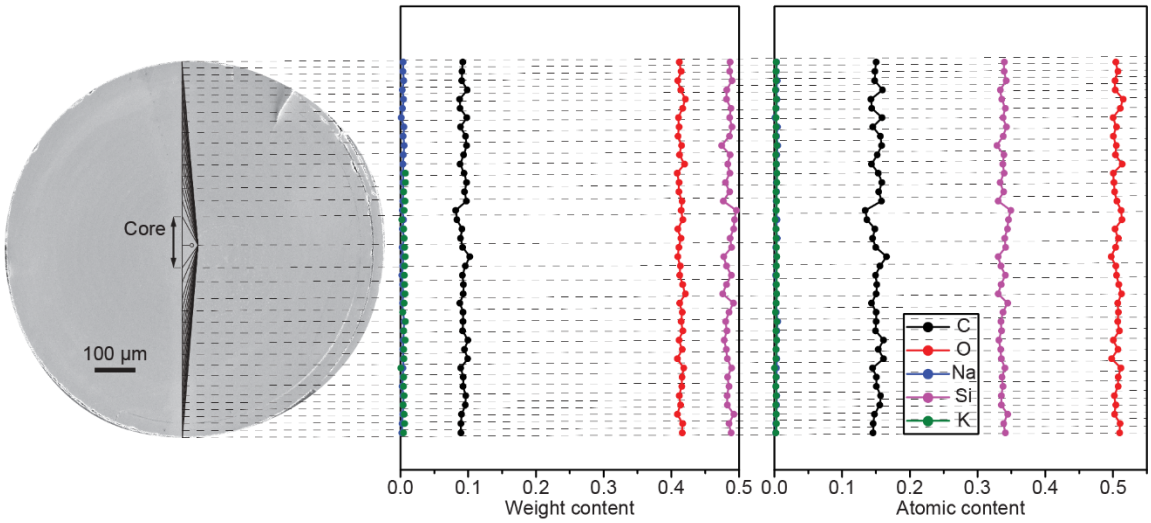


Figure 3.13. Weight contents and atomic contents of Si, O, C, and Na for the HS spicule correlated with the measurement locations.

Furthermore, measurements using Raman spectroscope were carried out to obtain the chemical bond distributions for Si-O-H, Si-O-Si, C-H, and Amide[6]. **Fig. 3.14** shows the typical point Raman measurement of the biogenic silica compared with the synthetic silica with the vibration modes of interest indicated. Specifically, Si-O-H stretching mode centered at v = 960 cm^{-1} which indicates the hydrated silica, Amide I stretching mode centered at v = 1620 cm^{-1}, and C-H stretching mode centered at v = 2950 cm^{-1} are observed in the peaks[6,40,115] (**Fig. 3.14**). In order to obtain the content of hydrated silica and organics, the peak area was extracted on the post-processed data from Raman image scans and used to calculate the area ratios, including Si-O-H/Si-O-Si, Amide/Si-O-Si, and C-H/Si-O-Si[6].

The Raman area scanning results of six cross sections from three species are shown in **Fig. 3.15-3.20**. First of all, other than the location of axial filament, no gradients of peak areas and area ratios were observed for all six samples, while some sudden increase or drop of the Si-O-Si vibration mode and organics vibration modes, respectively, are the results of measurements directly on the organic interfaces (**Fig. 3.15-3.20**). Secondly, the peak areas of the Si-O-Si, Si-O-H, Amide I, and C-H bonds are highest at the axial filament location, while the amide I content (i.e., Amide I/Si-O-Si) is smaller than the hydration content and C-H content which increase significantly at the axial filament location (**Fig. 3.15-3.20**). This indicates that the Silica is highly consolidated and dense compared to other regions as the location of axial filament is where the silica deposition starts. The etching of the axial filament leaves a hollow cylinder at the center of the spicule as shown in **Fig. 3.5** can be deemed as the collapse of the composite between organics and consolidated silica. Thirdly, the above-mentioned results, including the consistent peak area and peak ratio of the vibration modes of interest and the characteristics of axial filament, are true for both spicules with small and large cross-sectional radius (**Fig. 3.15-3.20**). Last but not least, significant increased peak centers and FWHMs were found for Si-O-Si and Si-O-H bonds at the axial filament location (**Fig. 3.15-3.20**).

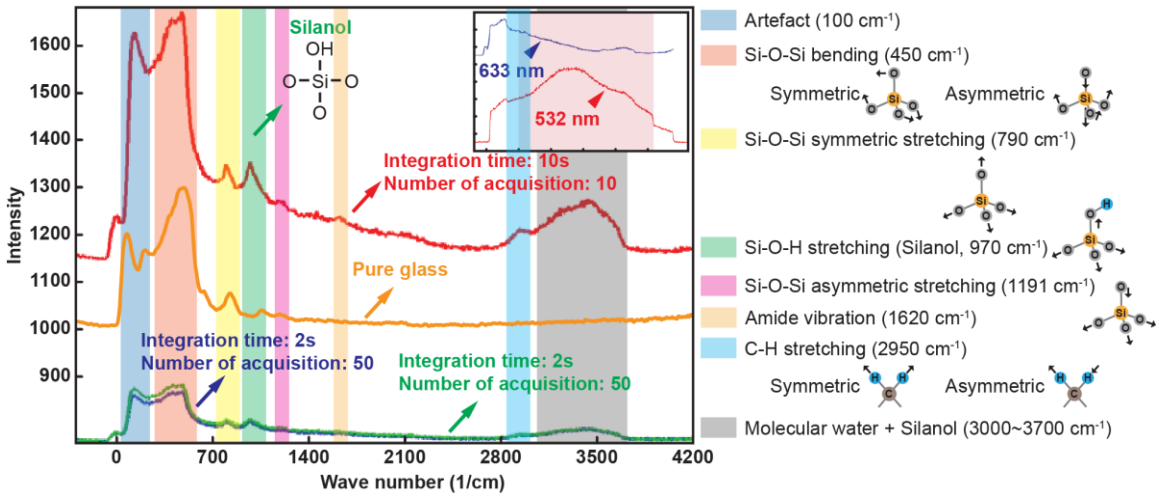


Figure 3.14. Raman spectrums and peak definitions of the biogenic and synthetic silica.

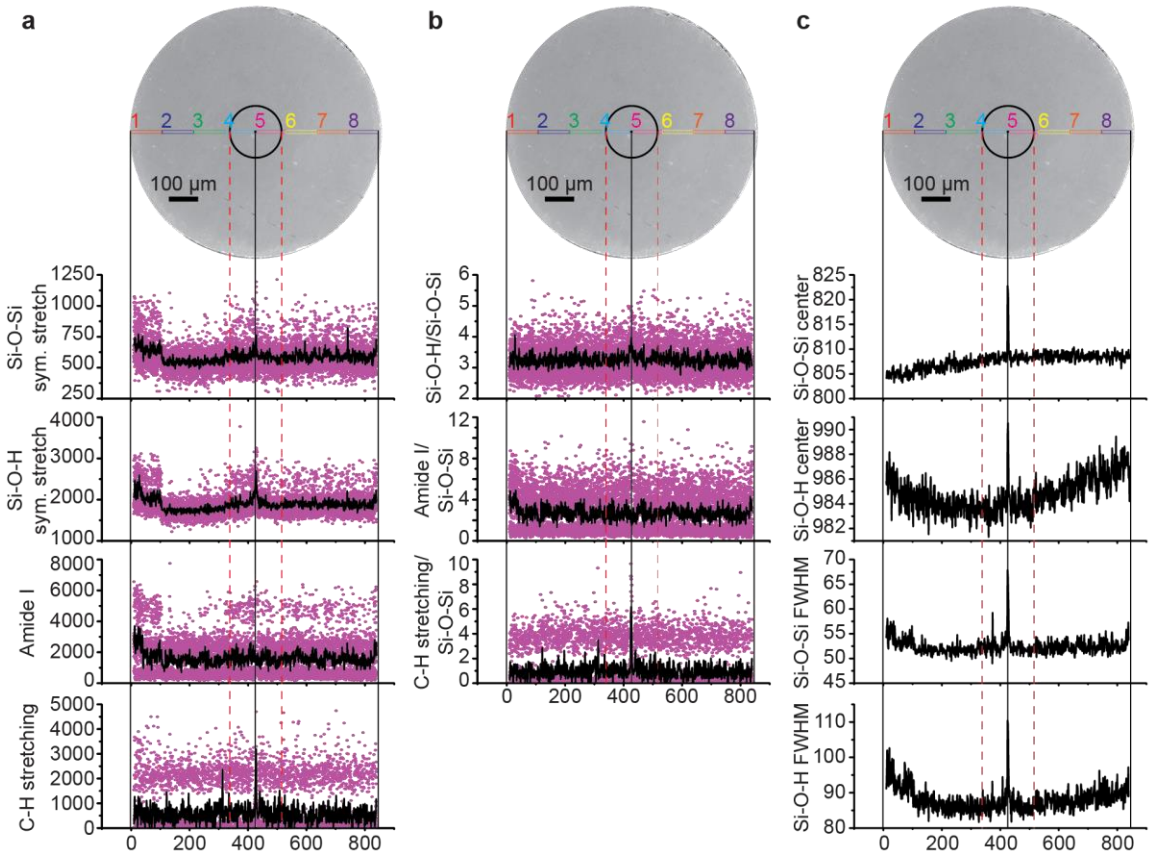


Figure 3.15. Peak characteristics from Raman scans of large COP spicule. (**a**) Peak area distributions of Si-O-Si, Si-O-H, Amide I, and C-H bonds. (**b**) Area ratios of Si-O-H/Si-O-Si, Amide I/Si-O-Si, and C-H/Si-O-Si. (**c**) Peak center and FWHM of Si-O-Si, Si-O-H, Amide I, and C-H bonds. The colored boxes on the SEM image of spicule indicate the regions scanned for stitching; purple line on the SEM image of spicule indicates the line scan location of nanoindentation; region enclosed by red dash lines indicates the Raman characteristics of the core region; black dash line indicates the location of axial filament; cyan dash line indicates the location with indentation; region enclosed by long red box indicates the useless data points due to the crack on the spicule.

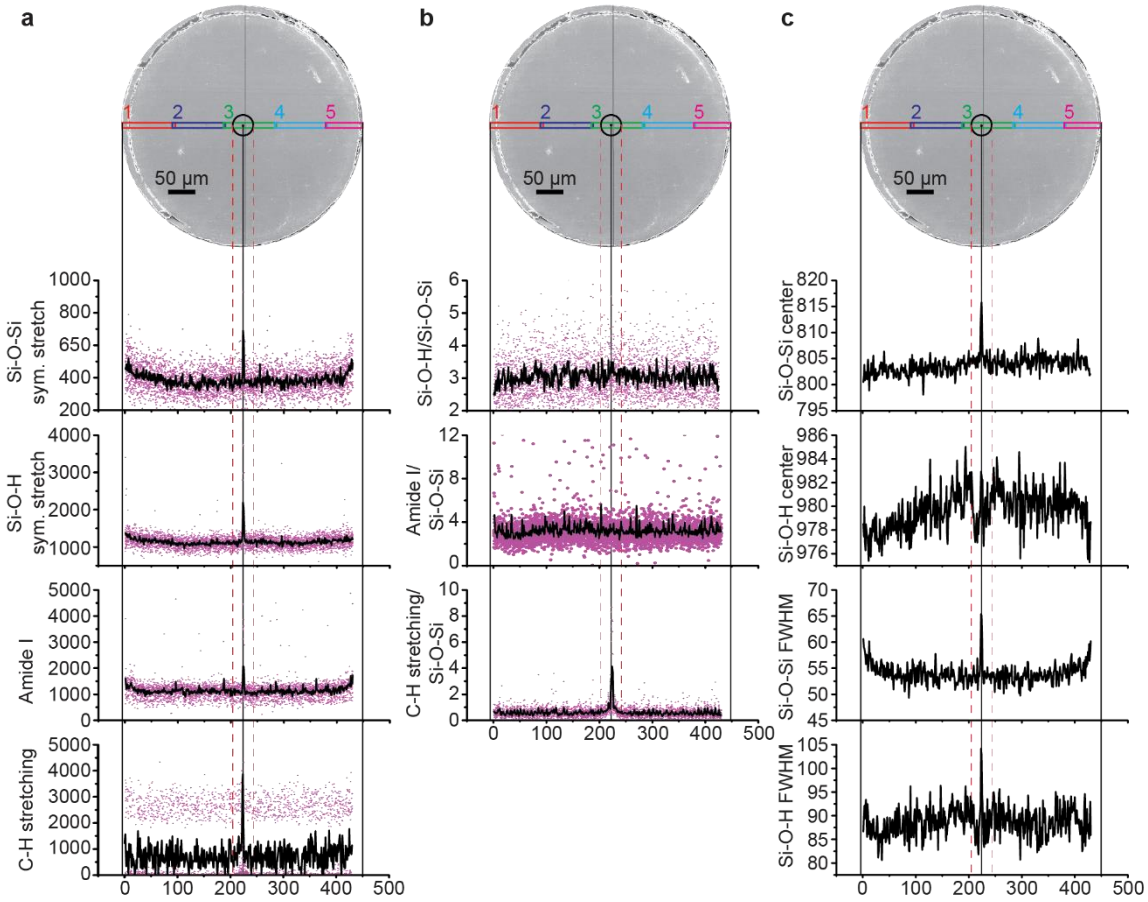


Figure 3.16. Peak characteristics from Raman scans of small COP spicule. (**a**) Peak area distributions of Si-O-Si, Si-O-H, Amide I, and C-H bonds. (**b**) Area ratios of Si-O-H/Si-O-Si, Amide I/Si-O-Si, and C-H/Si-O-Si. (**c**) Peak center and FWHM of Si-O-Si, Si-O-H, Amide I, and C-H bonds. The colored boxes on the SEM image of spicule indicate the regions scanned for stitching; purple line on the SEM image of spicule indicates the line scan location of nanoindentation; region enclosed by red dash lines indicates the Raman characteristics of the core region; black dash line indicates the location of axial filament; cyan dash line indicates the location with indentation; region enclosed by long red box indicates the useless data points due to the crack on the spicule.

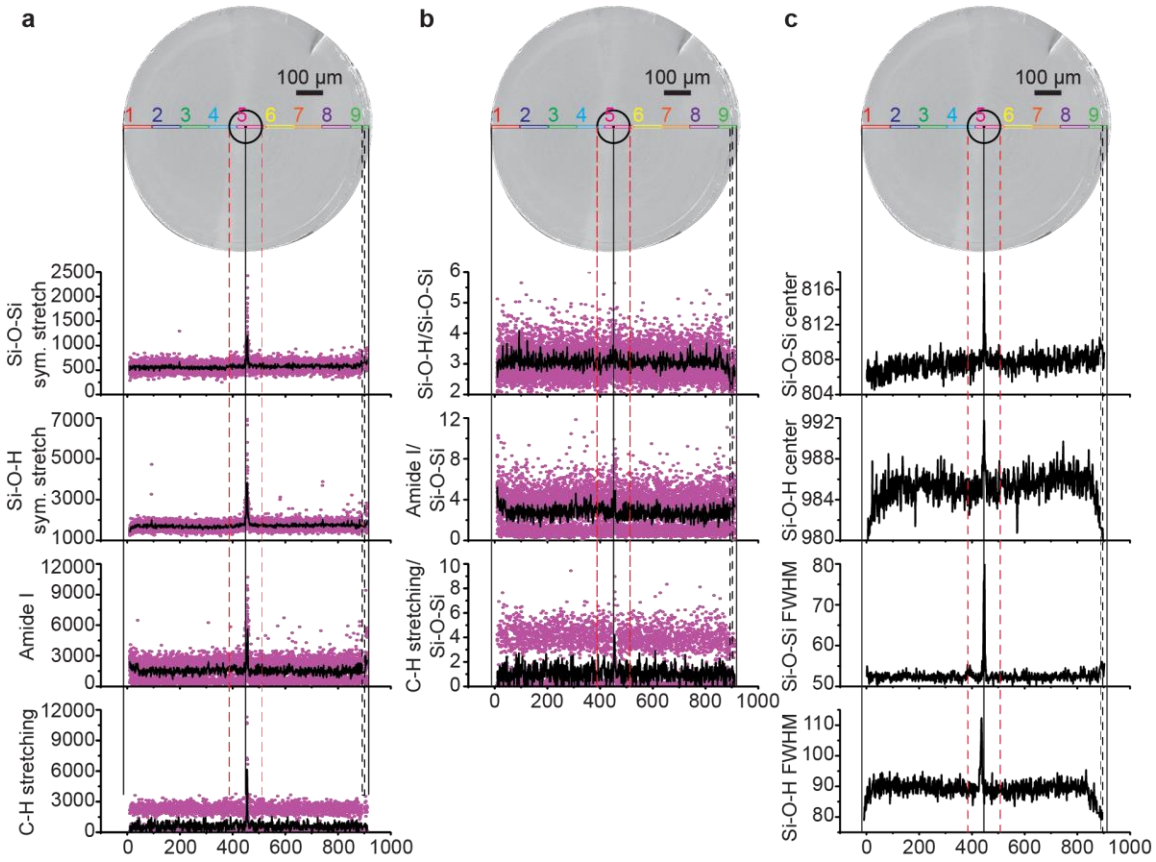


Figure 3.17. Peak characteristics from Raman scans of large HS spicule. (**a**) Peak area distributions of Si-O-Si, Si-O-H, Amide I, and C-H bonds. (**b**) Area ratios of Si-O-H/Si-O-Si, Amide I/Si-O-Si, and C-H/Si-O-Si. (**c**) Peak center and FWHM of Si-O-Si, Si-O-H, Amide I, and C-H bonds. The colored boxes on the SEM image of spicule indicate the regions scanned for stitching; purple line on the SEM image of spicule indicates the line scan location of nanoindentation; region enclosed by red dash lines indicates the Raman characteristics of the core region; black dash line indicates the location of axial filament; cyan dash line indicates the location with indentation; region enclosed by long red box indicates the useless data points due to the crack on the spicule.

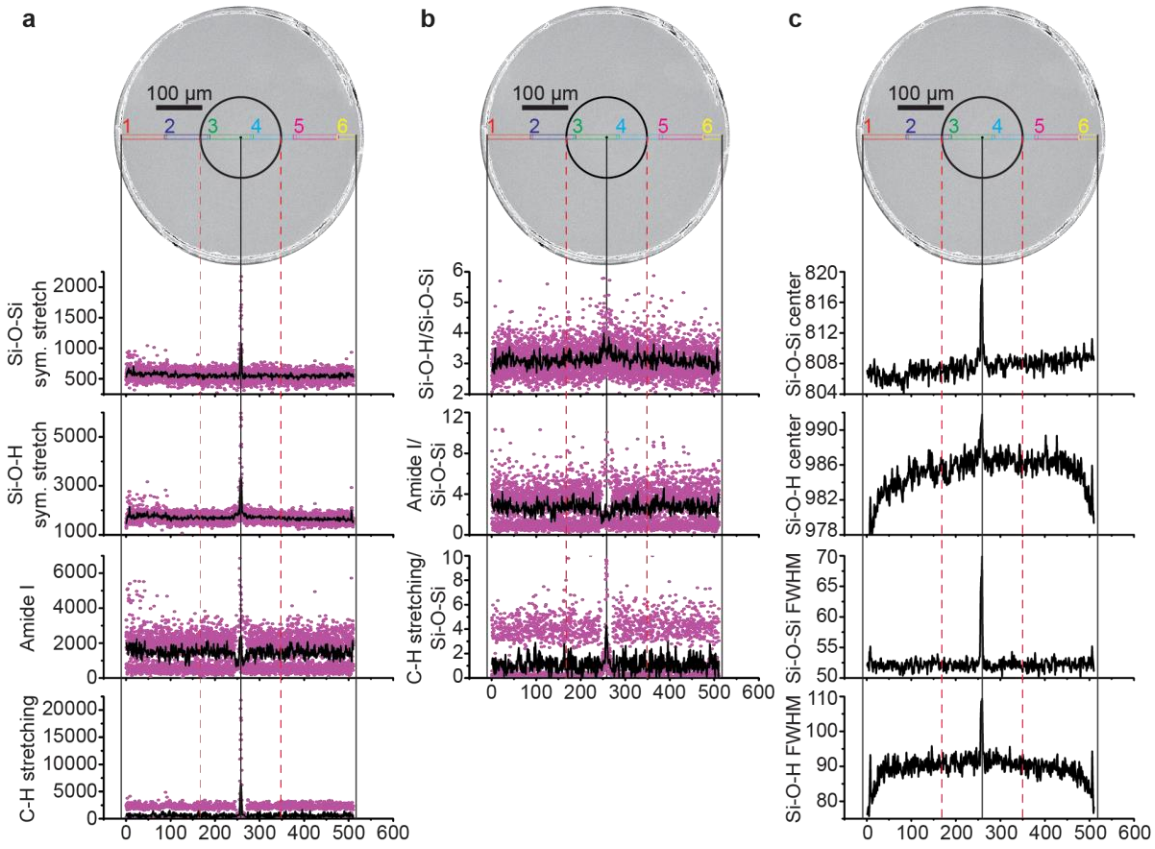


Figure 3.18. Peak characteristics from Raman scans of small HS spicule. (**a**) Peak area distributions of Si-O-Si, Si-O-H, Amide I, and C-H bonds. (**b**) Area ratios of Si-O-H/Si-O-Si, Amide I/Si-O-Si, and C-H/Si-O-Si. (**c**) Peak center and FWHM of Si-O-Si, Si-O-H, Amide I, and C-H bonds. The colored boxes on the SEM image of spicule indicate the regions scanned for stitching; purple line on the SEM image of spicule indicates the line scan location of nanoindentation; region enclosed by red dash lines indicates the Raman characteristics of the core region; black dash line indicates the location of axial filament; cyan dash line indicates the location with indentation; region enclosed by long red box indicates the useless data points due to the crack on the spicule.

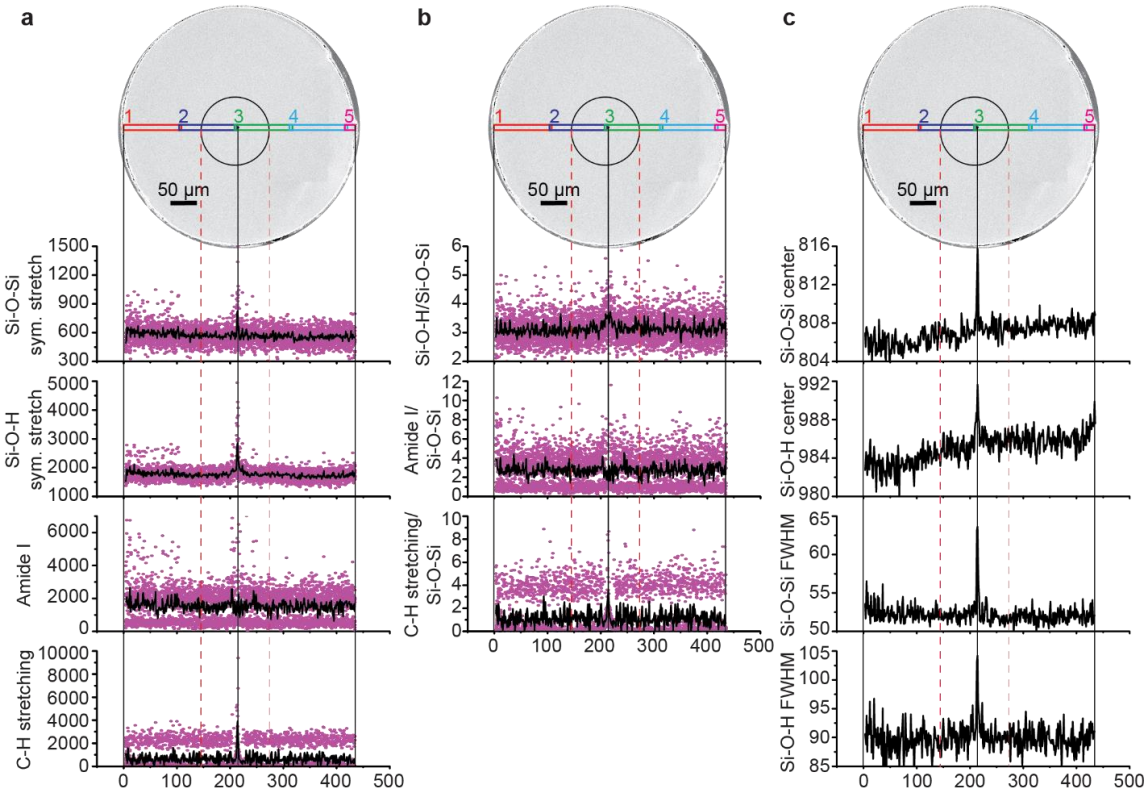


Figure 3.19. Peak characteristics from Raman scans of large SH spicule. (**a**) Peak area distributions of Si-O-Si, Si-O-H, Amide I, and C-H bonds. (**b**) Area ratios of Si-O-H/Si-O-Si, Amide I/Si-O-Si, and C-H/Si-O-Si. (**c**) Peak center and FWHM of Si-O-Si, Si-O-H, Amide I, and C-H bonds. The colored boxes on the SEM image of spicule indicate the regions scanned for stitching; purple line on the SEM image of spicule indicates the line scan location of nanoindentation; region enclosed by red dash lines indicates the Raman characteristics of the core region; black dash line indicates the location of axial filament; cyan dash line indicates the location with indentation; region enclosed by long red box indicates the useless data points due to the crack on the spicule.

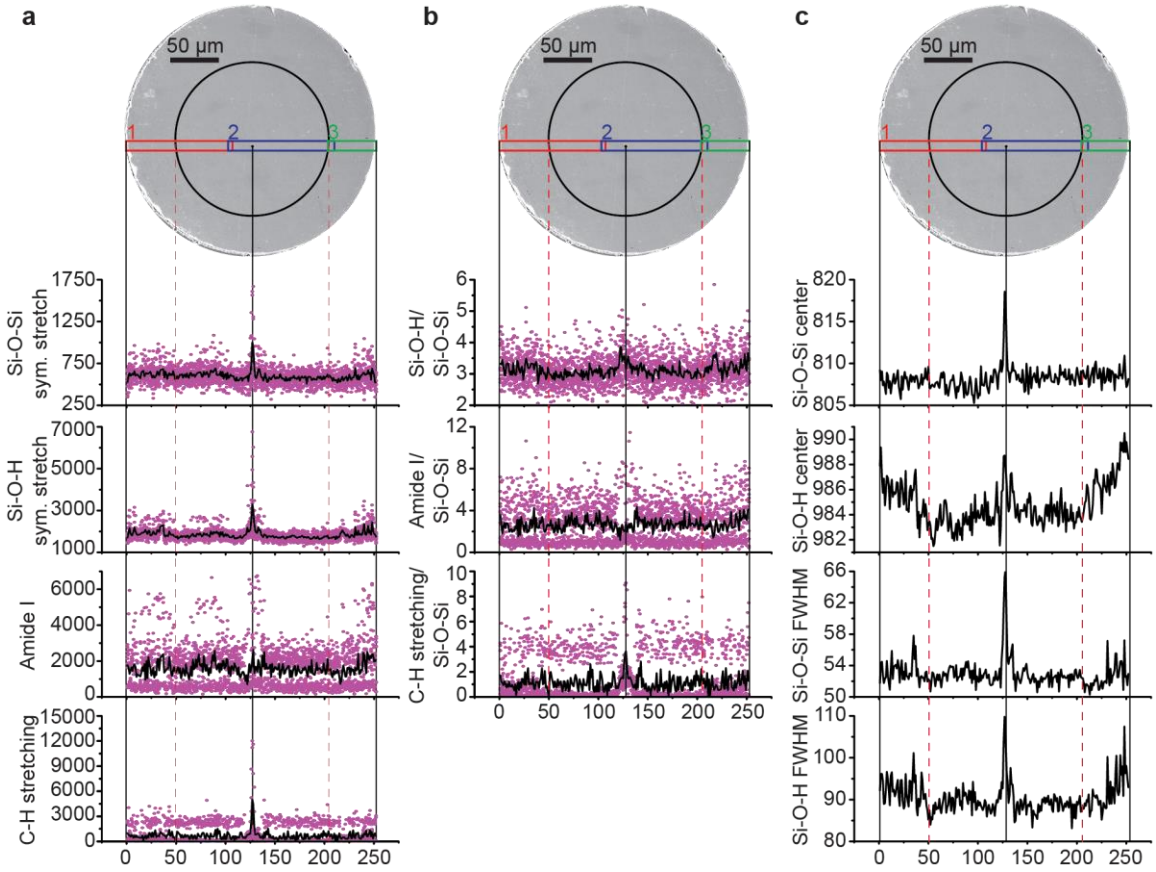


Figure 3.20. Peak characteristics from Raman scans of small SH spicule. (**a**) Peak area distributions of Si-O-Si, Si-O-H, Amide I, and C-H bonds. (**b**) Area ratios of Si-O-H/Si-O-Si, Amide I/Si-O-Si, and C-H/Si-O-Si. (**c**) Peak center and FWHM of Si-O-Si, Si-O-H, Amide I, and C-H bonds. The colored boxes on the SEM image of spicule indicate the regions scanned for stitching; purple line on the SEM image of spicule indicates the line scan location of nanoindentation; region enclosed by red dash lines indicates the Raman characteristics of the core region; black dash line indicates the location of axial filament; cyan dash line indicates the location with indentation; region enclosed by long red box indicates the useless data points due to the crack on the spicule.

3.4. Discussions and conclusions

This work provides a micro-structural study of the cylindrically laminated anchoring spicules from three selected Hexactinellid sponges *C. populiferum*, *H. sieboldin*, and *S. hawaiicus*, and detailed compositional-mechanical correlation on the biogenic silica of three types of anchoring spicules.

Our layer thickness measurements indicate that the thickness from the core to periphery of cross section of the anchoring spicule is not necessarily decreasing among Hexactinellid sponges[59]. As the increase of number of silica layers (> 20), achieving optimal decreasing trend of layer thickness provides only marginal improvements of strength compared to the randomly distributed layer thickness (**Fig. 3.3**-**3.4**)[58]. It is hypothesized that the additional control on generating optimal layer thickness may consume additional energy which decreases the efficiency of metabolism. Moreover, this layer thickness distribution is a result of bio-sintering process of originally laminated silica layers as demonstrated by the etched cross section of spicules (**Fig. 3.5**).

In addition, based on the compositional-mechanical results, the anchoring spicule utilizes this laminated structure to compensate the mechanical inferiority of biogenic in both strength and fracture toughness. From nanoindentation, we found no gradients of elastic modulus and hardness throughout the cross section of the anchoring spicules (**Fig. 3.6**-**3.8**). This is supported by the fact that no variations in weight percentage of elements (i.e., Si, O, and C) and chemical bonds (Si-O-Si, Si-O-H, amide I, C-H) exist in the biogenic silica throughout the cross section of the anchoring spicules (**Fig. 3.12**-**3.20**). This is in contrast to the previous results as the measurement results here are

correlated with the measurement locations which provides substantial conclusions[48,57]. Furthermore, the modulus and hardness of biogenic silica are less than those of synthetic silica which is a result of hydration and nanoparticulate structure of the biogenic silica (**Fig. 3.9**)[5]. This suggests that the mechanical properties of biogenic silica, which forms in ambient environment, is inferior to the synthetic silica. This is further supported by the fracture toughness measurement where the monolithic biogenic silica is more brittle than the synthetic silica despite the hydration (**Fig. 3.11**)[5]. Here, the independency of mechanical properties of biogenic silica on the humidity conditions during the experiment and sample treatment is hypothetically due to the already saturated silica or the relatively thin altered surface structure compared to indentation depth[118]. Yet, as demonstrated in this work, the laminated structure of spicule provides improved fracture toughness of biogenic silica comparable to or higher than the synthetic silica (**Fig. 3.11**)[5,64].

In summary, via careful correlation between measured locations and results, substantial evidences were provided in this work to demonstrate the consistent modulus and hardness as well as the compositional distributions throughout the cross section of anchoring spicules of Hexactinellid sponges *C. populiferum*, *H. sieboldin*, and *S. hawaiicus*. Instead of controlling the nanoscale structural-mechanical gradients, the sponges form spicules into cylindrically laminated structure for improvements in both strength and fracture toughness despite the lower modulus and hardness of biogenic silica than the synthetic silica. By utilizing similar laminated structure and stronger and stiffer artificial materials, cylindrical beams with significantly improved strength and toughness may be designed.

Chapter 4 The structural-mechanical understanding of cellular dome in the sieve plate of glass sponge *Eupletella aspergillum*

Combining chapter 5, this work is being prepared for publication:

H. Chen, L. Li, Quantitative multiscale structural-mechanical understanding of biomineralized lattice dome in the sieve plate of glass sponge *Euplectella aspergillum*, In preparation.

Sieve plate, covering the osculum of the glass sponge *Euplectella aspergillum*, exhibits a multiscale hierarchical spicule-based lattice dome. Existing work has provided limited qualitative observations of the sieve plate's biomineralized lattice. Here, the structural-mechanical correlations of the sieve plate, including the dome-shaped structure, Voronoi-like cellular pattern, and porous branch with increased height, were qualitatively and quantitatively explored. The sieve plates were found to have a dome shape resembling the elliptical paraboloid. In addition, the cellular patterns of sieve plates resemble to Voronoi tessellations with 77.7% similarity (relative densities from 40% to 60% and regularities from 0.4 to 0.6). Based on the structural characterizations, 2D planar and 3D dome-shaped bioinspired Voronoi-like cellular structures were generated to study the mechanical properties of the sieve plate, which reveals that, in general, the Voronoi-like patterns in sieve plates tend to provide stiffnesses comparable to the corresponding honeycomb lattices for protecting the osculum. Furthermore, the porous branch with increased height in sieve plate was found to have improved bending stiffness. This results in multi-functions of leaving large pore size for sponge's current pumping mechanism through the sieve plate while providing improved stiffness of the sieve plate.

This work provides not only a comprehensive understanding of sieve plate, but also inspirations to cellular dome design.

4.1. Introduction

Euplectella aspergillum, a species of Hexactinellid sponge, has been offering multiscale design strategies for composites or lattice materials, including the spicule, the silica building block, with cylindrically laminated silica layers to improve strength and fracture toughness[58,64,65] and ridged cylindrical skeleton with double-diagonal configuration to improve torsional rigidity, buckling strength, water permeability, and suppression of vortex shedding[70,71,73,75]. However, another structural component of the skeleton of *E. aspergillum*, sieve plate, which covers the osculum or the top opening of the cylindrical skeleton, has only limited qualitative observation-based studies[21].

The structural understanding is the first step to provide insights into the formation and mechanical functions of the biomineralized skeletons[2,71,83,119]. The sieve plate, by observation, exhibits a dome-shaped Voronoi-like lattice structure in millimeter-scale and silica spicule-based branches and cellular nodes in microscale[21]. Therefore, the comprehensive structural understanding of the sieve plate involves multiscale qualitative and quantitative studies, including studying the dome-shaped structure, characterizing the Voronoi-like cellular structure by regularity[120–128], and identifying individual spicules of sieve plate from the bundle of spicules which are significantly merged by synapticular bridging[129]. Here in this chapter, the dome structure, porous branch, and cellular pattern of sieve plate were studied while the spicule bundles were characterized in the next chapter for the study of sieve plate formation. The structures being explored here potentially provide contributions to the mechanical functions of sieve plate, which will be investigated via bio-inspired modeling.

Advantageous properties, such as lightweight, improved mechanical stiffness, strength, and toughness, are the motivations behind artificial dome structures and Voronoi cellular patterns. For dome structures, the self-supported solid and skeletal dome structures have been designed and built in architectures since ancient time[130]. In addition, lattice dome structures have been designed as the space frames where their deployable functions, seismic behaviors, instability, and damage behaviors are of most interest[131–135]. Moreover, the dome structure has been applied to designed architected lattice materials for improved stiffness, toughness, and damage tolerance[136,137]. For Voronoi cellular patterns usually found in both natural and engineering materials, the regularity of the Voronoi lattice play a role in determining the mechanical properties, including decreased Young's modulus, shear modulus, increased bulk modulus as the decrease of the regularity[128] as well as the increased fracture toughness at a range of regularity from 0.5 to 0.8[138]. In addition, structural hierarchy was incorporated into the design of Voronoi honeycomb structure, resulting in either self-similar hierarchical Voronoi honeycomb or combination of regular cellular structure with Voronoi honeycomb for improved stiffness and mode I fracture toughness[121,123–125]. Whether the dome-shaped Voronoi-like cellular lattice with porous branch in the sieve plates provides similar or other unique mechanical advantages such as stiffening to the cylindrical skeleton of the *E. aspergillum* remains an open question[21].

In this work, we first perform a comprehensive structural measurement of the dome-shaped Voronoi-like cellular structure of sieve plates in *E. aspergillum*. Next, the mechanical properties of each structural characteristic, including the dome-shaped geometry, the Voronoi-like pattern of the sieve plate and the porous branch with

increased height along dome thickness direction were studied via bio-inspired modeling, computational simulations, and experimental analysis. The results here provide i) the first structural-mechanical understanding of the sieve plate's macrostructure; ii) bio-inspired design of hierarchical cellular dome; and iii) structural fundamentals for the further understanding of sieve plate formation.

4.2 Materials and Methods

Sample preparations: Dried skeletons of glass sponge *E. aspergillum* were purchased from commercial sources. Five complete sieve plates were directly cut from the sponge's skeleton using a diamond saw blade for imaging and structural analysis. Subsequently, some sieve plate nodes were cut from the sieve plates for imaging.

Scanning Electron Microscope imaging: 15~20 nm platinum/palladium was coated to the sieve plates and sieve plate nodes for Scanning Electron Microscope (SEM) imaging. The entire sieve plate was imaged using a JEOL IT-500HE SEM system which has a montage function to automatically capture and stitch multiple SEM images to form a large-scale scanning image of the sieve plate. The images of sieve plate nodes were acquired in FEI Quanta 600 FEG with a typical working distance of ~12mm and a voltage of 15kV.

Micro-computed tomography analysis: To visualize and analyze the 3D skeletal lattice of the sieve plate, a micro-computed tomography (μ-CT) Skyscan system 1172 (Aartselaar, Belgium) was used, where the X-ray was operated at 80kV and 100μA. The projection images were acquired for each scan with a 180° sample rotation. These projection images

were captured by a Hamamatsu camera with a resolution of 2496 × 2496 pixels for sieve plate. The voxel resolution is 17.42μm and the exposure time is 0.968s for the entire sieve plates. The projection images were automatically reconstructed in the Skyscan system after acquisition. In addition to the entire sieve plate, the sieve plate branches were also captured using the pixel resolution of 3.83 μm in the Skyscan system. This high-resolution scanning allows the accurate relative density measurements and spicule counting of the sieve plate branches.

The reconstructed images were segmented in an open-source, machine learning-based software ilastik which was trained by manual labeling of a few regions of the sieve plate and background[139]. The segmented images were imported to a commercial tomography analysis software Avizo 2019.2 (Thermo Fisher Scientific, Massachusetts, USA) for 3D volume rendering, visualization, skeletonization, and quantitative structural analysis.

Structural analysis: Three most important structural features of sieve plates, including the dome-shaped structure, the porous branch, and the cellular structures (i.e., pore area and distribution, pore orientation, and cellular pattern), were characterized.

Dome structure: The height (*h*), long side (*l*), short side (*s*), and thickness (*t*) of the dome-shaped structures as shown in **Fig. 4.1a** were measured based on the μ-CT scanned 3D volume of sieve plate. The principal directions of the dome structure, including the directions of the long side (L), short side (S), and dome height (H) were defined in **Fig. 4.1**. The structural parameters were defined in **Table 4.1**. Furthermore, the sieve plate samples were fitted using the equation of elliptical paraboloid as:

$$\frac{z}{c} = \frac{x^2}{a^2} + \frac{y^2}{b^2} \qquad (4.1),$$

where x, y, and z are the coordinates of the points on the sieve plate, a, b, and c are the fitting parameters, which correspond to l_{fitted}, s_{fitted}, and h_{fitted} as defined in **Table 4.1**. By comparing the fitted dome structure of thickness t with the sieve plate, the relative density of the sieve plate ($\bar{\rho}_{sieve\ plate}$) can be obtained (**Fig. 4.2a and Table 4.1**).

Sieve plate branch: The structural parameters were defined in **Fig. 4.1b and Table 4.1**, including the branch length (l_b), branch width (w_b), and branch height (h_b). Here the direction of the branch height or dome thickness is denoted as T which is parallel to the branch height or dome thickness (**Fig. 4.1b**). In addition, the relative density of the sieve plate branch ($\bar{\rho}_{branch}$) is defined as the ratio between the amount of material volume of the branch and the volume enclosed by the boundary of the branch (**Fig. 4.2b and Table 4.1**). This porous branch provides a bio-inspired design of the lattice beam.

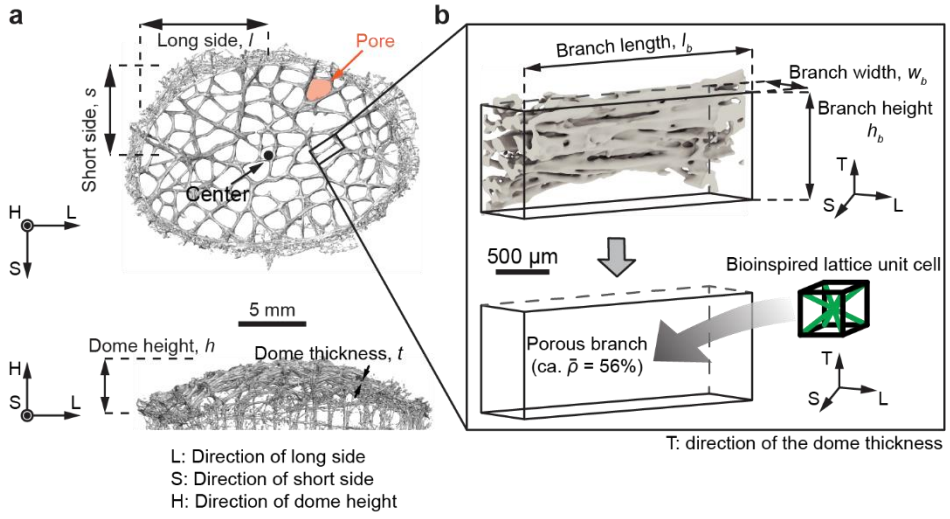


Figure 4.1. Schematics of the structural definitions for the sieve plate and its branch. (**a**) Definitions of the structural parameters for the sieve plate's dome structure. The

orange-highlighted region indicates one pore of the sieve plate. (**b**) Definitions of the structural parameters for the sieve plate's porous branch. The coordinate systems (L-S-H and L-S-T) for both structural features are given.

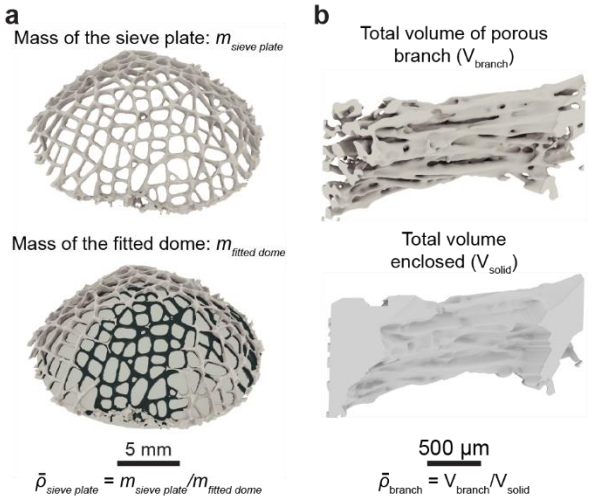


Figure 4.2. Schematic definitions of the relative densities of sieve plate (a) and sieve plate branch (b).

Table 4.1. Definitions of all structural parameters used.

Notation (unit)	Definition
h (mm)	Height of the sieve plate's dome structure
l (mm)	Long-side length of the sieve plate's dome structure
s (mm)	Short-side length of the sieve plate's dome structure
t (mm)	Thickness of the sieve plate's dome structure
h_{fitted} (mm)	Height of the fitted dome to the sieve plate
l_{fitted} (mm)	Long-side length of the fitted dome to the sieve plate
s_{fitted} (mm)	Short-side length of the fitted dome to the sieve plate

$\bar{\rho}_{sieve\ plate}$	Relative density of the sieve plates
l_b (mm)	Length of the sieve plate branch
w_b (mm)	Width of the sieve plate branch (parallel to the L-S plane)
h_b (mm)	Height of the sieve plate branch, which is identical to the dome thickness t
$\bar{\rho}_{branch}$	Relative density of the branch
A_{pore} (mm^2)	Area of the pores of sieve plates
k	Regularity index of the Voronoi patterns in the sieve plates
N-3, N-4, N-5	Nodal structure with 3, 4, or 5 connecting branches
$\bar{\rho}_{projected\ sieve\ plate}$	Relative density of the projected sieve plates on L-S plane

Cellular structure: Three characteristics were explored which are i) the cellular network information such as the pore size, pore centers, and the nodal structure; ii) the pore orientation and alignment, and iii) the cellular pattern. First of all, a cellular network analysis workflow proposed previously was used to perform skeletonization and feature extraction on the sieve plates and their projections on the L-S plane, including the nodal structure, pore areas, projected pore centers, pore morphologies via elliptical fitting, and pore alignment (**Fig. 4.1a,4.2a**)[2,83]. In particular, the pores projected on the L-S plane were fitted with elliptical shape, which yields the information of long side (l_{pore}) and short side (s_{pore}) of pores (**Fig. 4.3**). The aspect ratio of the pore (AR), which is considered the pore morphology here, is defined as:

$$AR = \frac{l_{pore}}{s_{pore}} \qquad (4.2),$$

Moreover, the pore orientation was defined as the angle between the long side of the pore and the long side of the sieve plate (α_{pore}) (**Fig. 4.3b**).

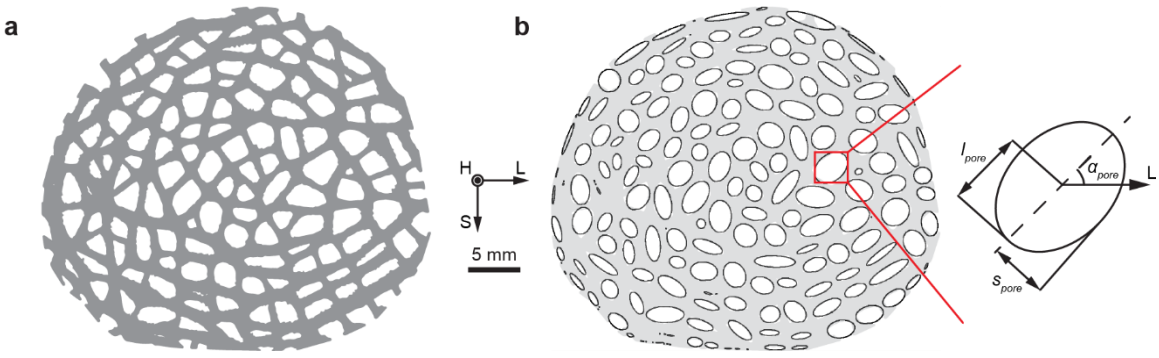


Figure 4.3. Pore morphologies and alignments. (**a**) A representative projected sieve plate on L-S plane. (**b**) The pores fitted with elliptical shape and the schematic definitions of long side, short side, and alignment of the pores.

To quantify the overall pore alignments in different orientations of the sieve plate, an alignment score (AS) was proposed which is defined as:

$$AS = \left\{ sum\left(AR_i \cdot \left(\frac{A_i}{A_{tot}} \right) \right) | \alpha_{pore,min} \leq \alpha_{pore,i} \leq \alpha_{pore,max} \right\} \quad (4.3),$$

where i indicates the i-th pore projected on the L-S plane, AR_i, A_i, and $\alpha_{pore,i}$ are the aspect ratio, area, and orientation of the i-th pore, A_{tot} is the total pore area of the projected sieve plate, $\alpha_{pore,min}$ and $\alpha_{pore,max}$ are the specified minimal and maximal bounds of the pore orientations. Therefore, the alignment score, which takes the aspect ratio and area ratio into accounts, calculates the pore alignment along a given orientation of the sieve plate (i.e., the orientation relative to the long side of the sieve plate). Here,

the alignment score was calculated for a given interval of sieve plate's orientation, for example, $0^{\circ} \leq \alpha_{pore,i} \leq 10^{\circ}$.

Finally, based on the obtained projected pore centers on the L-S plane, the Voronoi cells were generated which are then compared to the sieve plate's cells (**Fig. 4.4**) using a difference index *diff* adopted from[140]. The generated Voronoi cells were first dilated to the relative densities identical to the projected sieve plate ($\bar{\rho}_{projected\ sieve\ plate}$). Then, these two corresponding structures were exported as binary images for comparison. The index *diff* is defined as the ratio between the number of unmatched non-zero pixels (P_{diff}) and the number of non-zero pixels on the projected sieve plate ($P_{sieve\ plate}$) as shown in Eq. (4.4).

$$diff = \frac{P_{diff}}{P_{sieve\ plate}} \tag{4.4}$$

In addition, the regularity indices of the sieve plate's Voronoi pattern, adopted from the definition of previous work[126], were also obtained. Here, the regularity index was defined as the minimal distance between two pore centers divided by the pore distance of the corresponding regular honeycomb lattice with same number of pores as shown in **Fig. 4.5**:

$$k = \frac{s}{r} \tag{4.5},$$

where k is the regularity index, s is the minimal distance between the 2D pores of sieve plate, r is the pore distance of the regular honeycomb lattice counterpart ($k = 1$).

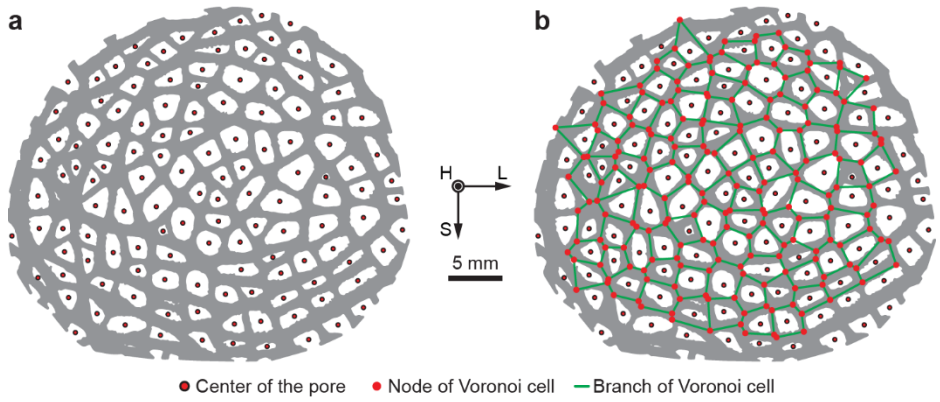


Figure 4.4. Cellular analysis and Voronoi tessellation. (**a**) A representative projected sieve plate on L-S plane and the recognized pore centers. (**b**) The Voronoi tessellation generated based on the recognized pore centers, which is compared to the projected sieve plate.

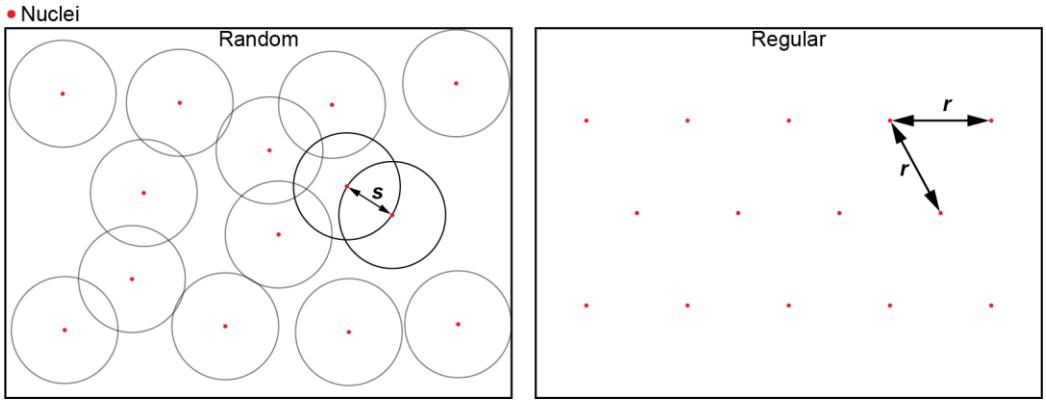


Figure 4.5. Definition of the structural parameters to calculate regularity index.

Modeling, fabrication, and experiment: Three types of bio-inspired models were built in this work, including the projected sieve plate on the L-S plane, 3D dome-shaped cellular structure mimicking the sieve plates, and the porous branch with increased height mimicking the sieve plate branch.

For the projected sieve plate, the images of the projected sieve plates on the L-S plane were cropped out into rectangular lattices in various directions relative to the L direction and converted into the 2D computer-aided design (CAD) models. Two types of control models were generated for mechanical comparisons: i) the 2D honeycomb cellular models with similar number of pores and same relative densities; and ii) the computer-generated Voronoi cellular lattice with same regularities and relative densities using the Simple Sequential Inhibition algorithm[138]. These models were used for mechanical simulations only as introduced later.

For the 3D dome-shaped cellular structure, the domes of elliptical paraboloid shapes obtained from sieve plate fitting were subtracted using Boolean operation by the H-direction-extruded pores of the projected sieve plates and the computer-generated honeycomb models with similar number of pores and same relative densities, respectively. The 3D CAD models were subsequently converted into Standard Tessellation Language (STL) models for 3D printing. The 3D models were fabricated using rigid resin in the Form 3 (Formlabs, USA), a stereolithography-based additive manufacturing machine. After fabrication, the bio-inspired 3D dome-shaped cellular models were utilized to mechanical experiments. The compression experiments along the H and L directions, respectively, were carried out using Instron 5944 tester under strain rate of 5×10^{-4}/s. The slope of the initial linearly parts of the force-displacement curves were used to obtain the stiffness of the 3D cellular dome which were further normalized by the measured weights.

For the bio-inspired porous branch, the body-center-cubic (BCC) lattice was used to simulate the unit cell topology of the sieve plate branch. This bio-inspired branch has

relative density of 56% and 73%, respectively, for comparison, while the it also has 1×3×10 unit cells and 2×6×20 unit cells along the directions of branch width, height, and length, respectively. The dimensions of the branch width, height, and length follow the averaged values of the measurements. In addition, control models were constructed, including branches with elliptical, rectangular, circular, and cubic cross sections. Here, the branch width of the elliptical and rectangular branches is identical to that of the sieve plate branch, while the mass of all control models is identical to that of the sieve plate branch.

Mechanical simulation: Projected sieve plate on the L-S plane, corresponding honeycomb lattice, computer generated Voronoi lattice, and bio-inspired porous branch were investigated using Abaqus/Standard 2016 (Dassault Systems, Vélizy-Villacoublay, France), a commercial Finite Element analysis package. For the projected sieve plate and the corresponding control models, the simulation models were meshed with ca. 1 million linear triangular elements (CPE3). A compressive strain of 0.1% along various directions of the projected sieve plate models was applied to obtain the elastic modulus. For the bio-inspired porous branch and the corresponding control models, cantilever beam bending (i.e., one end is fixed while loading is applied on another end) was applied as shown in **Fig. 4.5**. From the simulations, the bending stiffnesses ($E_{eff}I_{eff}$) of all branches were obtain using Eq. (4.6).

$$E_{eff}I_{eff} = \frac{Fl_b^3}{3\delta} \qquad (4.6),$$

, where E_{eff} and I_{eff} are the effective elastic modulus and effective area moment of inertia of the branches, respectively (solid branch has $E_{eff} = E_{solid}$, which is 40 GPa

simulating the biogenic silica of glass sponge *E. aspergillum*), F and δ are the resultant force and the applied deflection on the loaded end, respectively (**Fig. 4.6**), l_b is the length of branch as defined in **Table 4.1**.

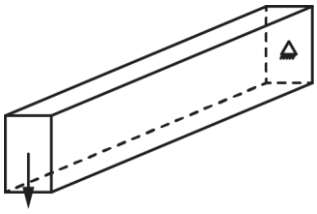


Figure 4.6. Mechanical simulations of cantilever beam bending.

4.3. Results

4.3.1. Introduction to the sieve plate

Sieve plate is a dome-shaped cellular structure covering the osculum (i.e., the top opening of the cylindrical skeleton) of glass sponge *E. aspergillum* (**Fig. 4.7a-c**). It exhibits a Voronoi-like cellular lattice structure (**Fig. 4.7c**). SEM image of the nodal structure, which is the interconnecting site between branches, of the sieve plate as shown in **Fig. 4.7d** demonstrates the silica spicule-based cellular structure. This is further supported by the stitched SEM images of the entire sieve plate where all nodes and branches are made of silica spicules (**Fig. 4.7e**). Therefore, the following structural features will be studied here: the dome structure, porous sieve plate branch, the cellular structure (i.e., the nodal structure, area, morphology and orientation of pores, and cellular patterns).

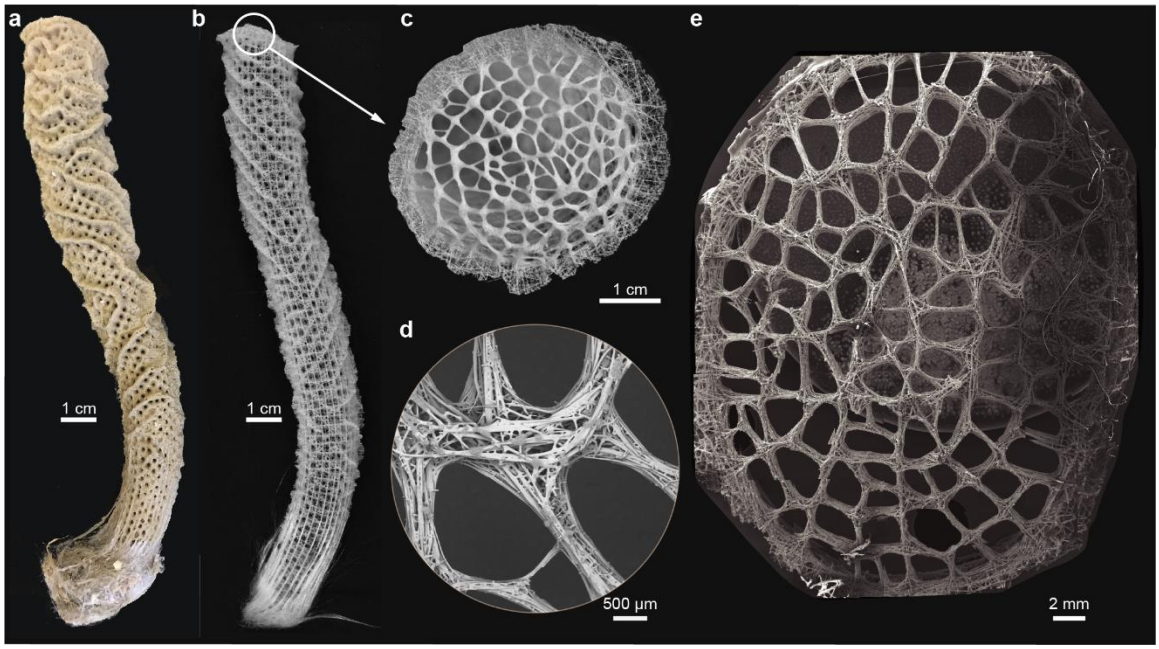


Figure 4.7. Introduction of the sieve plate structure in *E. aspergillum*. (**a**) Glass sponge *E. aspergillum* with preserved tissue covered. (**b**) The bare silica skeleton of *E. aspergillum*. (**c**) Optical image of the sieve plate. (**d**) SEM visualization of the spicule-based sieve plate node. (**e**) Large-scale stitched SEM image of the sieve plate demonstrating the spicule-based structure.

4.3.2. Structural quantification of sieve plate

Each structural feature was studied separately and quantitatively in this section, including the dome structure, porous branch, and cellular structure, including i) pore area, morphology, and alignment; and ii) cellular pattern.

Dome structure: Quantitative characterization of dome structure of the sieve plate was carried out following the structural definitions as shown in **Fig. 4.1a** and **Table 4.1**. The measured and fitted results were summarized in **Fig. 4.8**.

The dome characteristics (i.e., *l*, *s*, *h*, and *t*) were manually measured based on the 3D volume rendering of 5 sieve plate samples (**Fig. 4.8a,b**). The results show that the long side (l = 16.2 mm ~ 20.8 mm), short side (s = 11.5 mm ~ 17.7 mm), and height (h = 6.9 mm ~ 11.7 mm) are varied ca. 5 mm among samples, while the height of the dome is not correlated to the long side or short side of the sieve plate (**Fig. 4.8a,b**). In addition, the thickness of the dome (ca. 1 mm) varies little among samples and is also not correlated to other measurements (**Fig. 4.8b**). The heterogeneities in the dimensions of sieve plate are within the same order of magnitude.

Subsequently, the sieve plates were fitted using the ellipsoidal paraboloid surface as defined in Eq. (4.1) where the parameters a, b, and c represent the fitted long side (l_{fitted}), short side (s_{fitted}), and height (h_{fitted}) of the dome, respectively (**Fig. 4.8c**). The fitted results are slightly lower than those measured manually, which is also true for the averaged measured and fitted values of all sieve plate samples (**Fig. 4.8a,c,d**). This is because the dome fitting considers the overall shape of the sieve plate while manual measurements take the maximal values of all structural parameters (**Fig. 4.1a, 4.8a,c**). The fitting results combined with the measured dome thickness, as shown in **Fig. 4.8e**, were used to construct the 3D dome-shaped models which will be further converted to cellular models for mechanical understanding. Moreover, based on the fitted solid dome, the relative density of the sieve plate ($\bar{\rho}_{sieve\ plate}$) can be obtained as 51.6% ± 8.3% (**Fig. 4.2a,4.8e**).

Porous sieve plate branch: The sieve plate branches are spicule-based, porous, and rectangle-like in cross section. The relative density of the sieve plate branch is 55.9% ± 6.7% (**Fig. 4.2b**). In addition, the branch length (l_b), width (w_b), and height (h_b) of the

sieve plate were measured as 2.9 ± 0.7 mm, 0.3 ± 0.1 mm, and 0.9 ± 0.1 mm, in which the branch height (h_b) is identical to the dome thickness (t) (**Fig. 4.1b**). Therefore, l_b is ca. 10 times of w_b, while h_b is ca. 3 times of w_b. It can be hypothesized that the small branch thickness of the sieve plate allows the large cell size for sponge to pump water while the porous branch with increased height provides improve stiffness and lightweight properties to the sieve plate[34]. Furthermore, the number of spicules along the branch width and height were measured as ca. 3 and 7. Based on the ratio between h_b and w_b, the porous sieve plate branch can be represented by 2 unit cells of bio-inspired cellular lattice along the branch width and 6 unit cells along the branch height, which provides the structural origins to the later bio-inspired modeling of porous branch with increased height (**Fig. 4.1b**). Here, the BCC lattice structure was used to represent the lattice structure of sieve plate branch in order to ensure the shear stability of the branch with diagonals (**Fig. 4.1b**). More accurate bio-inspired modeling of the sieve plate branch may be proposed after in-depth microstructural understanding of the spicules and spicule bundles within the branches.

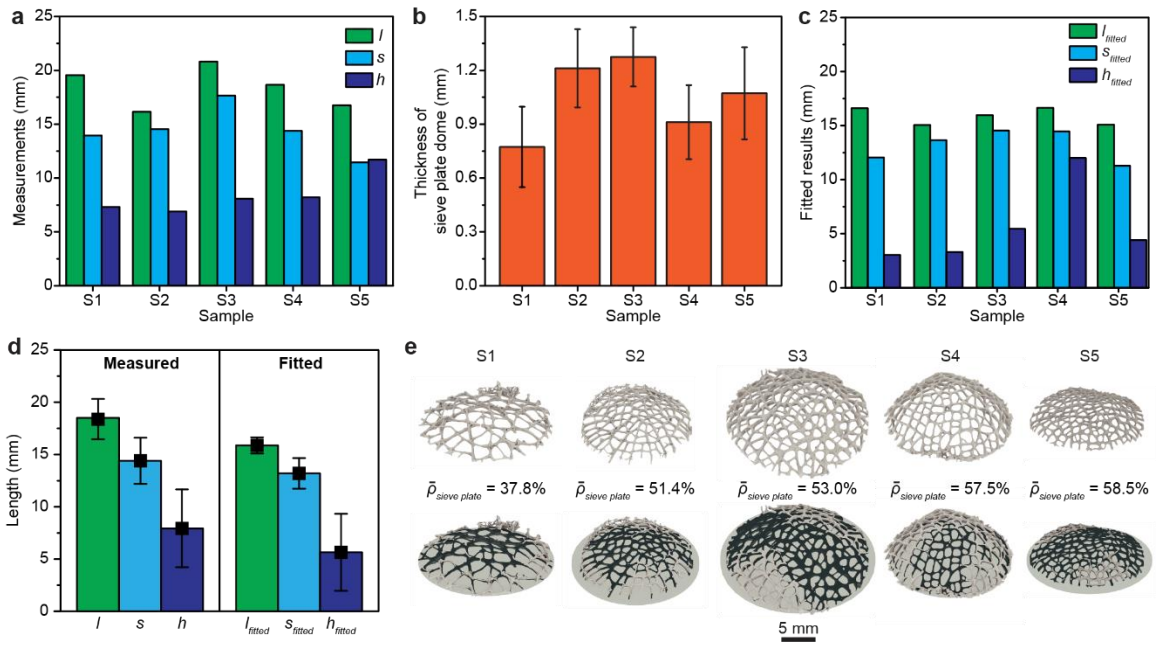


Figure 4.8. Characterization of the dome shape of the sieve plate samples. (**a,b**) Measured results of long side (l), short side (s), and height (h) (**a**) and thickness (t) (**b**) of the dome based on the 3D volume rendering from µ-CT scanning. (**c**) Fitting results of long side (l_{fitted}), short side (s_{fitted}), and height (h_{fitted}) of 5 different sieve plate samples. (**d**) Averaged measured and fitted long side, short side, and height of the sieve plate's dome structure. (**e**) 3D visualization of the sieve plate samples and the fitted solid dome with measured dome thickness.

Pore area, morphology, and alignment: A customized cellular network analysis workflow was used to skeletonize the sieve plate and identify the pores (**Fig. 4.9a**)[83]. The center of the pores can also be found based on the recognized pores (**Fig. 4.9a**). The pore areas are, on average, ca. 5 ~ 8 mm^2, while the variation within each sample is significant (**Fig. 4.9b**). To investigate this variation, the pore areas were plotted against the distance between the center of pore and center of the sieve plate (**Fig. 4.9a,c**). It is found that the

pore area has no trends from the periphery to the center of the sieve plates (**Fig. 4.9c and 4.10**). Moreover, the area of the projected pores on the L-S plane also show no trend from the periphery to the center of the sieve plates (**Fig. 4.11**). However, whether the total projected pore area is dependent on the projected area on L-S plane of the fitted elliptical paraboloid dome cannot be concluded due to the limited number of samples. It is hypothesized here that the larger the total projected area on L-S plane of the osculum, the larger the total projected pore area, as the larger skeletal body requires larger opening area for sponge's pumping mechanism[34].

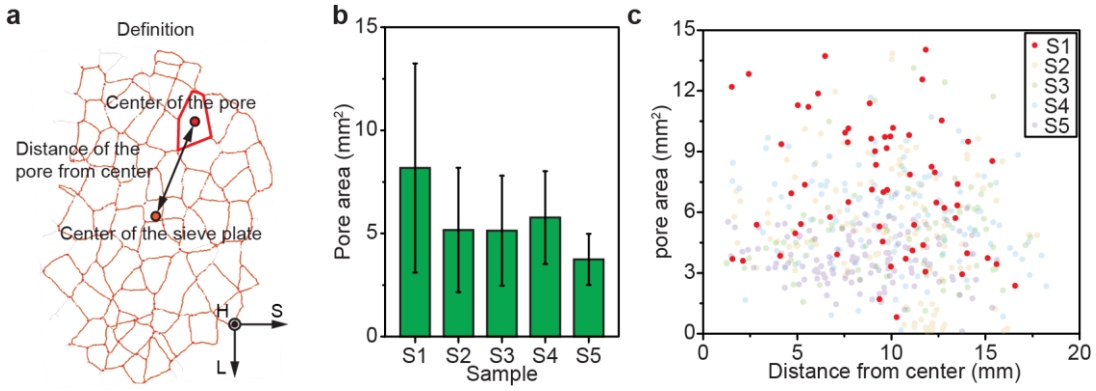


Figure 4.9. Pore area of the sieve plate samples. (**a**) 3D pore area and the variation of the sieve plate samples. (**b**) The schematic definition of the distance between the pore and the center of the sieve plate. (**c**) 3D pore area versus distance between pore center and the center of sieve plate.

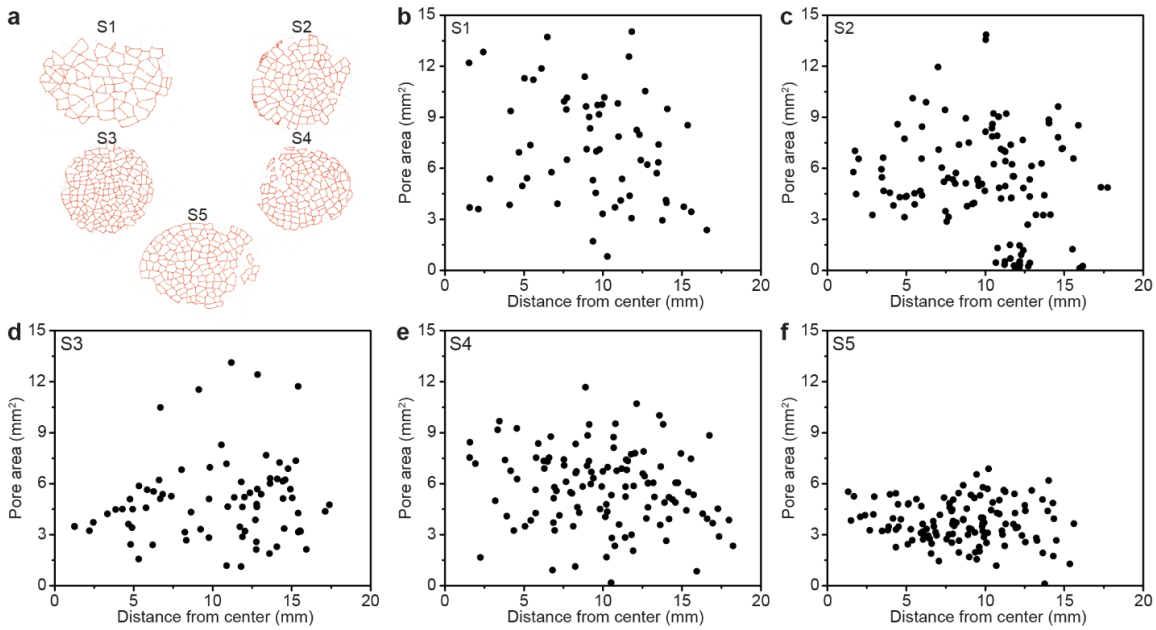


Figure 4.10. Pore area versus the distance between pore centers and center of sieve plate. (**a**) The 3D pores of different sieve plate samples for analysis. (**b-f**) Pore area versus the distance between pores and the center of each sieve plate.

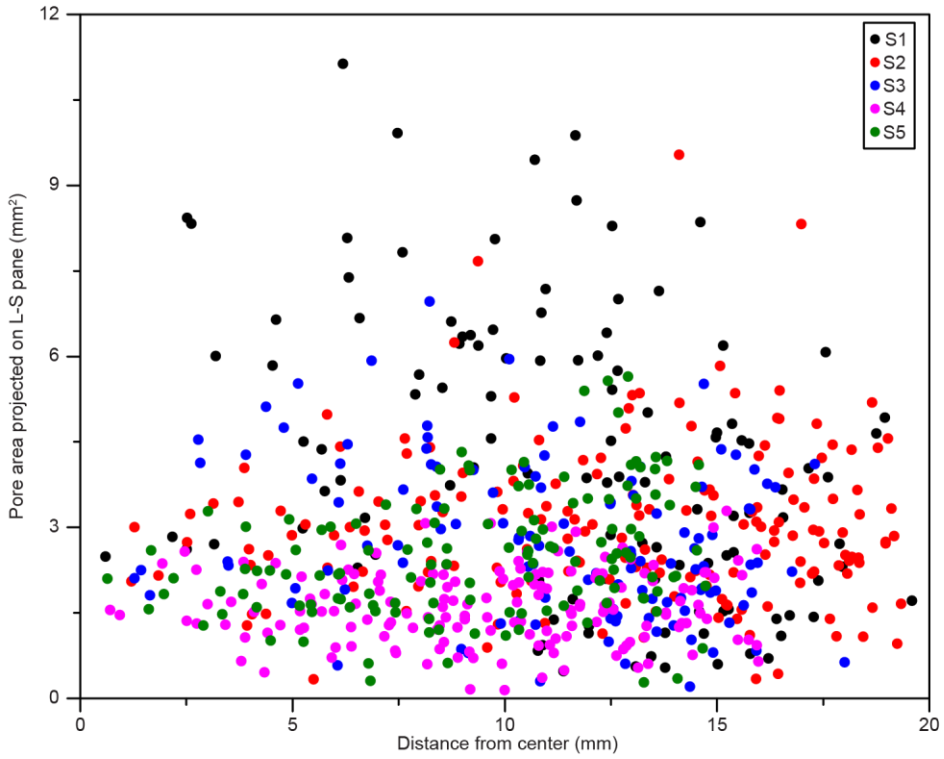


Figure 4.11. Projected pore area of sieve plate on L-S plane versus pore distance from the center of the sieve plate.

Other than the pore area, the morphology and alignment of the pores are critical to the mechanical performance of the cellular materials (**Fig. 4.3 and 4.12**). Here, the pore of sieve plate projected on the L-S plane is of interest. First of all, the distributions of area ratio of the projected pores were calculated (**Fig. 4.12a**), which generally show a concentration of area ratio distribution at ca. 0.005. Secondly, the projected pores were fitted with elliptical shape, which show good agreements between the fitted pores and actual projected pores (**Fig. 4.12b**). Based on the fitted elliptical pores, the aspect ratio of the pores as obtained in Eq. (4.2) shows a concentration at ca. 1.25~1.5 (**Fig. 4.12b**). Thirdly, the alignment score, which quantifies the pore alignment along specific sieve plate orientation, can be obtained from Eq. (4.3) (**Fig. 4.12c**). The result shows that the pores are most likely aligned along these orientation intervals of sieve plates: 0°-10°, 20°-40°, and 140°-160° (**Fig. 4.12c**). Therefore, these preferential pore alignments indicate that the sieve plate structure is anisotropic, which is correlated to the anisotropic mechanical properties as studied later.

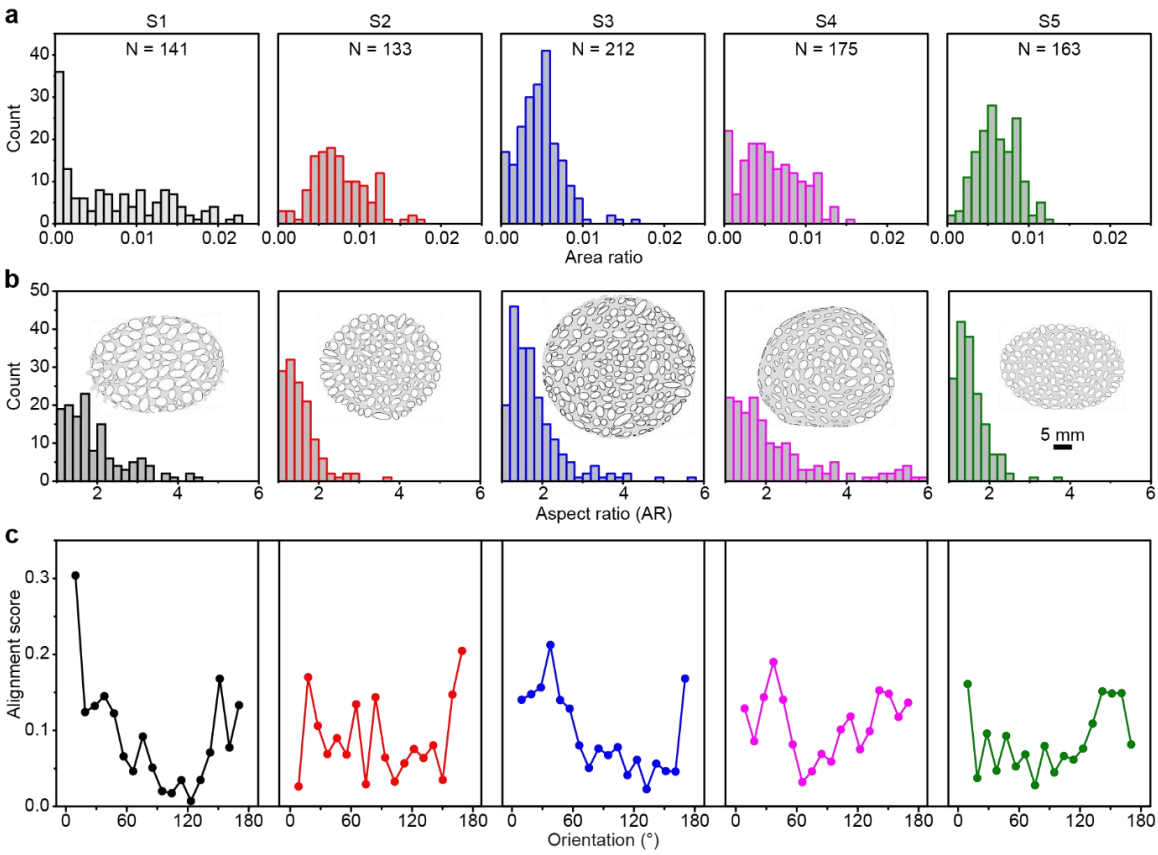


Figure 4.12. Characteristics of the projected pores on the L-S plane for all sieve plate samples. (**a**) Histogram distribution of the area ratio of each projected pore. N indicates the number of pores analyzed. (**b**) Histogram distribution of the aspect ratio of each projected pore fitted with elliptical shape. Insets show comparison between the original sieve plate pores and fitted elliptical pores. (**c**) Pore alignment score (area ratio times aspect ratio) of each 10° interval of sieve plate's orientation. The orientation in x-axis is the interval of α_{pore}.

Cellular pattern: Next, the nodal connections and cellular patterns were analyzed using the sieve plate projected on the L-S plane (**Fig. 4.13**). Firstly, the projected relative density of the sieve plates ($\bar{\rho}_{projected\ sieve\ plate}$) ranges from 37.6% to 59.4%,

corresponding to the total projected pore area from 264.2 to 545.1 mm^2 (**Fig. 4.13a**). After skeletonization, the nodal connections, including the N-3, N-4, and N-5 nodes were recognized, while the N-3 node takes the dominant role to form the sieve plates (**Fig. 4.13b, Table 4.1**). It can be found that many N-3 nodes are closed to each other which can be reflected to the large nodal structure (**Fig. 4.7e**), which may be a mechanism to stiffen and strengthen the local structure.

Furthermore, the projected pore centers were obtained to generate the Voronoi cells (**Fig. 4.4,4.13c**). These generated Voronoi cells were compared to the sieve plate's projected structure on L-S plane which agree well with each other (**Fig. 4.13c**). To quantify this comparison, the difference ratios ($diff$) as defined in Eq. (4.4) were calculated for all sieve plate samples, yielding an averaged concordance ($1 - diff$) of 77.7% ± 3.0% (**Fig. 4.13c**). This suggests that the projected sieve plate on L-S plane is a Voronoi-like cellular lattice. Therefore, the regularity index (k) of each Voronoi pattern generated from the projected pore centers of each sieve plate sample was calculated, resulting in values ranged from approximately 0.4 to 0.6 (**Fig. 4.13c**). This range of regularity index has an intersection with the range (0.5 to 0.8) where the fracture toughness is improved compared to regular honeycomb structure[138]. It is important to note that the nodal structure generated by Voronoi tessellation is usually N-3 node while the cellular network analysis identified N-4 and N-5 nodes (**Fig. 4.13b,c**). This is a result of very closed and large nodes potentially for local stiffening and strengthening as previously assumed (**Fig. 4.7e**).

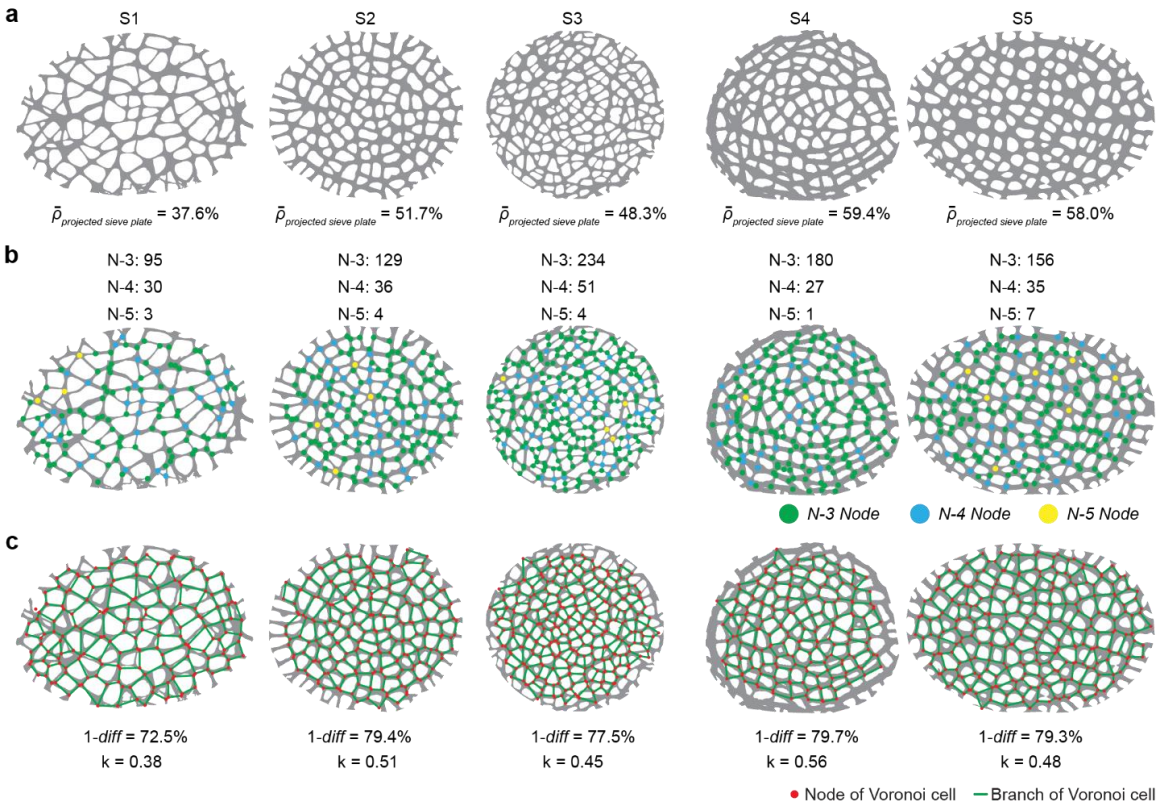


Figure 4.13. Cellular network and Voronoi pattern of the projected sieve plate on L-S plane. (**a**) Projected sieve plates on the L-S plane and their respective relative density ($\bar{\rho}_{projected\ sieve\ plate}$). (**b**) Node types of projected sieve plates on L-S plane. Green dot: N-3 node; cyan dot: N-4 node; yellow dot: N-5 node. (**c**) Overlaying of the projected sieve plate and the generated Voronoi lattice based on pore centers. The similarity between the projected sieve plate and corresponding Voronoi lattice and the calculated regularity index k are indicated.

These structural measurements indicate that the sieve plates are the dome-shaped Voronoi-like cellular lattices as hypothesized, while the Voronoi-like cellular pattern has an anisotropic shape as indicated by the pore alignments. The quantitative structural

understanding of the sieve plate, including the dome structure and cellular characteristics, were utilized to construct bio-inspired models for mechanical understandings.

4.3.3. Effect of the cellular dome structure on the stiffness

Based on the structural understanding, bio-inspired models, which capture the structural features of the sieve plate studied above, and corresponding control models were constructed to understand the mechanical performance of sieve plate. In this section, the mechanics of the Voronoi-like cellular dome in sieve plates were studied.

To investigate the mechanical performance of the Voronoi-like pattern of the sieve plates, mechanical simulations were performed on the projected sieve plate on the L-S plane and control models of computer-generated Voronoi lattice with same regularities and regular honeycomb lattice with same number of pores (**Fig. 4.14a-d**). For the projected sieve plate, loadings were applied in various directions as denoted by the angle θ, which defines the loading directions relative to the L direction of the projected sieve plate (**Fig. 4.14a**). Therefore, 0° represents the L direction, while 90° represents the S direction. The elastic moduli in various θ reveal that the modulus closed to the S direction is higher than modulus closed to the L direction for all sieve plate's cellular patterns studied as shown in **Fig. 4.14b**. This mechanical anisotropy can be explained by the correlation between elastic moduli and pore alignment scores as shown in **Fig. 4.15**: in general, the orientation with higher alignment score (usually ca. 30° and 150°) has higher elastic modulus. Whether this increased modulus closer to L direction is originated from biomechanics or the growth remains unknown. For comparison, compression simulations of the control models in X and Y directions (i.e., computer-generated Voronoi lattice and

the corresponding regular honeycomb lattice) were carried out to obtain their elastic moduli (**Fig. 4.14c,d**). It is found that, on averaged, the elastic moduli of the projected sieve plates are similar to those of the control models, suggesting that the regularities do not affect significantly the overall elastic modulus sieve plate's cellular patterns.

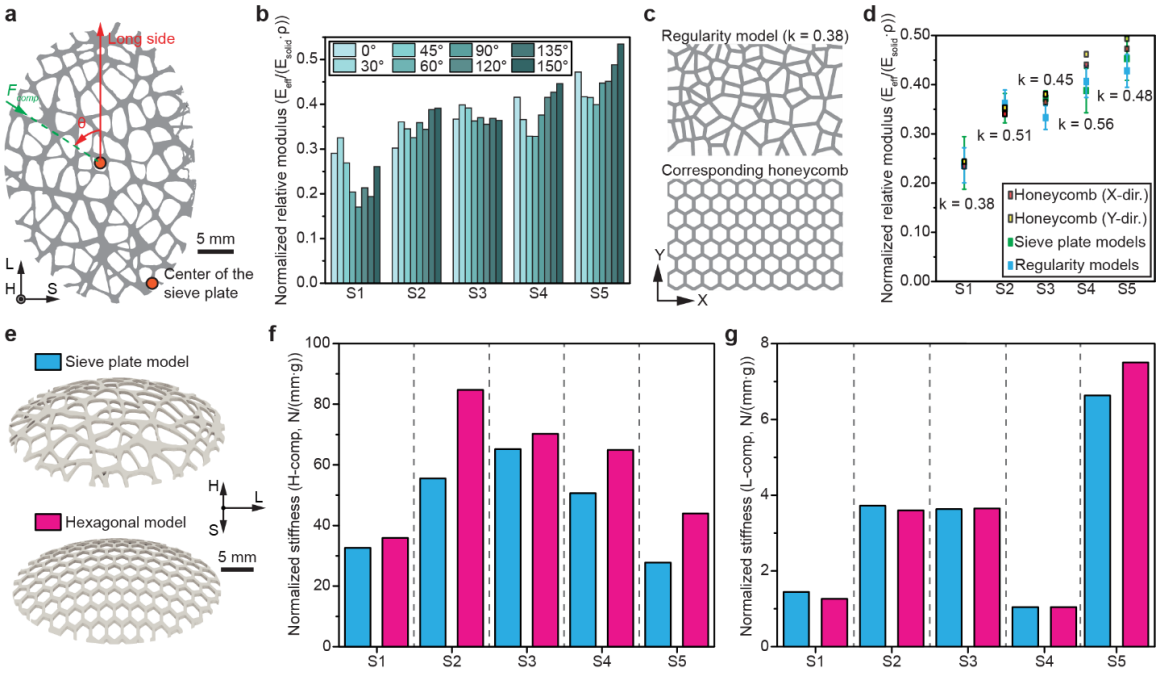


Figure 4.14. 2D modeling and simulations of the sieve plate. (**a**) 2D models of the projected sieve plate and the corresponding honeycomb lattice with similar relative density for comparison. The X and Y directions are defined in the coordinate system on the bottom left. (**b**) Relative modulus of 2D sieve plate models and the corresponding honeycomb lattices along X and Y directions.

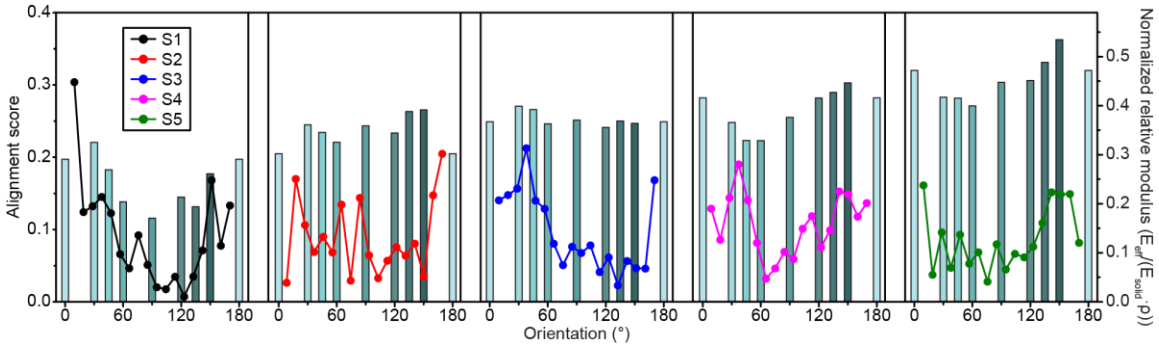


Figure 4.15. Correlation between elastic moduli and pore alignment score. The scatter points indicate the alignment score while the columns indicate the normalized relative modulus. The orientation in x-axis is the interval of α_{pore} or θ.

To study the combined effect of the dome shapes and Voronoi-like patterns of sieve plates, the cellular domes with sieve plate's projected cellular patterns and regular honeycomb lattice patterns were constructed for 3D printing fabrications and compressive experiments along H and L directions (**Fig. 4.14e-g, 4.16**). The normalized stiffnesses of the sieve plate models along H and L directions are smaller and similar to those of the honeycomb models, respectively (**Fig. 4.14f,g**). Therefore, in general, the sieve plate's Voronoi-like cellular pattern provides mechanical stiffness similar to the regular honeycomb structure, which provide protections to the osculum and interior of the sponge as previously hypothesized[21].

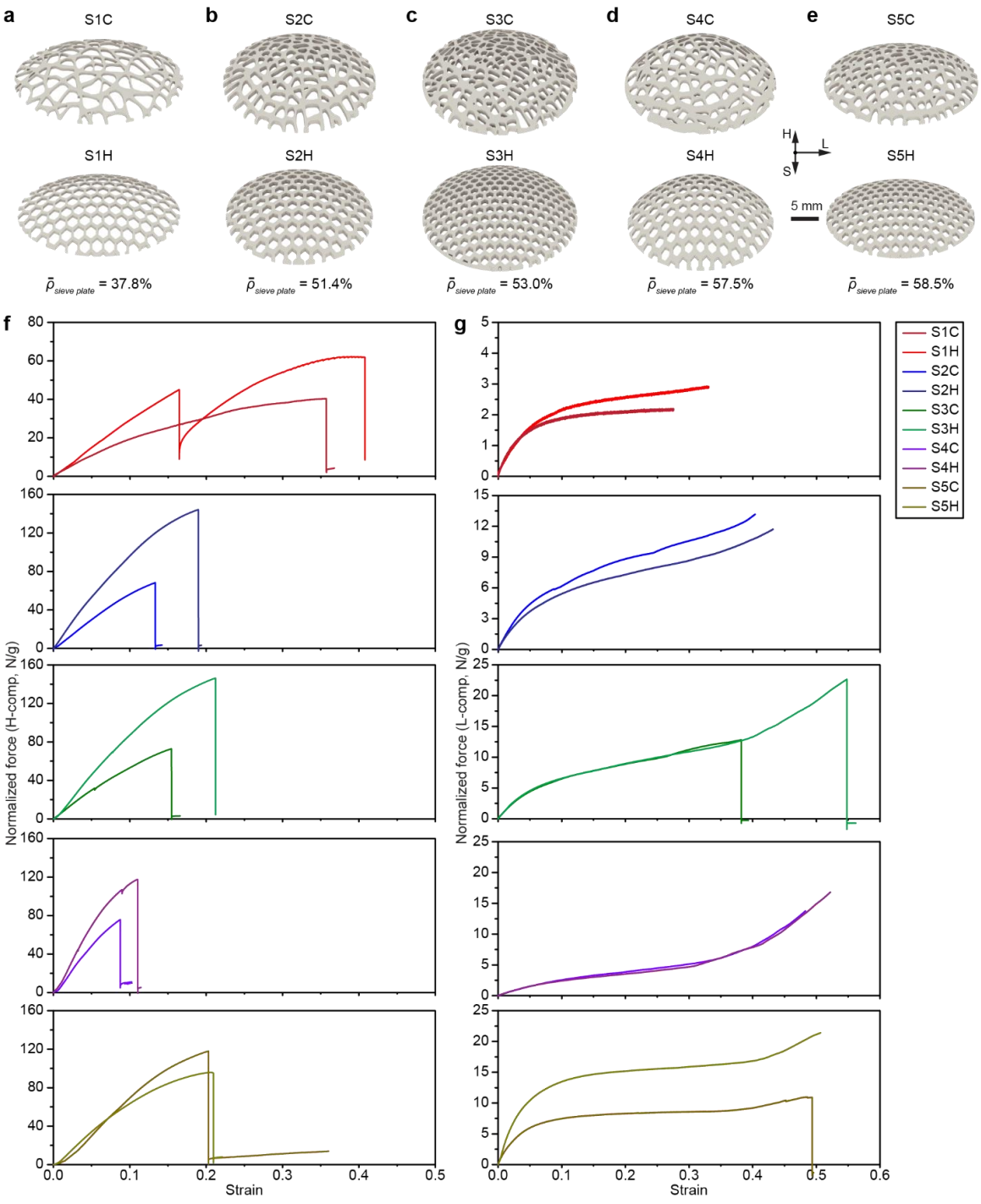


Figure 4.16. 3D bio-inspired modeling and experimental stress-strain curves of the cellular domes. (**a-e**) Five 3D bio-inspired dome-shaped models of the sieve plate and the corresponding honeycomb lattice with same relative density for comparison. "C" and "H" denote the models inspired by cellular sieve plate and models of honeycomb lattices,

respectively. (**f-g**) Curves of the normalized force versus strain of the models along height (Z) direction (**f**) and long side (R) direction (**g**).

4.3.4. Effect of the porous branch with increased height on the stiffness

Except for the dome structure and Voronoi-like cellular pattern of the sieve plates, porous branch ($\bar{\rho}_{branch} = 55.9\% \pm 6.7\%$) with increased height in the dome thickness direction (T) as found previously (**Fig. 4.2b**) is another structural feature which may contribute to the mechanical performance of sieve plates. Therefore, the bending stiffness of the bio-inspired porous branch was compared to solid branches with other types of cross sections (Materials and Methods, **Fig. 4.6,4.17**).

Based on the simulation results, two lessons can be learnt: i) the increase of branch height which is in the direction of bending load provides improvement of the bending stiffness compared to branches with height identical to the width; ii) The introduction of a certain level of porosity to the branch provide further improvement of the bending stiffness. In particular, the bio-inspired porous branch has approximately 25% and 120% improvements in bending stiffness compared to the elliptical/rectangular branches and circular/cubic branches, respectively (**Fig. 4.17d**). In addition, the increase of number of unit cells and the relative density both decrease this improvement of bending stiffness (**Fig. 4.17d**).

Whether the improvement of bending stiffness of sieve plate branch can increase the overall stiffness of the sieve plate needs to be discussed in details. For example, under loadings along H direction, the sieve plate branches are under both compressive and bending loads. Despite the increase of bending stiffness due to porosity, the compressive

modulus decreases (12.3 GPa compared to 40 GPa of silica solid). Considering the increase of cross-sectional area of porous branch under given material volume, in comparison, the compressive force taken by the bio-inspired porous branch is ca. 0.77 of that of the elliptical solid branch. This suggests a competing mechanism: the dominant deformation of the sieve plate branches (i.e., bending or compression) dictates the stiffness of sieve plate. In sieve plates, the relatively low rise (low dome height compared to the length of long and short sides, **Fig. 4.8**) results in predominant bending deformation of the sieve plate branches. Therefore, the increased branch height provides increase of bending stiffness of the sieve plate branch and hence the H-stiffness of the sieve plate (**Fig. 4.17**).

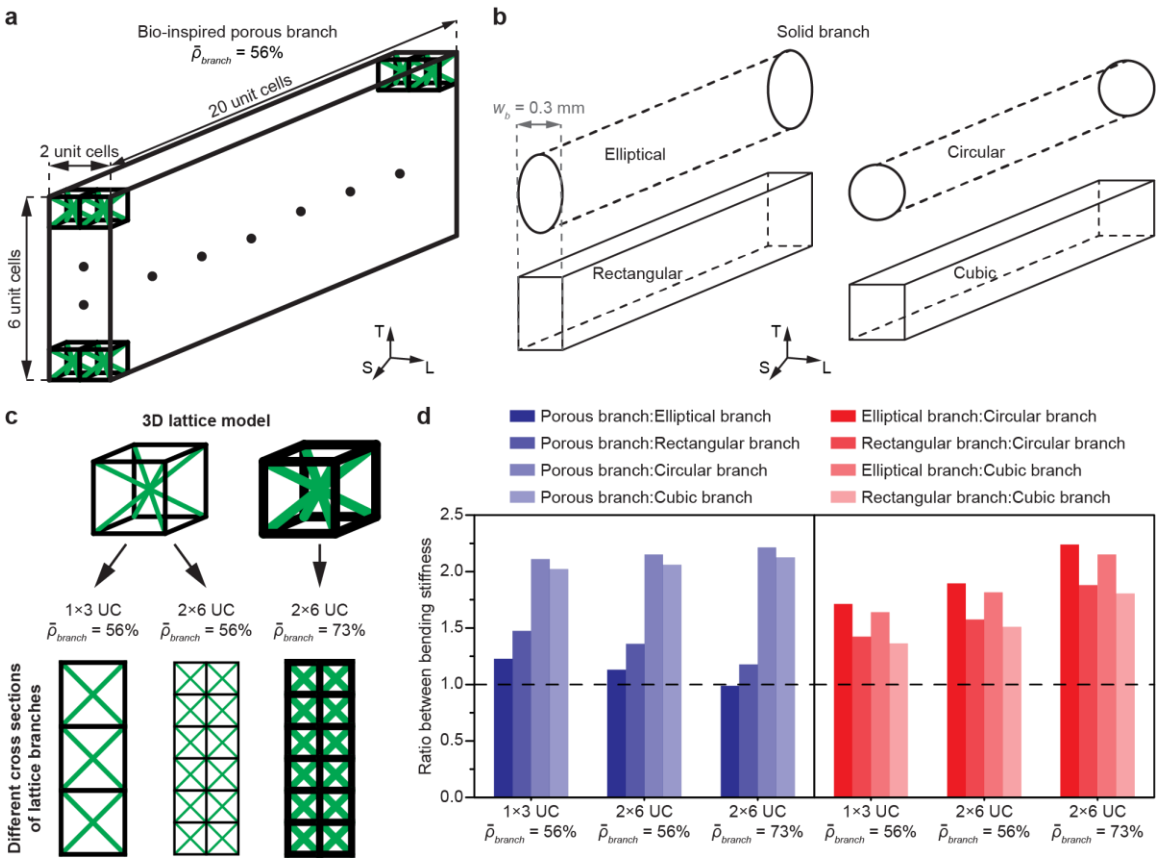


Figure 4.17. Modeling of the porous branch inspired by sieve plate and bending stiffness study. (**a**) The bio-inspired porous branch with increased height. There are 2×6×20 BCC unit cells along the directions of the branch width, height, and length. (**b**) Control models of solid branches with same material volume for comparison. The width of elliptical and rectangular branches is identical to that of the sieve plate branch as measured (ca. 3 mm). (**c**) Different porous branch designs with 1×3×10 and 2×6×20 unit cells numbers and with 56% and 73% relative density, respectively. (**d**) Ratio between bending stiffnesses. The blue columns are ratios between bending stiffnesses of lattice branches and solid branches. The red columns are ratios between bending stiffnesses of elliptical/rectangular solid branches and circular/cubic solid branches.

4.4. Discussions

In the present work, three important structural features of the biomineralized cellular lattice of sieve plate in glass sponge *E. aspergillum* were studied with quantitative characterizations, including the dome structure with the elliptical paraboloid shape, the Voronoi-like cellular pattern with anisotropic pore alignments for the sieve plate projected on the L-S plane, and the porous branch with increased height in the dome thickness direction (T). These structures lead to three main mechanical functions: i) the Voronoi-like cellular pattern of sieve plates has higher moduli in the directions closed to the long side than those closed to the short side, yet in general provides similar modulus compared to computer-generated Voronoi lattice and corresponding honeycomb; ii) the Voronoi-like dome structure of sieve plates has stiffness in H and L directions approaching the stiffness of the dome with honeycomb cellular pattern; and iii) the porous structure and increased height in sieve plate branch provide increased bending stiffness and hence the stiffness in H direction of the sieve plate. These structural-mechanical strategies found here suggest that the sieve plate tends to provide mechanical protections to the osculum and interior of the *E. aspergillum*. Despite its irregularity, the sieve plate can still provide stiffness closed to that of regular honeycomb lattice.

Except for the mechanical function, the increased height in the porous sieve plate branch may be a strategy to assist sponge's filtering feeding[34]. The glass sponge *E. aspergillum* filter water current through their cylindrical bodies and pump out from the osculum which is covered by the sieve plate. Therefore, it can be assumed that the increased height of sieve plate branches simultaneously maintains the large pore opening for efficient current pumping and improves the stiffness of the structure. This

understanding here may inspire cellular dome design with multifunctionalities such as improved stiffness, stabilities, sunlight penetration, and air circulation.

The porous nodal structure of the sieve plate is another critical structural unit which was explored in the next chapter. The porous sieve plate nodes, similar to the sieve plate branches, consist of fibrous spicule bundles which may inspire unique nodal design for lattice materials. The smooth transition using spicule fibers between the branches and nodes provides a strategy to reduce stress concentrations typically occurred at the sharp joints of artificial lattice materials. Therefore, exploring the spicule constructions at the sieve plate nodes and branches leads to in-depth microstructural and mechanical understandings of the sieve plate. As a demonstration of the mechanical performance, in-situ μ-CT compression of the sieve plate node (**Fig. 4.18**). The result demonstrated that the sieve plate node went through successive fracture where the locations touching the compression head and plate fracture while the interior remains intact (**Fig. 4.18**). This is a result of the cellular nature of the sieve plate node. A closer examination shows that the spicule delaminated and the synapticular bridging broke which separates individual spicules (**Fig. 4.18c-e**). Furthermore, the fracture locations can be uniformly distributed everywhere closed to the compression head and plate which prevents specific path of fracture and improves toughness (**Fig. 4.18f**). These mechanisms may contribute to the improvement of overall toughness of the sieve plate nodes and hence the sieve plate.

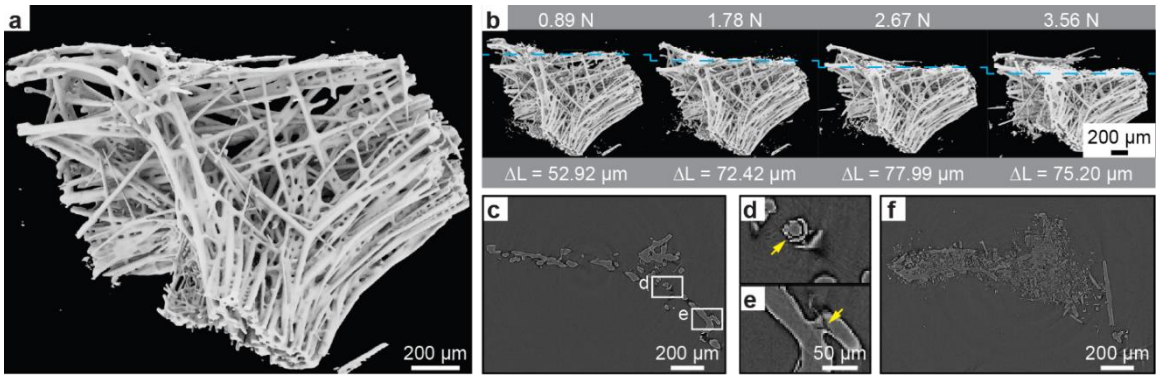


Figure 4.18. Deformation and fracture mechanisms of the sieve plate node. (**a**) 3D volume rendering of the sieve plate node for in-situ µ-CT compression. (**b**) The sequential 3D volume renderings of sieve plate node under different loading and displacement under in-situ µ-CT compression. (**c-e**) A projection image showing the spicule delamination (**d**) and synapticular bridging breakage (**e**). (**f**) Uniform fracture distribution of the sieve plate node under 3.56 N compressive load.

The structural understanding here provides fundamentals to understand the mechanical performance of the sieve plate. Yet, many mysteries still exist in the sieve plate such as the formation and its correlations to the structure and functions. Further exploring the microstructure not only provides better structural understanding and mechanical modeling of the sieve plates, but also helps the understanding of sieve plate's formation process which is the origin of its mechanical (e.g., improved stiffness) and biological functions (e.g., the filtering feeding and accommodation of symbiotic shrimps)[72]. Therefore, despite the structural-mechanical exploration here, the sieve plate presents a multifunctional properties at different stages of its formations which will be discussed in the next chapter.

4.5. Conclusions

In this work, we demonstrated that the sieve plate is a Voronoi-like cellular dome structure with an elliptical paraboloid shape while its porous branch has increased height to thicken the cellular dome. These structural features synergistically provide mechanical stiffness to the sieve plate, serving the mechanical function as a protection to the osculum and interior of glass sponge *E. aspergillum*. The observed preference of pore alignments (ca. 30° and 150° relative to the long side of the sieve plate) of the Voronoi-like pattern in the sieve plates results in the structural and mechanical anisotropy where the directions with preferred pore alignments have higher elastic modulus. In addition, the increased height in porous sieve plate branch may serve as a strategy to stiffen the sieve plate while maintaining the large pore size for sponge's efficient filtering feeding. We envisioned that the results here provide i) inspirations to multifunctional cellular dome design with improved stiffness, sunlight penetration, etc. Despite the first work to describe the structural-mechanical relationships of sieve plate, future studies are needed such as the microstructural studies to provide detailed structural understanding, accurate mechanical modeling, and understanding of the sieve plate's formation.

Chapter 5 Microstructure-based study of the formation of the sieve plate in glass sponge *Euplectella aspergillum*

Combing chapter 4, this work is being prepared for publication.

The structural-mechanical linkage of the cellular dome in the sieve plate of glass sponge *Euplectella aspergillum* has been previously explored, which reveals the balance between the pore opening area for sponge's current pumping and stiffness via dome thickening. As the origin of the functional trade-offs and potential inspirations to the engineering construction, exploring the formation of this multifunctional structure is significant. To approach this mystery, firstly, basic assumptions of sieve plate formation were made based on previous works. Secondly, new hypothesis and predictions of the sieve plate formation process were proposed based on the study of the microscale structures in sieve plate, including the spicule bundle connections, morphology of hexactines, and characteristics of individual spicules. Finally, the two-step formation process of the entire sieve plate is predicted: i) as a continuation of the cylindrical skeleton, the growth of sieve plate starts from the periphery towards the center which forms the initial tessellation for the accommodation of symbiotic shrimps; ii) some spicule bundles grow later to bridge the existing spicule bundles and form the final Voronoi-like tessellation for mechanical stiffness and sponge's current pumping. Other details during the formation such as the function of hexactines, growth sequence of different spicule types, local modifications due to bridging, were also demonstrated. This study provides understanding of a process of organisms to form Voronoi-like pattern different from grain growth mechanism.

5.1. Introduction

Euplectella aspergillum (class Hexactinellida), also known as the "Venus' flower basket", exhibits a biogenic silica-based lattice skeleton, which is of great interest to study its structures[21], formation[72], and mechanics[58,70,71]. Most of the works have been focused on two-folds: i) structural-mechanical properties of spicules such as the improved flexibility and strength due to the cylindrically laminated architecture with decreasing silica layer thickness[58,65]; and ii) the hydrodynamic-mechanical functions of the cylindrical skeleton such as the suppressed vortex shedding due to the ridge structure and the improved buckling strength due to the double-diagonal configuration[70,73]. Only limited qualitative study has been conducted for another skeletal component of *E. aspergillum*—sieve plate—which covers the osculum and hence influences the sponge's current pumping and stiffness of the end opening of the cylindrical skeleton[33]. In the previous chapter, it has been discovered that the sieve plate is a Voronoi-like cellular dome with porous branch of increased height which is a balance between large opening for sponge's current pumping and mechanical stiffness to protect the osculum and the interior of the sponge. To understand the origin of the multifunctional benefits and provide potential inspirations to engineering constructions, it is, therefore, significant to explore the formation process of the sieve plate.

The formation of the skeletons and their building block—spicule—of the Hexactinellid sponges have been previously qualitatively studied, which provides some fundamentals to the formation study in this work. For the spicule's formation, most of the studies are based on the anchoring spicule of species *Monorhaphis chuni*, which has diameter of a few centimeters[59–61]. At the initial stage of the spicule growth, the axial

organic filament and the cylindrical silica core are synthesized intracellularly in the sclerocytes, the cells specifically for mineral depositions. The proteins such as silicatein enzymatically assist the silicic acid precursor to form the amorphous and hydrated silica. Next, the formation becomes extracellular as the increase of the spicule's diameter and consists of growth along the longitudinal and diametrical directions. The spicule grows along the longitudinal direction via the extension of the axial filament and deposited silica rod as demonstrated by the highly concentrated silicatein around the tip of spicule[59]. While, to expand in diameter, the spicule grows silica laminates within a cylindrical protein shell formed by silicatein and lectin molecules. Some of these silica layers will be further merged together to form a thicker silica layer via a bio-sintering process[62]. It has been previously believed that the diametric growth of the spicule is a result of tip growing a new silica layer downward[59]. However, recent observations of the step surfaces and patches on the spicule, as well as the thin tip and thick spicule body demonstrate that the new layers of silica can be initially deposited anywhere and grow towards the tip and end of the spicule[61]. This layering formation mechanism also allows the thickening of the spicule bundles with the axial filaments of spicules closed. For the skeletons, their formation mechanisms and processes have been limitedly explored as in-situ observations in deep sea or laboratory cultivation of the deep-sea sponges are challenging. Yet, through structural exploration, two important understandings of the formation can still be obtained. Firstly, due to the structural protein F-actin in the axial filament, the spicules are not only able to extend and thicken, but they can also branch into various forms of networks to form complex skeletal lattices[53]. Secondly, by observing the skeletons of *E. aspergillum* at different growth stages, researchers have

postulated that the skeleton of the young sponge with flexible and thin silica spicules is first formed. The sponges' skeletons continue to grow in height and stiffen simultaneously via secondary silica deposition which merges large amount of small spicules into bundles to form the mature and stiff skeletons[21,72]. These previous understanding of the spicule and skeleton formations provide two basic hypotheses to the growth of sieve plate: i) the growth from bottom to the top of the skeleton implies that the sieve plate of *E. aspergillum* starts to grow at its periphery[70,72]; and ii) the sieve plates stay soft at the early stage and become stiff later via bundling of individual spicules[72].

Furthermore, the formation process of the sieve plate of *E. aspergillum* needs to balance three functional aspects: i) the accommodation of the symbiotic shrimps[72]; ii) enough pore opening of the sieve plate to allow sponge's current pumping; and iii) mechanical stiffness to prevent the collapse of osculum and protect the interior of sponge's cylindrical skeleton[21]. My previous work in the last chapter has already demonstrated that the final skeletal lattice of sieve plate balances the last two functions. However, to guarantee the accommodation of symbiotic shrimps, the sieve plate at the initial growth stage should be relatively flexible and possess relatively large pores compared to its final Voronoi tessellation. Therefore, third hypothesis of the sieve plate formation can be made based on its functions: the initial tessellation of the sieve plate, which allows the symbiotic shrimps to get in or out, has higher porosity than the final Voronoi-like tessellation of the sieve plate.

So far, three hypotheses of the sieve plate formation are proposed based on previous works. In this work, via the microstructural study on the sieve plate, including investigating the hexactines (a type of spicule with six-rayed structure), individual

spicules, and spicule bundles, some evidences were provided, more hypotheses were proposed, and a comprehensive picture of the sieve plate's formation was predicted. The results here provide not only understandings of the microstructure and formation of the sieve plate, but also a biological inspiration for constructing multifunctional lattice dome.

5.2. Materials and Methods

Sample preparations: Dried skeletons of the glass sponge *E. aspergillum* were purchased from commercial sources. The sieve plate nodes and a long strip of the sieve plate starting from the periphery of the sieve plate were cut from different skeletons using a diamond saw blade for imaging and short-range or long-range structural analysis, respectively.

Scanning Electron Microscope imaging: Prior to scanning electron microscope (SEM) imaging, sieve plates and sieve plate nodes were coated using ~20 nm platinum/palladium. Due to the complexity of the microstructures of sieve plate nodes, the coating is relatively thick to reduce the charging effect. The images were acquired in FEI Quanta 600 FEG with a typical working distance of ~12mm and a voltage of 15kV.

Micro-computed tomography analysis: Two different systems of micro-computed tomography (μ-CT) were used for different samples. For the sieve plate nodes, the synchrotron-based μ-CT at the 2-BM beamline in Advanced Photon Source (APS) was used. A monochromatic beam with 27.4 keV energy was used to acquire 1500 projection images (2560 × 1300 pixels per image) over 180° rotation of the samples. The 5× and

10× long-working-distance objective lenses were used to acquire the images with voxel size of 1.3 µm and 0.65 µm (i.e., fields of view of 3.33 mm × 1.69 mm and 1.66 mm × 1.38 mm), respectively, depending on the sample size. For the long strip of the sieve plate, the Skyscan µ-CT system 1172 (Aartselaar, Belgium) was used, where the X-ray was operated at 80 kV and 100 µA. The projection images with voxel resolution of 3.83 µm were acquired for each scan with a 180° sample rotation. These projection images were captured by a Hamamatsu camera with a resolution of 1280 × 1280 pixels, corresponding to the field of view of 4.9 mm × 4.9 mm. Multiple scans were conducted along the horizontal direction and stitched automatically to form a complete scan of the entire long strip of the sieve plate. The as-obtained projection images were further automatically reconstructed in the system.

The reconstructed images were segmented in a commercial tomography analysis software Avizo 2019.2 (Thermo Fisher Scientific, Massachusetts, USA). This software was also used for 3D volume rendering, visualization, and quantitative structural analysis. All tracings of individual spicules in spicule bundles were conducted manually in Avizo.

5.3. Results and discussions

5.3.1. Microstructural observations for sieve plate's cellular pattern formation

The sieve plate of *E. aspergillum* is a dome-shaped Voronoi-like biomineralized cellular lattice covering the osculum as shown in **Fig. 5.1a**. The macrostructures and mechanical stiffness of sieve plates have been explored previously, demonstrating that the sieve plates have increased dome thickness to maintain large enough pore opening and improve stiffness similar to the regular hexagonal lattice. The microstructures of the

sieve plate branches and nodes exhibit spicule bundles where the individual spicules are merged together by silica matrix (**Fig. 5.1b,c**)[21]. These branches and nodes were closely examined in **Fig. 5.2-5.10** to observe the unique microstructural features in sieve plates and provide structural bases to the cellular formation of sieve plate.

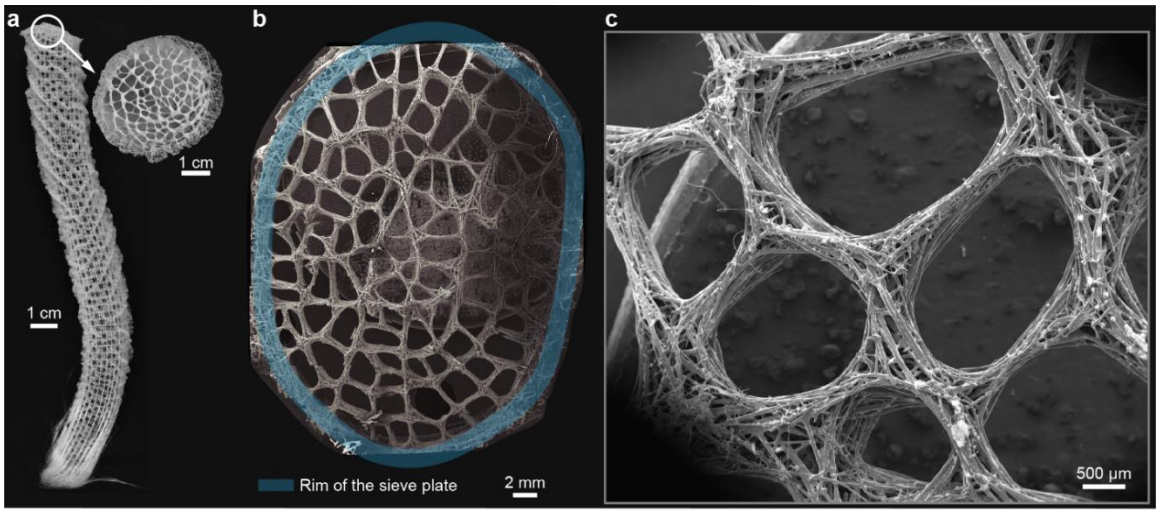


Figure 5.1. Introduction of the microstructure of sieve plate in *E. aspergillum*. (**a**) The bare silica skeleton of *E. aspergillum* (inset: biomineralized skeleton of the sieve plate). (**b**) Large-scale stitched SEM image of the sieve plate (cyan band: the rim of the sieve plate). (**c**) SEM image of the sieve plate branches and nodes showing the spicule-based microstructure.

The first observation is on the periphery (or rim) of the sieve plate where it is connected to the cylindrical skeleton (**Fig. 5.2**). SEM image and µ-CT volume rendering demonstrate that the cylindrical skeleton of E. aspergillum grows spicule bundles into the sieve plate from the longitudinal and circumferential spicule bundles. This indicates that

the sieve plate is a continuation of the cylindrical skeleton. Furthermore, this supports that the sieve plate starts to grow from its periphery to the center[70,72].

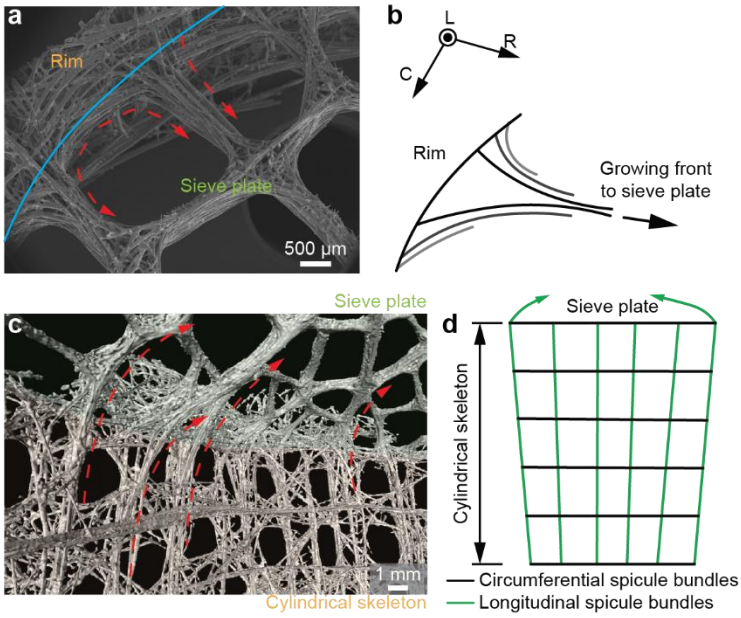


Figure 5.2. Observations of the rim of the sieve plate. (**a**) SEM image of the spicule bundles growing from the rim of the sieve plate which can be considered as the top-most circumferential spicule bundles of the cylindrical skeleton. (**b**) The schematic of the circumferential spicule bundles growing towards the center of sieve plate. (**c**) SEM image of the longitudinal spicule bundles in the cylindrical skeleton connecting to the sieve plate. (**d**) The schematic of the longitudinal spicule bundles growing towards the center of sieve plate.

For the sieve plate nodes, SEM images of the N-3, N-4, and N-5 nodes (i.e., nodes having 3, 4, and 5 branches interconnecting) of the sieve plate demonstrate the spicule-based cellular structure (**Fig. 5.3a-c**). This spicule-based cellular structure of sieve plate node is further demonstrated by the 3D volume rendering of the μ-CT scanned sieve plate

node (**Fig. 5.3d**). Closer examination using the SEM and µ-CT imaging of the sieve plate node found that there are several microscale structural features (**Fig. 5.3e-h**), including joints between spicules called synapticular bridging and megascleres of hexactine, tetractine, and diactine[129,141]. These observations generally agree with the previous qualitative descriptions of the sieve plate structure of *E. aspergillum*[21].

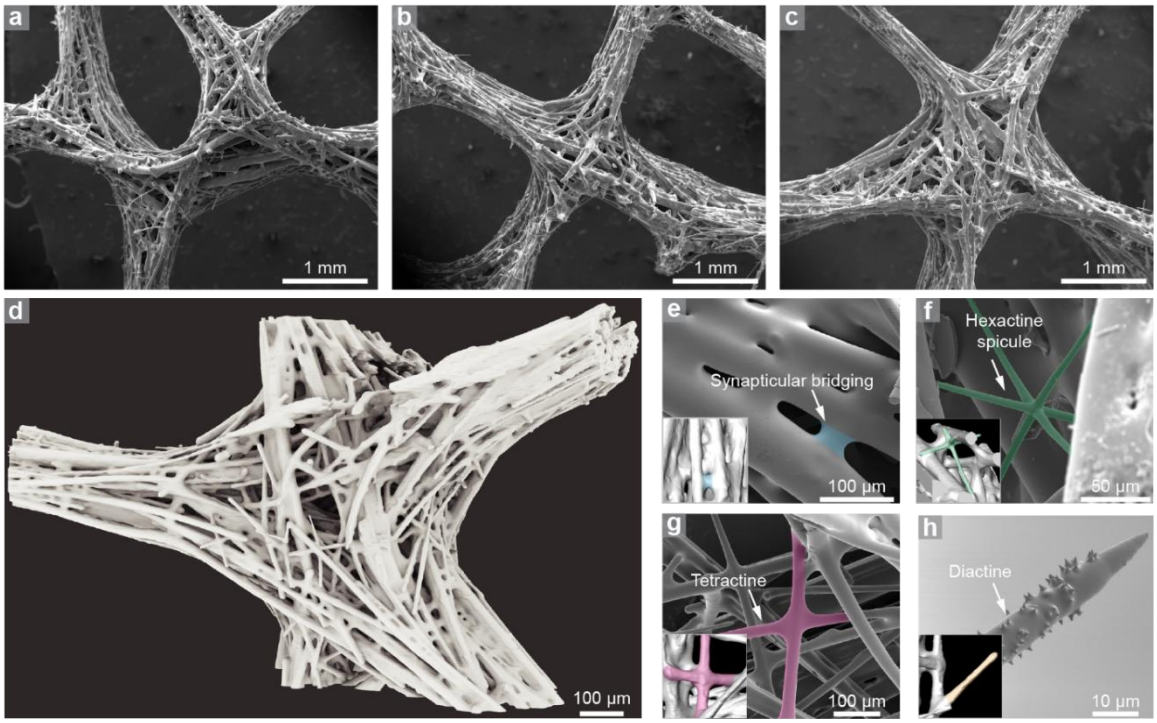


Figure 5.3. Microscale structure of sieve plate node. (**a-c**) SEM images of the N-3 (**a**), N-4 (**b**), and N-5 (**c**) sieve plate nodes. (d) 3D volume rendering of the N-4 sieve plate node obtained from µ-CT scanning. (**e-h**) The SEM imaging of (**b**) spicule-spicule joint, or synapticular bridging, (**c**) hexactine megasclere, (**d**) tetractine megasclere, and (**e**) diactine megasclere. The insets in (**e-h**) are the corresponding spicule structures found in µ-CT scanning.

For the sieve plate branches, except for the spicule bundles, a large amount of hexactine (spicule with six rays) megascleres was observed (**Fig. 5.4-5.5**). These hexactines were observed at the outer surface and interior of the sieve plate (**Fig. 5.4a-c, 5.3f**) or location that away from the sieve plate node (**Fig. 5.4d-f**). No matter where the hexactines are, they are usually very thin compared to spicules mainly constructing the sieve plate. Therefore, one hypothesis can be made that the excessive amount of hexactines do not provide significant mechanical functions such as stiffness and strength to the sieve plate. Furthermore, significant amount of hexactines were observed at the growing tips of the spicules such as the end of the growing spicules and the growing front of the additional branch (**Fig. 5.5**). Therefore, the second hypothesis for the hexactines was made, of which they assist the growth of the sieve plate by providing anchoring sites to the soft tissue for efficient silica deposition. Even though the current observations show that the hexactines remain and become parts of the sieve plate, whether there is any reabsorption of these hexactines is still unknown. In addition, whether other megascleres (tetractine and diactine, **Fig. 5.3g,h**) have similar or other functions remains unknown.

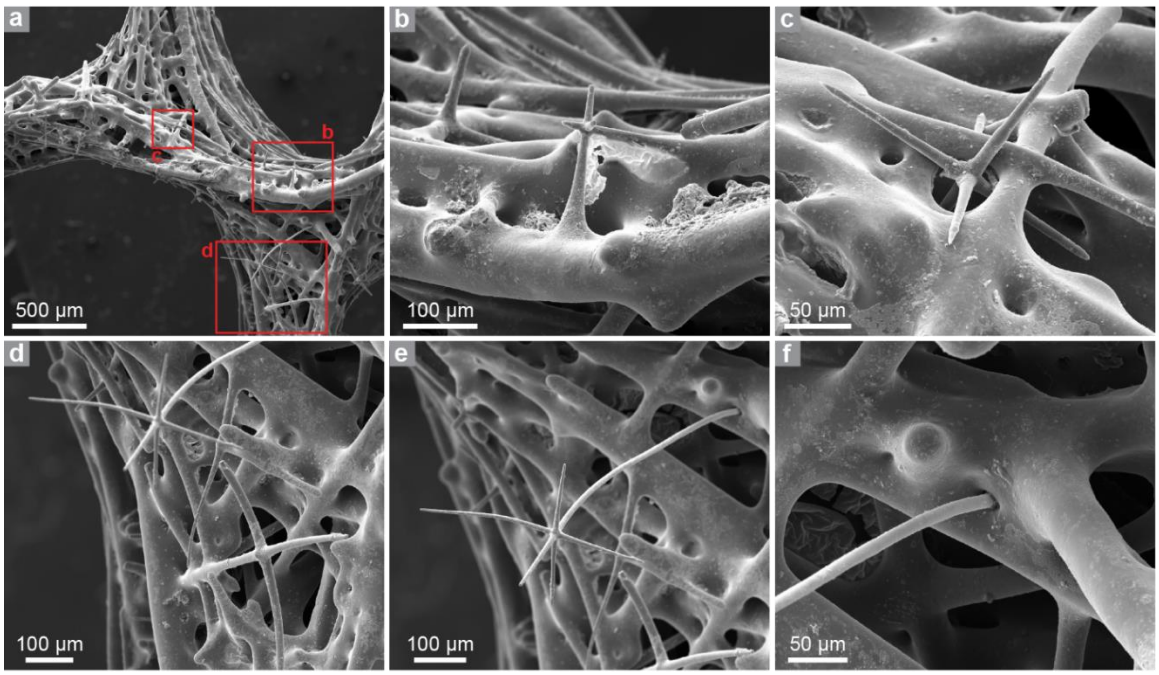


Figure 5.4. Hexactines in the sieve plate branches. (**a-c**) SEM images of the hexactines on the outer surface (**a,b**) and interior (**c**) of the sieve plate. (**d-f**) SEM images of the hexactines extended away from the sieve plate's outer surface.

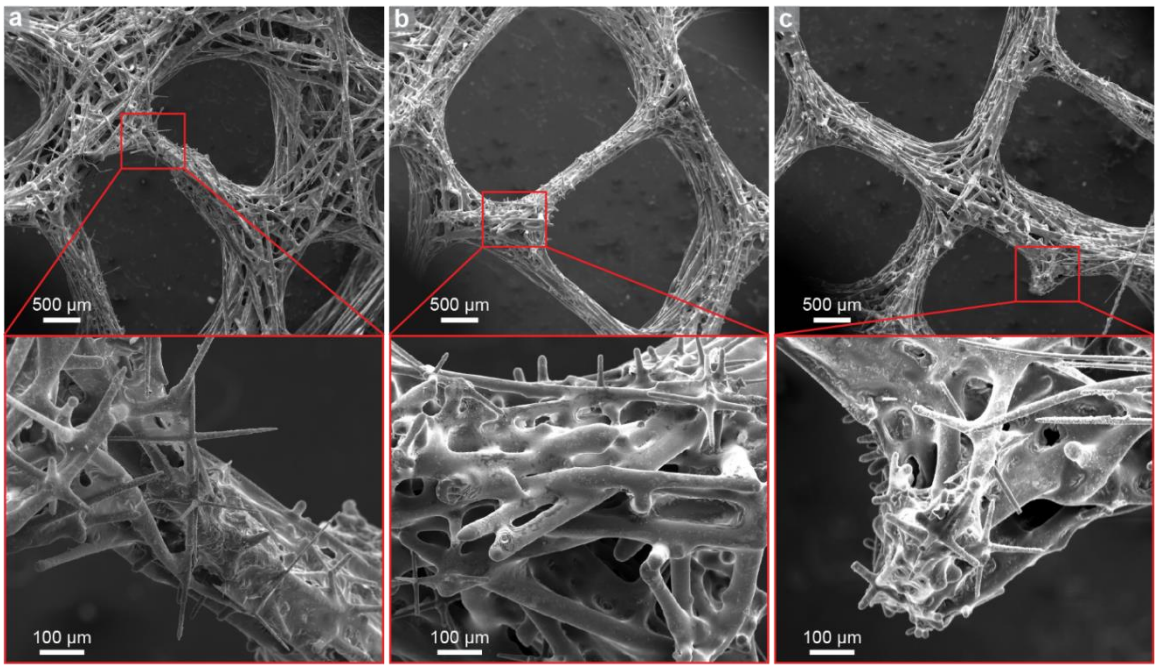


Figure 5.5. Hexactines at the growing tips of the sieve plate branches. (**a-c**) SEM images of hexactines at the end of the growing spicule bundles (**a,b**) and at the growing front of the sieve plate branch (**c**).

Next, how the sieve plate branches, which are also spicule bundles, are connected to each other is studied based on the SEM observations, which provides evidence of different tessellations at different growth stage of the sieve plate (**Fig. 5.6-5.10**). It is found that the N-3 nodes can be formed by bridging a branch onto the middle of another branch (**Fig. 5.6**) or mutual bridging by extending branches towards each other as shown in **Fig. 5.7** and **5.8**. It is hypothesized here that some bridging spicule bundles grow at a later stage after the initial tessellation of the sieve plate as demonstrated by the thin bundle of spicules in **Fig. 5.8** and provides reduction of the pore sizes for mechanical stiffening[2]. This bridging can also be observed for the formation of N-5 node (**Fig. 5.9**).

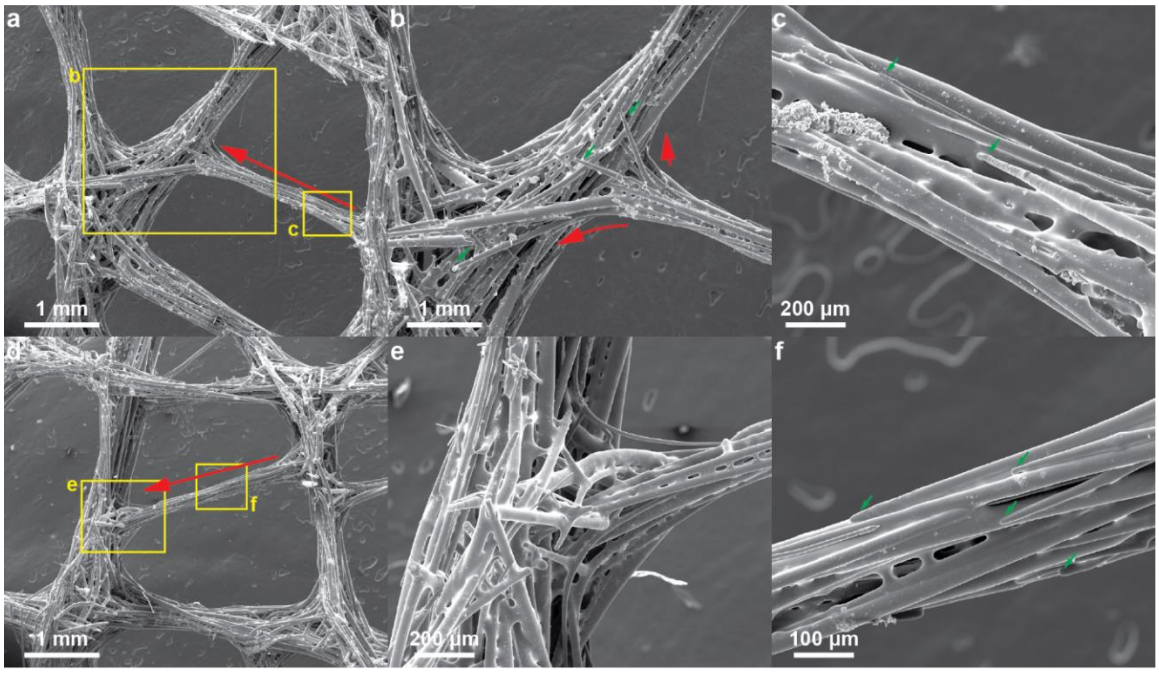


Figure 5.6. Formation of a N-3 node via bridging from an extending branch. Red arrow: the growing direction; green arrow: the end of the spicules indicating the growing fronts.

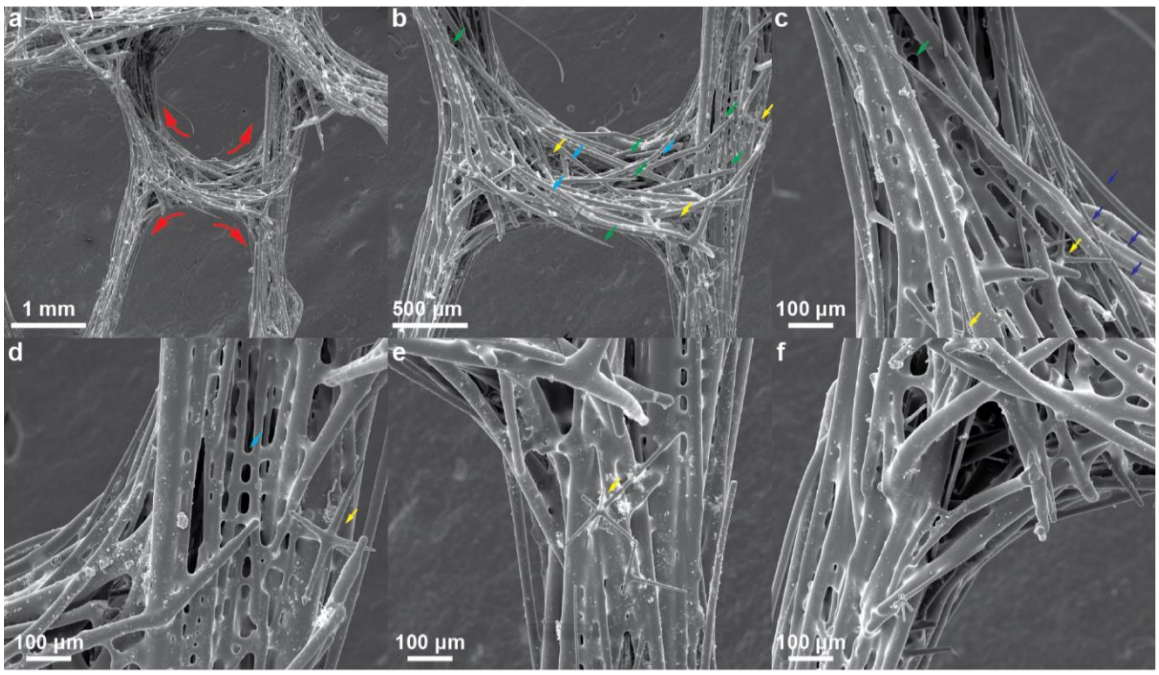


Figure 5.7. Formation of two N-3 nodes via bridging towards each other. Red arrow: the growing direction; green arrow: the end of the spicules indicating the growing fronts; yellow arrow: the hexactine megasclere.

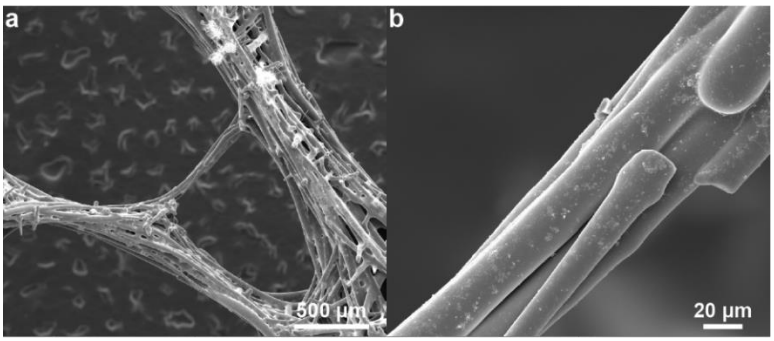


Figure 5.8. Further support of the formation of two N-3 nodes via bridging towards each other.

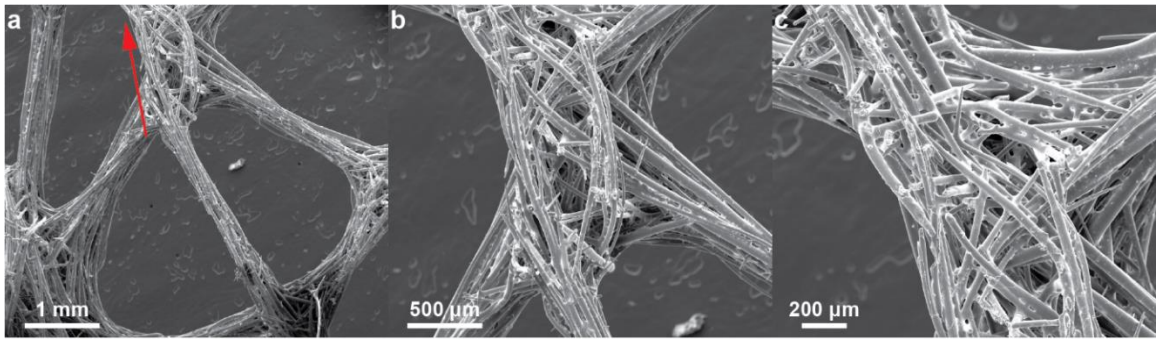


Figure 5.9. Formation of a N-5 node via bridging from one branch. Red arrow: the growing direction.

5.3.2. Characteristics and growth of individual spicules

The quantitative characterizations of individual spicules in the spicule bundles of sieve plate were carried out, which provides insights to the characteristics of different types of spicules and how the spicule bundles are built. Here, for short-range and long-range structural analysis, the individual spicules were traced in the sieve plate nodes and in a long strip of sieve plate containing multiple branches and nodes.

For the individual spicules in sieve plate nodes, the spicule tracing starts at the interior or outer surface of each vertex of the sieve plate to ensure the spicules at various locations were identified (**Fig. 5.10**). For example, 12 initiation locations were selected to start tracing the spicules in an N-4 node (**Fig. 5.10**). In addition, at least 5 spicules were traced from different locations to ensure the number of spicules for structural characterization.

Manual spicule tracings were performed on six different sieve plate nodes, including N-3 and N-4 nodes as they are the dominant types of nodes building the sieve plate (**Fig. 5.11a,c**). For N-3 nodes, based on the locations and morphologies of the traced spicules,

they are classified into inner straight spicule, outer straight spicule, inner curved spicule, outer curved spicule, and long bridging spicule (**Fig. 5.11b**). Here, the "inner" and "outer" denote the interior and exterior of the sieve plate nodes, while the "straight" and "curved" denote the morphologies of the spicule. The schematic of the N-3 node is based on all types of spicules together with the synapticular bridging (**Fig. 5.11b**). The vertices of the node converge to the spicule bundles which are the sieve plate branches (**Fig. 5.11b**). The 2D schematic is able to capture most of the microstructural features, implying that the structure along the direction of dome thickness is a repetition of this 2D schematic (**Fig. 5.11**)[21]. For N-4 node, the spicules are classified into four types of spicules in the schematic: inner straight spicule, outer straight spicule, outer straight secondary spicule, and outer curved secondary spicule (**Fig. 5.11c,d**). Here, the "secondary spicule" means the outer spicules grown on the framework formed by the straight spicules, providing a smooth transition at the N-4 nodes. Again, the 2D schematic captures the 3D microstructure of the N-4 nodes (**Fig. 5.11d**).

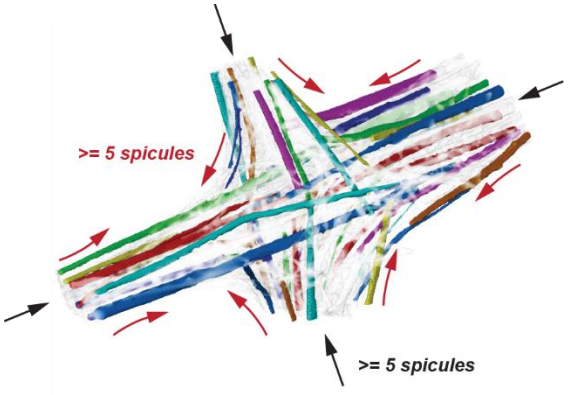


Figure 5.10. Spicule tracing of the sieve plate node. Spicule tracing initiates from the interior (black arrows) and outer surface (red arrows) of each vertex of the sieve plate node.

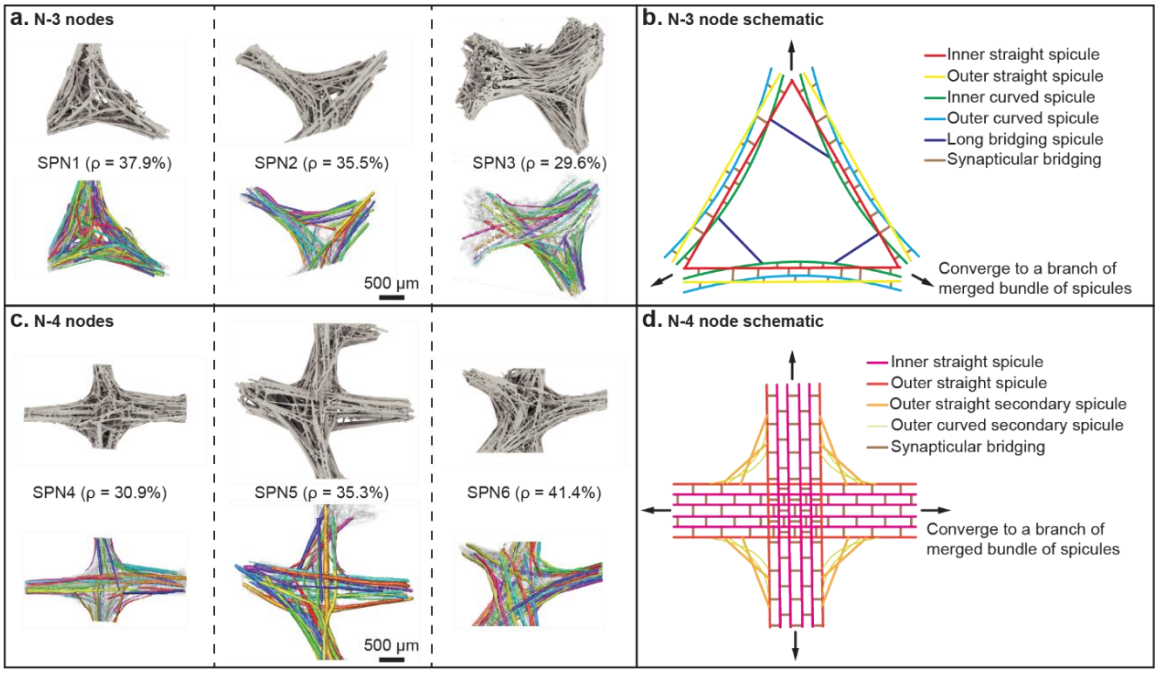


Figure 5.11. Spicules traced and classified within the sieve plate. (**a**) Spicules traced within the N-3 sieve plate nodes. (**b**) Schematic of the N-3 sieve plate node and classification of the spicules based on their locations within the sieve plate node. (**c**) Spicules traced within the N-4 sieve plate nodes. (**d**) Schematic of the N-4 sieve plate node and classification of the spicules based on their locations within the sieve plate node.

Furthermore, the traced spicules were skeletonized in Avizo which yields the thickness (i.e., radius) of the spicules as shown in **Fig. 5.12**. For the N-3 nodes, on average, the thickness of each type of the spicules only differs slightly (ca. 15 μm, **Fig. 5.12a**). Yet, for N-4 nodes, on average, the outer curved secondary spicules (ca. 10 μm) are usually thinner that other spicules (ca. 15 μm, **Fig. 5.12b**). Therefore, except for the outer curved secondary spicules, other spicules are usually ca. 15 μm in thickness for all

analyzed sieve plate nodes, suggesting that the mature individual spicules forming the sieve plates are similar everywhere. Moreover, since the silica spicule is brittle, how the significantly curved spicules (i.e., the outer curved secondary spicules) grow becomes an interesting question. Here, this question is explored from a mechanical perspective: the hypothetical residual surface stress was calculated based on the measured curvature of each outer curved secondary spicule and beam bending theory (**Table 5.1** and **Fig. 5.13**). It is found that the hypothetical surface stress is within the range of 200 to 500 MPa which falls closed to the strength (> 500 MPa) of spicules measured from tensile test[142]. However, this large residual surface stress is unlikely to develop in the skeleton of glass sponge which presents a risk of damage failure. Therefore, the curved spicules are most likely bent when it is still soft or the originally curved tissue scaffold deposits such curved spicules.

Table 5.1. Curvature and hypothetical residual surface stress of the outer curved secondary spicules of N-4 sieve plate nodes.

Model	Number of measurements	Thickness (R, μm)	Curvature (κ, μm^{-1})	Max. bending normal stress (surface stress, $(\sigma_y)_{max}$, MPa)
SPN4	7	9.7±2.5	0.0012±0.00055	464.8
SPN5	10	6.4±2.2	0.0015±0.00079	384.0
SPN6	8	5.5±1.7	0.0012±0.00043	264.0

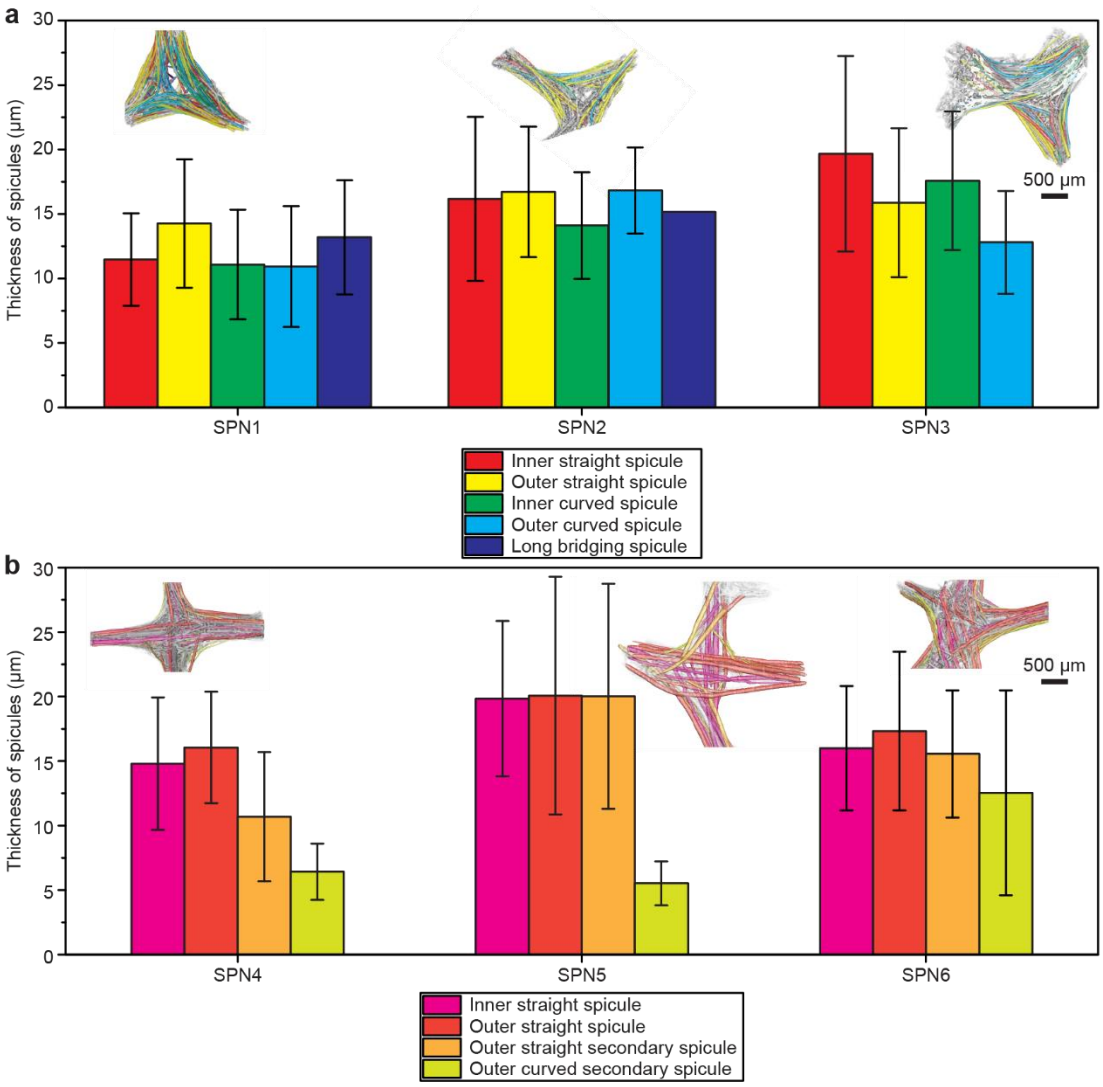


Figure 5.12. Thickness of each type of the spicule. (**a,b**) Thickness of each type of spicules within N-3 (**a**) and N-4 (**b**) nodes.

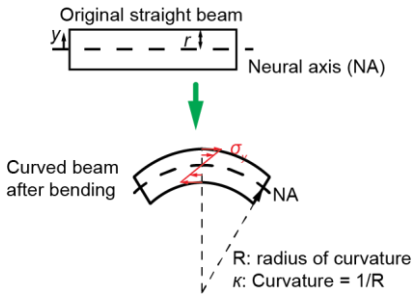


Figure 5.13. Classic beam bending theory to calculate the residual surface stress on the curved spicule.

For the long strip of sieve plate, spicule tracing was carried out, which reveals a single long spicule can span 15.1 mm long or 12 sieve plate nodes (**Fig. 5.14**). The spicules in the sieve plate are expected to grow even longer as the *E. aspergillum* is able to grow long anchoring spicules of several tens of millimeters[65]. In addition, the long spicules were accompanied by the relatively short spicules which may be a result of secondary silica deposition and thickening (**Fig. 5.14b**). The long spicules support that the long radially-arranged spicules can be formed starting from the rim of the sieve plate to provide initial tessellation as discussed later.

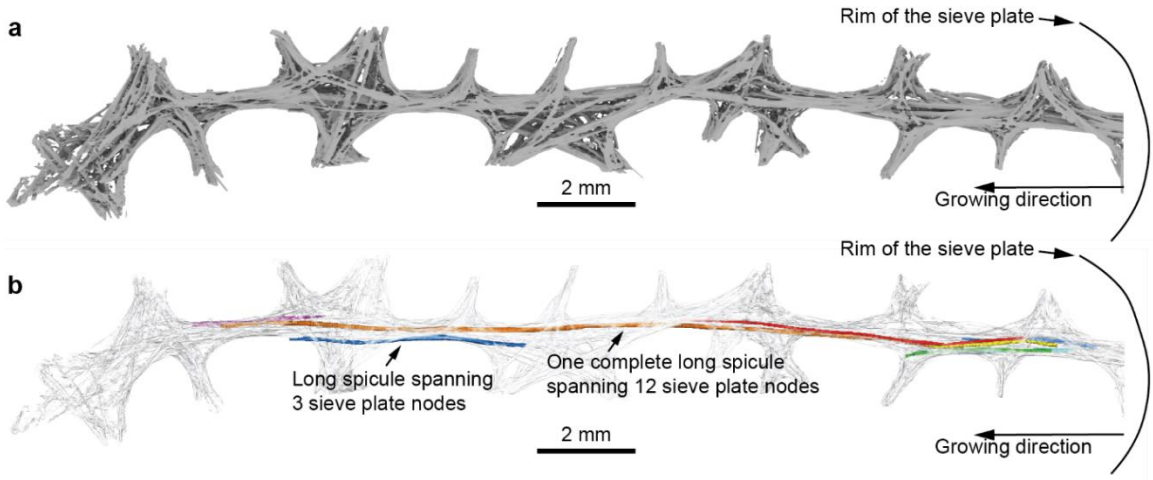


Figure 5.14. Long-range spicule tracing on a long strip of the sieve plate containing multiple nodes obtained from μ-CT scanning.

Here, the spicule tracing is based on the manual method. The spicule bundles of the sieve plates, in which the individual spicules are significantly merged by synapticular bridging or silica matrix, limit the accurate separations of spicules. So far, no existing automatic method is able to distinguish the bundled spicules unless the CT scanning has high enough resolution to capture the organic interface between silica layers of the spicule[58]. Nevertheless, being able to automatically traced the spicules not only makes the analysis efficient, but also provides more accurate spicule tracing and, thus, understanding of the sieve plates' microstructures

5.3.3. Formation process of the sieve plate

Based on the hypotheses made according to the previous literature and the present microstructural study, the formation process of the sieve plate is proposed.

Firstly, the hypotheses were summarized. Based on the previous works, we hypothesize that i) the growth from bottom to the top of the skeleton implies that the sieve plate of *E. aspergillum* starts to grow at its periphery[70,72]; ii) the sieve plates stay soft at the early stage and become stiff later via bundling of individual spicules[72]; and iii) the initial tessellation of the sieve plate, which allows the symbiotic shrimps to get in or out, is different from the final tessellation of the sieve plate. Based on the current works, some evidences can be provided for the above hypotheses and new hypotheses can be made: i) the sieve plate's spicule bundles start from both of the longitudinal and circumferential spicule bundles in the cylindrical skeleton; ii) the hexactine megascleres likely assist tissue anchoring for silica deposition; iii) the inner spicules grow first which is followed by the growth of the outer layers of spicules; iv) the individual spicules can grow until reaching ca. 15 μm in radius; v) the sieve plate has an initial tessellation with long spicules radiating towards the center, while later the bridging spicule bundles close some existing pores and form new sieve plate nodes.

Based on the aforementioned hypotheses, I predicted the formation process which is schematically shown in **Fig. 5.15**. At the beginning, the spicules of sieve plates are continuations of the longitudinal and circumferential spicule bundles where the hexactines concentrated at the growing front and the inner spicules grow earlier than the outer spicules (**Fig. 5.15a**). Next, the relatively straight spicule bundles starting from the rim of the sieve plates roughly grow radially towards the center, which forms the initial tessellations with large pores (**Fig. 5.15b**). At the mature stage, the spicule bundles bridge among the original spicule bundles to form the final Voronoi-like tessellations (**Fig. 5.15c,d**). Here, the initially grown spicule bundles become slightly curvy due to the

bridging (**Fig. 5.15b,c**). Some of the initially grown spicule bundles may still be straight as the further bridging occurs when the initial spicule bundles become stiffened (**Fig. 5.14a,e**).

In addition, the schematic of the final tessellation was compared to the Voronoi tessellation based on the projected pore centers, showing a good agreement (**Fig. 5.15c,d**). Yet, the generated Voronoi tessellation consists of N-3 nodes only while N-4 nodes exist in the Voronoi-like schematic, as some N-3 nodes in Voronoi tessellation are very closed to each other (**Fig. 5.15c,d**).

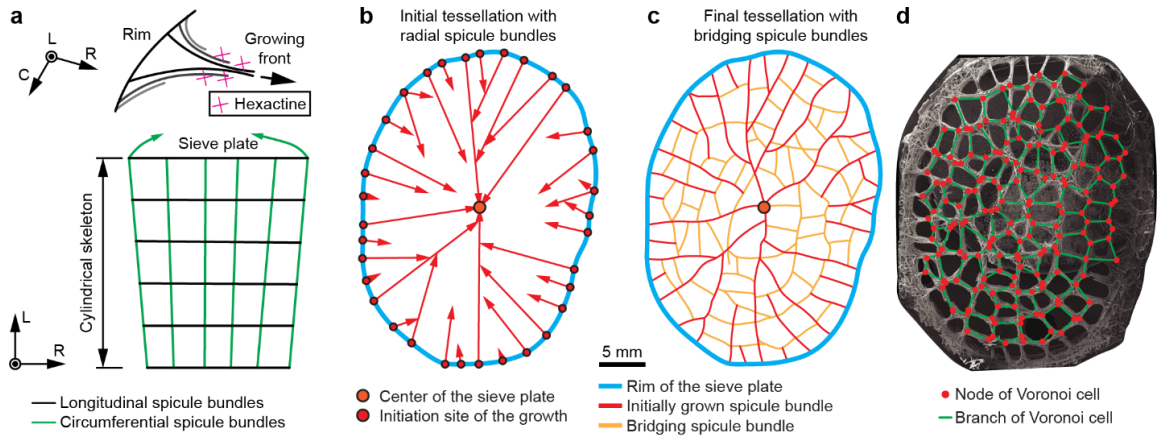


Figure 5.15. Proposed formation process of the sieve plate of *E. aspergillum*. (a) The schematics showing the spicule bundles grow as continuations of the longitudinal and circumferential spicule bundles in the cylindrical skeleton of *E. aspergillum*. At the top schematic, the gradually lighter color and smaller length of the black lines indicate the spicules gradually away from the interior of the spicule bundle. (**b**) The schematic of the initial tessellation due to the relatively straight spicules radiating towards the center of the sieve plate. (**c**) The schematic of the final tessellation. The initially grown spicule bundles as indicated by the red lines become curvy compared to the early stage. (d) Voronoi

tessellation based on the projected pore centers of the sieve plate overlaid on the actual sieve plate image.

5.4. Discussions

Here, a two-step formation process was proposed for the sieve plate of glass sponge *E. aspergillum*. This process is anticipated to achieve a balance between biological requirements at different growth stages, including the accommodation of the symbiotic shrimps, large enough pore area for the current pumping, and the mechanical stiffness to protect the osculum and interior of *E. aspergillum*[72]. In particular, the young flexible sponges allow the symbiotic shrimps to get in or out, suggesting that the flexible sieve plates have large pores at the time. Therefore, the initial tessellations of the young sieve plates do not provide any mechanical functions. When the sponges get mature, improving the mechanical stiffness to protect the osculum and interior of the sponges becomes the priority of formation, which results in a Voronoi-like tessellation based on the initial tessellation.

It is surprising that, without a complete framework or any grain growth mechanisms as found in the shell prisms[143], sieve plate is still able to maintain a Voronoi-like tessellation that provide stiffness similar to the regular hexagonal lattices. Some hypothetical driving forces may exist to form such tessellation: i) the spicules tend to grow towards center of the sieve plate which can be represented by a hypothetical alignment force pointing towards the center; ii) the bridging spicule may grow towards the center or circumferentially which can be driven by the same alignment force as above or a hypothetical centrifugal force. Implementing such hypothetical driving force

computationally may help us generate Voronoi-like structure in the way of sieve plate formation[144].

Furthermore, it is rarely found in the previous literature about how nature grows cellular dome structures, yet artificial cellular dome is ubiquitously built everywhere for architectures or lattice materials[136,137,145]. In the case of lattice materials with cellular dome topologies, the fabrication is enabled by additive manufacturing, which means that the formation of dome-shaped lattice materials can theoretically initiate and terminate everywhere[136,137,145]. In contrast, the solid dome architectures usually require centering, or the framework support, during the assembly until they are able to self-support, while the cellular domes such as the geodesic dome is usually assembled in a bottom-to-top sequence without centering yet with horizontal branches to assemble after each layer for self-supporting. The similarity in the formation between sieve plate and artificial lattice domes is the self-support without centering where the soft tissue and unstiffened spicules in sieve plate are able to maintain its geometry during growth. However, the main difference in the formation is that the sieve plate forms different cellular tessellations at different growth stages. The formation process studied here may guide the design and fabrication of cellular dome with different functions at different construction stages.

5.5. Conclusions

In this work, the formation process of the sieve plate was proposed based on our microstructural study and the previous works. For the microstructures, results show that the i) the large amount of hexactines was observed which hypothetically provide tissue anchoring for silica deposition; ii) various classes of spicules based on their morphologies

and locations were identified in sieve plate nodes which have ca. 15 μm in radius when mature; iii) long spicules spanning at least 12 nodes were found; and iv) the original and bridging spicule bundles were identified, supporting the different cellular tessellations of the sieve plate. Accordingly, a two-step formation process was proposed: i) the sieve plates grow from the periphery towards the center initially to form tessellations with radiating spicule bundles; ii) some bridging spicule bundles among the original spicule bundles grow to form the final Voronoi tessellation. This process is assumed to relate to different biological functions in different growth stage, including the accommodation of symbiotic shrimps at the young stage, and a balance between large enough pores and mechanical stiffness at the mature stage. This proposed formation process not only provides the understanding of the origins of the biological functions of sieve plate, but also provide a biological strategy to build cellular dome structure at different stages with different functions.

Chapter 6 Multifunctional properties of the lightweight lattice-based skeleton of the sponge *Euplectella aspergillum*

This work was published as a regular journal article: H. Chen, Z. Jia, L. Li, Lightweight lattice-based skeleton of the sponge Euplectella aspergillum, *Journal of the Mechanical Behavior of Biomedical Materials*, **135**, 105448 (2022)[71].

The glass sponge, *Euplectella aspergillum*, possesses a lightweight, silica spicule-based, cylindrical lattice-like skeleton, representing an excellent model system for bioinspired lattices. Previous analysis suggested that the *E. aspergillum*'s skeletal lattice exhibits improved buckling resistance and suppressed vortex shedding. How the sponge's skeletal lattice with diagonally-oriented reinforcing bundle of fused spicules and the ridge system behaves under different loading conditions and achieves dual mechanical and fluidic transport performance requires further investigation. Here, we first quantified the structural descriptors such as length and thickness of the bundle of fused spicules and hole opening diameter of the sponge skeletons with and without the soft tissue covered. Secondly, parametric modeling and simulations of the sponge lattice in comparison with other bioinspired designs under different loading conditions were implemented to obtain the structure-mechanical property relationship. Our results reveal that the double-diagonal reinforcements of the *E. aspergillum*'s lattices show i) tendency to maximize the torsional rigidity in comparison to longitudinal and radial modulus and flexural rigidity, and ii) independency of mechanical properties on the diagonal spacing, leaving freedom to control the hole-opening position for the sponge's fluid transport. Furthermore, our coupled fluid-mechanical simulations suggest that the ridge system spiraling the cylindrical lattice

simultaneously improves the radial stiffness and fluid permeability. Finally, we discuss the general mechanical strategies and design flexibility in the sponge's skeletal lattice. Our work provides understanding of the mechanical and functional trade-offs in *E. aspergillum*'s skeletal lattice which may shed light on the design of lightweight tubular lattices.

6.1. Introduction

Lattice materials have been extensively studied due to their tailorable physical properties such as thermal properties[146–148], energy absorption[7,19,149], stiffness and strength[8,9,150,151], and etc. Further introduction of multiscale hierarchical structures provides solutions to address the trade-off between the usually contradicting properties such as toughness and strength[7,9,15]. These lightweight structures developed by recent theoretical or computational approaches are often based on periodic or hierarchical lattices, which are different from the traditional porous materials that are often characterized by their stochastic porous structures[17,19,152]. In parallel, many natural structural materials found in the structural supports of plants and animals are also composed of lattice-like cellular structures, which exhibit the vast diversity of microstructural features and exceptional mechanical performance driven by evolutionary forces[19,81,153]. Therefore, the study of natural cellular lattices provides an important avenue to identify new design strategies for developing lightweight lattice materials.

Examples of natural biomineralized lattice-like materials include sea urchin spines[2,83,95], starfish skeletal elements (ossicles)[4,98,154,155], cuttlebone[119,156,157], diatom frustules[158–160], and glass sponge skeletons[30,41,70], which are mainly composed of brittle minerals like calcium carbonate or silica. Their remarkable stiffness, strength, and damage tolerance provide significant insights to design engineering ceramic lattices[58,65,84,95].

Some of the aforementioned natural lattice materials are composed of biogenic silica as constituent materials, such as diatom's frustules[158–160], Radiolaria's siliceous skeletons[161,162], and glass skeletons of the Hexactinellid sponges[22,41]. In particular, the deep-sea glass sponge *Euplectella aspergillum* has recently attracted extensive research

interests due to its hierarchically architected lattice skeleton with mechanical and optical properties[21,47,70]. The *E. aspergillum*'s cylindrical skeleton is a diagonally-reinforced rectangular lattice constructed from bundles of fused spicules (diameter, ~120 μm), which themselves are composed of concentric silica layers embedded in a laminated silica matrix and separated with thin proteinaceous interfaces (5-10 nm)[21]. At the individual spicule level, despite its extremely high content of brittle silica (~99 wt%), the glass spicule exhibits high flexibility and optimal strength improvement[58,64,65]. Previous works demonstrate the fracture toughness of the spicule is enhanced by the laminated structure; yet, this enhancement is small compared to that of the planar layered structure in nacre due to the suppression of crack arrestment mechanism[5,64,68]. At the intrinsic material level, nanoindentation-based studies revealed that the amorphous biogenic silica exhibits reduction of modulus, hardness and even fracture toughness, in comparison to synthetic glass, due to the hydration state and the particulate structure of the biogenic silica[5,6].

At the lattice level, the skeleton of the *E. aspergillum* exhibits a unique rectangular lattice pattern reinforced with the so-called double-diagonal branches (i.e., two parallel diagonally-oriented bundles of spicules) and a ridge system spiraling around the cylindrical skeleton[21,30,70]. Fernandes *et al.* designed 2D bioinspired models to quantitatively study the mechanical implications of the diagonal reinforcement within the rectangular lattice[70], which reveals that the double-diagonal configuration results in an improved buckling strength compared to lattices with a different number of diagonals. This buckling mode may most likely occur at the immature stage of the spicule growth when they are still flexible[70]. Yet, the bundles of fused spicules of the cylindrical skeleton due to secondary silica deposition are more likely to fail by direct fracture rather than buckling[21]. In addition,

Li *et al.* focused on the three-dimensional (3D) bioinspired lattice design of the sponge skeleton and found that the sponge skeletal structure with a double-diagonal configuration has a better strength-to-weight ratio compared to the cylindrical honeycomb hollow lattice[74]. They have also modeled a solid helical ridge structure and found a slight effective enhancement in resisting torsional loads. However, this bio-inspired ridge design does not resemble the actual sponge skeleton with ridges.

Moreover, the cylindrical skeleton with helically spiraling ridge system of the *E. aspergillum* not only provides mechanical support, but also facilitates the water flow through the organism's body for suppressing vortex shedding[34,35,73,75]. It was found that the solid cylinder under horizontal water flow induces vortex shedding which is highly undesirable in engineering designs due to the vortex-induced vibration (VIV), while the surface corrugations such as helical strakes provide suppression to such effect[76–78]. Similarly, the strake-like helical ridge system of *E. aspergillum* could be an important source of bioinspiration for designing surface corrugations of the cylindrical tubes. Indeed, recently, Falcucci *et al*. performed fluid simulations on the complete skeleton of the sponge and reported that the skeletal cylinder with structure can stabilize the flow wake after the cylindrical body and hence suppress the vortex shedding, especially at high speed of water flow[75]. However, one potential limitation of this work is that the porosity of the skeleton differs from the porosity of living *E. aspergillum* due to the presence of the soft tissue, which may alter the actual hydrodynamic response of the sponge[163]. The microscale opening of the holes on the dermal membrane and the complex multiscale canal system at the tissue for filtering impede the direct passage of water flow[79,164,165]. Later, Fernandes *et al*. constructed models that highly resemble the actual living sponge and performed

comprehensive hydrodynamic analysis[73]. They found that the ridge, despite providing ineffective contributions to the mechanical resistances to compression, torsion, bending, and hydrostatic pressure, plays a critical role in suppressing vortex shedding for the bioinspired cylindrical model[73]. In addition, the bioinspired cylindrical model with porosity similar to the actual living sponge provides more significant vortex shedding suppression than the highly porous model and the complete skeletal model[73]. More surprisingly, the maze-like distributions of the ridge system on the cylindrical lattice are adapted for improving the effect of vortex shedding suppression in the *E. aspergillum* sponges, while the ridge system either ideally spirals along one or opposite directions provides relatively inefficient contributions to this effect[73].

To understand the mechanical properties in the skeletal lattice of *E. aspergillum*, specifically the potential mechanical optimization or trade-offs, a comprehensive parametric mechanical study which considers the quantitative structural descriptors and various loading conditions is required. In addition, existing research on the hydrodynamics of the sponge's skeleton did not consider the mechanical reaction to the external water flow. Whether the ridge can provide mechanical advantages, except for the suppression of vortex shedding, to resist radial loading induced by water flow, requires a fluid-mechanical coupling study. Therefore, in this work, we first perform detailed structural measurements on the cylindrical skeleton and ridge such as the branch length, thickness, and extruded length of the ridge. Based on the structural measurements, we performed bioinspired modeling and conducted computational simulations to obtain the mechanical properties. The fully parametric modeling and simulations allow us to conduct a systematic investigation of the effects of these structural descriptors on

mechanical properties to discover the property trade-offs under different loading conditions. Furthermore, our bioinspired porous models with ridge and the fluid-structure coupling simulations reveal the effects of the ridge structure on the permeability and stress distribution under the horizontal water flow. Finally, the mechanical strategies, including the design flexibility (i.e., sensitivity of the mechanical properties to structural variations), in the *E. aspergillum*'s skeletal lattice, and the limitations of this work were discussed.

6.2. Materials and Methods

Sample preparation: Dried *E. aspergillum* sponges were purchased from Esty. The dried skeletons were cut into small pieces using a low-speed diamond saw. The structural descriptors such as branch length and thickness were obtained from the measurement on these skeletons. Three skeletons of the dried sponge with relatively large structural discrepancies were selected for structural measurements under optical microscope to account for the heterogeneity of the natural materials (**Fig. 6.1** and **Fig. 6.2**). In addition, the *E. aspergillum* sponge specimens with preserved tissues covered for structural measurements were obtained from the Museum of Comparative Zoology at Harvard University (**Fig. 6.3**). The measurements were directly made on the complete samples without damage.

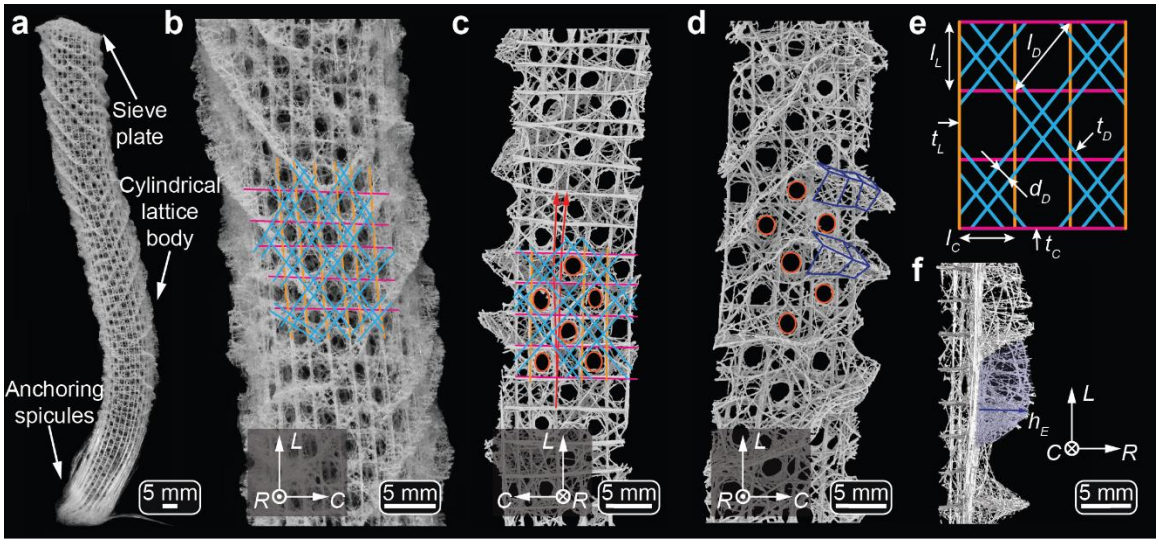


Figure 6.1. Introduction of the skeleton of *E. aspergillum* sponge. (**a**) Skeleton of a complete *E. aspergillum* sponge with sieve plate, cylindrical lattice body, and the anchoring spicule bundle. (**b**) A zoomed-in graph of the skeleton with structural schematic indicated. Pink lines are branches in longitudinal (L) direction. Orange lines are branches in circumferential (C) direction. Blue lines are the diagonals. (**c**) 3D volume rendering of the inner surface of the skeleton from X-ray CT scanning. Orange ellipses indicate the opening holes. Secondary spicules are very thin spicules that distributed in various orientations of the cells aside from the opening holes. The red arrow lines indicate the "dislocation" structure of the skeletal lattice. (**d**) 3D volume rendering of the outer surface of the skeleton from X-ray CT scanning, showing the ridge structure spiraling around the cylindrical skeleton indicated in blue boxes. Orange circles or ellipses indicate the opening holes. (**e**) Structural descriptors in the schematic model to define the skeletal structure of the *E. aspergillum* sponge. (**f**) Side view of the ridge. The area shaded in blue indicates the ridge structure.

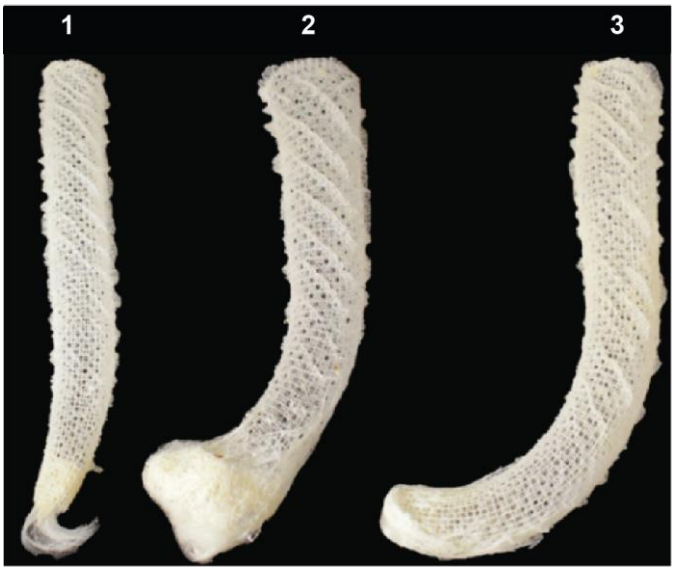


Figure 6.2. Three *E. aspergillum* sponge samples used into structural measurements. The morphology of three samples are distinct to account for the heterogeneity of the biological samples.

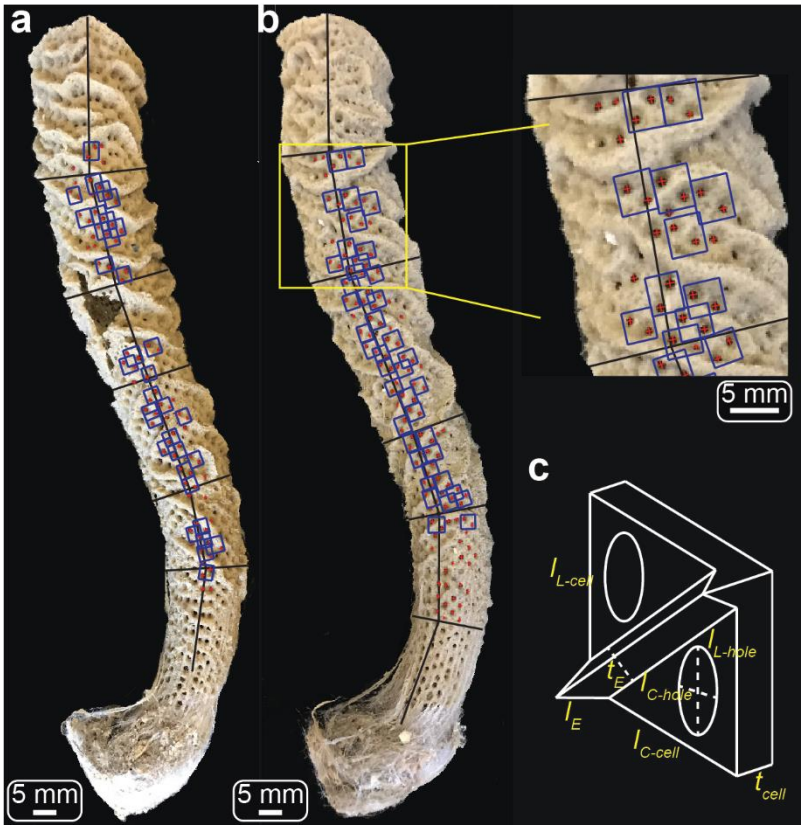


Figure 6.3. Structural measurements for CFD simulations. (**a**) First and (**b**) second *E. aspergillum* sponge with tissue for structural measurements. Zoomed-in graph shows the measurements of the dimensions of the holes (red crosses) and cells (blue boxes). (**c**) Graphical definitions of the structural descriptors for modeling.

μ-CT analysis: To visualize the skeletal structure, the skeletal lattice of *E. aspergillum* sponge was scanned using a high-resolution *μ*-CT Skyscan system 1172 (Aartselaar, Belgium), where the X-ray was operated at 80kV and 100 μA (**Fig. 6.1c,d**). The field-of-view of the camera is 17.84 mm × 22.30 mm. 273 projection images under exposure time of 5.082s were acquired for each scan with a 180° sample rotation. The projection images were captured by a Hamamatsu camera with a resolution of 1280 × 1024 pixels and 17.42 μm of voxel size. Multiple scans were conducted for one skeleton along the longitudinal

direction and stitched automatically to form a complete scan. The 3D stack of images was further automatically reconstructed in the system.

The reconstructed image stack was segmented using an open-source, machine learning-based software ilastik[139]. We trained the program by manually labeling a few regions of the skeleton and background, respectively, which were subsequently fed to the machine learning algorithms, including Gaussian filters and Random Forest with 100 trees classifier[166]. The segmented data was further imported to a commercial tomography analysis software Avizo 9.5 (Thermo Fisher Scientific, USA) for 3D volume rendering and visualization.

Structural measurement of biological samples: The structural descriptors for the sponge-like model are defined in **Fig. 6.1e** and **Table 6.1**, among which the l_C, l_L, t_C, t_L, and h_E are measurable. No definite measurements of t_D and d_D can be made because the configuration of the diagonals is not regular enough compared with the rectangular lattice frame. In addition, due to the relatively random nature of the thin spicule distribution in the ridge structure, we only use h_E, or the height of the ridge from the cylindrical skeleton, to quantitatively describe the ridge structure (**Fig. 6.1f**). The measurements were conducted under an optical microscope (ZEISS Axiocam ERc 5s, German). The values obtained were used to calculate the aspect ratios such as the aspect ratio of the cell (l_C/l_L), aspect ratios of the longitudinal (t_L/l_L) and circumferential (t_C/l_C) branches. Moreover, structural measurements were performed on the *E. aspergillum*'s cylindrical body with preserved tissue covered. The measurements were directly made on the optical

images (**Fig. 6.3**). The measurable values are l_{C-cell}, l_{L-cell}, l_{C-hole}, and l_{L-hole}, while other values such as t_{cell} and t_E are estimated (**Fig. 6.3 and 6.4**).

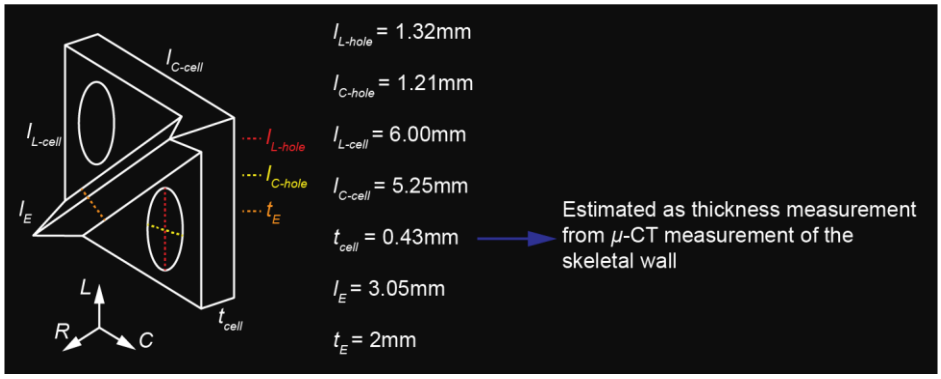


Figure 6.4. Schematic model and measurement results of the structural descriptors for modeling. The selection and calculation of the values for structural descriptors are illustrated.

Table 6.1. Definition of structural descriptors for lattice skeleton.

Parameters	Definition
l_C	Length of the branch along the circumferential direction
t_C	Thickness, or radius, of the branch along the circumferential direction
l_L	Length of the branch along the longitudinal direction
t_L	Thickness, or radius, of the branch along the longitudinal direction
l_D	Length of the diagonals
t_D	Thickness, or radius, of the diagonals
d_D	Distance between diagonals in a rectangular cell
h_E	Extruded height of the ridge structure

Biomimetic modeling: A customized script was developed to realize the modeling of the rectangular lattice (RL), double-diagonally reinforced lattice (DDRL), all-diagonally reinforced lattice (ADRL) and single-diagonally reinforced lattice (SDRL) (**Fig. 6.5**).

Among the models, the DDRL is the sponge-like model while the others are similar variational models for comparative study. We first constructed 2D unit cell of the lattices and then rotated and translated the 2D unit cell to form a 3D cylindrical lattice with 36 rectangular cells in circumferential direction (C direction). The model was further repeated along the longitudinal direction (L direction) to form 72 layers of cylindrical rectangular cells. Hence, the long cylindrical lattices allow loadings such as compression along longitudinal and radial direction, torsion, and bending. The structural descriptors and aspect ratios are tailorable in the script for fully parametric modeling and simulations. The fully parametric modeling and simulation script was written in Matlab (MathWorks, California, USA) where the model construction, input file writing, Abaqus simulation, post-processing of results, are all automated after defining the range and interval of investigated structural descriptors.

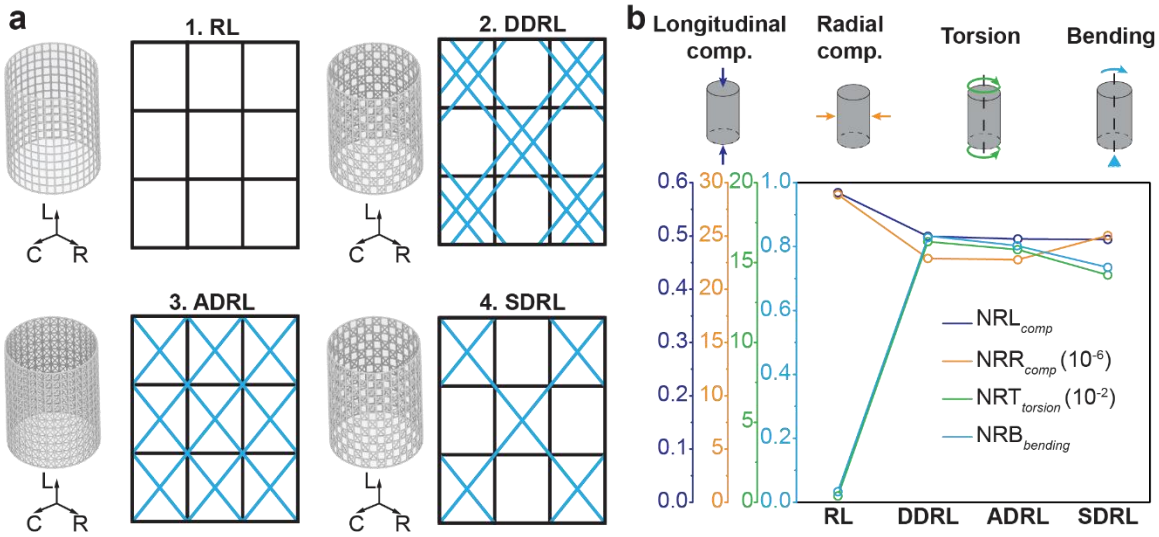


Figure 6.5. Structural designs and mechanics of four types of lattice structure. (**a**) 2D layout and corresponding 3D structure of (**1**) rectangular lattice (RL), (**2**) double-diagonally reinforced lattice (DDRL, sponge-like lattice), (**3**) all-diagonally reinforced

lattice (ADRL), and (**4**) single-diagonally reinforced lattice (SDRL). (**b**) Normalized relative longitudinal modulus (NRL_{comp}), radial modulus (NRR_{comp}), torsional rigidity ($NRT_{torsion}$), and flexural rigidity ($NRB_{bending}$) of four lattices.

Mechanical simulations: All simulations were carried out using the commercial Finite Element analysis package Abaqus/Standard 2016 (Dassault Systems, Vélizy-Villacoublay, France). Timoshenko beam model (Timoshenko beam element, B31, mesh size of 0.2 mm) were used for stiffness simulations. The simulation models of the cylindrical lattices of 15.04 mm in radius have 72 rectangular cells in the longitudinal direction and 36 rectangular cells in circumferential directions. To calculate linear stiffnesses, including the modulus along longitudinal and radial directions, torsional rigidity, and flexural rigidity, static analysis was performed for all parametrically modeled cylindrical lattices. The samples were loaded by 0.1% strain for compressions, by one-degree rotational displacement for torsion, and deflection of 0.1% of the lattice tube's length for cantilever beam bending, respectively. The isotropic elastic modulus and the Poisson's ratio of silica used in all simulations were 40 GPa and 0.17, respectively, where the Poisson's ratio of fused silica is used herein[6,167]. Shear modulus is, thus, 17.09 GPa. The elastic properties, including compression moduli in longitudinal (L_{comp}) and radial (R_{comp}) direction, torsional rigidity ($T_{torsion}$), and bending rigidity ($B_{bending}$), of RL, DDRL, ADRL, and SDRL, were obtained from the simulations, which were further used to calculate the normalized relative (NR) property parameters according to

$$NR(\cdot)_{(mode)} = \left(\frac{(\cdot)_{(mode)}}{S_{(mode)}}\right) / (\frac{\rho_{lattice}}{\rho_s'}) \qquad (6.2.1),$$

where $(\cdot) = L, R, T, B$ depending on the loading modes and loading directions, $(mode) = comp, torsion, bending$, $S_{(mode)}$ is the elastic modulus, torsional rigidity (i.e., the product of shear modulus and polar moment of inertia), or flexural rigidity (i.e., the product of Young's modulus and second moment of area) of a thin-walled cylindrical tube with the base material (*i.e.*, silica), $\rho_{lattice}$ is the density of the lattice, ρ_s is the density of silica, and ρ_s' is the effective density of the thin-walled tube. The wall thickness of the thin-walled cylindrical tube was taken as 0.26 mm which is two times of the measured t_L (**Table 6.2**). The radius, the elastic modulus, and Poisson's ratio of the thin-walled cylindrical tube are 15.04 mm, 40 GPa, and 0.17, respectively. Therefore, the calculated values of S_{comp}, $S_{torsion}$, S_{bend}, and ρ_s' are 1.38 GPa, 95.00 N·m^2, 111.15 N·m^2, $3.45 \times 10^{-2}\rho_s$, respectively. We performed mesh sensitivity tests on the DDRL model as an example (**Fig. 6.6**) and demonstrated that the values of NRL_{comp} converge with the mesh size smaller than 0.2mm. Therefore, we chose 0.2mm as the mesh size of B31 element for all simulations to balance modeling efficiency and accuracy.

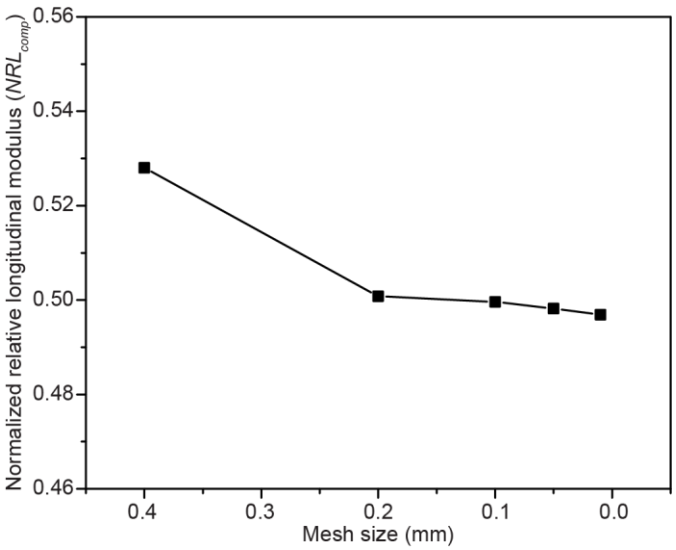


Figure 6.6. Sensitivity of the NRL_{comp} of DDRL to the mesh size.

Table 6.2. Measurement results of the structural descriptors for the skeletal lattice of the *E. aspergillum* sponge.

Sample	Number of measurements	l_C (mm)	l_L (mm)	t_C (mm)	t_L (mm)
Sample 1	574	2.32 ± 0.50	2.62 ± 0.26	0.12 ± 0.02	0.14 ± 0.06
Sample 2	417	2.31 ± 0.39	3.33 ± 0.35	0.12 ± 0.02	0.13 ± 0.05
Sample 3	426	2.78 ± 1.58	3.51 ± 0.33	0.12 ± 0.02	0.13 ± 0.02
All	1417	2.45 ± 0.97	2.88 ± 0.95	0.12 ± 0.02	0.13 ± 0.05

Fabrication and experiments: To validate the simulation results and observe deformation and fracture behaviors under longitudinal (L) and radial (R) compression, experimental samples of RL, DDRL, ADRL, and SDRL, were fabricated through Form 2 (Formlabs, USA) which is a stereolithography-based additive manufacturing machine. Clear resin, which is 2800 MPa in elastic modulus and 65 MPa in tensile strength, was used to fabricate all the samples. After 3D printing, all samples were post-cured in Form Cure for 2 hours to stiffen the originally ductile polymer. Experiments were performed

immediately after post-curing of the samples to avoid degradation of the polymer material. Compression experiments were carried out in Instron 5944 mechanical tester (Instron, USA). Strain rate of $10^{-3}/s$ was used consistently for all compression experiments.

Fluid-structure simulations: We simulated the water flow and calculated the velocity and pressure field as water passes through the biomimetic models for computational fluid dynamics (CFD) simulations in Abaqus/CFD (Dassault Systems, Vélizy-Villacoublay, France). The solver utilizes a hybrid finite-volume and finite-element method to solve the three-dimensional incompressible Navier–Stokes (N-S) equations[168]. A trapezoid scheme was used to integrate the equations in time. Moreover, steady-state results were obtained and used for further permeability analysis and structural mechanical simulations once the energy and pressure reach stable values. Based on the pressure distribution, the effective permeability (k) of the models were evaluated using the following equation[169]:

$$k = v\frac{\mu t}{\Delta P} \qquad (6.2.2),$$

where v is the flow velocity, μ is the dynamic viscosity of the fluid, ΔP is the evaluated pressure drop, and t is the characteristic thickness of the structure (here the value t_{cell} is utilized). The finite-sized sponge structure, instead of the entire sponge structure, is used to simulate how the ridge structures affect the fluid properties locally (**Fig. 6.7**). Despite a wide range of flow rates at various depths (36-5050 m) of the living habitat of *E. aspergillum*, in this work, water was set to pass through the solid models with an inlet velocity of v = 100 mm/s[28,34,73]. The surfaces of the sponge-inspired model employ a no penetration, no slip boundary condition (**Fig. 6.7a**). By contrast, the side surfaces are given

as symmetric boundaries, where water can slip freely on the surface without penetration (**Fig. 6.7a**). At the corresponding conduit outlet, a constant gauge pressure (0 Pa) was further imposed. The water was modeled as a Newtonian fluid with a density of ρ = 1 g/cm^3 and a dynamic viscosity of μ = 0.001 Pa·s [170]. As the thickness of our planar models (t_{cell}) is 0.43 mm which is taken as the characteristic length L, the flow rate used in this work corresponds to Reynolds numbers (Re) of 43 ($Re = \frac{\rho u L}{\mu}$). Due to this low-Reynolds number character, the simulation is based on a laminar flow without introducing turbulent models [171]. Unstructured tetrahedral elements were created to describe the complex 3D sponge models with the narrow passages. The final mesh comprises 8~10 million elements (seven elements for the narrow features). The mesh condition is shown in **Fig. 6.8**, demonstrating a dense tetrahedral mesh (size: 0.004mm) near the surface of the solid models and a coarse mesh at the far field (size: 2mm). This distribution of mesh size ensures the boundary layer at the surface of the model. Moreover, as the flow field is steady, a weakly coupled fluid-mechanical interaction was implemented in the simulation. That is, we first calculated the surface pressure from the CFD model and then applied the extracted pressure as a distributed load in the solid simulation (**Fig. 6.7b-e**). The solid mechanical simulations were also implemented in ABAQUS, utilizing the general statics module. The density, elastic modulus, and Poisson's ratio of the silica composing the sponge-lattice structures are 2.17 g/cm^3, 40 GPa, and 0.17, respectively. A control model without ridge was also constructed to account for the weight change due to the addition of ridge. To keep the Reynolds number consistent, we did not change the thickness of the model but varied proportionally the modulus of the constituent material (73.32 GPa).

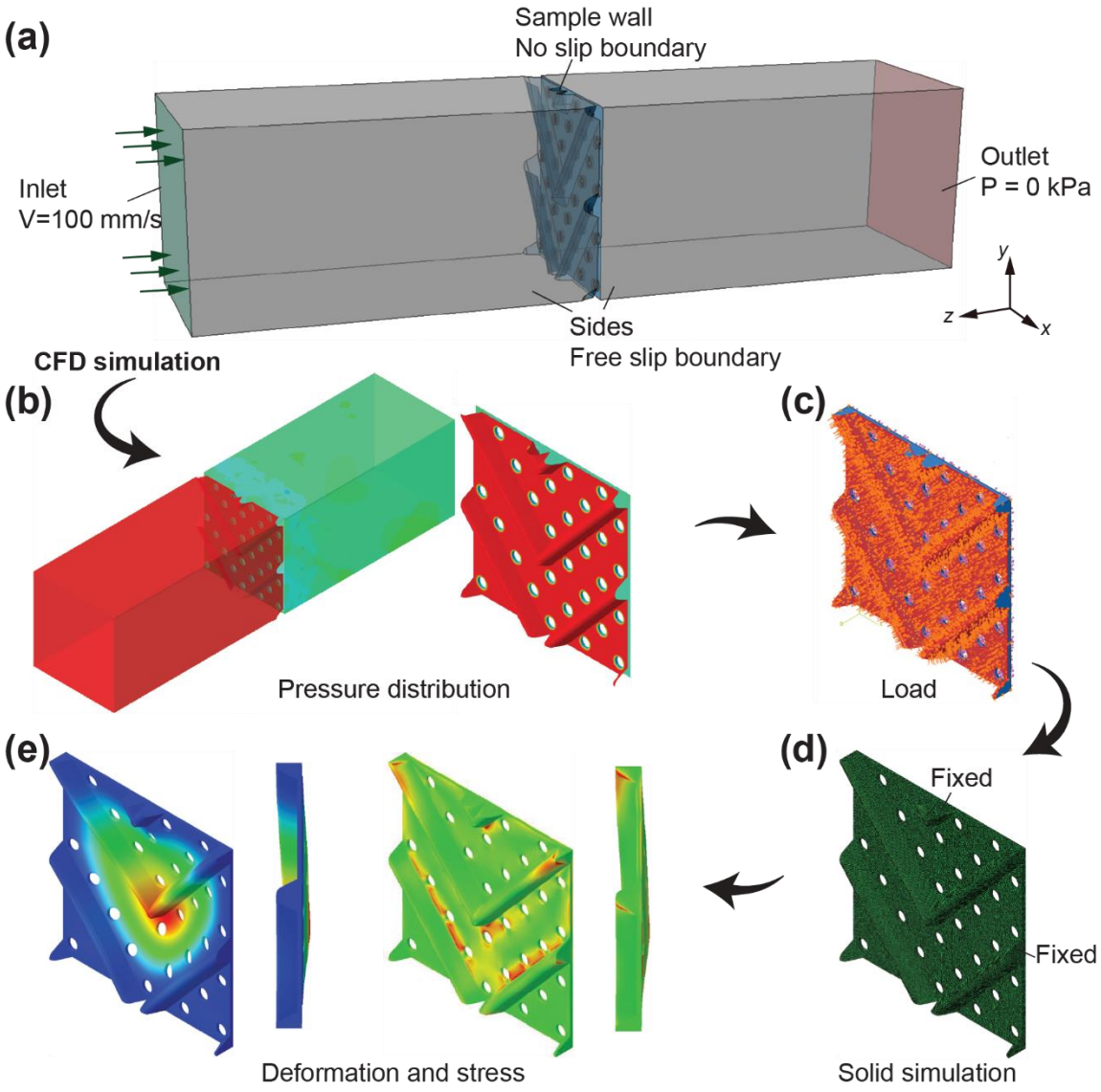


Figure 6.7. The fluid-structure coupled simulation. (**a**) The fluid domain and the setup of boundary conditions in CFD simulation. (**b**) Simulated pressure distribution applied as the (**c**) distributed load in the (**d**) solid simulation. (**e**) Calculated structural deformation and stress distribution from the solid simulation.

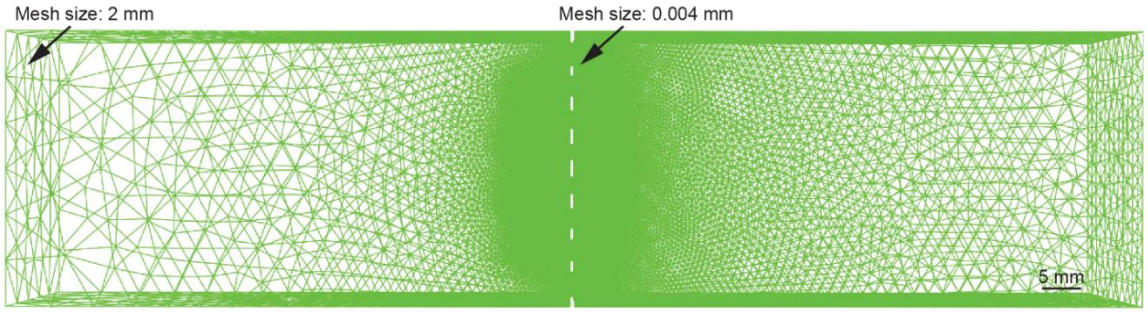


Figure 6.8. The distribution of mesh for fluid simulations in Abaqus.

6.3. Results

6.3.1. Skeletal lattice structure of *E. aspergillum*

As shown in **Fig. 6.1a**, the dried glass skeleton of the *E. aspergillum* sponge consists of a top sieve plate, a lattice-based cylindrical cage, and bundles of anchoring spicules at the bottom [21]. The cylindrical body is characterized by the rectangular lattice structure, where the constituent bundles of fused spicules run along the circumferential and longitudinal directions of the sponge body, respectively (pink and orange lines, **Fig. 6.1b**). The rectangular lattice is reinforced with diagonal bundles of fused spicules (blue lines, **Fig. 6.1b**), which are spaced in every second rectangular cell [30]. In addition, the diagonal reinforcement typically spread across the passing cells via two main bundles of fused spicules, forming the "double-diagonally reinforced rectangular lattice" [21,70]. Numerous secondary, thin spicules with random orientations are also present inside the rectangular cells with diagonal reinforcements (**Fig. 1b**). This rectangular lattice with double-diagonal bundles of fused spicules in every second cell not only offers mechanical reinforcement, but also allows the structure to have controlled openings in the skeletal system for fluid passage (as will be discussed in detail later, **Fig. 6.1c**). As shown in the 3D rendering based on high-resolution μ-CT reconstructions, these openings are highly circular with smooth

curvatures (Orange circles, **Fig. 1c**). Lastly, the ridge system helically spirals around the exterior of the sponge skeleton and is often placed in every second diagonally-reinforced cell, equivalent to every fourth rectangular cell (**Fig. 6.1d**) [1]. We noted that the ridges are often oriented in one or opposite directions at different locations of the cylindrical cage, exhibiting a maze-like structure (**Fig. 6.1d**) [73].

The schematic diagram in **Fig. 6.1e** summarizes the double-diagonally reinforced rectangular lattice with relevant structural parameters (as defined in **Table 6.1**). Here we utilized a cylindrical coordinate system, where L, R, and C represent longitudinal, radial, and circumferential directions of the cylindrical lattice, respectively. We have conducted systematic measurements of the structural parameters from three sponge specimens, including the lengths ($l_L = 2.88 \pm 0.95\, mm$ and $l_C = 2.45 \pm 0.97\, mm$), thicknesses ($t_L = 0.13 \pm 0.05\, mm$ and $t_C = 0.12 \pm 0.02\, mm$) of the unit cells, and the height of ridge ($h_E = 3.05 \pm 0.58\, mm$) (**Fig. 6.1f**, and **Table 6.1-6.3**). Due to the local random spacing of the diagonal bundles of fused spicules, the distance between the double-diagonal bundles of fused spicules (d_D) and their thicknesses (t_D) are not measurable. For the modeling of the lattice structure, we calculated the aspect ratios, including the aspect ratio of bundles of fused spicules ($t_C/l_C = 0.051 \pm 0.006$ and $t_L/l_L = 0.045 \pm 0.010$) and cell ($l_C/l_L = 0.809 \pm 0.113$), which are critical structural parameters for the properties of the architected lattices [9,11,172] (**Table 6.4**). Despite the relatively large variations of the length and thickness values, the skeleton maintains the aspect ratios of the branches and rectangular cells over the long-range macroscopic radius changes of the cylinder (**Fig. 6.2 and Table 6.2,6.4**). We observed that one of the strategies to maintain this aspect ratio is the introduction of "dislocation" structure in the skeleton as indicated by the red arrow

lines in **Fig. 6.1c** where the insertion of the additional longitudinal branches further separates the circumferential branches.

Table 6.3. Measurement results of the ridge structure and overall structure for the skeletal lattice of the *E. aspergillum* sponge.

Sample	N of measurements	h_E (mm)	Tube radius (mm)	Density (g/cm^3)	Relative density
Sample 1	195	3.16 ± 0.77	13.95 ± 0.31	0.018	24.05%
Sample 2	139	2.92 ± 0.59	13.40 ± 0.77	0.021	28.12%
Sample 3	142	2.92 ± 0.59	18.62 ± 0.78	0.014	18.84%
All	476	3.05 ± 0.58	15.04 ± 2.14	0.018	24.06%

Table 6.4. Aspect ratios of the branch and cell of the skeletal lattice of the *E. aspergillum* sponge.

Sample	t_C/l_C	t_L/l_L	l_C/l_L
Sample 1	0.055 ± 0.007	0.054 ± 0.008	0.898 ± 0.069
Sample 2	0.052 ± 0.005	0.039 ± 0.006	0.702 ± 0.065
Sample 3	0.045 ± 0.002	0.038 ± 0.003	0.793 ± 0.099
All	0.051 ± 0.006	0.045 ± 0.010	0.809 ± 0.113

6.3.2. Modeling and simulations of bioinspired lattices

To investigate the mechanical properties of the *E. aspergillum* sponge's skeleton, we constructed lattice models with sponge-like configurations as well as two variational models with different diagonal configurations, and performed systematic finite element-based mechanical simulations. These models include the rectangular lattice (RL, the control model without diagonal reinforcement), the double-diagonally reinforced lattice (DDRL, sponge-like lattice), the all-diagonally reinforced lattice (ADRL), and the single-diagonally reinforced lattice (SDRL) (**Fig. 6.5a**). 2D lattice units and corresponding 3D cylindrical lattices (36 rectangular cells along the C direction) of these four models were

generated using in-house MATLAB scripts. The structural parameters measured above were used in generating these models, while a nominal diagonal spacing (d_D/l_D) of 0.25 was used for the DDRL model. All models were designed to have the same relative density and aspect ratio of branches and rectangular cells based on the measured value of the *E. aspergillum* sponge (24%, **Table 6.3,6.4**).

Here we conducted mechanical simulations with various loadings, including L compression, R compression, torsion, and bending, on the four cylindrical lattice models to comprehensively account for most possible loading types due to the water flow [33,34]. The as-obtained normalized relative properties calculated using Eq. 2.1 are summarized in **Fig. 6.5b**. First of all, the presence of diagonal reinforcements, regardless of diagonal configurations, leads to significant increase in torsion ($NRT_{torsion}$) and bending ($NRB_{bending}$) resistance in comparison to those of the RL model (ca. 40 and 25 times increase, respectively), despite a slight decrease in compression moduli (NRL_{comp} and NRR_{comp}). In addition, three diagonally reinforced models (*i.e.*, DDRL, ADRL, and SDRL) exhibit similar values for all mechanical parameters: NRL_{comp} (DDRL: 0.501; ADRL: 0.493; SDRL: 0.491), NRR_{comp} (DDRL: 2.298×10^{-5}; ADRL: 2.270×10^{-5}; SDRL: 2.498×10^{-5}), $NRT_{torsion}$ (DDRL: 0.163; ADRL: 0.158; SDRL: 0.142), and $NRB_{bending}$ (DDRL: 0.827; ADRL: 0.802; SDRL: 0.736). These results indicate that the presence of diagonal reinforcements stabilizes the rectangular lattice, leading to increased torsional and bending resistance while slightly sacrificing the longitudinal and radial compressive stiffness. Moreover, the diagonal configurations do not have significant effects on the lattice stiffnesses (**Fig. 6.5b**).

We further validated our simulation results by fabricating the four types of cylindrical lattices through a stereolithography-based 3D printing approach and conducting mechanical measurements (**Fig. 6.9**). For the printed models, the thicknesses of all branches were doubled compared to the sponge skeleton in order to make the 3D printing process feasible and the resulting samples are shown in **Fig. 6.9**. Compression experiments along L and R directions, respectively, were conducted, which yields the stress-strain curves as in **Fig. 6.10**. The elastic modulus extracted from the experiment were plotted with simulation results in **Fig. 6.11**, showing a good agreement between experiments and simulations.

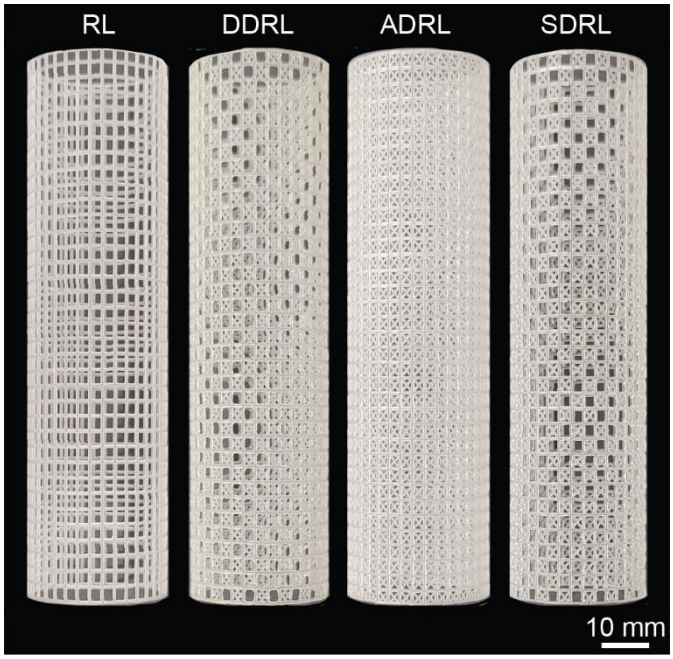


Figure 6.9. Experimental samples of four types of cylindrical lattices, including RL, DDRL, ADRL, and SDRL from left to right.

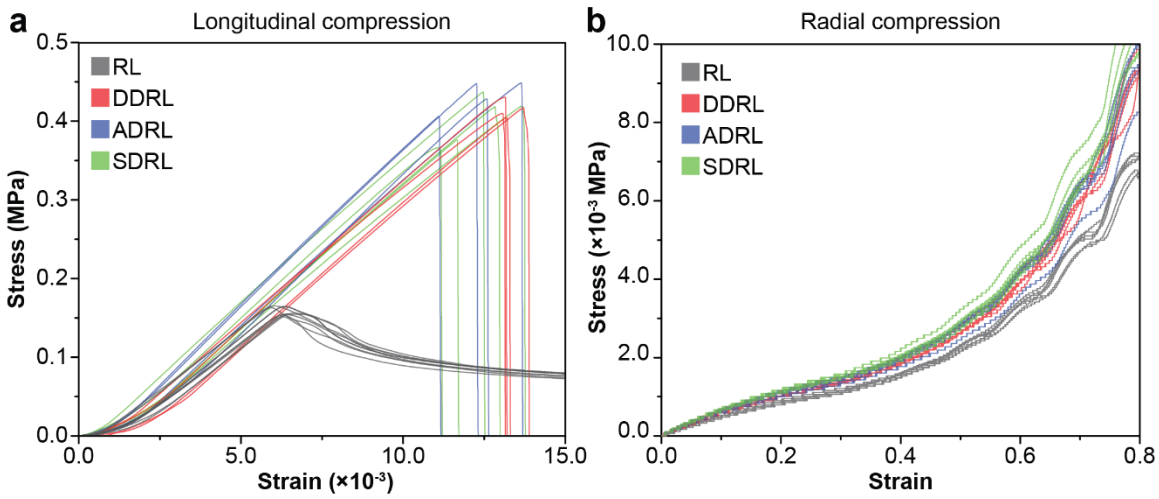


Figure 6.10. (a,b) Experimental stress-strain curves for (a) longitudinal and (b) radial compressions, respectively, on the RL, DDRL, ADRL, and SDRL, respectively.

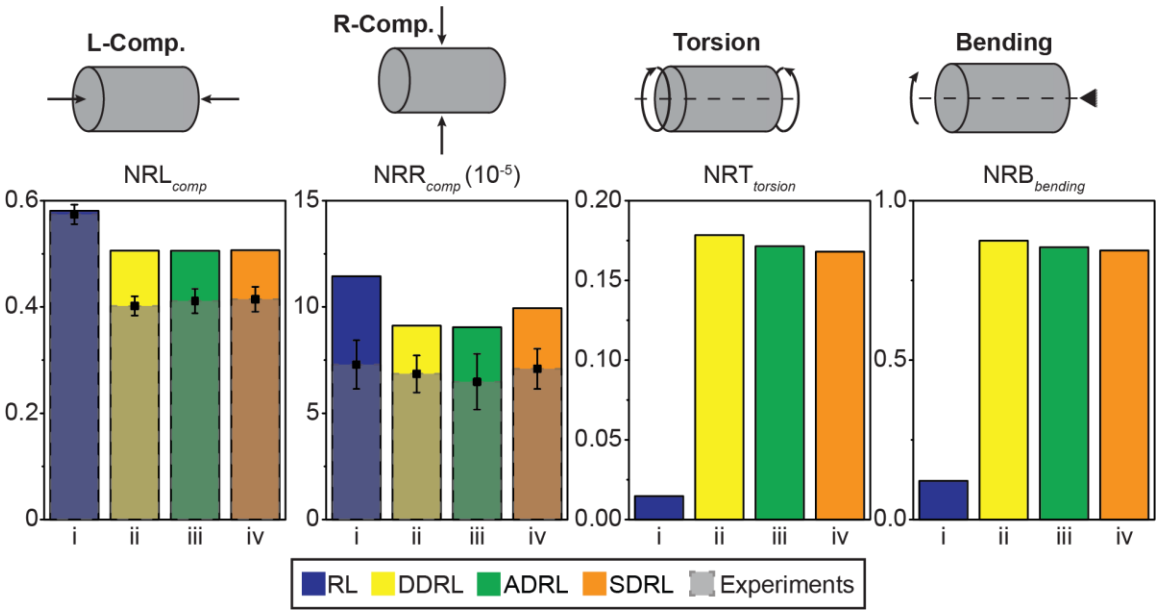


Figure 6.11. Linear elastic mechanical properties from simulations and experiments. Normalized relative longitudinal modulus (NRL_{comp}), radial modulus (NRR_{comp}), torsional rigidity ($NRT_{torsion}$), and flexural rigidity ($NRT_{bending}$) of the RL (blue bars),

DDRL (yellow bars), ADRL (green bars), and SDRL (orange bars). Experimental results of NRL_{comp} and NRR_{comp} are indicated as transparent gray bars.

6.3.3. Parametric modeling and simulations of the bioinspired lattices

We next investigated the mechanical properties of the sponge lattice and its bioinspired variations by conducting parametric computational modeling. To understand the effects of the rectangular cell geometry and the thickness of diagonal bundles of fused spicules, we systematically varied l_C/l_L (0.40 to 1.16) and t_D/l_D (0.005 to 0.024), while keeping d_D/l_D constant (0.25). First of all, as summarized in **Fig. 6.12**, despite some slight variations, the property contour graphs do not change significantly among three diagonally reinforced lattice models, especially for the DDRL and ADRL models. This indicates that the configuration of the diagonals has a negligible effect on the mechanical behaviors, consistent with the previous result obtained from models with a single relative density (**Fig. 6.5b**). Secondly, the measured values of l_C/l_L (0.809 ± 0.113) and relative density (24%) of the *E. aspergillum* sponge show tendency to maximize $NRT_{torsion}$, while the compression and bending performances are inefficient (red dots with error bar, **Fig. 6.12a,b**), which demonstrates a clear performance trade-off among different loading conditions. Thirdly, the half number of the diagonals in the SDRL model results in the decrease of $\rho_{relative}$ under same structural parameters and hence alters the property contours where the deep yellow region moves upward for NRL_{comp}, downward for NRR_{comp}, rightward for $NRT_{torsion}$, and to the bottom right for $NRB_{bending}$ (**Fig. 6.12c**). These results are the consequence of the dependencies of i) NRL_{comp} and NRR_{comp} on the l_C/l_L, ii) $NRT_{torsion}$ on t_D/l_D, and iii) $NRB_{bending}$ on both l_C/l_L and t_D/l_D (**Fig. 6.12**).

Specifically, the longitudinal and radial moduli depend significantly on l_C/l_L, while showing insensitivity to t_D/l_D. The results are attributed to the fact that the longitudinal and circumferential bundles of fused spicules mainly support the loads in longitudinal and radial directions, respectively. In contrast, the torsional resistance is more sensitive to t_D/l_D as the diagonals sustain the shearing load induced by torsion, while the flexural rigidity has strong correlations with both l_C/l_L and t_D/l_D, as the bending induces the normal stress mainly supported by the longitudinal branch and the curvature change resisted by the diagonals (**Fig. 6.5b** and **Fig. 6.12**).

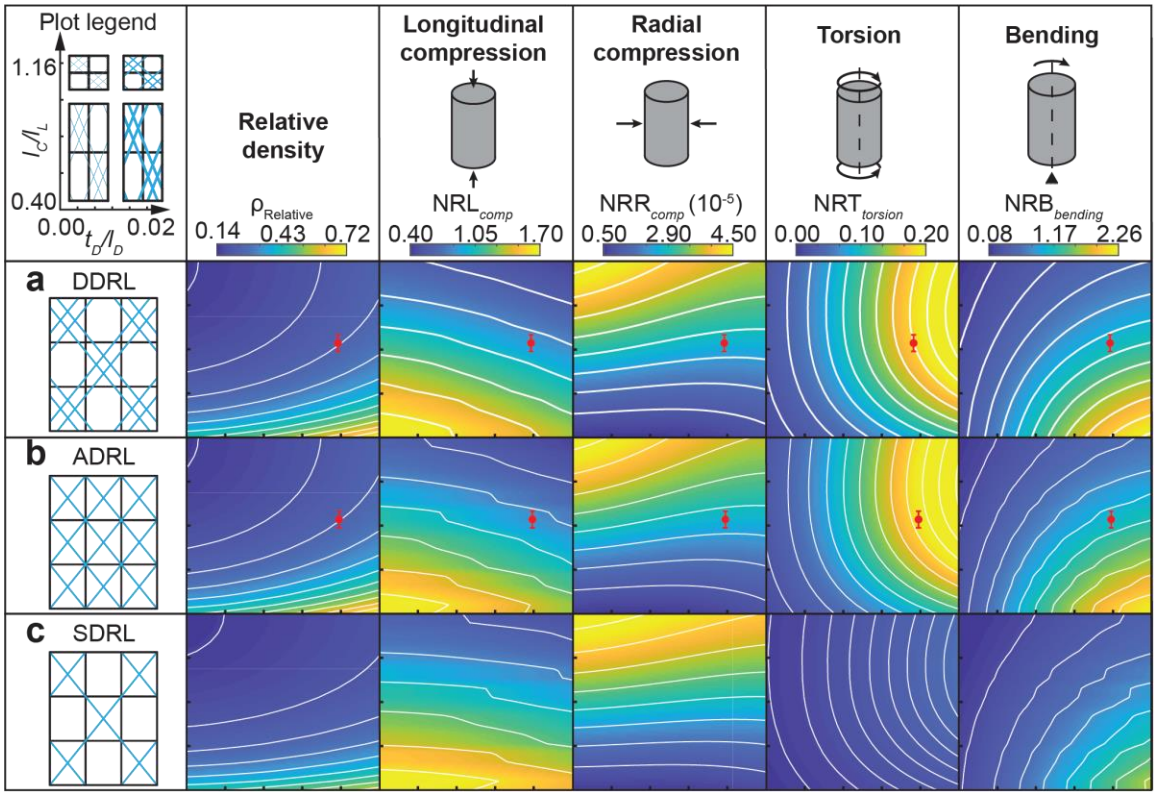


Figure 6.12. Linear mechanical properties from fully parametric modeling and simulations of models with diagonal reinforcements. The contour plots of the relative density ($\rho_{Relative}$), normalized relative longitudinal modulus (NRL_{comp}), radial modulus

(NRR_{comp}), torsional rigidity ($NRT_{torsion}$), and flexural rigidity ($NRT_{bending}$) of the (**a**) DDRL, (**b**) ADRL, and (**c**) SDRL. The color scale bars and loading modes are shown above the contour plots. The red dots in (**a**) and (**b**) with standard deviation as error bar indicate the location that agree with the measured l_C/l_L and relative density of *E. aspergillum* sponge (24.06%). The graph on the top left indicates the schematic legend showing the variation of the aspect ratio of the lattice cell (l_C/l_L, 0.4~1.16) and aspect ratio of the diagonals (t_D/l_D, 0.005~0.024).

The result suggests the configuration of diagonal bundles of fused spicules does not play a significant role in determining the mechanical properties of the lattice skeleton (**Fig. 6.12a,b**). We further confirmed this by investigating the effects of the spacing between the two diagonals for the DDRL model. Here, we only varied d_D/l_D (0.10 to 0.38) and t_D/l_D (0.005 to 0.024) and performed corresponding mechanical simulations. As shown in **6.13**, the variation of the d_D/l_D indeed does not affect all stiffnesses, supporting previous results. In fact, ADRL and SDRL can be considered as DDRLs with d_D values of $l_D/2$ and 0, respectively, which underlies the similarity of the property contours for the three models (**Fig. 6.12**).

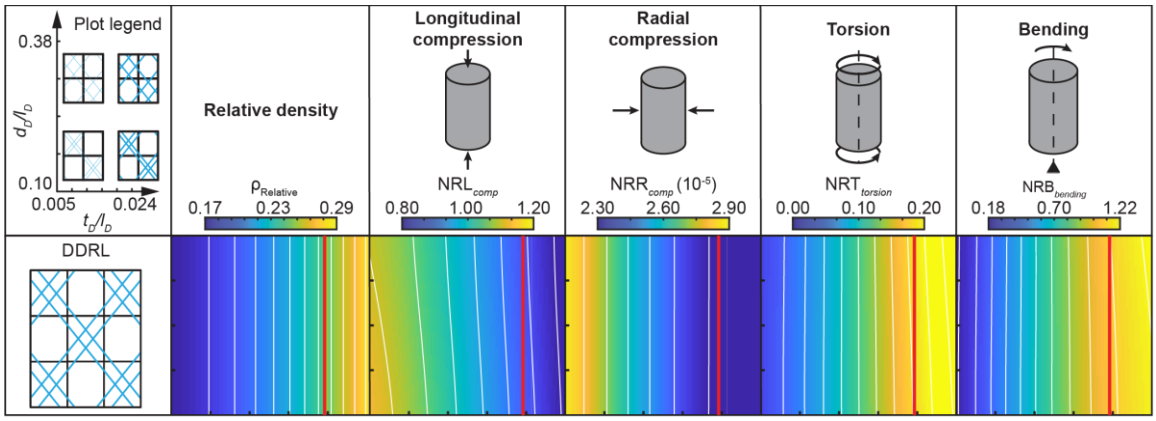


Figure 6.13. Mechanical implication of the spacing of the diagonals (d_D/l_D) in DDRL model. The contour plots of the normalized relative longitudinal modulus (NRL_{comp}), radial modulus (NRR_{comp}), torsional rigidity ($NRT_{torsion}$), and flexural rigidity ($NRT_{bending}$) of the DDRL. The color scale bars and loading modes are shown above the contour plots. The red lines indicate the location that agree with the relative density of *E. aspergillum* sponge. The graph on the top left indicates the schematic legend showing the variation of the aspect ratio of spacing of the diagonals (d_D/l_D, 0.10~0.38) and aspect ratio of the diagonals (t_D/l_D, 0.005~0.024).

6.3.4. Structure and mechanics of the ridge structure

In addition to the double-diagonal reinforcement, the *E. aspergillum* sponge skeletal lattice also exhibits another unique feature which is the ridge system spiraling around the cylindrical skeleton (**Fig. 6.1d,f**). As previously mentioned, the mechanical and hydrodynamic functions of different ridge systems have been investigated, which demonstrates its minor contributions to the mechanical properties, yet significant suppression of vortex shedding [73]. Hereby, different from previous works [73,74], we devised multiple ridge models and investigated mainly the radial response of the ridge

structure (**Fig. 6.14**). As shown in **Fig. 6.14a-h**, we constructed two types of bioinspired ridge structures depending on whether the spicules of ridge are connected to the rectangular unit cells (model CL) or the diagonal branches (model D). Note that the ridge system in the *E. aspergillum* sponge is a combination of two designs, where the spicules of ridge are randomly connected to both node types (**Fig. 6.1f**). To investigate the effects of orientations of the ridge as observed in the *E. aspergillum* sponges, we further modeled two scenarios, i.e., ridge spiraling on the cylindrical lattice in one orientation (1O) or two opposite orientations (2O) (**Fig. 6.14d,h**). Therefore, four lattice models in total were generated, which are CL-1O, CL-2O, D-1O, and D-2O. It is worthy to note that the spacing between ridges is consistently four rectangular cells similar to the skeletal structure of the sponge, which does not leave large gaps without ridge structure compared to the model with ridge spiraling in opposite directions in previous work (**Fig. 6.14d,h**) [73]. How the aforementioned variations in designs (i.e., ridge orientations and spicule connections) of ridge systems affect the mechanical properties of sponge's cylindrical lattice and whether the sponge has limitations in the flexibility of constructing the ridge system are to be analyzed here. For comparison, two control models were constructed, i.e., the original DDRL model and the modified DDRL model with increased t_D/l_D (denoted as DDRL-TD) and proportionally increased thickness for all types of branches (denoted as DDRL-PT) in order to achieve the same relative density of the models with ridges (**Fig. 6.14i**).

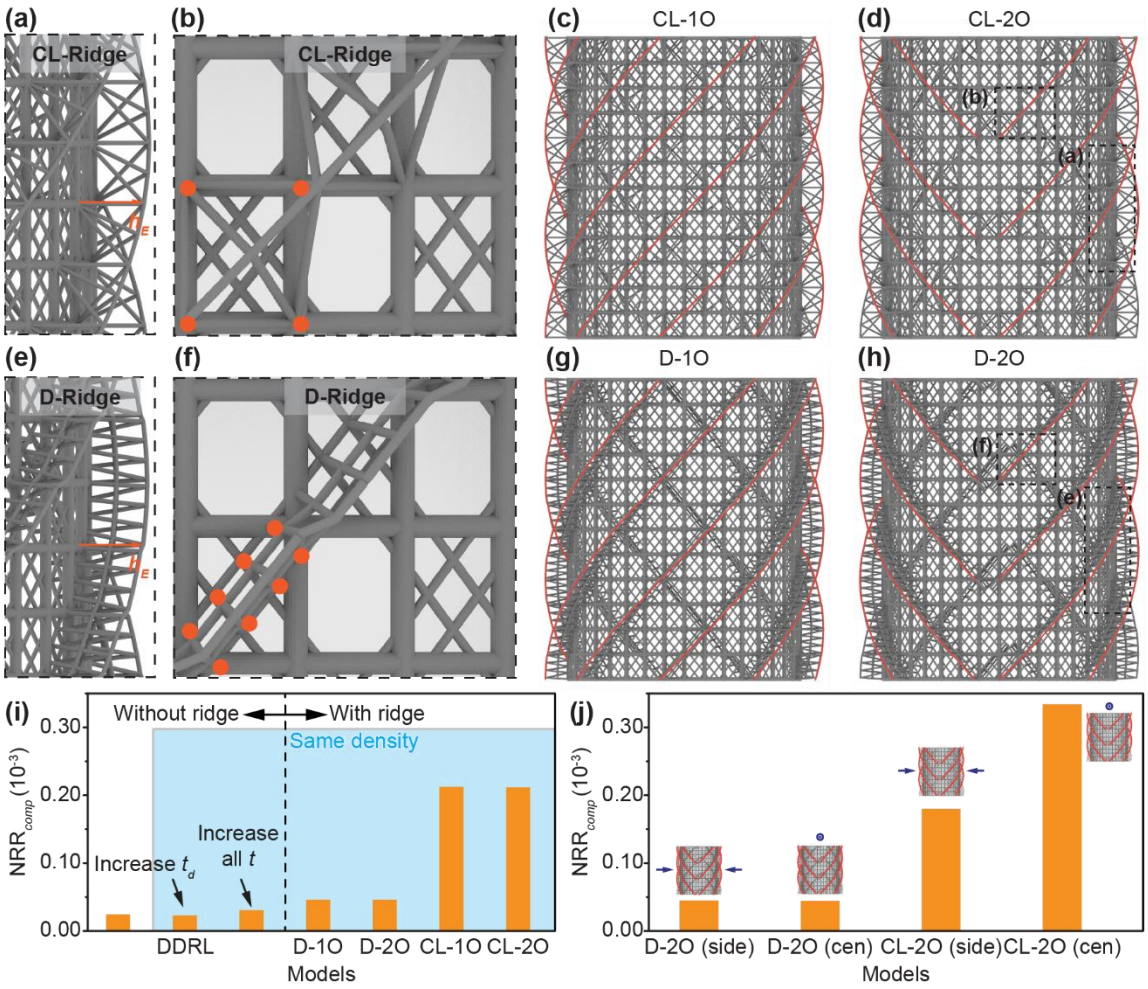


Figure 6.14. Design and radial stiffness of the ridge structures. (**a,b**) CL model where the branches extrude from the nodes intersecting the branches in C and L directions (indicated by orange dots). (**c,d**) 3D structure of the cylindrical lattices with ridge spiral around the lattice in (**c**) one orientation (CL-1O) and (**d**) two opposite orientations (CL-2O). (**e,f**) D model where the branches extrude from the nodes on the diagonals (indicated by orange dots). (**g,h**) 3D structure of the cylindrical lattices with ridge spiral around the lattice in (**g**) one orientation (D-1O) and (**h**) two opposite orientations (D-2O). (**i**) Normalized relative radial modulus (NRR_{comp}) of the DDRL with or without ridge structures. The DDRL has two variational models for comparison which are the one with diagonal thickness increased (DDRL-TD) and the one with all branch thickness

proportionally increased (DDRL-PT). They have the same relative density to the models with ridge. (**j**) Normalized relative radial modulus (NRR_{comp}) of the D-2O and CL-2O under two types of radial loading orientations. Radial compression is applied on either the "side" or "cen" directions, respectively, as indicated by the blue arrows. The "side" and "cen" loading directions are perpendicular and parallel to the plane of symmetry between ridges in opposite directions.

We conducted similar mechanical simulations on the models with ridge under four different loading conditions. As expected, the DDRL-TD model show a slightly reduced NRL_{comp}, similar NRR_{comp}, and enhanced $NRT_{torsion}$ and $NRB_{bending}$ compared to the original DDRL model due to the increased material volume in the diagonals (**Fig. 6.14i,6.15**). Additionally, the introduction of ridge structures results in less enhancement of NRL_{comp}, $NRT_{torsion}$, and $NRB_{bending}$ compared to directly adding materials to diagonals, indicating the ineffective contributions of the ridge structure to those properties (**Fig. 6.14i**) [73]. In contrast, a significant increase in NRR_{comp} was observed, especially for the CL models (~9-fold increase and ~1-fold increase for CL and D models, respectively, compared to the DDRL-TD and DDRL-PT models, **Fig. 6.14i**). Moreover, we performed compressions along two dissimilar radial directions for 2O design, namely, the "side" and "cen" loading directions which are perpendicular and parallel to the plane of symmetry between ridges in opposite directions, respectively (**Fig. 6.14j**). The simulation results indicate that the spiraling orientations of ridge have small effects for the D-2O model to all mechanical properties, while for CL-2O design, the

radial modulus along the “cen” direction is ~50% higher than that along the “side” direction (**Fig. 6.14j,6.15**).

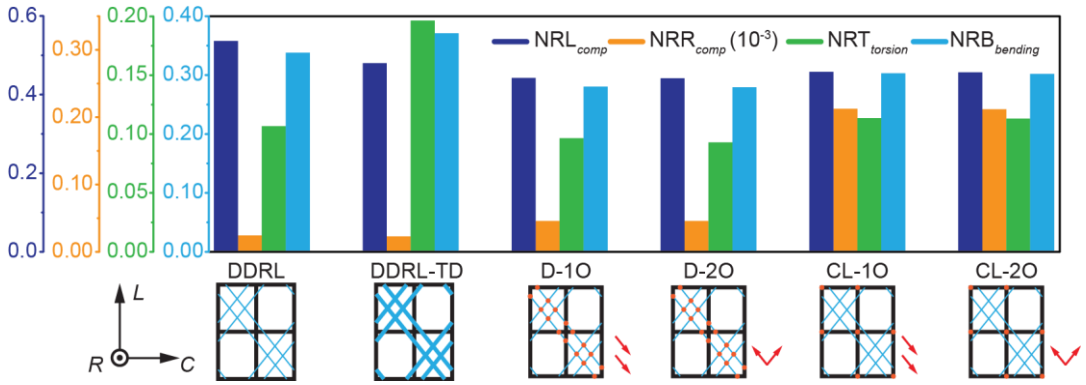


Figure 6.15. Mechanics of the ridge structures. Normalized relative longitudinal modulus (NRL_{comp}), radial modulus (NRR_{comp}), torsional rigidity ($NRT_{torsion}$), and flexural rigidity ($NRT_{bending}$) of the DDRL with or without ridge structures. The legend and schematic models are shown on the bottom. The red arrows pointing to the same orientation and opposite orientation in schematic legends indicate the ridge spiraling along one orientation and two opposite orientations, respectively.

We again fabricated the models through 3D printing and conducted mechanical testing to validate our simulation results (**Fig. 6.16**). The stress-strain curves (**Fig. 6.17a**) for longitudinal compression show catastrophic failure, while radial compression experiments reveal a strain-hardening behavior (**Fig. 6.17b**). The experimental results agree well with the simulation results in terms of longitudinal compression, however, the radial stiffness of CL model obtained from experiments is significantly smaller than that of the simulation (**Fig. 6.18**). This discrepancy could be a result of defects and imperfections after fabrication.

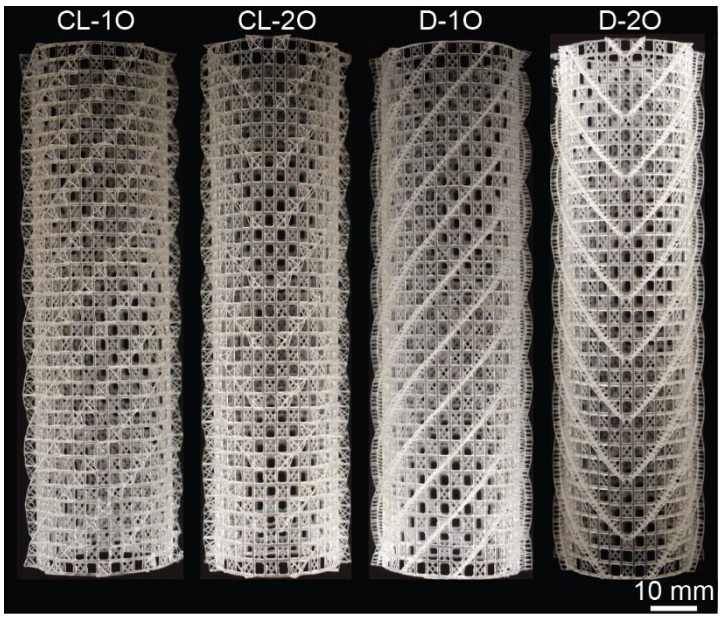


Figure 6.16. Experimental samples of four types of cylindrical lattices with ridge structure (CL-1O, CL-2O, D-1O, and D-2O from left to right).

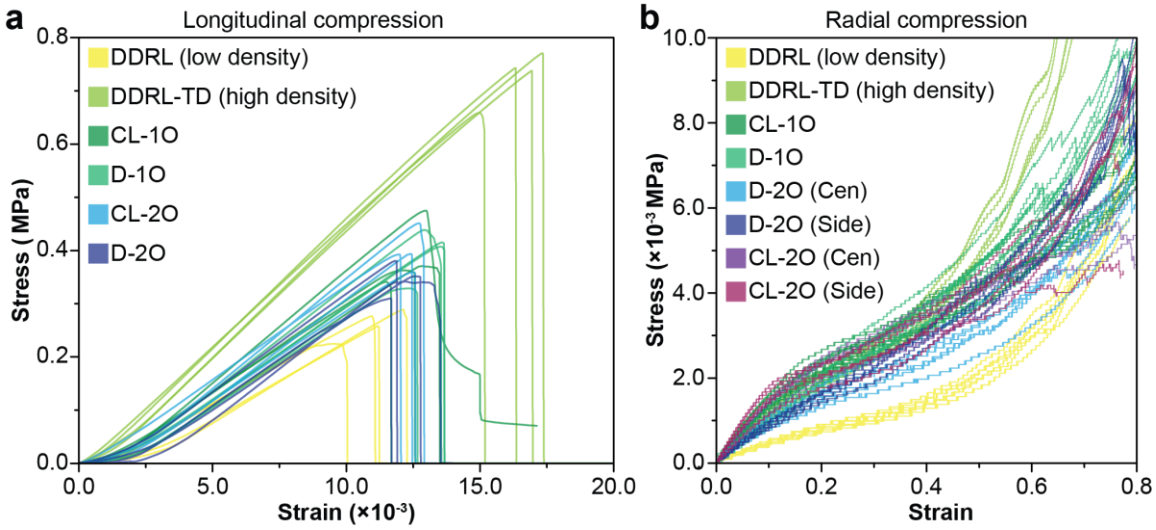


Figure 6.17. (a-b) Experimental stress-strain curves for (a) longitudinal and (b) radial compressions, respectively, on the DDRL with or without ridge structures.

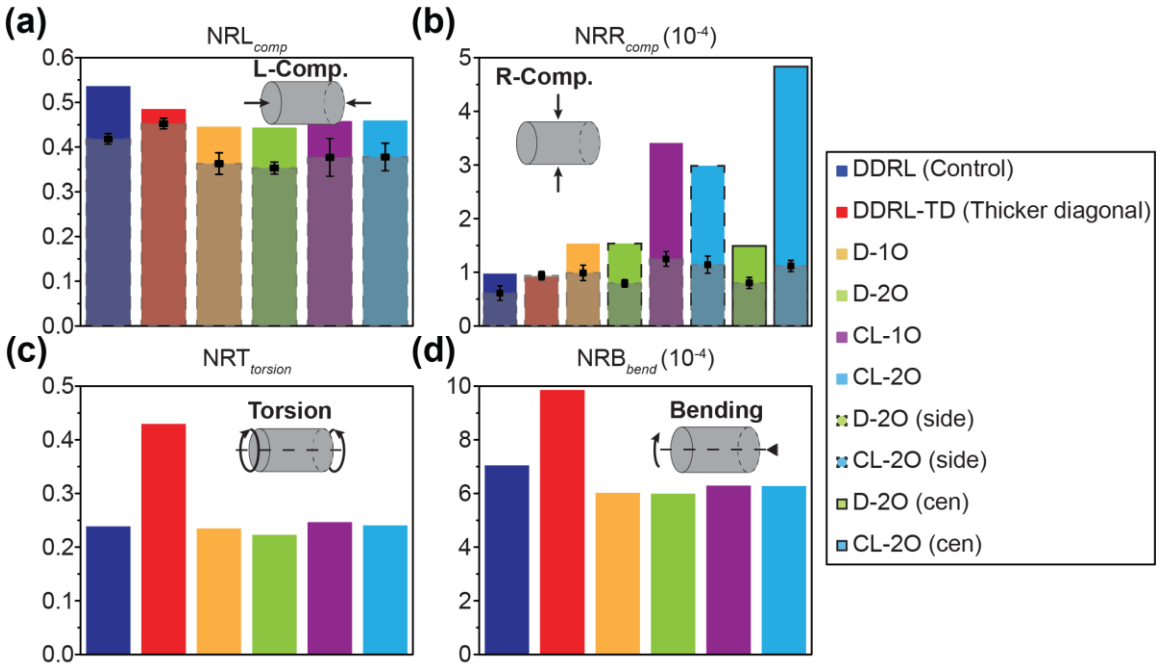


Figure 6.18. Experimental and simulation results of the cylindrical lattices with ridge structures. (**a**) Normalized relative longitudinal modulus (NRL_{comp}), (**b**) radial modulus (NRR_{comp}), (**c**) torsional rigidity ($NRT_{torsion}$), and (**d**) flexural rigidity ($NRT_{bending}$) of the DDRL with or without ridge structures from simulations and experiments. Experimental results of NRL_{comp} and NRR_{comp} are indicated as transparent gray bars. Radial compression is applied on either the "side" or "cen" of the lattice with opposite ridge, respectively, as indicated by the blue arrows in **Fig. 6.14j**.

6.3.5. Fluid-mechanical behaviors of the ridge structure

As introduced earlier, the ridge system helically spiraling along the *E. aspergillum*'s cylindrical lattice facilitates the water flow through the sponge's body for stabilizing the cylindrical structure yet ineffectively contributes to its mechanical properties [73]. Here we found improved radial stiffening attributed to the ridge structure (**Fig. 6.14i**). As the next step, to study whether the ridge provides radial stiffening to resist radial loading induced

by the water flow and how the ridge regulates the local fluidic transport, we devised planar bioinspired models with and without ridge for the fluid-mechanical coupling simulations (**Fig. 6.7,6.19**). We first examined the preserved *E. aspergillum* sponge specimens provided by the Museum of Comparative Zoology at Harvard University (**Fig. 6.19a-c**). The tissue completely fills the rectangular cells with diagonal reinforcing bundle of fused spicules and the ridges, while leaving the rest of cells to form opening holes for filtration feeding purposes (**Fig. 6.19c**) [34,79]. Due to the rectangular geometry of the lattice cells, the opening holes are slightly elliptical with their major axes ($l_{L-hole} = 1.3 \pm 0.2\,mm$) and minor axes ($l_{C-hole} = 1.2 \pm 0.2\,mm$) along the L and C directions, respectively. Combining the previous measurement of the skeletal lattice, we developed three representative simplified solid models for coupled fluid-mechanical simulations, which are No ridge (model without ridges), 1O-Ridge (model with the ridge spiraling in one orientation), and 2O-Ridge (model with the ridge spiraling in two opposite orientations (**Fig. 6.7,6.19e,f**, **Table 6.5**). Despite this effort in obtaining structural information of the sponge skeleton close to its native state, it is important to note that the hole sizes measured from the preserved samples may still deviate from the actual pore sizes on the dermal membrane for the living sponge [79,164]. Yet, with relatively limited information, the herein measured sizes of the elliptical pores are adopted in designing our simplified bioinspired models which results in a 2D porosity of ~8% close to 6% used in the existing reference [73].

Table 6.5. Measurement results of the structural descriptors defining the schematic model for fluid simulations.

Sample	l_{L-Cell} (mm)	l_{C-Cell} (mm)	l_{L-hole} (mm)
Sample 1	5.25 ± 0.44	4.71 ± 0.37	1.27 ± 0.20
Sample 2	5.62 ± 0.66	5.19 ± 0.49	1.36 ± 0.15
All	6.00 ± 0.60	5.25 ± 0.50	1.32 ± 0.17

Sample	l_{C-hole} (mm)	l_{C-Cell}/l_{L-Cell}	l_{C-hole}/l_{L-hole}
Sample 1	1.12 ± 0.18	0.901 ± 0.088	0.884 ± 0.105
Sample 2	1.17 ± 0.19	0.929 ± 0.094	0.868 ± 0.135
All	1.21 ± 0.19	0.917 ± 0.092	0.875 ± 0.124

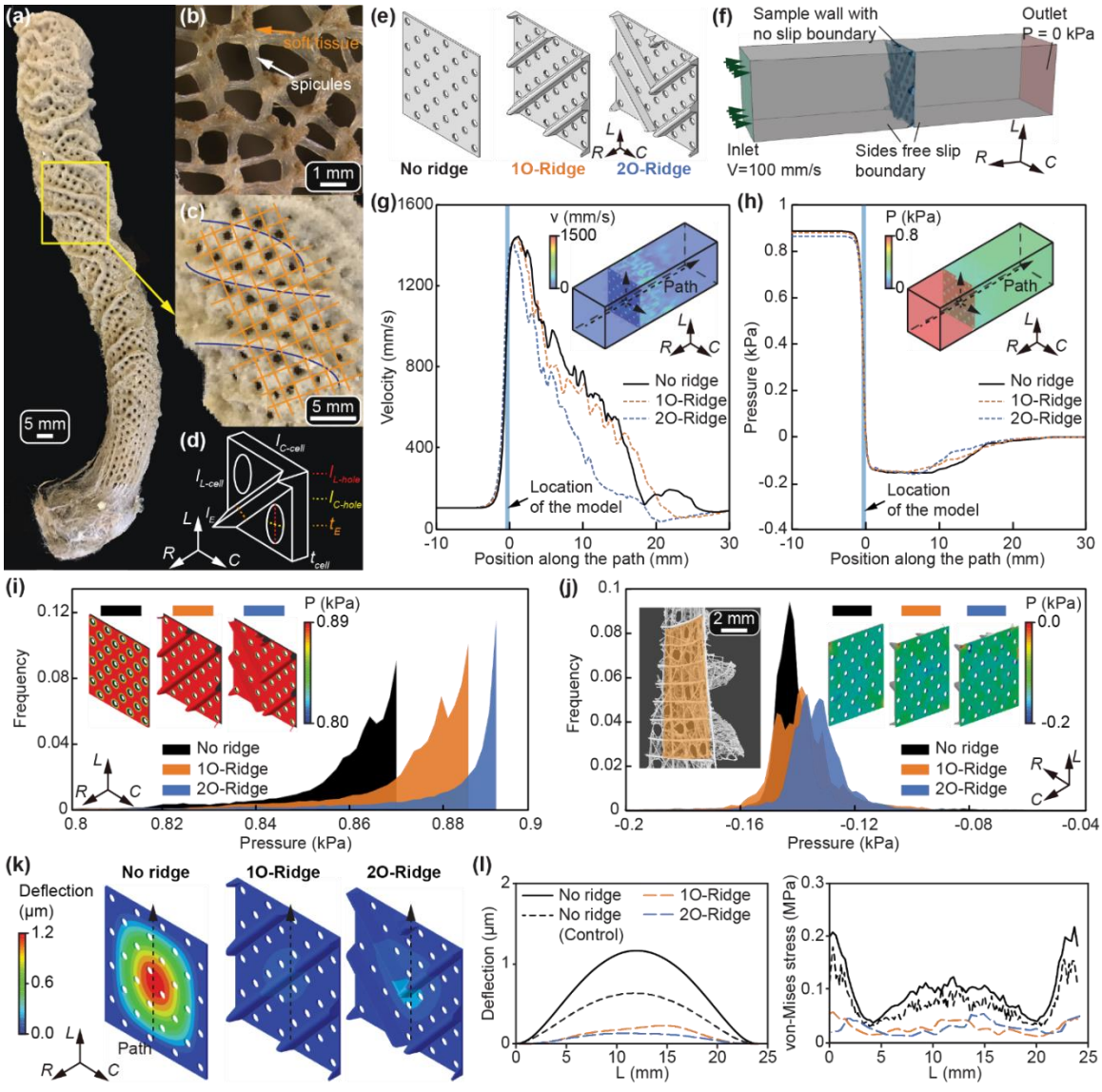


Figure 6.19. Hydrodynamics and mechanics of the bio-inspired models. (**a**) Morphology of the *E. aspergillum* sponge covered with preserved tissue. (**b**) Sieve plate

of the *E. aspergillum* sponge covered with tissue. Orange arrow: tissue. White arrow: bundle of fused silica spicules. (**c**) A zoomed-in graph of the cylindrical skeleton covered with tissue. Blue lines: trace of the ridges. Orange boxes: rectangular cell structure. (**d**) Schematic model and structural descriptors for fluid-mechanical simulations. (**e**) Three solid models, including No ridge, 1O-Ridge, and 2O-Ridge models, for the fluid-mechanical simulations. (**f**) Fluid simulation configuration showing the water inlet, outlet and boundary conditions. (**g,h**) Profiles of (**g**) velocity and (**h**) pressure, respectively, along the central path defined in the insets for three models in (**e**). (**i,j**) Pressure distributions on the (**i**) front and (**j**) back sides, respectively, of three models due to the water flow. (**k**) Deflection distributions within three models. (**l**) Deflection and von-Mises stress distribution of three models in (**e**) along the path indicated in (**k**).

The simulation configuration was shown in **Fig. 6.7f** which was introduced previously in detail in section 2.7. This allows us to analyze the hydrodynamic behaviors such as fluid velocity and pressure (**Fig. 6.19g,h**) as well as the mechanical behaviors such as deformation and corresponding stress distributions of the solid models (**Fig. 6.19i-l**). For the hydrodynamic aspect, the flow velocity, pressure drop, and the resultant fluid permeability calculated using Eq. 2.2 of three models are summarized (**Table 6.6,6.7**). The flow velocities were probed from three different locations along the central path (*i.e.*, locations with maximum velocity, $x = 5mm$, and $x = 10mm$, **Fig. 6.19g** and **Table 6.6**), while the pressure drops were obtained by calculating the difference between the far-field inlet and outlet pressures for three models (**Fig. 6.19h** and **Table 6.7**). Firstly, introducing ridge reduces the velocity in the flow wake due to the increase of the

area of friction, and thus the drag, to the flow (**Table 6.6**). A comparison of the velocity profile reveals that the models with ridge exhibit shorter wakes compared to the No ridge model (**Fig. 6.20**). Secondly, the flow wakes of the models with ridge structures show greater velocity fluctuations in the L-C plane compared to the No ridge model (**Fig. 6.21**), while the symmetry of the No ridge and 2O-ridge models suppress the velocity fluctuation along the R direction (**Fig. 6.22**). Thirdly, the 2O-Ridge model is found to reduce pressure drop and enhance the fluid permeability by 2.7%, more advantageous in improving fluid permeability and hence slightly better flow rectification function than the 1O-Ridge design (**Table 6.7**). This increase in the permeability is likely due to the prevention of abrupt change of fluid cross section and pressure difference (ΔP in Eq. 6.2.2) via the introduction of ridge structure as a flow guiding system. For the mechanical aspect, the surface pressure distributions on three models were obtained, which demonstrates the positive pressure on the front side and negative pressure on the back side (**Fig. 6.19i,j**). Careful examination of the pressure distributions reveals that the models with ridge tend to shift the front-side pressure to a larger value while shifting the back-side pressure to a less negative value (**Fig. 6.19i,j**). This surface pressure distribution allows us to perform mechanical simulations on the solid models and investigate how the ridge structure affects the radial deformation of the *E. aspergillum* (**Fig. 6.7**). Despite the enhanced drag by the ridge structure, compared with the No ridge model with proportionally enhanced elastic modulus, the models with ridge present approximately 50% reduction of the maximum deformation and maximum stress (**Fig. 6.19k,l,6.23**). This is consistent with the enhanced radial elastic modulus of the cylindrical lattice with ridge in the parametric mechanical study (**Fig. 6.14i**). In addition,

compared to the 1O-Ridge model, the 2O-Ridge model exhibits slightly less deformation yet similar stress distribution (**Fig. 6.19k,l,6.23**). This radial stiffening by ridge may be attributed to the analog of ridge to the rib design which is usually the reinforcing strategy in engineering structure [173].

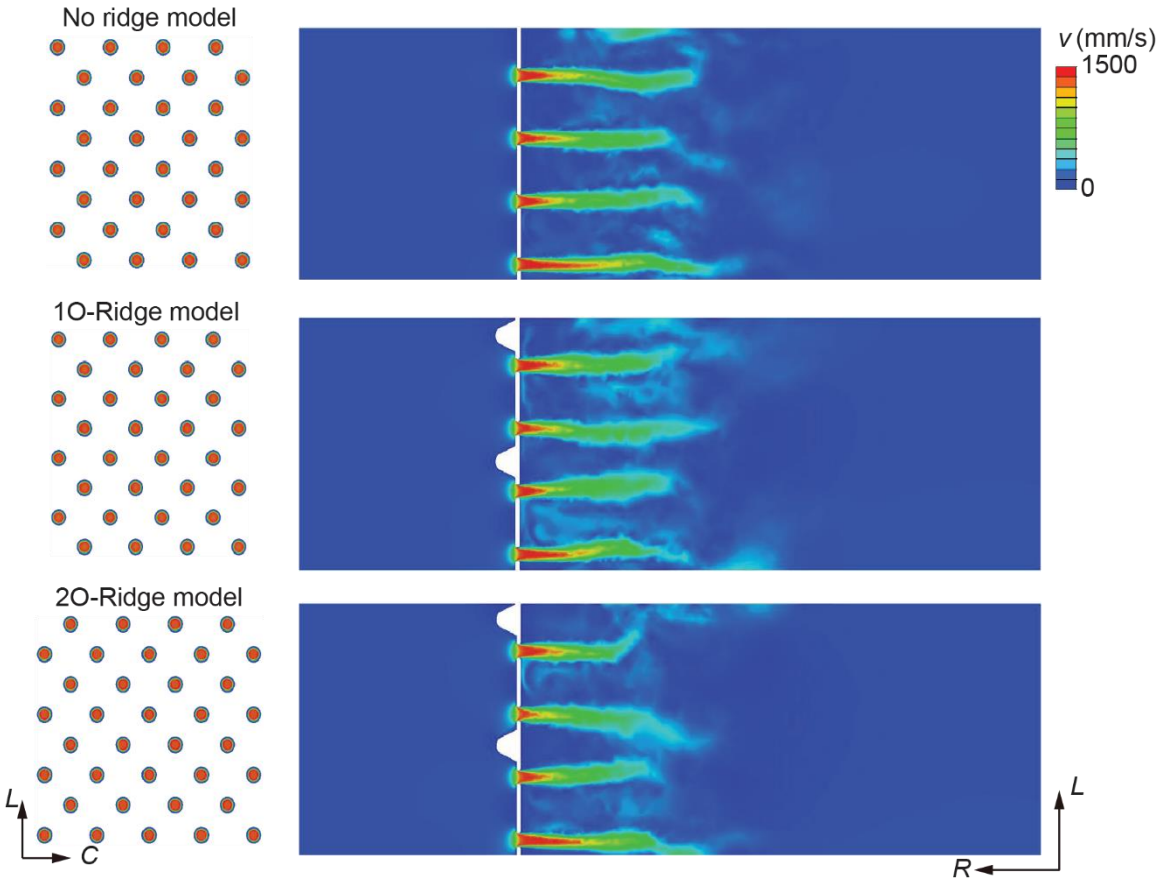


Figure 6.20. 2D velocity profile of three CFD models, including (a) No ridge model, (b) 1O-Ridge model, and (c) 2O-Ridge model on the (left column) L-C plane and (right column) L-R plane. The dark solid lines indicate the length of flow wake behind the solid models of three models.

Table 6.6. Comparison of the velocity distribution among three biomimetic models.

Models	V_{max} (m/s)	Reduction	$V_{x=5mm}$ (m/s)	Reduction	$V_{x=10mm}$ (m/s)	Reduction
No ridge	1.445	N.A.	0.941	N.A.	0.779	N.A.
1O-Ridge	1.433	0.8%	0.792	15.8%	0.702	9.9%
2O-Ridge	1.416	2.0%	0.716	23.9%	0.349	55.2%

Table 6.7. Comparison of the pressure drop and permeability among three biomimetic models.

Models	Pressure drop ΔP (kPa)	ΔP reduction (kPa)	Permeability (mm^2)	Permeability improvement
No ridge (control group)	0.8884 ± 0.0011	N.A.	0.0480	N.A.
1O-Ridge	0.8820 ± 0.0011	0.0064	0.0483	0.72%
2O-Ridge	0.8650 ± 0.0005	0.0233	0.0492	2.70%

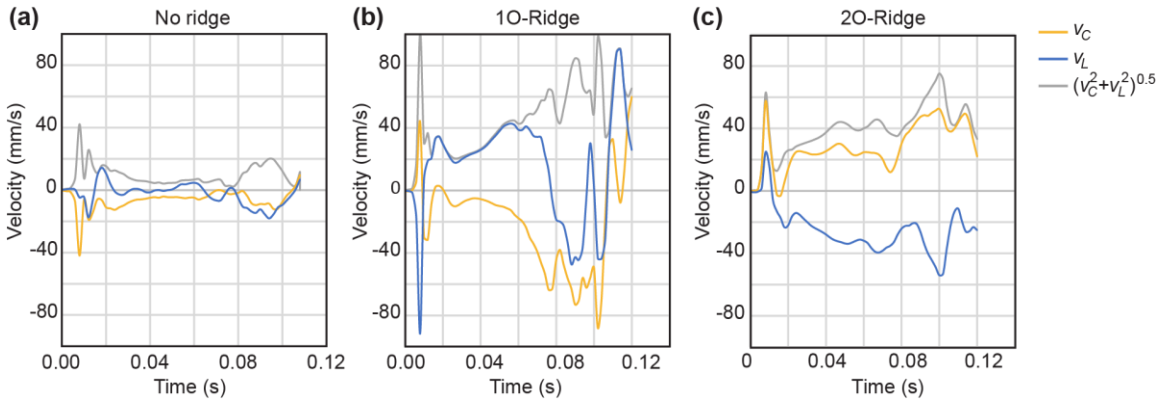


Figure 6.21. Time evolution plots of the velocities probed 5 mm downstream in L direction, C direction, and L-C plane, respectively, for (a) No ridge model, (b) 1O-Ridge model, and (c) 2O-Ridge model.

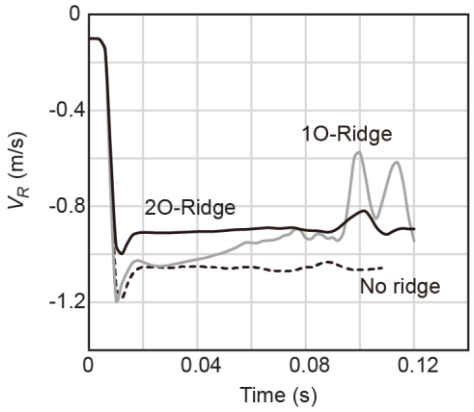


Figure 6.22. Time evolution plots of the velocity probed 5mm downstream in R direction for No ridge model, 1O-Ridge model, and 2O-Ridge model.

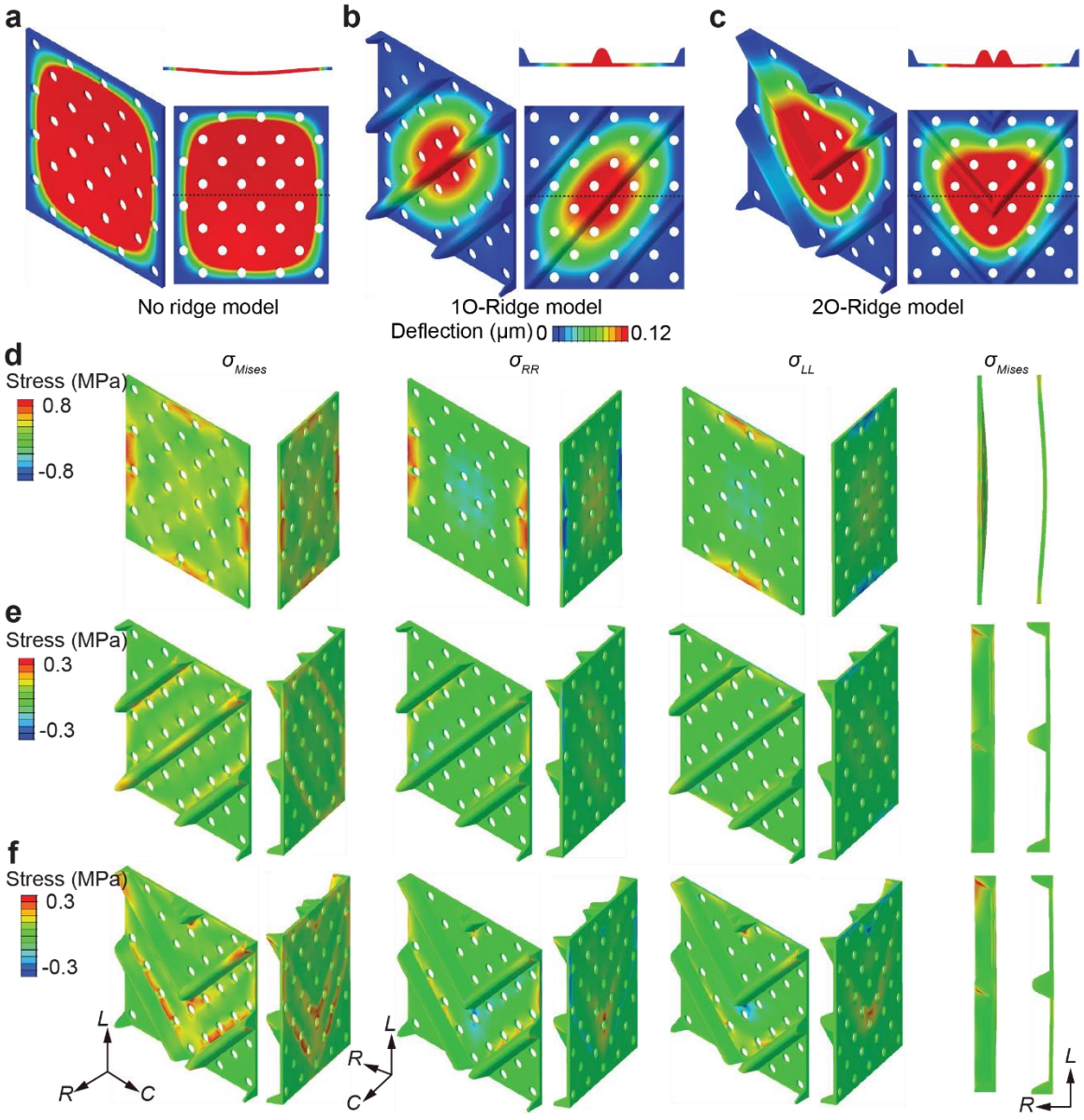


Figure 6.23. Mechanical reaction of the models with or without ridge structures under pressure exerted by water flow. (**a-c**) Deflection (500 times magnified) of (**a**) No ridge model, (**b**) 1O-Ridge model, and (**c**) 2O-Ridge model due to water flow. (**d-f**) Von-Mises stress (σ_{Mises}), out-of-plane stress (σ_{RR}), and in-plane stress (σ_{LL}) distribution of the (**d**) No ridge model, (**e**) 1O-Ridge model, and (**f**) 2O-Ridge model.

6.4. Discussions and conclusions

In this work, the mechanical properties of the *E. aspergillum* sponge's skeleton were investigated parametrically under various loadings, and several mechanical design features for the biological lattice were revealed as follows. Firstly, the presence of the diagonal reinforcements in the rectangular lattice (i.e., DDRL, ADRL, and SDRL models) is critical for enhancing the torsional and bending resistance (i.e., $NRT_{torsion}$ and $NRB_{bending}$) where shearing loads are involved, despite a slight reduction in the efficiency of longitudinal and radial compression's resistance (i.e., NRL_{comp} and NRR_{comp}) (**Fig. 6.5b**). The higher nodal connectivity, which resulted from the diagonal connections, improves the rigidity of the rectangular lattice structure [17]. Secondly, our parametric study indicates that the sponge's skeletal structure tends to maximize torsional rigidity, with slight sacrifice of effective resistance to compression and bending. It is worth to note that for all skeletal lattices that we measured, l_C/l_L remains consistent despite local variations of the tubular skeleton's curvature and diameter, which suggests a limitation of design flexibility of the cylindrical lattice skeleton for the tendency of maximizing the torsional rigidity (**Fig. 6.2,6.12**). In addition, our parametric results show that the increase of l_C/l_L will further improve the $NRT_{torsion}$ but significantly reduce the NRL_{comp} and $NRB_{bending}$ of the cylindrical skeletal lattice (**Fig. 6.12**). This mechanical trade-off among NRL_{comp}, $NRB_{bending}$, and $NRT_{torsion}$ may be one reason for the limitation of the design flexibility and achieving a maximized torsional rigidity. Thirdly, the tendency of maximizing torsional rigidity with slight sacrifice of other properties may be biologically relevant. Although speculative, the dominant horizontal water flow may exert mostly radial compression, bending and torsion loads on the *E. aspergillum* [34,75]. The bending

deformation is mainly sustained by the sponge's flexible yet strong bundle of anchoring spicules, and the resistance of radial pressure is enhanced by ridge structure, which leaves the torsional loading to be mainly supported by the cylindrical lattice with the diagonal reinforcement [58,65]. In addition, our modeling found that the distance between the double diagonals has no observable effects on the linear mechanical properties of the cylindrical lattice, including longitudinal modulus, radial modulus, torsional rigidity, and flexural rigidity (**Fig. 6.13**). This is attributed to the similarity among the cylindrical lattice models in this work (**Fig. 6.5**) where the ADRL and SDRL can be considered as DDRLs with d_D values of $l_D/2$ and 0, respectively (**Fig. 6.11**), which may provide design flexibility to other functions. Indeed, the sponge's skeletal lattice structure is most similar to the DDRL model as it provides fluid-mechanical coupling advantages, including i) allowing the tissue coverage of every second holes with diagonals and hence leaving other "empty" cells open for fluid transport and flow regulation [73,79] and ii) enhancing buckling strength at the initial stage of spicule growth [70]. Fourthly, the relatively uniform spacing between diagonals in the rectangular cells could provide better assistance for growing secondary spicules and anchoring the tissues (**Fig. 6.1**). Similar to the uniform spacing of the diagonal reinforcement, the secondary spicules, which are relatively randomly distributed in the cells with diagonal reinforcements, may also provide convenient and uniform anchoring locations for soft tissues with minimal weight increase. Finally, the helical ridge, as another unique structural component, on the cylindrical skeleton provides significant radial stiffening to help resist the loads generated by water flow (**Fig. 6.14,6.19**).

The unique ridge system found in the skeleton of *E. aspergillum* contributes to both the mechanical and hydrodynamic properties. For the mechanical aspect, we found ineffective

contribution of the ridge to the resistances to the longitudinal compression, torsion, and bending (*i.e.*, reduction of NRL_{comp}, $NRT_{torsion}$ and $NRB_{bending}$), consistent with the results in the previous work (**Fig. 6.15**) [73]. In contrast, the ridge structure provides significant stiffening along the R direction (*i.e.*, increase of NRR_{comp}) which help resist the radial deformation due to horizontal water flow as demonstrated by our proposed fluid-mechanical simulations (**Fig. 6.14,6.19e,f**). Here, the ridge acts as a radial reinforcement for the cylindrical lattice, which is similar to the rib design in reinforced engineering structures [173]. For the hydrodynamic aspect, the models with ridge provide some improvement in permeability, which demonstrates the multifunctionality of the ridge structure (**6.7**). This permeability improvement may be a strategy of assisting the water to flow through the sponge for filtering feeding [34,79]. It is worth to note that the conclusions above are independent of the ridge's spiraling orientations, which provides freedom to distribute the ridge for other purposes (**Fig. 6.14,6.19**). Indeed, the actual ridge system in the *E. aspergillum* exhibits combinations of both 2O-Ridge and 1O-Ridge models, which results in an enhanced adaptation for the suppression of vortex shedding (**Fig. 6.1,6.14**) [21,73]. However, it is currently unknown whether the ridge's distribution in *E. aspergillum*'s skeleton represents an better design of radial reinforcement which requires bioinspired modeling of such maze-like distribution of ridges for mechanical and fluid-mechanical coupling studies [73]. Moreover, ridge connections exhibit local combinations of CL-Ridge and D-Ridge types in the actual ridge system of the *E. aspergillum* (**Fig. 6.1f**). Our simulation results indicate that the CL-Ridge and D-Ridge models provide radial stiffening to a different degree (**Fig. 6.14i**). These findings suggest that the *E. aspergillum* does not specifically control the spicule connection for the ridges for maximizing radial stiffness

(**Fig. 6.14i**). This may be attributed to the limitation of skeletogenesis and potential benefit for soft tissue attachment.

A couple of limitations of the current work are worth to discuss here. Firstly, our work is limited by the current insufficient knowledge about the relevant loading conditions for the live *E. aspergillum* sponges in their natural habitat at a wide range of depth in the sea where variations of flow speed may exist [34,73]. Here, compressions in longitudinal and radial directions, torsion, and bending were considered, which is a rather comprehensive set of loading conditions for the tubular structure. Enabled by the submersibles and sensors, previous works successfully monitors the incurrent and excurrent water flows as well as feeding behaviors of some Hexactinellid sponges such as *Aphrocallistes vastus* and *Rhabdocalyptus dawsoni* at the sea floor [22,33,34,174]. Similar in-situ techniques may be used to monitor the loading conditions for *E. aspergillum*, which will provide further insights in explaining the findings in this work. For example, we demonstrated that the sponge's skeleton exhibits a tendency to maximize torsional rigidity (**Fig. 6.12**). As previously discussed, we may provide hypothetical explanations to this loading and optimization tendency as follow: i) the asymmetric water flow may induce torsional loading to the sponge; and ii) the torsional loading is mainly sustained by the diagonally-reinforced rectangular cells while others are supported by anchoring spicules (bending loads) or rectangular lattice (compressive loads). Further biomechanical information may help to test such hypotheses. Secondly, the planar porous models used in this study deviates from the actual living *E. aspergillum* because the microscale pores at the body surface may change after preservation (**Fig. 6.19a-c**) [79,164]. In addition, the complex canal system of the Hexactinellid sponges' tissue, which itself

represents a multiscale structure, has not been incorporated into bioinspired modeling for mechanical and hydrodynamic studies [73,75,79,163,164]. Furthermore, the planar bio-inspired models here do not consider the mechanical contribution and active water pumping of the soft tissue which may affect the water flow around the sponge and hence the mechanical behaviors [34,163]. Therefore, how the actual pore structure and tissue model affect the results such as permeability enhancement and radial stiffening remains open questions [169]. Filling such knowledge gaps may deliver us important message about the filtering feeding and inspire the design of porous structure with mechanical-hydrodynamic coupling functions [34]. We also note that our simplified models do not capture the fluid field around the entire cylindrical body with ridges such as the vortex shedding suppression [73]. Nevertheless, the coupled fluid-mechanical simulations in this work reveal the local fluidic field and the mechanical deformation of the cylindrical lattice with tissue covered, providing a local mechanism for the macroscale behaviors [75].

In summary, by combining quantitative structural measurement, bioinspired parametric modeling and mechanical simulations, and coupled fluid-mechanical analysis, we revealed that the lattice-based skeleton of the sponge *E. aspergillum* adopts the structure similar to the DDRL model with ridge structures to resolve the trade-offs among multiple loading conditions. Our results suggest that the *E. aspergillum* skeleton shows tendency of maximizing the torsional resistance, while the ridge structure provides enhanced radial stiffening and permeability with sacrifice of other mechanical resistances (compression in longitudinal direction, bending, and torsion). The quantitative analysis in this work provides further understanding of the mechanical and hydrodynamic properties of the

skeletal lattice of *E. aspergillum* sponge, which also provides useful information in the design of multifunctional low-density tubular lattice structure.

Chapter 7 Multiscale functionally graded lattice and mechanics of the sea urchin spine of *Heterocentrotus mammillatus*

This work was published as a regular journal article of a work series:

1. T. Yang, Z. Wu, H. Chen, Y. Zhu, L. Li, Quantitative 3D structural analysis of the cellular microstructures of sea urchin spines (I): Methodology, *Acta Biomaterialia*, **107**, 204-217 (2020)[83].

2. H. Chen, T. Yang, Z. Wu, Y. Zhu, L. Li, Quantitative 3D structural analysis of the cellular microstructures of sea urchin spines (II): Large scale analysis, *Acta Biomaterialia* **107**, 218-231 (2020)[2].

Biological cellular materials have been a valuable source of inspiration for the design of lightweight engineering structures. In this process, a quantitative understanding of the biological cellular materials from the individual branch and node level to the global network level in 3D is required. Here we adopt a multiscale cellular network analysis workflow to analyze the biomineralized porous structure of sea urchin spines from the species *Heterocentrotus mammillatus* over a large volume (*ca.* 0.32mm^3). A comprehensive set of structural descriptors is utilized to quantitatively delineate the long-range microstructural variation from the spine center to the edge region. Our analysis shows that the branches gradually elongate (~50% increase) and thicken (~100% increase) from the spine center to edge, which dictates the spatial variation of relative density (from ~12% to ~40%). The branch morphology and network organization patterns also vary gradually with their positions and orientations. Additionally, the analysis of the cellular network of individual septa provides the interconnection characteristics between adjacent

septa, which are the primary structural motifs used for the construction of the cellular structure in the edge region. In summary, the large-volume stereom of the sea urchin spine exhibits a multiscale functionally graded structure. Moreover, combining the extracted long-range cellular network and finite element simulations allows us to efficiently examine the spatial and orientational dependence of local effective Young's modulus across the spine's radius. The structural-mechanical analysis here sheds light on the multiscale functionally graded structures of *H. mammillatus'* porous spines, which could provide important insights for the design and modeling of lightweight yet strong and damage-tolerant cellular lattices.

7.1. Introduction

Many organisms construct their structural skeletons based on porous microstructures, such as wood[153,175,176], trabecular bone[177–179], and echinoderms' skeletal elements (*e.g.*, ossicles in starfish, spines and tests in sea urchins)[81,180]. These materials usually possess unique combinations of structural and mechanical properties such as low density, controlled anisotropy, high strength and damage tolerance via their judicious control over the spatial distribution of solid materials across multiple length scales. In particular, the biomineralized skeletal elements in echinoderms, which are composed of highly porous magnesium calcite meshwork (mineral content > 99 wt%)[84], known as stereom, represent a unique group of natural cellular materials because of their characteristic morphology and mechanical properties[87,90,95]. The echinoderms' stereom structures show vast variations among different species, within different skeletal elements in an individual animal, and even within the same skeletal element[88,89,181]. A quantitative description and understanding of the 3D porous structure from the individual branch (or trabecula) and node (or interconnection) level to the global network level is required for further understanding of the mechanics and morphogenesis mechanisms of these cellular structures as well as for the development of biomimicry analogs. Ting et al. reported a multiscale cellular network analysis pipeline tailored for echinoderms' stereom structures[182]. Here, I utilize this methodology to conduct a systematic analysis of the stereom structure from the sea urchin spines from *Heterocentrotus mamillatus* (Linnaeus, 1758) over a large volume.

The sea urchin *H. mamillatus* has been a popular model system for studying the structural and mechanical properties of sea urchin spines, which is mainly motivated by

its remarkable damage tolerance through the "graceful failure" behavior[84,85,95,183–185]. This lightweight material also achieves excellent penetration resistance under local indentation loading[95,186,187]. The multiscale structures of *H. mamillatus* spines, similar to other echinoderms' stereoms, have been elucidated by numerous studies through 2D imaging analysis primarily based on scanning electron microscopy (SEM)[88,89,181,184,188]. Following Smith's classification on stereom's structural types[87,181], the stereom structures in *H. mamillatus*' spines have been qualitatively described as the laminar stereom with a multilayered construction in the center region (also known as medulla), the labyrinthic stereom with radial alignment (known as septa) between center and growth rings, which are the micro-perforate stereom with a much lower porosity[84,85,87,95]. The *H. mamillatus* spines thus represent one of the most delicately architected stereom structures among all sea urchin species. Based on 2D SEM images, the organization of branches and pores has been described by several parameters such as pore diameter and branch size, suggesting a certain degree of orderliness in the stereom of different regions[80,89].

Previous 2D-based investigations on *H. mamillatus*' stereom structures are inadequate to provide quantitative information of their 3D morphology of individual branches and nodes as well as the porous network organization at the skeletal level. Recent 3D analysis based on X-ray micro-computed tomography (μ-CT) provides qualitative visualization and characterization of internal 3D microstructures (*e.g.*, smooth transition between branches, branch profile, etc.) of echinoderms' stereoms[91,94,189,190]; however, the quantitative analysis in 3D has often been limited to porosity estimation or small volume analysis[88,90]. Here a quantitative cellular network analysis of the *H. mamillatus'* spines at skeletal level was conducted via a customized methodology. Compared to previous

investigations, a more comprehensive set of structural descriptors was adopted to elucidate both short- and long-range structural characteristics in 3D of the *H. mamillatus* spines, including i) node characteristics; ii) inter-branch angle; iii) curved branch length and node-to-node branch length (*i.e.*, branch distance); iv) tortuosity; v) average, minimum, and central branch thicknesses; vi) branch morphology; vii) branch orientation; and viii) ring structure[90]. The correlations between branch location and parameters i and iii ~ v, as well as the correlations between branch orientation and structural parameters i and iii ~ v were investigated. Moreover, structural analysis was performed on isolated septum to investigate the interconnection characteristics between adjacent septa. The cellular network information obtained from this multiscale analysis was also used to investigate the spatial variation of the mechanical properties across the entire volume of interest via finite element modeling of the extracted cellular networks.

7.2. Materials and Methods

Specimens and electron microscopy: Dried *H. mamillatus* spine specimens were purchased from Etsy Inc. The cylindrical shape of the spines measures 1.0-1.5 cm in diameter and *ca.* 10 cm in length (**Fig. 7.1a,b**). A cylindrical coordinate system is used throughout this work, where L, R, and C represent the spines' longitudinal, radial, and circumferential directions, respectively. SEM images were obtained from FEI Quanta 600 FEG with a typical working distance of 8 mm and an acceleration voltage of 5 keV. Samples were coated with platinum/palladium (~15 nm) prior to SEM imaging.

Synchrotron-based µ-CT measurement: The synchrotron-based µ-CT measurement was conducted at the beamline 2-BM at the Advanced Photon Source (APS), Argonne National Laboratory. A monochromatic beam (centered at 27.4 keV, corresponding to a wavelength of 0.45 Å) was used. 1500 projection images were acquired over a 180-degree rotation for each tomography scan with a rotation speed of 0.5 degree/second. The projection images were collected by using a PCO Edge high speed CMOS detector (2560 × 1300 pixels). The imaging system was equipped with 5× and 10× long-working-distance objective lenses, resulting in an isotropic voxel size of 1.3 µm and 0.65 µm, with corresponding fields of view of 3.33 × 1.69 mm and 1.66 × 1.38 mm, respectively. For the data presented in this work, the 5× objective lens was used in order to cover large scan volumes. The specimens were elongated blocks (~2 mm, ~2 mm, ~10 mm in L, C, and R directions, respectively) cut along the radial direction from the spine center to the periphery with a low-speed diamond saw (colored box, **Fig. 7.1b**). Consecutive scans along the R direction with ~90 µm overlaps between adjacent scans were acquired. The tomography data were then stitched together using Fiji/ImageJ to obtain single continuous 3D dataset for the entire rectangular block[191]. Multiple specimens were scanned but the data analysis presented in this work is based on a single dataset.

Multiscale cellular network analysis: The collected projection images were first reconstructed by using the open source software TomoPy[192], which utilizes a standard Fourier grid reconstruction algorithm, one of the back projection methods[193]. The reconstructed data was subsequently segmented by using another open source, machine learning-based software ilastik[139]. The segmentation program was trained by manually

labeling some regions of the mineral phase in sea urchin spines. Then the image stack was automatically labeled by Gaussian filters and Random Forest with 100 trees classifier[194]. The final stitched data and corresponding 3D rendering of the reconstructed volume for analysis is shown in **Fig. 7.2**.

Next, a customized analysis pipeline was utilized to conduct the quantitative characterization of the cellular network from the spine center to edge[182]. This pipeline includes skeletonization, network cleaning and registration, and multiscale feature extraction and analysis[182]. In particular, the network cleaning step based on iterative branch trimming and node merging is necessary to eliminate dangling branches and node clusters, which is a significant issue for stereom-like structures with short and thick branches. Herein 5.9 μm and 6.5 μm were used as the merging distances for center (yellow area, sub-volumes 1~3) and edge (cyan area, sub-volumes 4~10, **Fig. 7.2a,d,e**) regions, respectively, in the skeleton trimming step. For the analysis here, the branches and nodes within 19.5 μm from the periphery of the analyzed volume were removed to void edge effects such as incomplete branches.

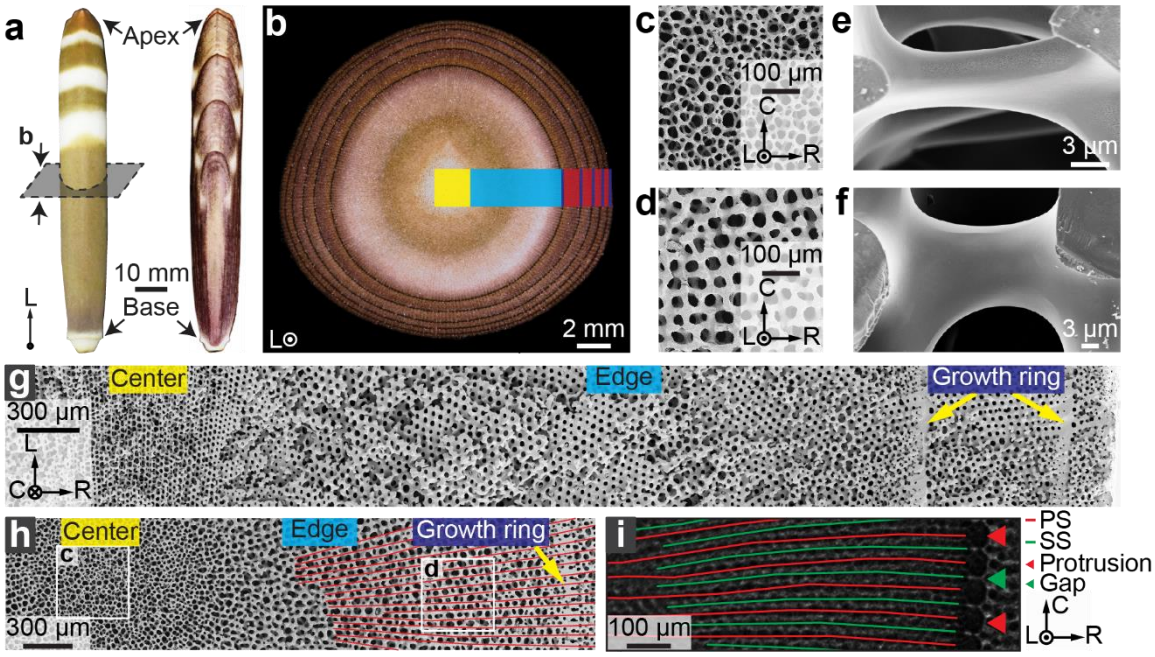


Fig. 7.1. An overview of the spine structure of *H. mamillatus*. (**a**) Optical image of the spine of *H. mamillatus* (left) and its cross-section cut along the longitudinal (L) direction (right). (**b**) Optical image of the transversely-cut cross-section of the spine (yellow area: center region; cyan area: edge region; red area: inter-growth ring stereom; blue area: growth ring). Scanning electron micrographs (SEM) images of the porous stereom in (**c**) the center region and in (**d**) the edge region with radiating septa as indicated in the white boxes in (**h**), respectively. SEM images of the representative branches (**e**) in the center region and (**f**) in the region of radiating stereom, respectively. SEM images of the cross-section of (**g**) L(longitudinal)-R(radial) plane and (**h**) R(radial)-C(circumferential) plane from the center region (left) towards the margin of the spine (right). Note that the growth rings are indicated by yellow arrows, and septa are traced by red lines. (**i**) Traces and definitions of primary septa (PS) and secondary septa (SS) based on X-ray projection images in the R-C plane.

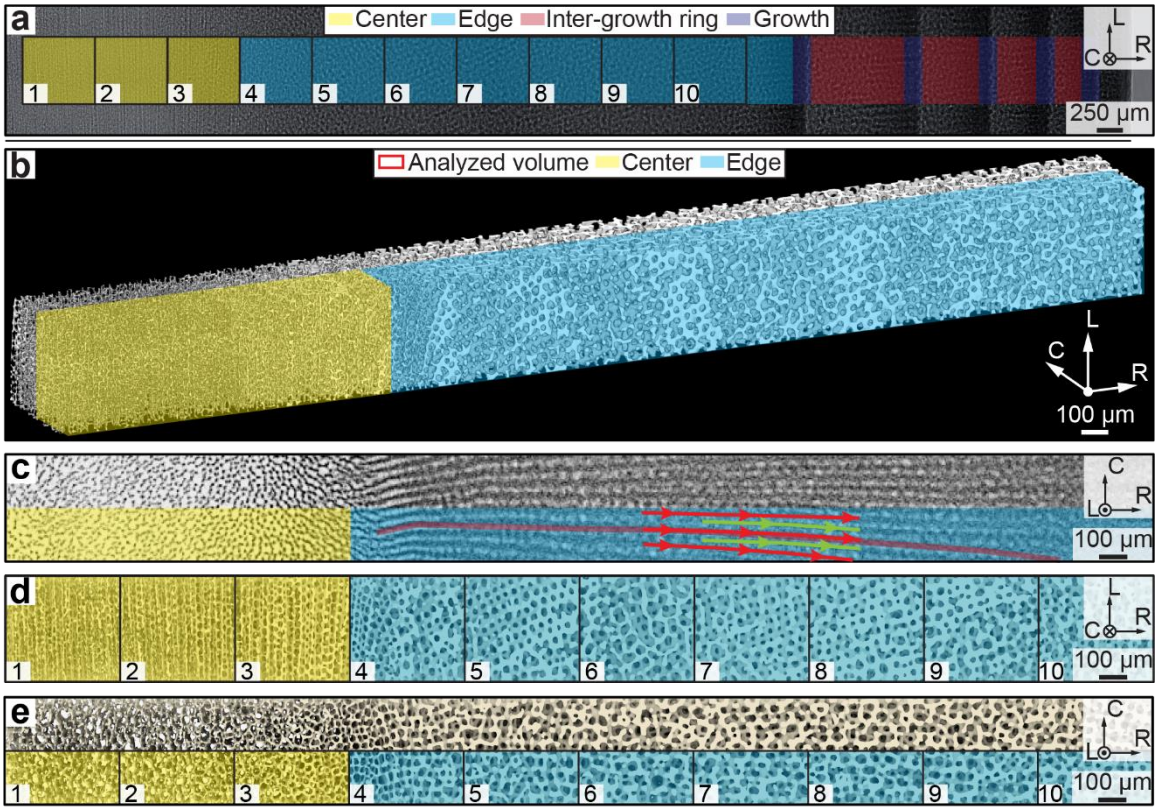


Fig. 7.2. Overview of the selected volume for structural analysis. (**a**) Synchrotron X-ray projection image of the imaged sample, which covers the volume from the spine center region to the margin of the spine: the center region (yellow boxes), the edge region (cyan boxes), the growth rings (blue boxes), and the inter-growth ring stereom (red boxes). The center and edge regions are separated in sub-volumes labeled by number 1 to 10 and used for quantitative analysis. The location and orientation of this sample is shown in Fig. 1B. (**b**) Volume rendering of the fully reconstructed stitched 3D volume with center and edge region differentiated (red box: analyzed volume). (**c**) X-ray projection image of the analyzed volume in the R-C plane. The thick red line indicates a representative septum for analysis. The red and green streamlines represent the primary and secondary septa, respectively. Volume renderings of the (**d**) L-R and (**e**) R-C cross-

section of the cut strip (area shaded with yellow and cyan: center and edge regions, respectively, which were used for analysis).

For the multiscale feature analysis based on the extracted cellular network, a comprehensive set of structural descriptors were used as defined in **Table 7.1** and **Fig. 7.3**. The detailed definitions can be found in this reference[83]. In particular, to better account for the large branch morphology variation from the spine center to the edge region, an even fourth-order polynomial was used here:

$$t_i(x_i)/t_{min} = (a((x_i - x_{min})/l)^2 + 1)^2 \qquad (7.2.1),$$

where x_i is the coordinate of the location *i* measured from one end of the branch; t_i is the thickness at location *i*; t_{min} is the minimum thickness of the branch; x_{min} is the coordinate at t_{min}; l is the branch length; and a is the fitting parameter (**Fig. 7.3**). Profiling functions with an even fourth-order polynomial has also been used for fitting branch thickness of synthetic open-cell foams[195–197]. Another modification is related to the ring detection algorithm[83]. The ring type is specified by the number of branches in a ring, such as 4-B, 5-B, 6-B, and 7-B rings. The centroids of the rings were calculated and considered as the locations of the rings. Here we carried out a plane fitting for the detected rings to evaluate the flatness of rings, where the method of linear least squares was used to calculate coefficient of determination (R^2) of the fitting. The fitting equation is as follow:

$$aX + bY + cZ + d = 0 \qquad (7.2.2),$$

where *a*, *b*, *c*, and *d*, are coefficients of the 3D plane equation, *X*, *Y*, and *Z* denote the coordinates of the points on the branch in L, C, and R direction. Eq. (7.2.2) was arranged

into $F = -\frac{a}{c}X - \frac{b}{c}Y - \frac{d}{c}$, where F is the fitted value of Z. Eq. (7.2.3) shows the calculation of R^2.

$$R^2 = 1 - \frac{SS_{res}}{SS_{tot}} \qquad (7.2.3),$$

where $SS_{res} = \sum_i (F_i - \bar{Z})^2$ is the explained sum of squares, $SS_{tot} = \sum_i (Z_i - \bar{Z})^2$ is the total sum of squares. F_i represents the *i*-th fitted value of the Z, Z_i is the i-th data of the actual Z coordinate and $\bar{Z}$ is the average value of all actual Z coordinate. The detected rings with $R^2 \geq 0.5$ (*i.e.*, relatively flat rings) were selected for analysis here. Furthermore, the rings with a higher number of branches (higher-B rings) were neglected if all nodes of the rings with a lower number of branches (lower-B rings) overlapped with the nodes of the corresponding higher-B rings.

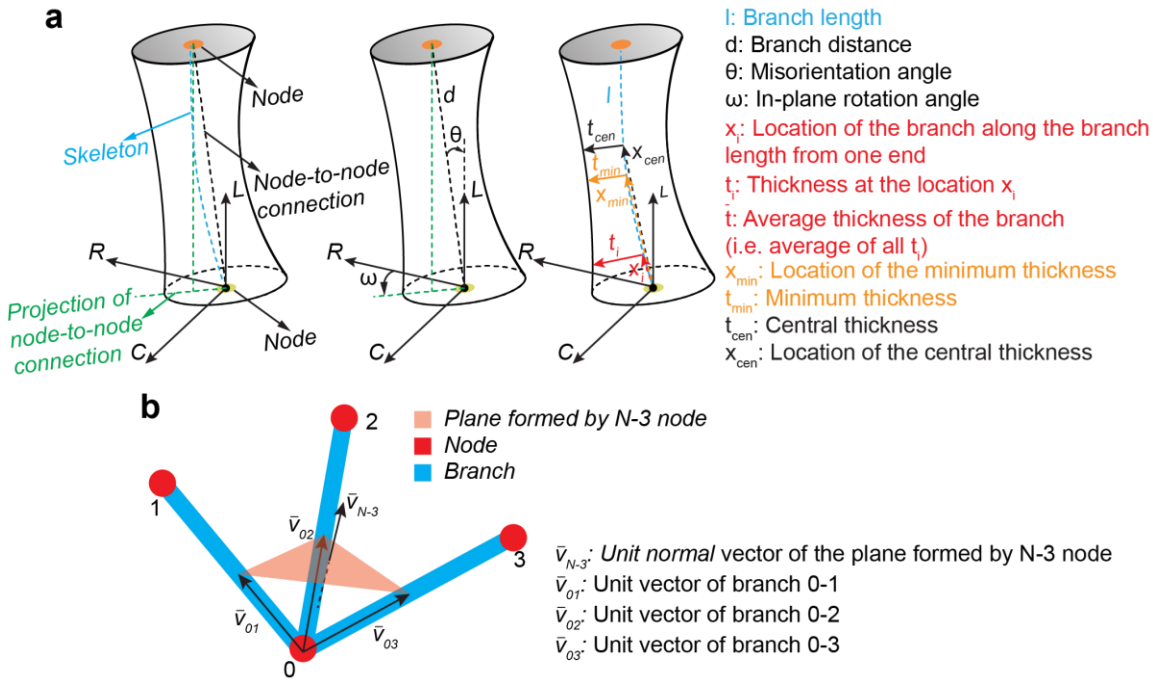


Fig. 7.3. Definition of parameters and simulation setup. (**a**) Definition of the branch length (l), branch distance (d), misorientation angle (θ), in-plane rotation angle (ω), and parameters for Equation 1. (**b**) Definition of the unit vector of N-3 node

Table 7.1 Illustration of each descriptor for structural analysis

Descriptor name	Explanation
Nodal configuration	The connectivity (or coordination number) of each node, N-i type with i = 3~6 denoting the coordination number;
N-3 orientation	3D orientation of the normal of the plane formed by a N-3 node;
Branch length	The length of the curved path between two nodes (l);
Branch distance	The Euclidean distance between two nodes (d);
Tortuosity	The ratio of branch length to branch distance (l/d);
Inter-branch angle	The angle between two branches at each N-3 or N-4 node (γ);
Branch thickness	The average ($\bar{t}$), minimum (t_{min}), and central thicknesses (t_{cen}) or the thickness at different location of a branch (t_i);
Branch morphology	The profile of the branch surface which is quantitatively described by an even 4-th order polynomial;
Branch orientation	The orientation of branch about principal axes of the spine, θ denotes the angle between branch and L

	direction, ω denotes the angle between projected branch on R-C plane and the R direction;
Ring structure	Loop formed by a certain number of successively connecting nodes, i-B type with i = 4~7 denoting the number of branches of a ring;
Ring size	The diameter of the fitted circle in the fitted ring plane (d_{ring}).

Finite element analysis: The registered network connectivity and branch-level information allow us to construct beam models for static analysis. Abaqus/Standard 2016 (Dassault Systems, Vélizy-Villacoublay, France) was used to conduct mechanical Finite Element (FE) analysis. Ten representative volumes (each measures 195 × 156 × 195 μm in L, C and R directions, respectively) were isolated from the ten sub-volumes for finite element analysis. The models were meshed with the Timoshenko beam element B31[198], and mesh size of 0.2 was used for all beam models. The average branch thickness of the corresponding branch obtained from the network analysis was assigned to each beam. The effective isotropic elastic modulus and the Poisson's ratio of calcite used in the simulations were 109 GPa and 0.291, respectively[199]. The model was subjected to compression by using two hypothetical rigid plates meshed with 2D discrete rigid elements. The beam elements that are within 10 μm from the plates were tied to the plates. The compression simulation was achieved by fixing the bottom plate while the top plate was only free for displacement in either L, C, or R direction with a maximum strain of 0.1%. Simulations along three principal directions (*i.e.*, the L, C, and R directions) for each sub-volume were conducted. The effective Young's modulus and stress contour were obtained from these compression simulations. Despite the potential discrepancy between the actual and simulated effective modulus due to the beam model used to represent thick and short beams in the edge region[18], the simulation results are sufficient

for a comparative study to illustrate the trend of the spatial variations in effective modulus

7.3. Results

7.3.1. Structural overview of the analyzed volume

The *H. mamillatus* spines exhibit an intricate spatial control in their porous microstructure from the spine center to edge, as qualitatively summarized in **Fig. 7.1** and **Fig. 7.2**. Here I broadly divide the cross section of the spine into the following four structural regions: 1) the center region, 2) the edge region with radiating septa, 3) the growth rings, and 4) the inter-growth ring stereom (**Fig. 7.1b,g,h** and **7.2a**). The center region is usually characterized by a lighter coloration shown in optical images (**Fig. 7.1b**). The stereom exhibits the Voronoi-like pattern of pores with thin branches of no preferred alignment when viewed in the R-C plane (**Fig. 7.1c,d**), consistent with the network analysis results conducted for a local volume in the center region[182]. In contrast, the edge region shows variations in pigmentation and the stereom has controlled radial alignment with much thicker branches (**Fig. 7.1e,f**). The growth rings are circular dense layering structures wrapping around the spines (**Fig. 7.1b,g,i** and **7.2a**)[88,200]. According to previous studies, the number of growth rings in an individual spine varies from 1 to 12, depending on the age of sea urchins[200].

This work focused the analysis on the volume from the center to the first growth ring, and the stereom beyond the first growth ring was not included, as shown in **Fig. 7.2b-c**. The reasons are two-fold. Firstly, as the stereom in the growth ring regions approaches to a fully dense structure, the current network analysis algorithm cannot accurately identify

the underlying structure. Secondly, the stereom structures in the edge region and the inter-growth ring regions appear to have the same structural organization (**Fig. 7.1g** and **7.2a**)[88]. The volume used for network analysis measures 0.390 × 0.195 × 4.193 mm in the L, C, and R directions, respectively (**Fig. 7.2b-e**). The analyzed volume was divided into 10 sub-volumes for location-dependent structural and mechanical analysis, where sub-volume 1-3 and 4-10 represent the center and edge regions, respectively (**Fig. 7.2d,e**). **Fig. 7.2d,e** show the 3D rendering of the volume of interest in L-R and R-C planes, respectively, from which the gradual change in branch morphology and size as well as the network organization can be observed.

The edge region is characterized by the radially aligned stereom, which is previously termed as the septum structure (**Fig. 7.1h,i** and **7.2c,e**)[88]. Here, the μ-CT results reveal that the septa can be further classified into two types, *i.e.*, the primary septa (PS) and secondary septa (SS) (**Fig. 7.1i** and **7.2c**). The secondary septa represent the additional septa that are later inserted between two connecting adjacent primary septa when their spacing is increased to a threshold value of *ca*. 50 μm. Based on the X-ray projection images in the R-C plane, the primary septa usually connect to the "solid protrusions" of the growth ring while the secondary septa extend to the gap between two adjacent primary septa (**Fig. 7.1i**). In the analyzed volume, sub-volume 7 marks the location of the initial insertion of one secondary septa, and sub-volume 4-6 and sub-volume 7-10 contain 4-5 and 2-3 primary septa, respectively (**Fig. 7.2c-e**). The branches connecting adjacent septa are denoted as interseptal branches (ISB).

7.3.2. Characteristics of nodes

Fig. 7.4 summarizes the node characteristics in the analyzed volume. Nodes with more than six connections (*i.e.* N-7, N-8, *etc.*), comprising only 0.2% of all nodes (N = 19,784), were not considered in the analysis as they could be artifacts resulted from the node merging. The spatial distributions of N-3, N-4, N-5 and N-6 nodes are shown in **Fig. 7.4a,b**. Without seeing the clustering of a specific node type, we inferred a uniform spatial distribution of different node types. It can be concluded that for all sub-volumes, N-3 and N-4 nodes are the dominating node types in number, and the occasional appearance of N-5 and N-6 nodes may enhance the structural stiffness and strength[17]. The center region (*ca.* 150,000 nodes/mm^3, sub-volume 1-3) has approximately twice the density of nodes as the edge region (*ca.* 60,000 nodes/mm^3, sub-volume 4-10), with the maximum density of nodes in the sub-volume 3 towards the center/edge transition followed by a significant drop (sub-volume 4) (**Fig. 7.4c**). The ratios of N-3: N-4: N-5: N-6 nodes in each volume are, however, relatively conserved in ten sub-volumes (**Fig. 7.4d**).

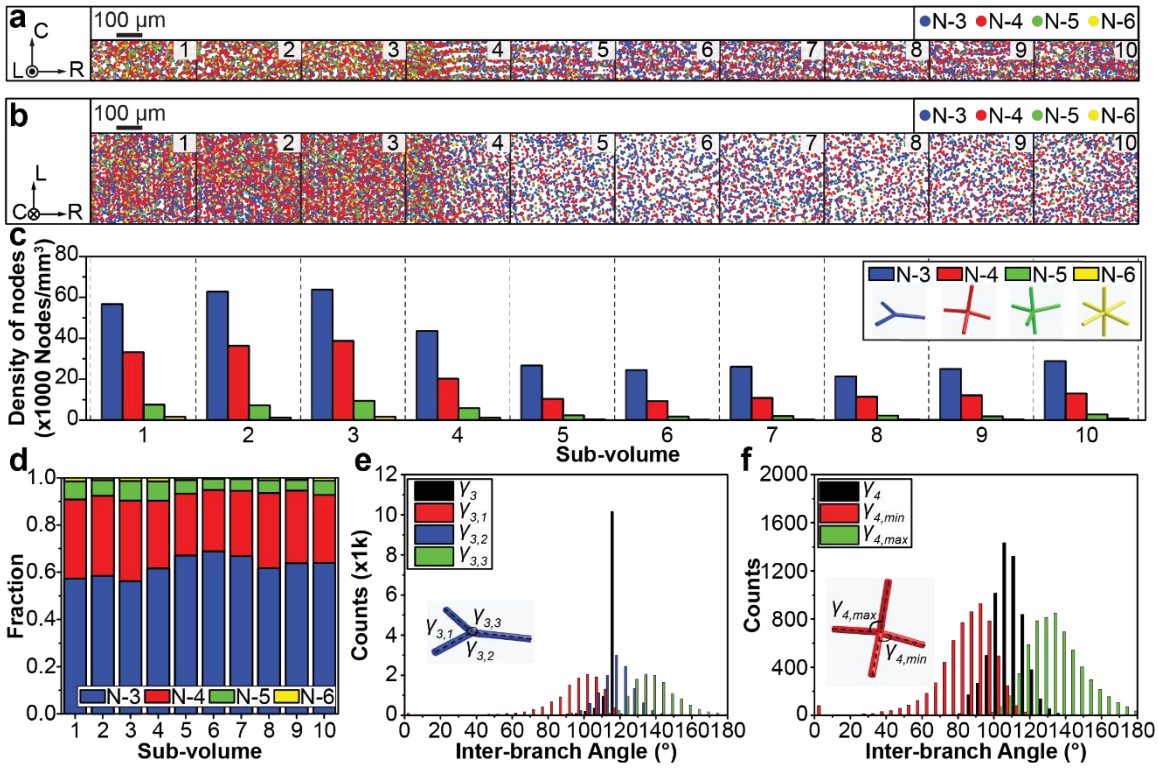


Fig. 7.4. Quantitative analysis of node characteristics in the volume of interest.

Spatial distribution of nodes colored by node types visualized on (**a**) the R-C plane and (**b**) the L-R plane, respectively. Blue: N-3 nodes; red: N-4 nodes; green: N-5 nodes; yellow: N-6 nodes. The 10 sub-volumes are labeled numerically. (**c**) The density of different node types in ten separate sub-volumes. The inset shows the schematic diagrams of the ideal N-3, -4, -5 and -6 nodes. (**d**) Number fraction of different node types in ten separate sub-volumes. (**e**) Histogram of smallest ($\gamma_{3,1}$), median ($\gamma_{3,2}$), largest ($\gamma_{3,3}$) and mean ($\gamma_3 = (\gamma_{3,1} + \gamma_{3,2} + \gamma_{3,3})/3$) inter-branch angles for N-3 nodes. Inset: schematic diagram of the inter-branch angles for a N-3 node. (**f**) Histogram of the smallest ($\gamma_{4,min}$), largest ($\gamma_{4,max}$), and mean (γ_4) inter-branch angles for N-4 nodes. Inset: schematic diagram of the inter-branch angles for a N-4 node

We correlated the results of node characteristics with the X-ray projection images of the *H. mammillatus* spine where the primary septa, secondary septa, and interseptal branches can be clearly distinguished (**Fig. 7.5**). As expected, in the sub-volume 4 with no secondary septa, the nodes are predominantly located on the primary septa when viewed in the R-C plane. In contrast, the distribution of nodes is much more random and uniform in the sub-volume 7 due to the insertion of secondary septa.

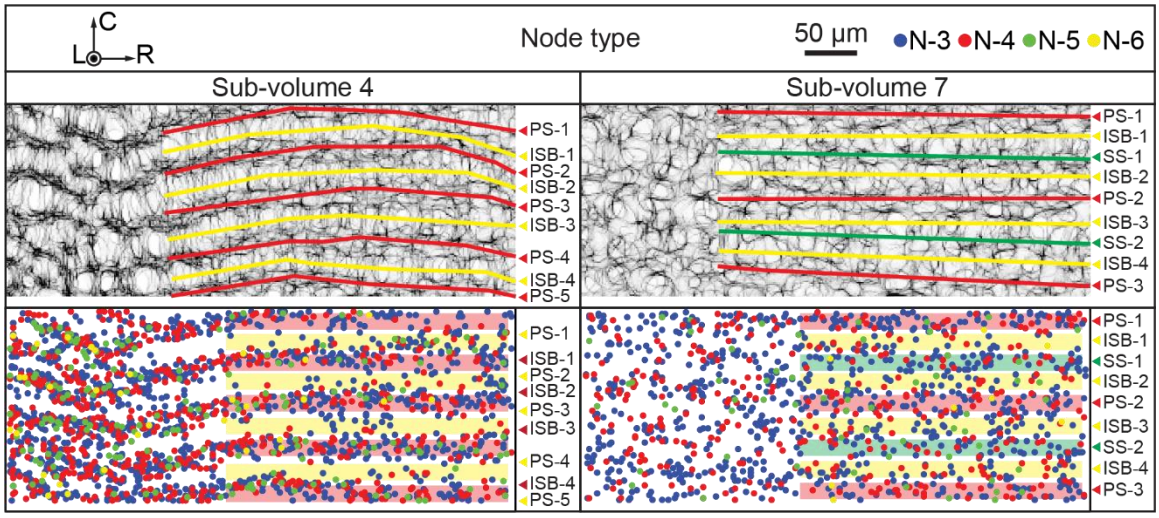


Fig. 7.5. Zoomed-in view of the distribution of nodes on R-C plane in sub-volumes 4 and 7. Red arrow & red line: primary septa (PS); green arrow & green line: secondary septa (SS); yellow arrow & yellow line: interseptal branch (ISB). PS, SS, AND ISB are shaded in red, green, and yellow, respectively.

We also performed analysis on the inter-branch angles for the N-3 and N-4 nodes of the entire volume (**Fig. 7.4e,f**). The mean and standard deviation for the smallest, median, and largest inter-branch angles for N-3 nodes are obtained as 95.90° ± 16.44°, 117.92° ± 10.96°, and 137.98° ± 13.15°, respectively (N = 12,005). The mean and standard

deviation of all inter-branch angles of N-3 nodes is 117.27° ± 5.78°, which is close to the inter-branch angle of the ideal 3-branch node (*i.e.*, 120°). For N-4 nodes, the smallest and largest inter-branch angles are 84.13° ± 17.28° and 133.17°±14.92°, respectively (N = 6,166). The mean and standard deviation of all inter-branch angles of N-4 nodes is 108.69° ± 9.11°, which approaches to the bond angle of the idealized diamond lattice (*i.e.*, 109.5°).

A detailed analysis of the planarity index and orientation distribution for N-3 nodes was summarized in **Fig. 7.6**. The planarity index of an N-3 node is defined as the unitless distance between the node and the plane constructed by three unit vectors along the connecting branches starting from this node[83,201]. The spatial distribution of the N-3 nodes colored by their corresponding planarity indices is presented in **Fig. 7.6a,b**, where location dependent variation was not observed. 95% of the planarity indices is less than 0.3, which is within 18º offset from an ideal flat plane. The result agrees with the average inter-branch angle measurements of the N-3 nodes and demonstrates that the branches connecting to an N-3 node reside nearly in a common plane. The orientation distribution of the N-3 nodes with their corresponding planarity indices for each sub-volume is shown in **Fig. 7.6c**. For orientation of N-3 nodes, θ and ω are defined as the angle between the normal of the plane formed by N-3 node (*i.e.*, $\bar{v}_{N-3}$, **Fig. 7.3b**) and L direction and the angle between the projection of $\bar{v}_{N-3}$ on R-C plane and R direction, respectively (see details in **Fig. 7.3b**). A clear gradual transition is observed: in the center region (sub-volume 1-3), the N-3 nodes exhibit a preferred alignment with $\theta \approx 0^{\circ}$ or 90º, whereas the edge region exhibits no preferred distribution of θ angles; in contrast, the uniform distribution in ω is maintained throughout the entire volume (**Fig. 7.6c**). This result

indicates that in the center region, the N-3 nodes preferably face along or perpendicular to the L direction, and for the N-3 nodes facing perpendicular to the L direction, they are randomly pointed in the R-C plane.

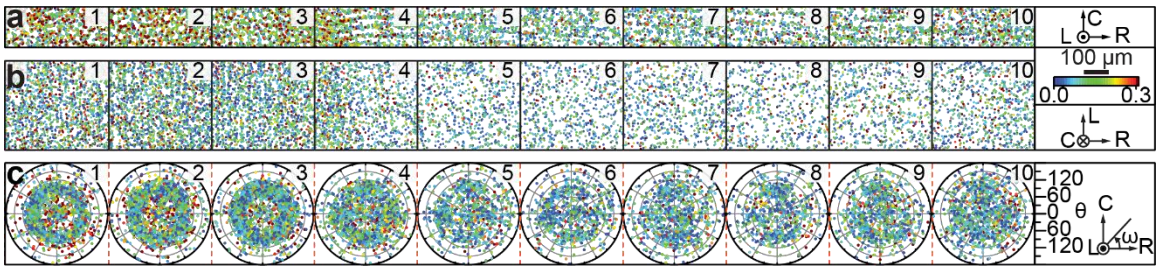


Fig. 7.6. Planarity and orientation of N-3 nodes. Spatial distribution of the N-3 nodes colored by their corresponding planarity indices visualized on (**a**) the R-C plane and (**b**) the L-R plane, respectively. (**c**) Orientation of N-3 nodes versus planarity index of the ten sub-volumes

7.3.3. Characteristics of branches

As qualitatively demonstrated in **Fig. 7.1d,f**, the thickness (*i.e.*, radius), length, and morphology of the branches vary significantly in different regions along the R direction. With the cellular network analysis, we quantified the variations on branch length and orientation (**Fig. 7.7**), branch distance (**Fig. 7.8**), tortuosity (**Fig. 7.9**), branch thickness (**Fig. 7.11-7.13**) and branch morphology (**Fig. 7.14** and **7.15**) for the analyzed volume. A detailed analysis is also provided for the center/edge transition region (sub-volume 4) and the region with the initial insertion of secondary septa (sub-volume 7) (**Fig. 7.10**).

Spatial distribution and alignment of branch: The spatial distribution of branches colored by their corresponding branch lengths in the entire volume is shown in **Fig.**

7.7a,b (N = 32,573). It is evident that the density of branches in the center (*ca*. 250,000 branches/mm^3, sub-volume 1-3) is as more than twice as that in the edge region (*ca*. 100,000 branches/mm^3, sub-volume 4-10) (**Fig. 7.7a-d**), which is the result of the high density of nodes in the center region (**Fig. 7.4a-c**). The orientation of branches exhibits clear difference in the center and edge regions (**Fig. 7.7c**). More specifically, the angle θ as defined in **Fig. 7.3** for the branches in the center (sub-volume 1-3) mostly approaches either to 0° or 90°, which indicates that most branches orient approximately parallel or perpendicular to the L direction (**Fig. 7.7c**). This result is consistent with the qualitative observation of preferred alignment of branches in the SEM image (**Fig. 7.1g**), 3D reconstruction (**Fig. 7.2d**), and the detailed analysis results performed in a small volume close to the center region[83]. Such orderliness of branch orientations is not observed in the edge region (sub-volume 4-10, **Fig. 7.7c**).

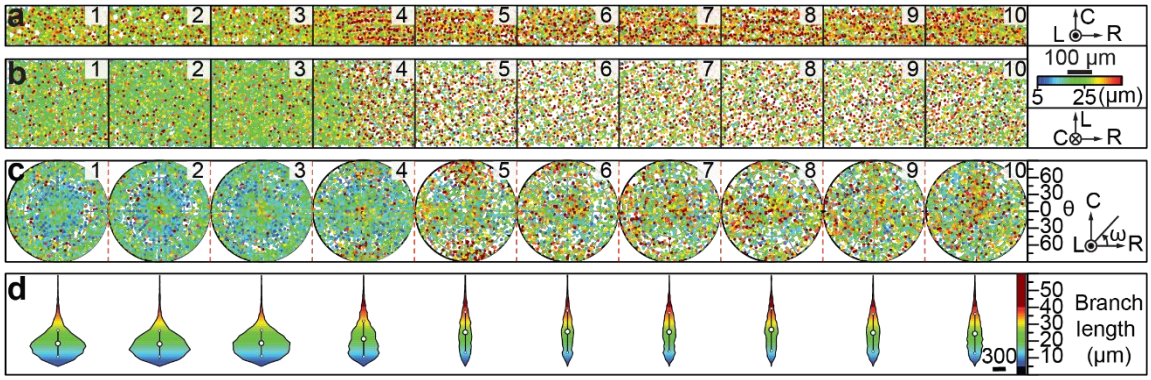


Fig. 7.7. Quantitative analysis of branch length. Spatial distribution of branches colored by branch length visualized on (**a**) the R-C plane and (**b**) the L-R plane, respectively. (**c**) Orientation of branches versus branch length of the ten separate sub-volumes. (**d**) Violin plots (mirrored histograms) of branch length for each sub-volume, where mean values and standard deviations are indicated as error bars. The number of

data points corresponding to a given value range of the branch length is indicated by the scale bar on the lower right corner.

Length, distance, and tortuosity of branch: Variation in the mean branch length (l) is observed in the sea urchin spine with a ~50% increase in the edge region (21-27 μm, sub-volume 4-10) as compared to the center region (18-19μm, sub-volume 1-3) (**Fig. 7.7d**). Following the similar trend of l, the Euclidean distance between two connecting nodes (d) is ~50% higher in the edge region (18-22 μm, sub-volume 4-10) than in the center region (15-16μm, sub-volume 1-3) (**Fig. 7.8d**). The tortuosity, defined as the ratio between branch length and branch distance (l/d), is therefore highly conserved throughout the entire volume and no spatial or orientational dependencies were observed (**Fig. 7.9**). 90% of the tortuosity values are smaller than 1.3, indicating that the majority of branches are only slightly curved. We note that the branches on the primary septa are usually shorter than the interseptal branches connecting two adjacent primary septa (sub-volume 4), while the introduction of secondary septa in sub-volume 7 reduces this difference (**Fig. 7.10a,b**). This feature can be also observed in the branch length-orientation plots, where the yellow and red data points in the sub-volume 4 and 5 are concentrated to the branches with ω close to 90º and 270º and θ towards 90º (**Fig. 7.7c**).

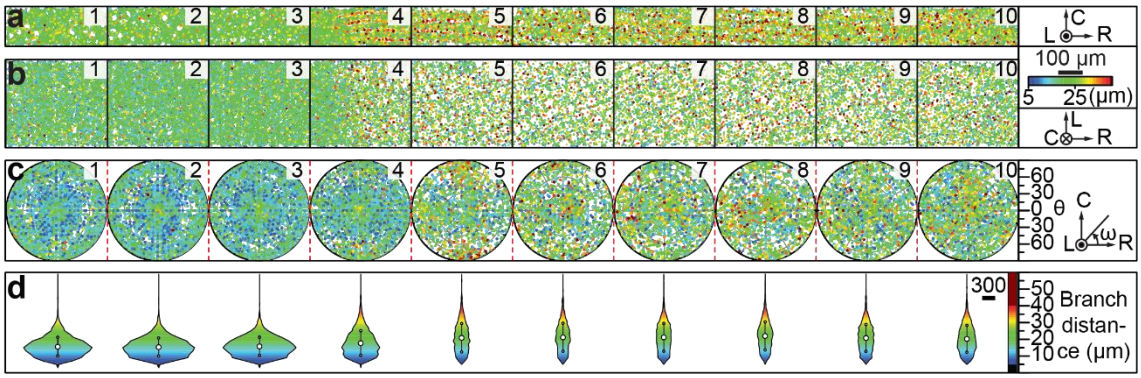


Fig. 7.8. Quantitative analysis of branch distance. Spatial distribution of branches colored by branch distance visualized on (**a**) the R-C plane and (**b**) the L-R plane, respectively. (**c**) Orientation of branches versus branch distance of the ten separate sub-volumes. (**d**) Violin plots (mirrored histograms) of branch distance for each sub-volume, where mean values and standard deviations are indicated as error bars. The number of data points corresponding to a given value range of the branch length is indicated by the scale bar on the lower right corner.

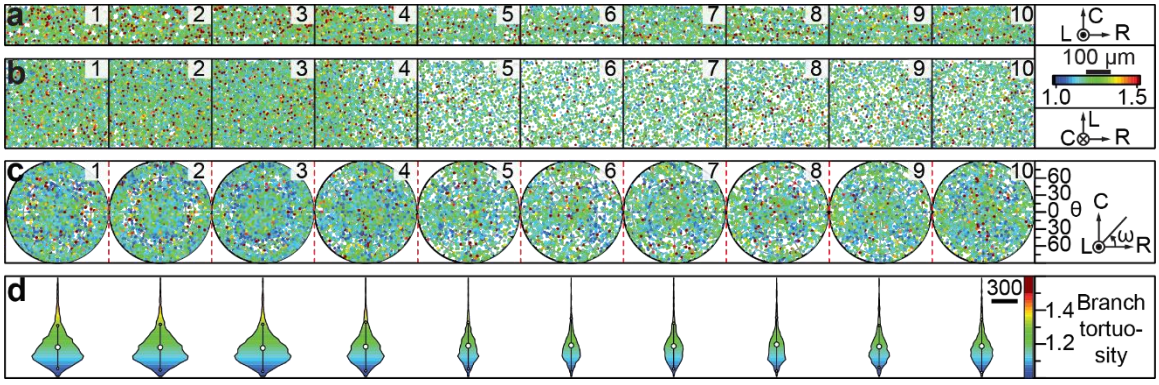


Fig. 7.9. Quantitative analysis of branch tortuosity. Spatial distribution of branches colored by branch tortuosity visualized on (**a**) the R-C plane and (**b**) the L-R plane, respectively. (**c**) Orientation of branches versus branch tortuosity of ten separate sub-volumes. (**d**) Violin plots (mirrored histograms) of branch tortuosity for each sub-

volume, where mean values and standard deviations are indicated as error bars. The number of data points corresponding to a given value range of the branch length is indicated by the scale bar on the lower right corner.

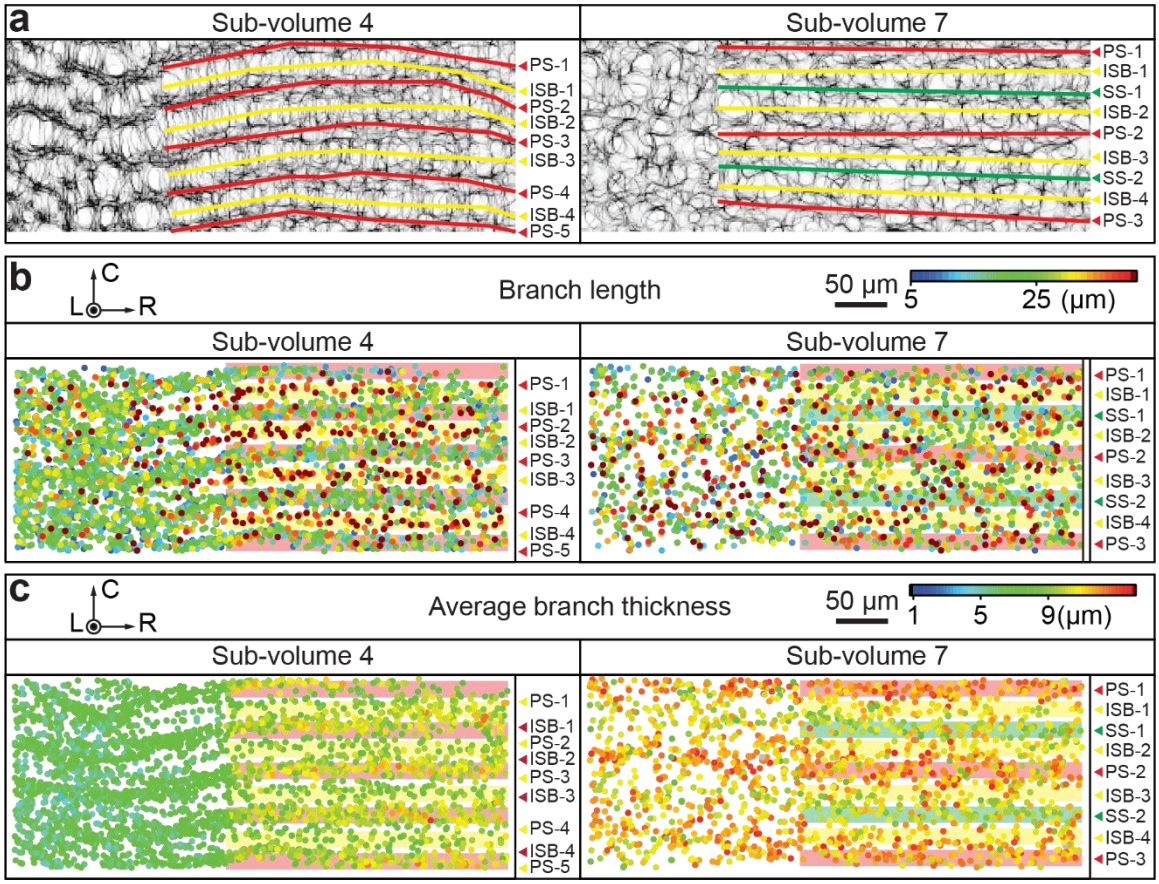


Fig. 7.10. Detailed structural analysis on the sub-volumes 4 and 7. (**a**) Trace of septa and interseptal branches based on the volumetric views on the R-C plane. (Red arrow & red line: primary septa; green arrow & green line: secondary septa; yellow arrow & yellow line: interseptal branch). Spatial distribution of branches colored by (**b**) branch length and (**c**) average branch thickness visualized on the R-C plane, respectively. The backgrounds in (**b**) and (**c**) are shaded by PS (red), SS (green), and ISB (yellow), respectively.

Average, minimum, and central branch thickness: **Fig. 7.11**, **Fig. 7.12**, and **Fig. 7.13** summarize the mapping of average, minimum, and central branch thickness, respectively, in relation to the branch location and orientation. Only branches with tortuosity less than 2 and length within 5 μm to 40 μm were selected (98.6% of all branches) for branch thickness analysis to avoid artifacts (*e.g.*, excessively long or curved branches) and inaccurate fitting of branch morphology. The following trends are observed:

i) the mean values of each measurement of thickness in the edge region (*e.g.*, average thickness, 8-11 μm, sub-volume 4-10) are approximately twice as those in the center region (*e.g.*, average thickness, 5-6 μm, sub-volume 1-3) (**Fig. 7.11-7.13**), which is consistent with the previous 2D measurement in the similar positions of the spines[89].

ii) in the center region (sub-volume 1-3), the branches aligned closely along the L direction ($\theta < 30^{o}$) are slightly thicker (colored in cyan) compared to branches with $\theta > 60^{o}$ (see **Fig. 7.11c**, **7.12c**, **7.13c** and **Table 7.2**). This is also consistent with the results conducted on a small volume close to the center region in the first paper of this work series[83].

iii) in the edge region, the thickness exhibits a wider distribution than that in the center region (**Fig. 7.11d**, **7.12d**, and **7.13d**).

iv) according to the histograms shown in **Fig. 7.12d** and **7.13d**, we found that the central thickness is on average ca. 0.5 μm thicker than the minimal thickness of a branch.

v) the branches comprising the primary septa plane are thicker than the branches connecting adjacent septa (*e.g.*, average branch thickness, 9.8 μm vs. 9.2 μm, sub-volume 4) and the branches on secondary septa (*e.g.*, average branch thickness, 11.5

μm vs. 10.5 μm, sub-volume 7) (**Fig. 7.10a,c**. Also see the detailed quantification in Section 3.5).

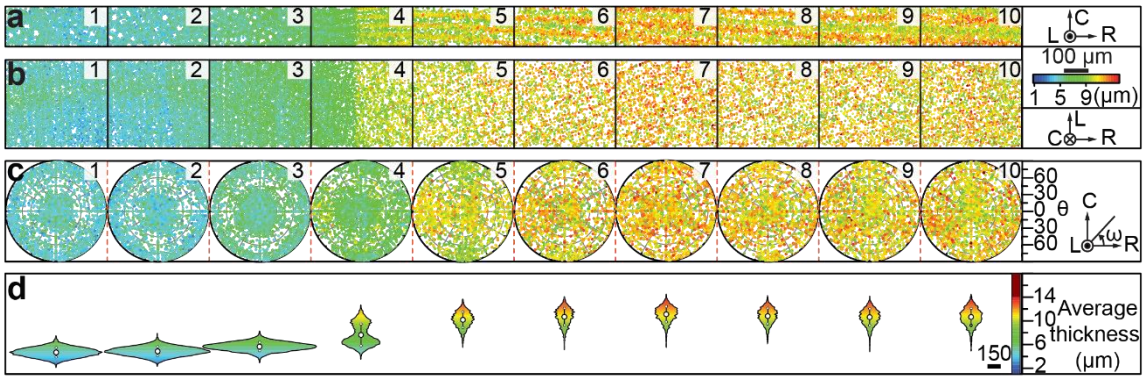


Fig. 7.11. Quantitative analysis of average branch thickness. Spatial distribution of branches colored by average thickness visualized on (**a**) the R-C plane and (**b**) the L-R plane, respectively. (**c**) Orientation of branches versus average thickness of the ten separate sub-volumes. (**d**) Violin plots (mirrored histograms) of average branch thickness for each sub-volume, where mean values and standard deviations are indicated as error bars. The number of data points corresponding to a given value range of the branch length is indicated by the scale bar on the lower right corner.

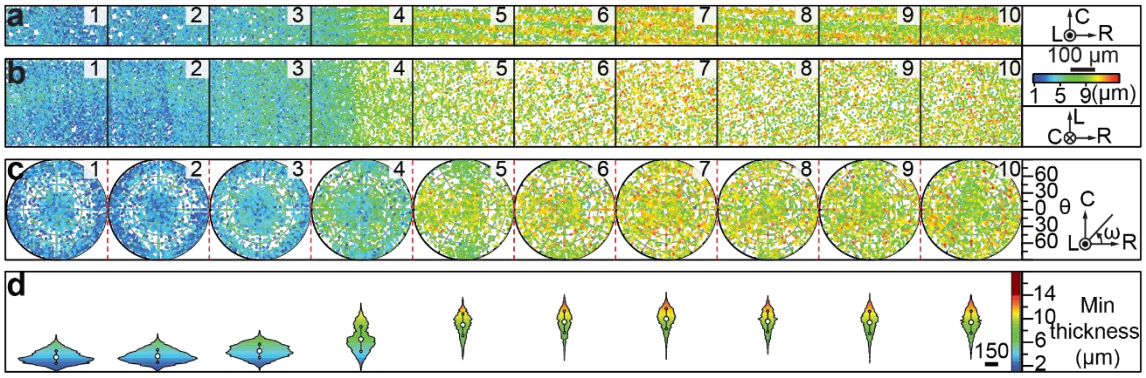


Fig. 7.12. Quantitative analysis of minimum branch thickness. Spatial distribution of branches colored by minimum branch thickness visualized on (**a**) the R-C plane and (**b**) the L-R plane, respectively. (**c**) Orientation of branches versus minimum branch thickness of ten separate sub-volumes. (**d**) Violin plots (mirrored histograms) of minimum branch thickness for each sub-volume, where mean values and standard deviations are indicated as error bars. The number of data points corresponding to a given value range of the branch length is indicated by the scale bar on the lower right corner.

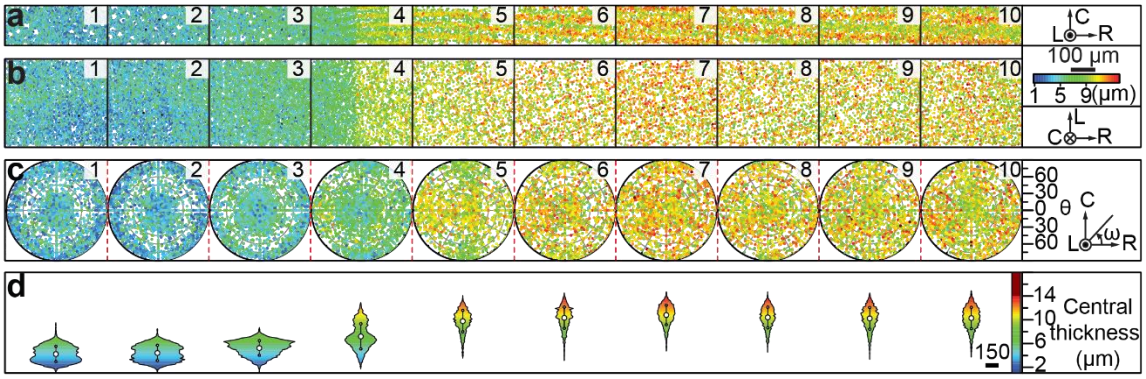


Fig. 7.13. Quantitative analysis of central branch thickness. Spatial distribution of branches colored by central branch thickness visualized on (**a**) the R-C plane and (**b**) the L-R plane, respectively. (**c**) Orientation of branches versus central branch thickness of ten separate sub-volumes. (**d**) Violin plots (mirrored histograms) of central branch thickness

for each sub-volume, where mean values and standard deviations are indicated as error bars. The number of data points corresponding to a given value range of the branch length is indicated by the scale bar on the lower right corner.

Table 7.2. Average, minimum, and center thickness of branches of θ < 30º and θ > 60º.

	Sub-volume 1		Sub-volume 2		Sub-volume 3	
	θ < 30º	θ > 60º	θ < 30º	θ > 60º	θ < 30º	θ > 60º
Average thickness ($\bar{t}$)	4.7 ± 0.8	4.6 ± 0.8	4.8 ± 0.7	4.8 ± 0.8	5.6 ± 0.6	5.6 ± 0.8
Minimum thickness (t_{min})	3.6 ± 1.0	3.3 ± 1.0	3.7 ± 0.1	3.5 ± 1.0	4.5 ± 1.1	4.4 ± 1.2
Central thickness (t_{cen})	4.2 ± 1.3	4.1 ± 1.3	4.4 ± 1.2	4.2 ± 1.3	5.2 ± 1.2	5.1 ± 1.3

Surface morphology of branch: The spatial and orientational distribution of the fitting parameter a used to describe the curviness of branches are summarized in **Fig. 7.14a-c**. The result indicates that the branches in the center region (yellow and red data points, sub-volume 1-3) are steeper (*i.e.*, larger a's) than those in the edge region (blue and cyan data points, sub-volume 4-10) (**Fig. 7.14a-c**). The variation of branch morphologies in each sub-volume can be better visualized in **Fig. 7.14d**, where all thickness data in each sub-volume were fitted together using Eq. 1. The mean of the minimum thickness and mean branch length in each sub-volume were used as t_{min} and l, respectively, in Eq. 1 to calculate the average thickness (t_i) at each location of a branch (x_i) in the corresponding sub-volume. It can be clearly observed that branches in the center region (sub-volume 1-3, **Fig. 7.14d**) have steeper curvature in surface morphologies, which is primarily due to the relatively short and thin branch in the center region (**Fig. 7.7d** and **7.11d**). In addition,

in the center region, the branches with $\theta > 60^{o}$ usually have a curvier profile than the branches with $\theta < 30^{o}$, consistent with the SEM observations (**Fig. 7.15**).

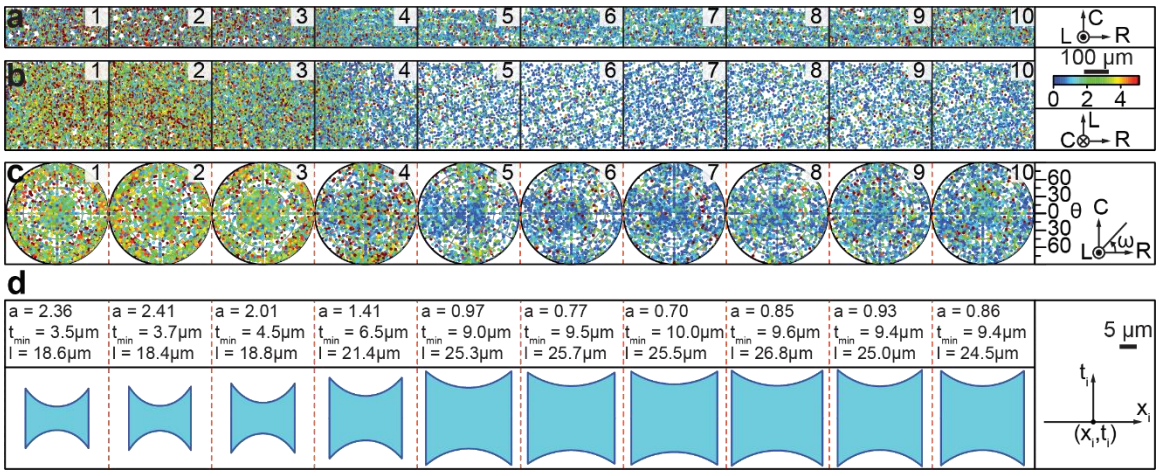


Fig. 7.14. Quantitative analysis of branch morphology. Spatial distribution of branches colored by their fitting parameters a as defined in Eq. 7.2.1 visualized on (**a**) the R-C plane and (**b**) the L-R plane, respectively. (**c**) Orientation of branches versus fitting parameters of ten separate sub-volumes. (**d**) Schematic diagrams of the branch morphology in ten separate sub-volumes along with the parameters substituted in Eq. 7.2.1.

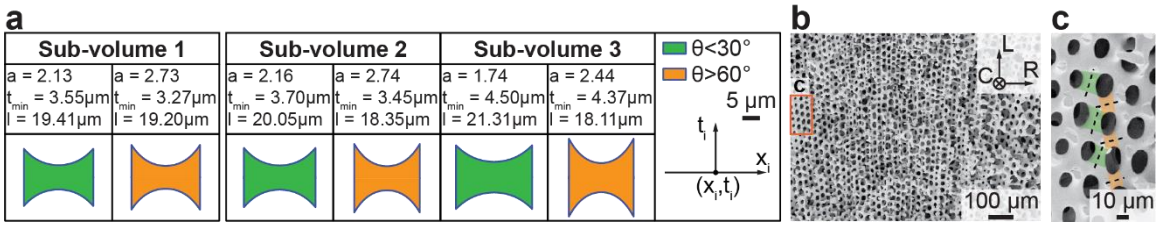


Fig. 7.15. Detailed quantitative analysis of branch morphology in the center region. (**a**) Schematic diagrams of branches closely aligned to L direction ($\theta < 30°$) and oriented

close to R-C plane ($\theta > 60°$). (**b**) SEM image of the representative center region. (**c**) SEM images of the representative branches of $\theta < 30°$ (green) and $\theta > 60°$ (orange).

7.3.4. Characteristics of ring structure

The distribution of detected ring structures for different ring types is shown in **Fig. 7.16a,b**. As a result of a relatively larger density of nodes and branches, more rings exist in the center region (*ca*. 280,000 rings/mm^3, sub-volume 1-3) than in the edge region (*ca*. 120,000 rings/mm^3, sub-volume 4-10) (**Fig. 7.16d**). In all sub-volumes, the density of 4-B, 5-B, and 6-B rings is in increasing order, while the density of 7-B rings decreases (**Fig. 7.16d**). This suggests that the density of rings with more than 7 branches may further decrease and 5-B and 6-B rings take the dominant roles in constructing the spine's stereom structure. The majority of 5-B and 6-B rings in the structure, indicating a large amount of pseudo-hexagonal pattern, is considered a result of the large number of N-3 and N-4 nodes (**Fig. 7.4c**). Besides, the fraction of 4-B rings in the center region (16%~22%, sub-volume 1~3) is higher than that in the edge region (9%~14%, sub-volume 4~10) (**Fig. 7.17**). In addition, we observed a corresponding increase in the number fraction of 7-B rings in sub-volume 7, which is attributed to the insertion of the secondary septa that may lead to the local network modifications.

The orientation of rings, described by the angle between the normal of the fitted ring plane and the L direction (θ) and the angle between the projected normal on the R-C plane and the R direction (ω), is correlated with different ring types as shown in **Fig. 7.16c**. Specifically, in the center region, a majority of the rings are oriented

approximately perpendicular to the L direction ($\theta \approx 90^{o}$) without a dependency on ω, whereas this trend is less obvious in the edge region.

Following the first paper, the size of the rings (d_{ring}) is defined as the fitted diameter of the enclosed ring circle[83]. Despite the presence of variations, the mean ring sizes of 4-B, 5-B, 6-B, and 7-B are in an increasing order (**Fig. 7.17e**). Each type of rings has approximately 1.4 times increase in size from the center to the edge region (**Fig. 7.17e**), consistent with the 2D measurements on pore sizes using SEM images[89]. The ring size of each ring type is also correlated with the ring orientation as shown in **Fig. 7.18a-d**. Throughout the entire volume and for all types of rings, the rings with their normal directions pointing towards the R direction have larger size (data points in green, yellow, and red) than those pointing to the C direction (data points in blue or cyan) (**Fig. 7.18a-d**). This is supported by the histogram of average size of rings of two separate orientations and of different types in each sub-volume (**Fig. 7.18e**), where the rings pointing towards the R direction ($-60^{o} \leq \omega \leq 60^{o}$ or $120^{o} \leq \omega \leq 240^{o}$) are ~1.3 times larger in diameter than those pointing towards the C direction ($60^{o} \leq \omega \leq 120^{o}$ or $240^{o} \leq \omega \leq 300^{o}$) (**Table 7.3**). The orientation-dependency of ring size (**Fig. 7.18a-d**) suggests that the branches comprising the septum is more closely packed than the branches connecting the adjacent septa. This is consistent with the previous quantitative analysis (**Fig. 7.10c**) where the ISB's are thinner and longer than the branches comprising the septum.

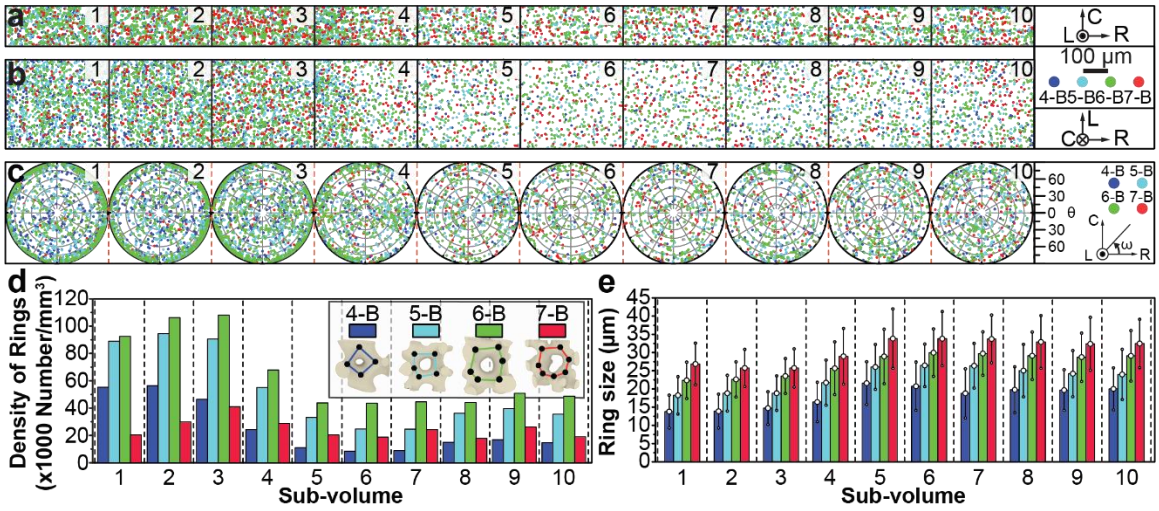


Fig. 7.16. Quantitative analysis of the ring structures. Spatial distribution of the identified rings colored by ring types visualized on (**a**) the R-C plane and (**b**) the L-R plane, respectively. Blue: 4-B rings; cyan: 5-B rings; green: 6-B rings; red: 7-B rings. (**c**) Orientation of rings versus ring types of ten separate sub-volumes. (**d**) The number density of different ring types in ten separate sub-volumes. Inset images show representative renderings of different ring types. (**e**) Histograms of the ring sizes for different ring types in ten separate sub-volumes.

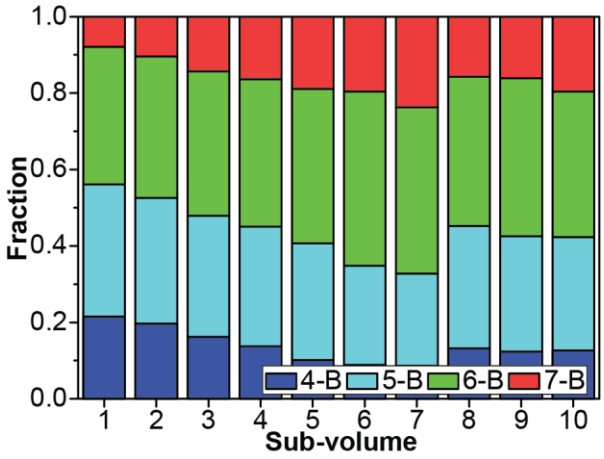


Fig. 7.17. Number fraction of each type of rings in ten separate sub-volumes.

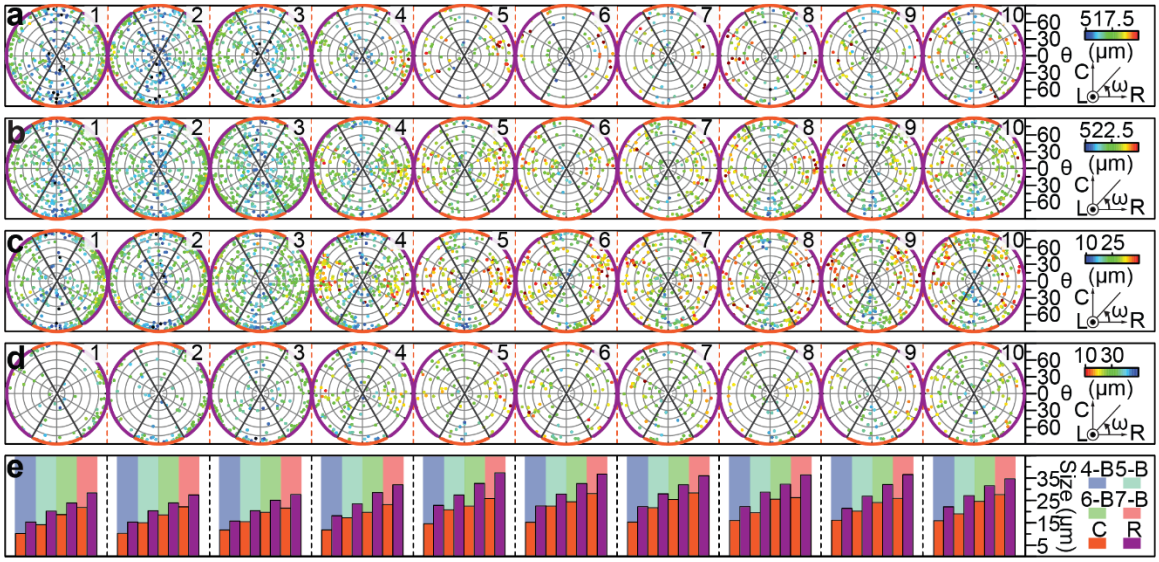


Fig. 7.18. Orientation-dependency of ring size. Branch orientation versus the ring size (d_{ring}) of (**a**) 4-B, (**b**) 5-B, (**c**) 6-B, and (**d**) 7-B rings, respectively. Note that the purple and orange lines separate the rings according to ω for size analysis. (**e**) Ring size of different types of rings oriented closely to C direction (i.e. 60º < ω < 120º or 60º < ω < 120º) and oriented closely to R direction (i.e. -60º < ω <60º or 120º < ω < 240º).

Table 7.3. Ring size (μm) of different types of rings pointing towards R and C directions.

Sub-volumes	4-B C	4-B R	5-B C	5-B R
1	10.3 ± 3.4	15.3 ± 4.0	14.1 ± 4.2	20.2 ± 4.3
2	10.3 ± 3.5	15.3 ± 4.3	15.1 ± 4.2	20.3 ± 4.3
3	11.8 ± 4.3	15.8 ± 4.1	15.5 ± 4.0	20.4 ± 4.2
4	11.9 ± 3.7	18.2 ± 4.9	17.2 ± 4.5	23.5 ± 5.9
5	14.6 ± 5.0	22.8 ± 5.1	20.8 ± 5.1	27.4 ± 5.7
6	15.2 ± 6.0	22.5 ± 5.8	22.5 ± 4.4	27.8 ± 5.7
7	15.3 ± 5.8	22.2 ± 5.7	21.7 ± 4.8	28.0 ± 5.7
8	16.0 ± 5.1	22.3 ± 5.8	19.5 ± 5.8	28.7 ± 5.5
9	16.1 ± 4.9	21.4 ± 5.1	20.2 ± 5.6	26.9 ± 5.3
10	15.9 ± 6.0	22.1 ± 4.3	19.0 ± 5.8	27.2 ± 5.5
Sub-volumes	6-B C	6-B R	7-B C	7-B R
1	18.6 ± 4.5	23.8 ± 4.4	21.9 ± 5.1	28.3 ± 5.0
2	18.5 ± 4.6	23.9 ± 4.1	22.1 ± 4.4	27.5 ± 4.5

3	19.7 ± 4.4	25.0 ± 4.1	21.5 ± 5.0	27.6 ± 4.1
4	19.7 ± 5.1	28.5 ± 6.4	23.1 ± 6.0	31.9 ± 6.6
5	22.5 ± 6.1	32.6 ± 5.5	25.8 ± 6.9	37.3 ± 5.8
6	24.4 ± 5.0	32.6 ± 5.4	28.0 ± 5.4	36.8 ± 6.5
7	25.4 ± 5.7	31.9 ± 4.8	28.3 ± 4.3	36.0 ± 6.0
8	25.6 ± 5.9	32.3 ± 5.3	26.3 ± 5.7	36.4 ± 5.2
9	24.1 ± 5.7	32.1 ± 5.0	25.9 ± 5.3	36.5 ± 5.0
10	24.6 ± 6.7	31.5 ± 5.7	27.6 ± 5.8	34.6 ± 5.8

7.3.5. Structure of septum

Septum refers to the radially aligned stereom structure, which is the primary building block of *H. mamillatus*' spines in the edge region[85,88]. As mentioned earlier, two types of septa are identified, *i.e.*, the primary (PS) and secondary (SS) septa, where the insertion of secondary septa is *ca.* 1.25 mm away from the center, corresponding to sub-volume 7 in the analyzed volume (**Fig. 7.1h** and **7.2d,e**).

In the region without the presence of secondary septa (*e.g.*, sub-volume 4), each primary septum resembles a pseudo-hexagonal pattern when viewed in the L-R plane (**Fig. 7.19**). Each septum is directly connected to the adjacent primary septa via interseptal branches. In the sub-volumes with the presence of secondary septa (*e.g.*, sub-volume 7-10), the positions of the primary septa, the secondary septa, and the interseptal branches can be clearly identified when viewed along the L direction based on X-ray projection images (**Fig. 7.20a,b**). The morphological characteristics of each structural type can be visualized by the cross-sectional reconstruction slices in the L-R plane (**Fig. 7.20c**). Again, the primary septa (PS-1, -2, and -3) resemble the pseudo-hexagonal pattern consistently, yet the secondary septa (SS-2 and -3) have a more random pattern and less connectivity of branches than the primary septa (**Fig. 7.20c**). In addition, the interseptal branches (ISB-1, -2, -3, and -4) connecting a primary septum to an adjacent

secondary septum typically exhibit circular cross sections, suggesting that these branches are primarily aligned along the C direction.

We then isolated an individual primary septum, as shown in the synchrotron X-ray projection image (**Fig. 7.2c**), and conducted a quantitative network analysis. The detected skeleton network again reveals the pseudo-hexagonal pattern of the septum structure in the background (**Fig. 7.20d**). Moreover, most of the node types are N-3 and N-4 nodes in the primary septa. **Fig. 7.20e** schematically illustrates the structures of N-3 (blue) and N-4 (red) nodes associated with the interseptal branches from a septum with an idealized hexagonal pattern. Statistical analysis on the detected node types indicates that the interseptal branches are extruded predominantly from N-3 (53%) and N-4 (36%) nodes of the septa and less from N-5 (9%) and N-6 (2%) nodes (**Fig. 7.20f**). SEM images of a primary septum with manually traced skeleton and positions of interseptal branches demonstrate consistent results with the 3D analysis (**Fig. 7.20g**). This structure is also evident by directly overlaying the cross-sectional images of a primary septa and its associated interseptal branches, where many interseptal branches are located on the branches instead of nodal points from septa (**Fig. 7.20h**). Moreover, the interseptal branches on two different sides of a septum are often dislocated from each other by extruding from different nodes of the septum, which results in the high fractions of N-3 and N-4 nodes for interseptal branches (**Fig. 7.20i**). Additionally, our quantitative analysis revealed that the interseptal branches are thinner (average thickness, 8.5 ± 1.5 μm vs. 10.8 ± 1.5 μm), longer (branch length, 29.7 ± 11.6 μm vs. 26.3 ± 13.2 μm), and slightly more curved on average (tortuosity, 1.21 ± 0.14 vs. 1.19 ± 0.15) than the branches comprising the septum.

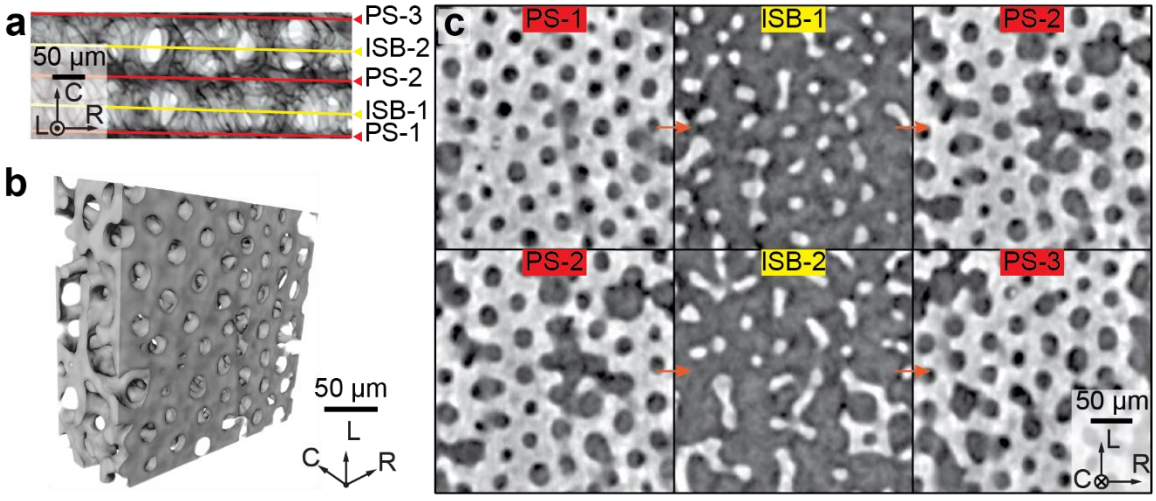


Fig. 7.19. Structural analysis of a single septum without secondary septa. (**a**) X-ray projection image of representative septa (red line & red arrow: primary septa; yellow line and yellow arrow: interseptal branch). (**b**) A representative volume in the edge region to visualize the primary septa. (**c**) A sequence of X-ray CT images to visualize the structural difference among primary septa and interseptal branches

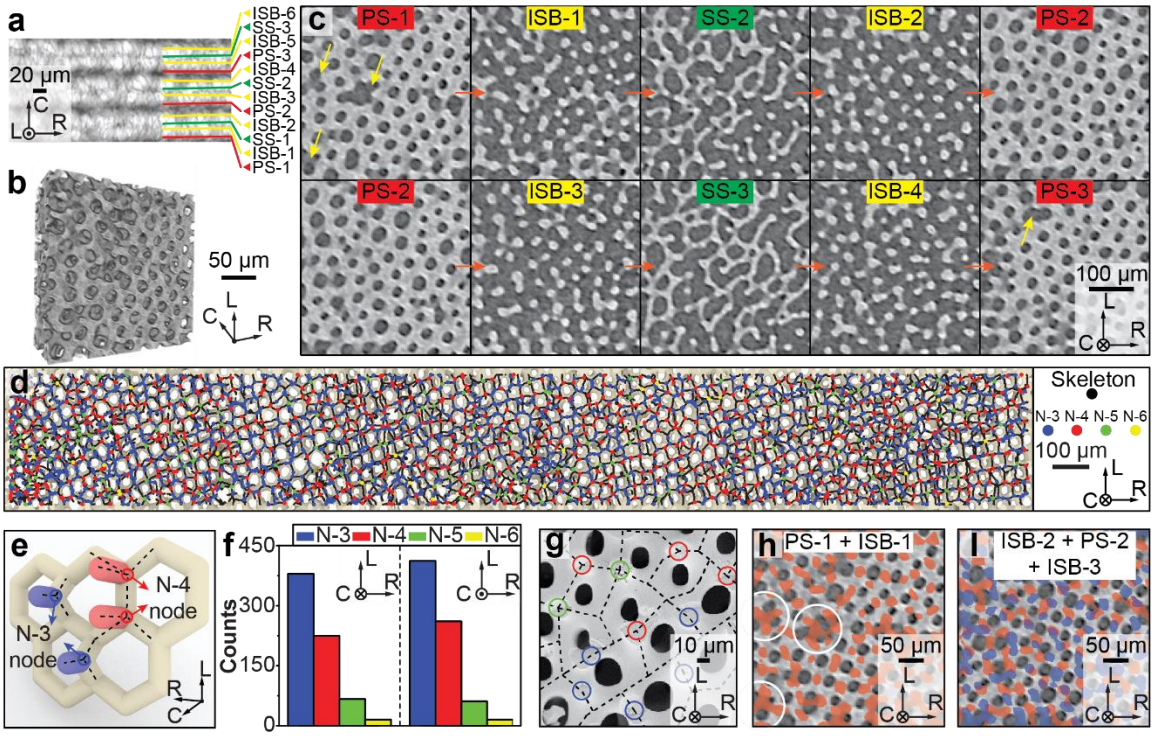


Fig. 7.20. Structural analysis of septa. (**a**) A representative X-ray projection image taken from the edge region, illustrating the presence of the primary septa (PS, red lines), secondary septa (SS, green lines), and interseptal branches (ISB, yellow lines) when viewed in the R-C plane. (**b**) A 3D rendering of the corresponding volume. (**c**) A sequence of reconstruction images illustrating the structural difference among primary septa, secondary septa, and interseptal branches, viewed at the L-R plane. The locations of these slices are indicated by the corresponding lines shown in (**a**). (**d**) Skeleton and nodes on an isolated septum as shown in Fig. 2C. (**e**) A schematic diagram of the interseptal branches with N-3 (blue) and N-4 (red) nodes; (**f**) Histograms of different node types for interseptal branches originated from the two sides of the septum; (**g**) SEM image of a representative region of septum with manually detected interseptal branches colored by node types (blue ring: N-3 nodes; red ring: N-4 nodes; green ring: N-5 nodes); (**h**) A reconstruction image of a septum (PS-1, grey) overlaid by the positions of

interseptal branches (ISB-1, red) from one side of the septum. White circles highlight the regions with the hole-like defects on the primary septum, which are "sealed" by connected interseptal branches. (**i**) A reconstruction image of a septum (PS-2, grey) overlaid by the adjacent interseptal branches on two sides of the septum (ISB-2, red, and ISB-3, blue).

7.3.6. Variation of mechanical properties

The variation of the cellular architecture from the center to the edge region revealed above suggests the local variation of mechanical properties in *H. mamillatus* spines, which is confirmed with our FE analysis on the extracted network skeleton (**Fig. 7.21a**). The von-Mises stress contours under compressions along the L, C, and R directions for two representative sub-volumes are shown in **Fig. 7.22a,b** (see **Fig. 7.21b-d** for complete results). The calculated effective Young's modulus of each sub-volume along the three principal directions are summarized in **Fig. 7.22c**. First of all, the effective modulus along the three principal directions in the sub-volume 1 and 2 (relative density, ~12 vol%) are always smaller than those in the other sub-volumes in the edge region (relative density, ~40 vol%) (**Fig. 7.22c,d**)[88]. Secondly, the effective modulus along the L direction is approximately three times higher than those along the R and C direction in the sub-volume 1-3 (on average, 7.3 GPa vs. 2.3 GPa vs. 2.0 GPa for L, R, C, respectively) (**Fig. 7.22c**). Furthermore, the effective modulus in three principal directions, especially L direction, are dramatically increased since sub-volume 3. Compared with the center region, the edge region exhibits less mechanical anisotropy,

but the effective modulus along the R and L direction is slightly higher than that in the C direction (**Fig. 7.22c**).

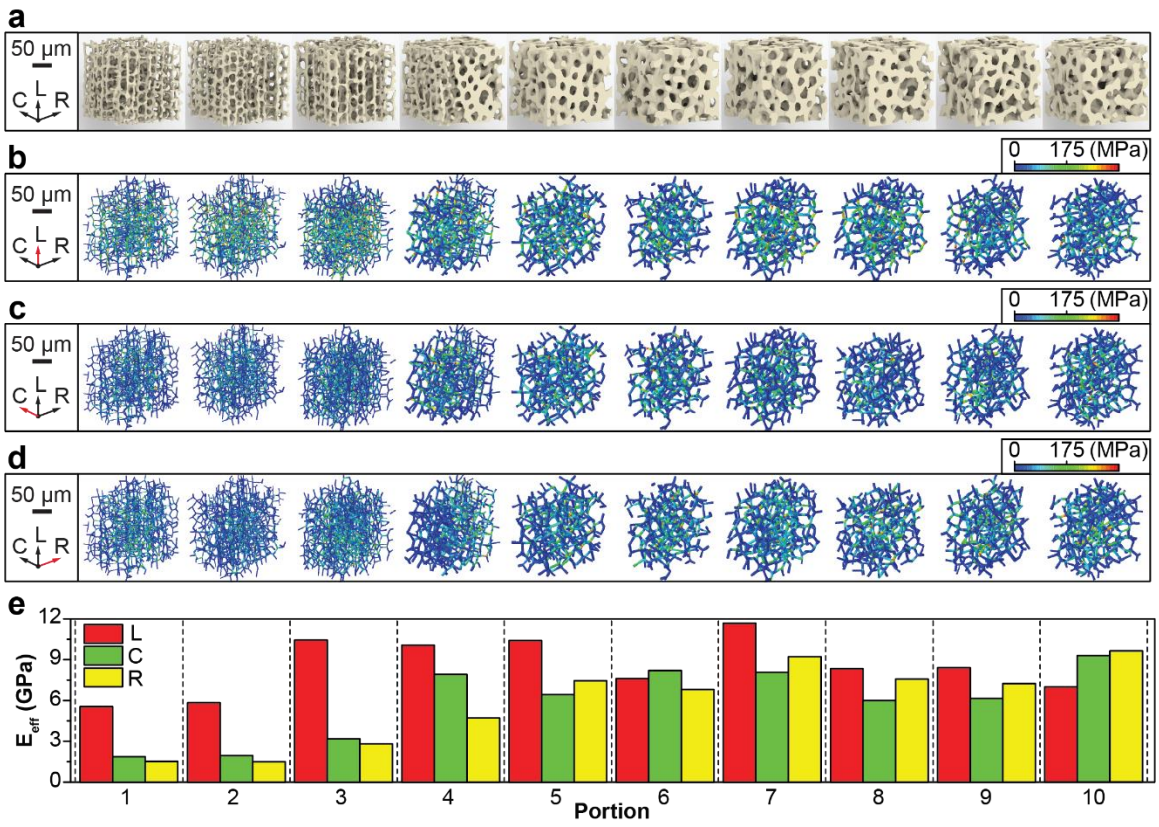


Fig. 7.21. Summary of the finite element simulations. (**a**) Ten portions of equal volume isolated from ten sub-volumes for simulations. Von-Mises stress contours of ten beam models under compressions along (**b**) L, (**c**) C and (**d**) R directions. (**e**) Histogram to summarize the Young's modulus in L, C, and R directions.

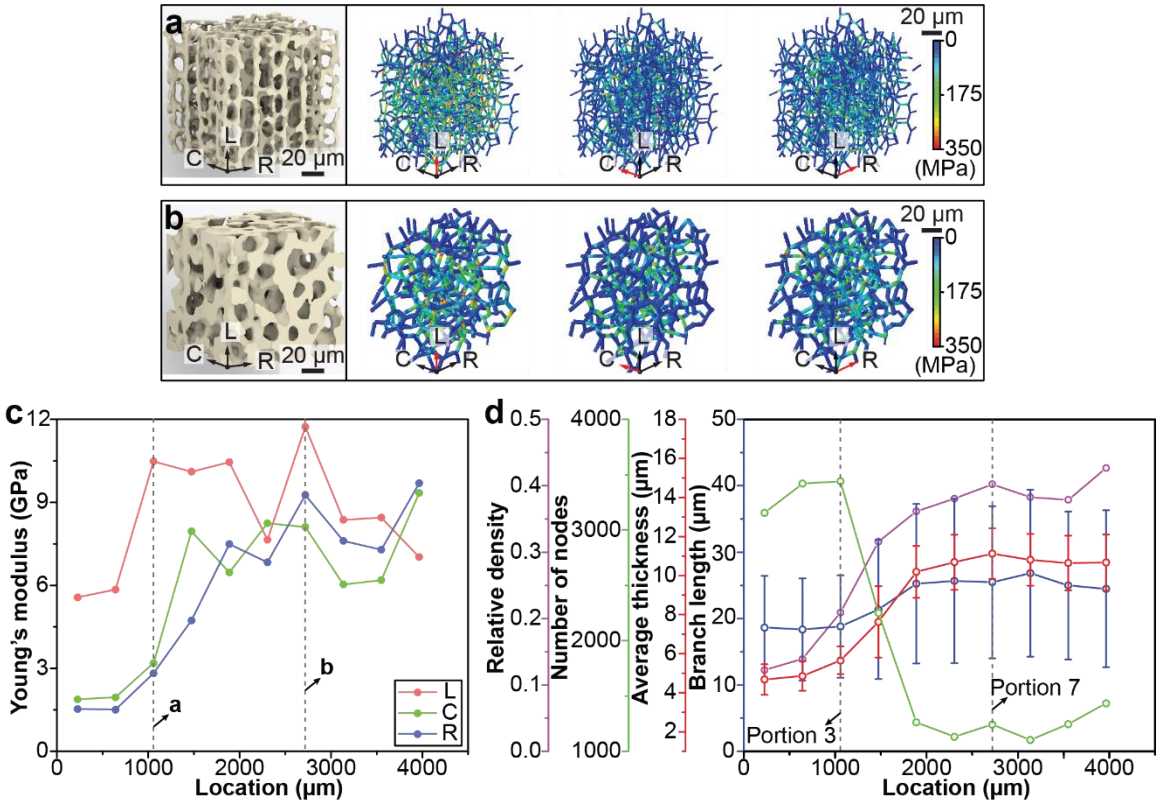


Fig. 7.22. Summary of the structural and mechanical variations across the volume of interest. Representative contours of von-Mises stress for sub-volume of portions (**a**) 3 and (**b**) 7. The red arrows in the coordinate system indicate the compression direction. (**c**) Variations of the effective Young's modulus in L, C, and R directions for the ten sub-volumes. (**d**) Variations of the branch length, average branch thickness, density of nodes, and the relative density for the ten sub-volumes.

7.4. Discussions

7.4.1. Nodal configurations for lightweight and robust cellular structure

Ting et al. demonstrated that the stereom structure in the center region of *H. mamillatus* spines is constructed primarily with low-connectivity nodes (*i.e.*, N-3 and N-4 nodes)[83]. The large volume analysis here reveals that this also applies to the edge region,

although the network organization pattern and the branch morphology vary significantly from the spine center to edge. In particular, the majority of interseptal branches avoid connecting to the nodal points in the septum plane, maintaining a network structure consisting of low-connectivity nodes in septa. Construction of porous structures with low-connectivity nodes have been also observed in trabecular bone[201] and the stereom structure of the test of the sea urchin *Echinocynamus pusillus*[90].

It is well known that the nodal configuration directly affects the mechanical properties of cellular solids[17]. In particular, according to the node connectivity, cellular solids can be broadly classified into bending- and stretching-dominated structures, where the latter is usually more desired due to its high mechanical efficiency[17,19]. For 3D foams, the minimum node connectivity to achieve stretching-dominated cellular structures is 12[17]. This also represents one of the design strategies for developing stretching-dominated metamaterial lattices for improved mechanical performance recently[8,9,11,19]. Our analysis indicates that the stereom structure in sea urchin spines falls in the category of bending-dominated lattice. It is currently unknown why these natural porous structures adopt this design rule, which may be constrained by the underlying formation processes. The relatively high density and rigid joints between branches may alleviate the bending deformation under external loads[18]. In addition, the N-3 and N-4 nodes in sea urchin spines approach ideal triangle-like and tetrahedron-like structural motifs, which are stable under tension and compression[11,17,19,201]. This also suggest that the branches connected by N-3 and N-4 nodes tend to evenly orient in 3D so that the least amount of material is used to maximally span the 3D space. Similar observation has been reported in human trabecular bone[201].

7.4.2. Galleried stereom in the center region and laminar stereom in the edge region

The combined results based on qualitative visualization and quantitative 3D network analysis suggest different stereom types in the center and edge region. In the center region, the stereom resembles more closely to the galleried type instead of the previously reported laminar type[88,89]. In this galleried structure, the stereom exhibits preferred branch alignment in the L direction, which is also evident from the branch chain analysis results[83]. These branches are further interconnected by horizontal branches, forming cylinder-like pores approximately parallel to the L direction[87]. This is supported by qualitative observations (**Fig. 7.1g**), branch orientations **(Fig. 7.7c)**, and ring orientations (**Fig. 7.16c**). As discussed in[83], this structural organization correlates well with the stereom growth process in the center region, where the stereom initially grows as micro-spines oriented along the L direction, followed by the formation of horizontal "bridges" that connect adjacent micro-spines and finally the branch thickening via sequential mineral depositions[202].

In the edge region, the structural analysis on septa substantiates that the stereom in this region resembles the laminar type. Each lamina (*i.e.*, septum) is connected to adjacent ones by branches extruded towards the C direction (*i.e.*, interseptal branches)[87]. Each septum plane exhibits a pseudo-hexagonal porous pattern composed with thicker and shorter branches in comparison to the interseptal ones. These septum planes are radially aligned and connected with the "solid protrusions" of the growth rings. Moreover, secondary septa are inserted when the spacing between the primary septa is greater than *ca*. 50um, resulting the "pore-splitting" morphology reported earlier[88]. This

strategy avoids the formation of very long branches, maintaining a relative constant range of branch length throughout the spine cross section. As the building material of stereom is the brittle magnesium calcite[86,203], this strategy may be beneficial to enhance the damage tolerance by eliminating long branches.

7.4.3. Structure-mechanics interplay for *H. mammillatus* spines

The different organization patterns and orientation-dependent branch thickness directly control the magnitudes and anisotropy of the stereom's local mechanical properties. First, although the center region has a significantly higher node density, the thin branches results in the high porosity and hence the lower effective modulus in all directions in comparison to the edge region. In addition, the galleried stereom in the center region with thicker branches aligned towards the L direction leads to a high mechanical anisotropy, *i.e.*, higher stiffness in the L direction. In the edge region, as the primary septa planes are radially aligned (*i.e.*, the L-R plane) and consist of thicker and shorter branches in comparison to interseptal branches, the stereom exhibit higher stiffness in the R and L directions. Compared to the center region, the stereom in the edge region is more isotropic due to the presence of interseptal branches aligned in the C direction.

Sea urchin spines are subject to different types of external forces, including hydrodynamic forces from ocean waves, attacks from predators, and forces to wedge themselves into small holes for protection[91,92,95,204]. In particular, some sea urchins "sacrifice" their spines to pierce to their predators and break off [91]. Therefore, the loading modes for sea urchin spines are complex, which may include axial compression, axial

torsion and bending[91,92,95]. The *H. mammillatus* spines achieve a high axial stiffness (*i.e.*, in the L direction) as evident by the fact that the local effective stiffness in both center and edge regions are the highest compared to the other two directions. This is due to the longitudinal alignment of thicker branches in the center region and the septa structure in the L-R plane. In addition, the bending and torsional resistance is enhanced through the gradual increase in local stiffness in three principal directions due to the increase in branch thickness and relative density from the spine center to edge. This follows the general strategy to increase the moment of inertia by placing more materials at the periphery, a classical strategy utilized by a variety of natural systems to enhance bending and torsional resistance while minimizing weight[85,205,206]. Lastly, the radial alignment of "dense" septum structures also enhances the resistance to radial compression (*i.e.*, high relative modulus in the R direction). A similar structure has been observed in the mineralized tiles (known as tesserae) in the skeletons of elasmobranch fishes, where the stiffness of individual tessera in the radial direction is enhanced through the radially-aligned "spoke-like" structures with a high mineral density and local mechanical properties[207].

7.4.4. Local structural modifications

Structural defects have been shown to play a critical role in controlling the mechanical performance of cellular solids or lattice structures[106,208–211]. Our network analysis reveals that, although the stereom structure follows some general organization patterns, such as the galleried and laminar forms in the center and edge region respectively, local structural modifications exist, particularly in the regions that appear to

be structural defects. For example, a careful examination of the pseudo-hexagonal pattern of the primary septa reveals the presence of large holes (*ca.* 30 μm in comparison to the typical hole size of *ca*. 20 μm for septa) (yellow arrows in PS-1 and PS-3, **Fig. 7.20c**). The interseptal branches "close" these large defect-like holes by forming interconnected branches as shown in the overlaid image between PS and ISB (white circles, **Fig. 7.20h**). In addition, we observed that horizontal branches bridge large transverse holes in the center region, which may serve as reinforcing structures to the local defects[83]. These observations indicate that, unlike engineering lattice structures, organisms are able to modify and reinforce local defects in their porous structures with additional branches and connections.

7.4.5. Limitations of current work

Several aspects require further investigations in order to fully understand the mechanical properties of sea urchin spines. First of all, the growth ring has been shown to play an important role in determining the mechanical performance of *H. mamillatus* spines, especially the inelastic behavior[85,97]. Further study by combining dense growth rings and the gradient stereom analyzed here could offer further insights. Secondly, although our beam model-based FE analysis by using the extracted cellular network provides an efficient approach to evaluate local mechanical variations, it cannot capture the contributions from the curved branch and nodal morphology in stereom. Unlike stereom structures, many conventional and architected engineering cellular materials comprise of branches with uniform thickness and sharp connections[7–9,11]. Further analysis can be achieved by incorporating the obtained branch profiling information with

geometric modeling methods such as implicit functions and BLINN transformation[212,213]. In addition, our current modeling approach allows us to construct arbitrary models with given network topology and hence isolate the effect of different parameters (*e.g.*, network topology, distribution of branch thickness or aspect ratio, etc.). The anisotropic mechanical properties of calcite should be also considered in further analysis of the overall mechanical performance of sea urchin spines, as they are often considered as large single crystals[214].

7.5. Conclusions

In this study, we adopted a self-developed multiscale network analysis algorithm to conduct, to the best of our knowledge, the first comprehensive, quantitative analysis of the cellular network on the *H. mammillatus* spines over a large volume in 3D[83]. The structural descriptors, including node characteristic, branch thickness, length, distance, tortuosity, orientation, and ring structures, were used to investigate the structural variation from the spine center to the edge region over millimeter scales. At the individual branch and node level, our analysis shows that the porous stereom network in the spine is primarily composed of nearly ideal N-3 and N-4 nodes, allowing for the maximal occupation of 3D space using least amount of materials and mechanical robustness. From the center to the edge region close to the first growth ring, despite of the decreased number density of branches, the branch length increases ~50% yet the branch thickness doubles, collaboratively resulting in a gradual increase of relative density of the stereom from *ca.* 12% in the center region to *ca.* 40% in the edge region. In addition, the

branches exhibit location- and orientation-dependent branch morphology variations from the center to the edge based on the fitting results of branch profile.

Our analysis also reveals the drastic difference in the 3D network organization patterns between the center and the edge region. The center region is composed of branches oriented parallel or perpendicular to the L direction, exhibiting a galleried stereom type instead of the laminar stereom type as reported earlier. In the edge region, the stereom exhibits a laminar construction based on "septa" that are aligned along the R direction. Each primary septum resembles a pseudo-hexagonal pattern on the L-R plane, which has branch thickness, on average, ~1μm thicker than the interseptal branches connecting to the adjacent septa. Moreover, approximately 50% of the interseptal branches are connected to the branches instead of nodal points of the septum wall, forming many N-3 nodes. As the spacing between the primary septa increases towards the spine's edge, initially less-ordered secondary septa with thinner branches are inserted between adjacent primary septa. With the quantified branch- and network-level information, the local mechanical properties of the stereom structure are investigated, which reveals the underlying functionally graded cellular structure, particularly in terms of effective modulus variation and mechanical anisotropy.

The quantitative multiscale cellular network analysis results conducted on the *H. mamillatus* spines here could provide important insights in the design and development of the 3D bio-inspired materials and structures with low density, high strength and damage tolerance. Also, enabled by the extensive progress of advanced 3D additive manufacturing, the fabrication of these functionally-graded, micro- or nano-architected structures inspired by sea urchin spines becomes feasible[7–9,11,215]. We also envision that

this large-scale cellular network analysis approach could be readily applied to other sea urchin spines for potential inter-specific structural comparison, or other echinoderms' porous skeletal elements such as sea star's ossicles, or other natural cellular materials in general.

Chapter 8 Dislocation engineering in the biomineralized microlattice of the ossicle of starfish *Protoreaster nodosus*

Ossicle, as a building unit of the endoskeleton of the starfish, radially covers the entire starfish as a protective armor. In previous work, we demonstrated that the ossicle is a diamond triply periodic minimal surface structure which contains microscopic 60° and screw dislocations that structurally similar to those in the crystals with diamond cubic lattice. This work further provides a comprehensive characterization of the dislocations with the emphasis on i) the unique type and core structures of microlattice dislocations in ossicle; and ii) quantitative structures surrounding the dislocation core. The result demonstrates distinct core morphologies and types in 60° and screw dislocations compared to those in diamond and silicon, which show additional or modified connections to avoid large pores. In addition, quantitative analysis around the dislocation cores reveals structural distortions around the core structure within one unit-cells, indicating smaller dislocation core size than those in the diamond and silicon. Finally, based on the observed biological structural features, how to harness the crack deflection mechanism by microlattice dislocation as previously demonstrated is discussed. The introduction of dislocation into 3D architected lattice for improved toughness is envisioned.

8.1. Introduction

Starfish, which belongs to the phylum *Echinodermata*, possesses star-shaped body entirely covered by radially arranged porous stones, named as ossicle, made of magnesium-doped calcite ($(Ca_xMg_{1-x})CO_3$)[84,98,99,154,155,216]. These porous ossicles are interconnected by soft organic fibers which governs the locomotion of the starfish and hence inspires extensive works on the starfish-inspired design of robotics[98,99,155,217–220]. In addition, starfish as well as other echinoderms including sea urchin and sand dollar, build the biomineralized skeletons as protective or mechanical support systems; therefore, their mechanical performances are of substantial interest for the design of lattice materials[4,80,88,98,221].

Understanding their multiscale structures is the logical first step and, in fact, researchers have made significant attempts on the qualitative and quantitative analysis on the microscale and nanoscale structures of echinoderms, such as the comprehensive quantitative cellular analysis of the sea urchin test and spine[2,90]. Recently, it has been found that the ossicle of starfish possesses diamond triply periodic minimal surface (TPMS) micro-lattice and constituent calcite that diffracts as single crystal[4]. Specifically, the diamond-TPMS micro-lattice's [111] direction is aligned with the c-axis of the constituent calcite[4]. Moreover, cellular structural analysis and dislocation analysis on the nodal distribution of the diamond lattice reveal 60° and screw dislocation structure in microscale similar to those found in diamond and silicon crystals with diamond cubic lattice[4,103,104,222]. These microlattice dislocations, as revealed by the in-situ micro-computed tomography (μ-CT) compression testing, deflect the crack propagation which is the mechanism for enhancing the damage tolerance of ossicle[4].

The dislocation-like structure is not uncommon in biomineralized materials and has been studied in terms of their structures and mechanics[2,223–228]. For example, the radially arranged and interconnected septa (or laminar stereom) of sea urchin spine in the edge region exhibits additional insertion of radial secondary septa when approaching the periphery, generating a local edge-dislocation-like distortion[2]. This edge-dislocation-like local modification is also found in the skeletal lattice of Hexactinellid sponge *Euplectella aspergillum* along the longitudinal axis of the cylindrical body[71]. It can be hypothesized that such additional insertion has two benefits: i) avoid the large gap between septa in sea urchin spine or between longitudinal branches in sponge's skeleton as the increase of cylindrical radius, which fulfills the space-filling purpose[227,229]; and ii) mechanically stiffen and strengthen the local region. In addition, screw-dislocation-like structure, which is the connection center of 3D spiraling laminates, has been discovered in nacreous shells and bivalve *Placuna placenta*, offering enhanced mechanical properties. In nacreous shells, the screw-dislocation-like connections serve the spacing-filling function, facilitates the spiral growth of the nacre, and interlocks the tablet's relative motions to strengthen the material[223,224,226,229]. Later, Gao et al.'s bio-inspired modeling work provided a computational demonstration that the screw-dislocation-like structure reinforces and toughens the composite by conditional spiral delamination[230]. Yet, Li et al. argued that the nacre obtains much less toughness improvement from screw dislocation-like structure than the shell of *P. placenta,* as the small tablets allow the crack propagation along the inter-tablet organic interface[225]. Furthermore, Li et al. demonstrated significant toughening and damage localization of the shell of *P. placenta* due to a series of mechanisms, including crack deflection and interconnection, ligament

bridging, and etc., activated by screw dislocation connections[225]. Therefore, understanding the dislocation-like structures and the functional purposes in biomineralized materials provide inspirations to the introduction of the crystallographic defects in the design of architected lattices and composites.

Traditional cellular lattice materials are usually periodic architectures, which have demonstrated their unique tailorable multiscale architectures and mechanical properties[7,8,11,172]. Previously, attempt has been made to introduce structures in crystallography such as grain boundary, precipitations, and phases, for the lattice design, which are found to provide mechanical strengthening and toughening to the original brittle lattices[106]. They have also demonstrated the availability of the famous Hall-Petch relationship in microscale lattice design[106]. Therefore, the previously mentioned dislocation structure in the micro-lattice of ossicle and the induced crack deflection mechanism lead us to wonder the unique dislocation structures and the potentials in harnessing the mechanical benefits of such structure.

Based on the previous study of the 3D multiscale structure of the ossicle, this work qualitatively and quantitatively characterizes the microscale dislocation structures with emphases on i) the dislocation types and core structures uniquely found in ossicle; ii) the quantitative structural descriptions of the dislocation core; and iii) providing insights in the how ossicle attenuate the structural modification due to the dislocation-like irregularities. Finally, future modeling of microlattice dislocations, including edge, 60°, and screw dislocations, in 3D architected lattice is discussed.

8.2. Materials and Methods

Sample preparation: Fresh starfish *P. nodosus* was obtained from Gulf Specimen Marine Laboratories Inc. (Florida, USA). To remove the organic tissues and expose the skeletal ossicles, the frozen fresh starfish with organics was soaked in bleach (6.05% sodium hypochlorite) for 20 mins. Subsequently, to remove the connective organic fibers between ossicles, the skeleton was further soaked in bleach for two hours and rinsed with deionized water. Small cubic volumes with < 2mm size were cut from the ossicles using a diamond saw blade for imaging and in-situ mechanical testing.

Scanning Electron Microscopy: Scanning electron microscope (SEM) equipped with a Quanta 600 FEG Environmental SEM (FEI, OR) was used to image the fracture surface of the starfish ossicles. The samples were coated using Platinum/Palladium (Pt/Pd) with ca. 10nm to reduce charging effects. The images were acquired at an acceleration voltage of 20 kV and a working distance of ~12mm.

Micro-computed tomography: The ossicles were scanned at the beamline 2-BM with energy of 27.4 keV at the Advanced Photon Source in Argonne National Laboratory. The tomographic scans were acquired over a 180-degree rotation of the sample and with an exposure time of 0.035s per image, resulting in 1500 projection images. The beamline was equipped with a PCO Edge high-speed CMOS detector (2448×1024 pixels) and 5× long-working-distance objective lens to capture images with isotropic voxel resolution of 0.690 μm of the projection images.

Reconstruction and segmentation: The projection images obtained from the X-ray micro-computed tomographic (μ-CT) scans were reconstructed using an open-source Python package Tomopy to obtained the reconstructed images, which were used for segmentations in an open-source machine learning-based software, ilastik 1.3.2[139,192]. The reconstructed and segmented images were visualized and further analyzed in Avizo 2019.2 (Thermo Fisher Scientific. MA, USA). Furthermore, based on the binary images, the dislocations were identified and segmented manually.

Cellular network analysis and dislocation analysis: The customized cellular network analysis pipeline was utilized to quantitatively analyze the cellular lattice structure and obtain the network of branch and nodes[2,182]. As the ossicle possesses a diamond lattice structure, the structural descriptors used in this study were defined in **Fig. 8.1** and **Table 8.1**. The orientation of branch 1 was defined as the local [111] direction of the tetrahedral unit of the diamond lattice (**Fig .8.1**). Here, the global [111] direction is considered the normal direction of the starfish's plane[4]. The branch length and thickness as well as the orientations were also defined in **Fig. 8.1** and **Table 8.1**.

The as-obtained nodal coordinates of the diamond lattice obtained from the network analysis were imported to Ovito for dislocation analysis using the built-in Dislocation Extraction Algorithm (DXA), which yields the dislocation lines and the corresponding dislocation types with Burgers vectors[231,232].

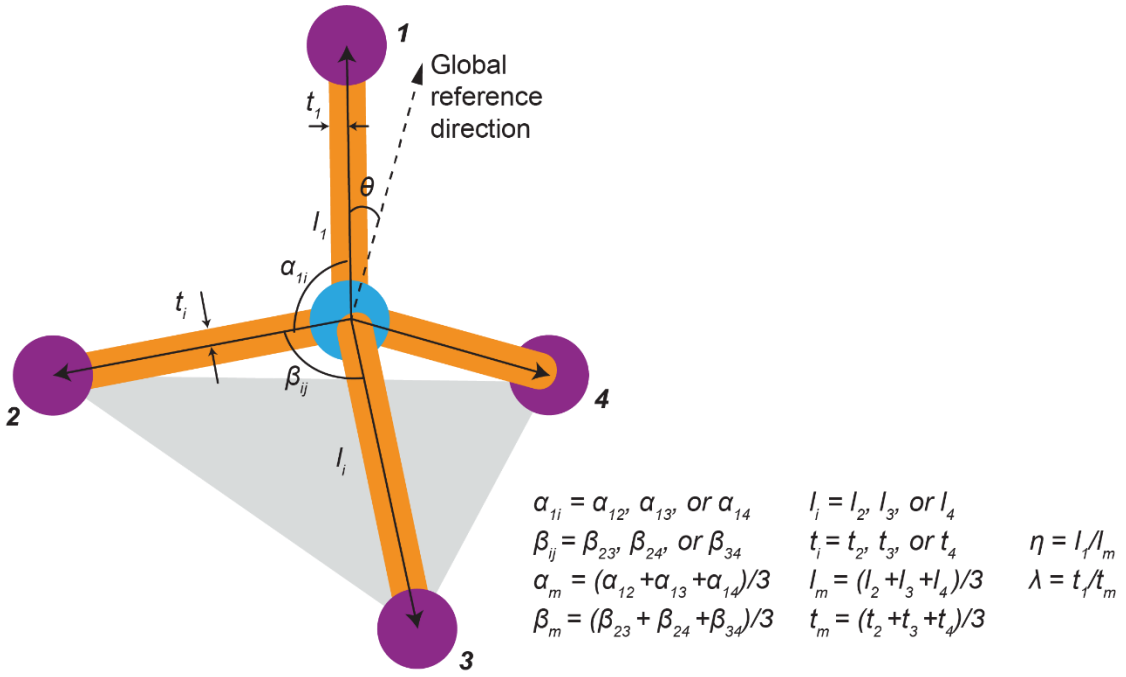


Fig. 8.1. Schematic diagram of a tetrahedron unit showing the structural descriptors used in this study.

Table 8.1 Definition and parameters of structural descriptors for lattice network analysis used in this study.

Description	Definition
N	Node type or nodal connectivity
θ (°)	Crystal orientation (angle between the local [111] orientation of the tetrahedron unit and the global reference orientation which is usually the normal direction of ossicle)
$\bar{\rho}$	Volume fraction, or relative density
l_1 (μm)	Length of branch 1, which is in the [111] direction
l_i (μm)	Length of the branch inclined to [111] direction, l_2, l_3, and l_4, where $i = 2, 3, 4$
l_m (μm)	Average length of branches inclined to the [111] direction
η	Length ratio, $\eta = l_1/l_m$

t_1 (μm)	Thickness, or radius, of branch 1
t_i (μm)	Thickness of the branch inclined to [111] direction, t_2, t_3, and t_4, where $i = 2, 3, 4$
t_m (μm)	Average thickness, or average radius, of branches inclined to the [111] direction
λ	Thickness ratio, $\lambda = t_1/t_m$
α_{1i} (°)	Inter-branch angles between branch 1 and one of the inclined branches, α_{11}, α_{12}, α_{13}, where $i = 2, 3, 4$
β_{ij} (°)	inter-branch angles among inclined branches, β_{23}, β_{24}, β_{34}, where $i, j = 2, 3, 4$
α_m (°)	Average value of three inter-branch angles between branch 1 and one of the inclined branches
β_m (°)	Average value of three inter-branch angles among branch 2,3, and 4
γ_m (°)	Average value of inter-branch angle in a tetrahedron unit, $(\alpha_m + \beta_m)/2$

Modeling of dislocations in architected lattice: The open-source script Atomsk was used to introduce dislocations in the diamond architected lattice[233]. The locations of the atoms in a diamond cubic lattice with 0.36 nm lattice constant, which is the lattice constant of diamond, were first generated. Then one or more edge dislocations were inserted into the diamond lattice to obtain the shuffle-set edge dislocation with core morphology similar to that found in diamond[234]. Subsequently, bond generation with a cutoff radius of 0.17 nm using open-source software Ovito was used to connect the atoms and generate the branches of diamond lattice with dislocations. Based on the nodal connections, lattices with dislocation defects can be generated.

8.3. Results

8.3.1. Dislocation structures in the starfish ossicles

The entire endoskeleton of the starfish *P. nodosus* is covered by a series of ossicles, a calcareous building block, as shown in **Fig. 8.2a**. Here, the normal direction of the starfish is defined as the direction from oral to aboral sides, which is usually considered the global reference direction (**Fig. 8.1**). Because, in general, the [111] direction of the diamond-TPMS lattice in ossicle is roughly along this direction[4]. The 3D volume rendering of the cross section of an ossicle shown in **Fig. 8.2b** shows the regular pattern across the entire volume of ossicle. Further 3D volume rendering of the cubic volume of the ossicle and the corresponding skeletal structure demonstrate the diamond-TPMS micro-lattice of the ossicle (**Fig. 8.2c,d**)[4]. What is uniquely found in this diamond-TPMS microlattice is the dislocation structure observable via 2D SEM imaging (**Fig. 8.2e**).

Previously, our group has provided a detailed structural characterization of the dislocations in 3D and revealed two types of dislocations, including the 60° and screw dislocations, as shown in **Fig. 8.3**[4]. Prior to the description of the dislocation structures, the global reference orientations of the ossicle analyzed in this work (relative density of 51.7% and occupied volume of 1.06 μm^3), which has the orthogonal bases of $[111]$, $[1\bar{1}0]$, and $[11\bar{2}]$, were defined (**Fig. 8.2a** and **Fig. 8.3a**). The locations of dislocations can be visualized by analyzing the nodal positions of the ossicle using Ovito, which assists the volume extraction for further dislocation analysis (**Fig. 8.3b**). Firstly, it has been found that the dislocation in ossicle as shown in **Fig. 8.3c,d** (overall dislocation line of $\boldsymbol{\xi} = [111]$ and Burgers vector of $\boldsymbol{b} = \frac{1}{2}[01\bar{1}]$) consists of a series of 60° dislocation cores (dislocation line of $\boldsymbol{\xi_{60°}} = [\bar{1}0\bar{1}]$ and Burgers vector of $\boldsymbol{b_{60°}} = \frac{1}{2}[01\bar{1}]$) of shuffle-

set and glide-set, depending on the location of inserted atomic plane[4]. These consecutive 60° dislocations form a zig-zag pattern which is generally along the $[111]$ direction. For the screw dislocation found in ossicle (**Fig. 8.3e,f**), the overall Burger's vector $\boldsymbol{b^s}$ and $\boldsymbol{\xi^s}$ ($\frac{1}{2}[112]$) are parallel, while closer examination also shows zig-zag pattern of local screw dislocations (Burgers vector $\boldsymbol{b_s}$ and dislocation line $\boldsymbol{\xi_s}$ of $\frac{1}{2}[011]$) as a result of the consecutive kinks that leads to the overall $[112]$ direction[4]. Secondly, previous work has presented some quantitative studies of the skeleton around the dislocation core, which has revealed two discoveries[4]: i) for 60° dislocation, the branches on the "compressive" and "tensile" sides of the cores have reduced and increased lengths, respectively, whereas the branch thickness remains relatively uniform; and ii) for screw dislocation, the stretched branches due to the spiraling core are truncated by N-3 nodes (i.e., nodes with 3 coordination number) due to the consecutive kink structure.

The cubic volumes from the ossicle as shown in **Fig. 8.3** are used for further qualitative and quantitative structural analysis in the following sections.

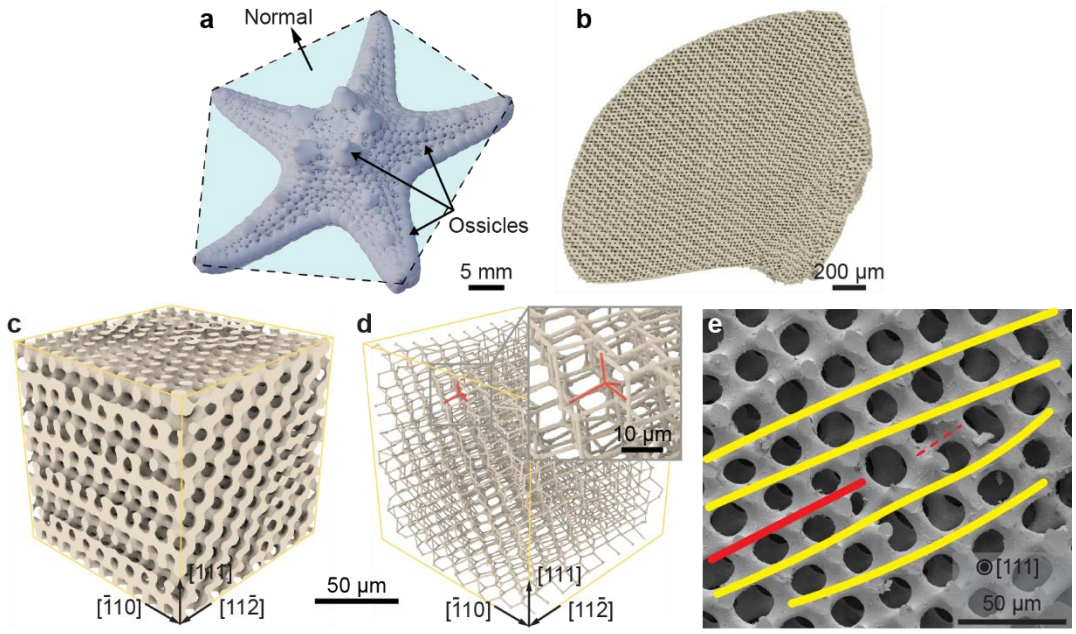


Figure 8.2. Introduction to the structures of the ossicles in *P. nodosus*. (**a**) Photo of the endoskeleton of *P. nodosus*, indicating the ossicles and normal direction from oral to aboral sides. (**b**) Volume rendering of the cross section of an ossicle showing the regular pattern. (**c**) 3D volume rendering of the cubic volume extracted from ossicle showing a 3D regular lattice structure. (**d**) The corresponding skeletal network of an ossicle volume. (**e**) SEM image of an example of dislocation structure in ossicle. The dash line indicates an additional branch separating the core.

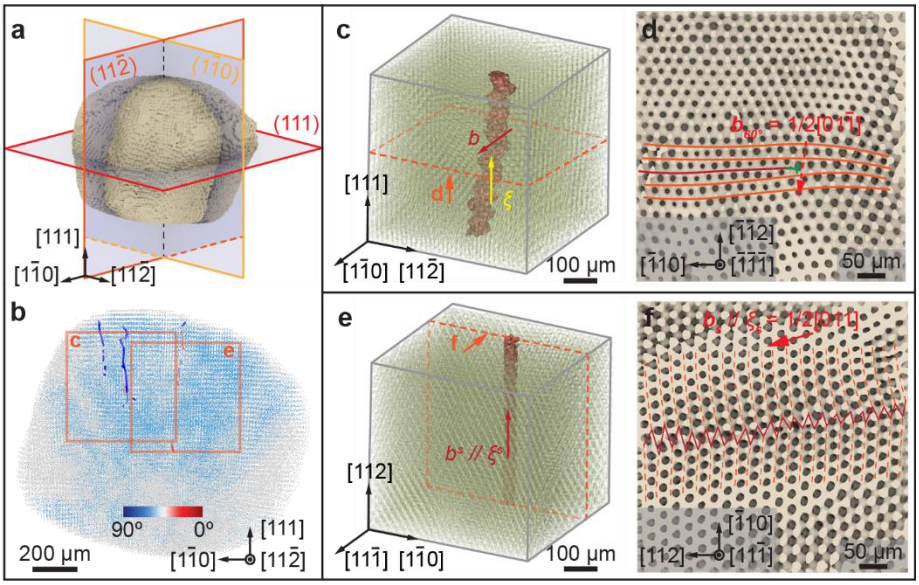


Fig. 8.3. Dislocations in ossicle and its inversed structures. (**a**) 3D volume rendering of a representative ossicle in starfish, defining the global reference of [111], [1$\bar{1}$0], and [11$\bar{2}$]. (**b**) Dislocation lines identified in the representative ossicle and the cubic volumes for dislocation analysis. (**c**) Isolated volume with a 60° dislocation colored in red. (**d**) 2D visualization of the 60° dislocation. (**e**) Isolated volume with a screw dislocation colored in red. (**f**) 2D visualization of the screw dislocation.

8.3.2. Core structures of 60° dislocation in ossicle

After isolating the cubic volume containing the 60° dislocation, the morphological (i.e., branch connections at the dislocation core) and quantitative analyses (i.e., the quantitative structural descriptors at and surrounding the dislocation core, **Fig. 8.4**) were conducted.

First of all, the entire dislocation core of 60° dislocation as well as the one and two cells surrounding the dislocation core were isolated as shown in **Fig. 8.4a** which will also be later used for quantitative analysis. By connecting the center of the dislocation cores,

the local zig-zag pattern of the dislocation line and the shuffle-set and glide-set dislocation cores can be observed, which is consistent with the previous finding (**Fig. 8.4a(i),b(i,ii)**)[4]. In addition, the "compression" (comp.) and "tension" sides of the dislocation correspond to the side with and without additional plane insertion, respectively (**Fig. 8.4a(ii,iii)**). The quantitative analysis will be performed separately on both sides.

Moreover, by examining each dislocation core, three basic types and three reconstructed types of connections of dislocation cores can be identified (**Fig. 8.4b,c**). The three basic types are glide-glide connections, shuffle-shuffle connections, and shuffle-glide connections, which has been previously found either in the ossicle or in the diamond crystal lattice (**Fig. 8.4b**)[4,235]. The reconstructed types, including the reinforced-shuffle (additional connection at the cell enclosed by 8 branches, or 8-ring cell), double-shuffle (two adjacent shuffle-set cores on the same plane), and double-glide (two adjacent glide-set cores on the same plane connecting by an N-5 node), are rather distinct, while the double-glide core corresponds to one of the stable core structure found in silicon crystal (**Fig. 8.4c**)[236]. This reconstructed cores discovered here is hypothesized as a unique structure in biological skeletal lattices to reduce the branch length and cell size to achieve local stiffening due to the structural defect[2,4,17].

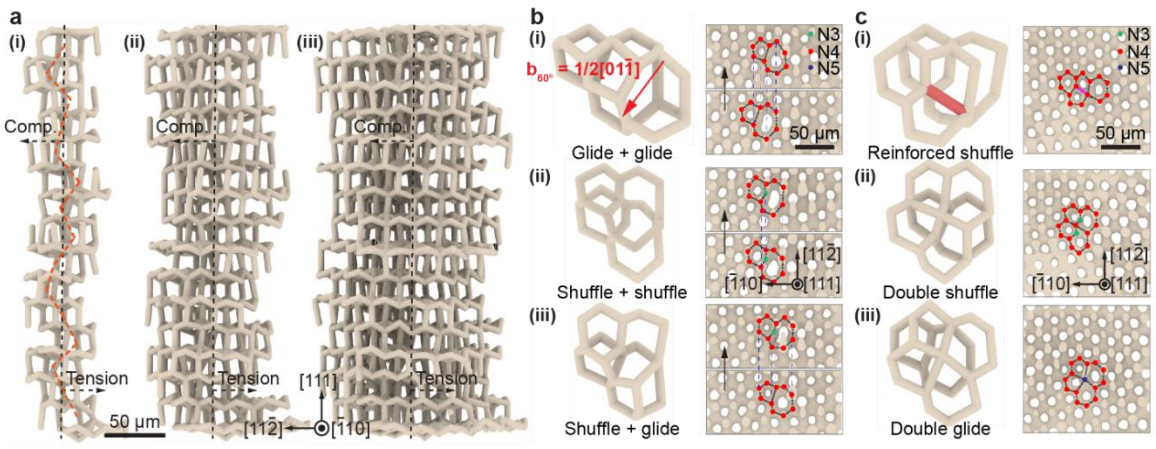


Figure 8.4. Morphological analysis of the 60° dislocation in the representative ossicle. (**a**) 60° dislocation($b_{60°} = 1/2[01\bar{1}]$) with core only (**i**), one cell surrounded (**ii**), and two cells surrounded (**iii**). (**b**) Basic core morphologies, including consecutive glide-set cores (**i**), consecutive shuffle-set cores (**ii**), and consecutive shuffle-glide core (**iii**). (**c**) Reconstructed core morphologies, including reinforced shuffle (**i**), double shuffle (**ii**), and double glide structures (**iii**).

Next, quantitative analysis of the 60° dislocation core and its surrounding structure were performed as summarized in **Fig. 8.5**. The structures are classified into the core and surrounding structures on the tension and compression sides, respectively, depending on the location of the inserted plane (**Fig. 8.5a**)[105]. Firstly, on average, the branch thickness and branch length in [111] (i.e., t_1, l_1) and non-[111] directions (i.e, t_m, l_m) are unchanged within two cells (**Fig. 8.5b**). However, t_1 and l_m are approximately 1 μm and 4 μm larger on the tension side than the compression side (**Fig. 8.5b**). Secondly, **Fig. 8.5b** demonstrates that this structural variation around the core is within one cell of the diamond lattice, which is further supported by the branch thickness and branch length mapping surrounding the core in **Fig. 8.5c**. Thirdly, the crystal orientation θ as defined in

Fig. 8.1 and **Table 8.1** remains consistent and unaffected by the 60° dislocation core (**Fig. 8.5c**). Therefore, the dislocation core radius in the ossicle, defined as the radius of the region structurally affected by the dislocation core, is less than 40.3 μm, which is approximately 1.3 times of the lattice constant (ca. 34.0 μm) of ossicle's diamond-TPMS lattice as previously found[4]. This core radius is also an important structural characteristic of dislocation in atomic crystals, while this value, obtained from computational simulations in previous work, is summarized in **Table 8.2** for diamond and silicon crystals with diamond cubic lattice structure. Differently, the core radius for crystal lattice is defined as the radius of the cylindrical region where the deformation is not describable by classical elasticity. By comparison, the ratio between core radius and lattice constant of 60° dislocation in ossicle (r_0/a) is similar to and larger than those of the 60° dislocation cores of diamond and silicon lattices, respectively (**Table 8.2**). But generally, the 60° dislocation core radius in ossicle, diamond, and silica are approximately the size of a single unit cell. However, due to the different definition of core radius, the structural effect of 60° dislocation in ossicle is within the core radius, while the deformation in atomic crystals outside of core radius due to dislocation still exists which is governed by elasticity[237]. Therefore, stereom in ossicle blocks the long-range structural effect and has an advantage in minimizing the structural effect due to 60° dislocation.

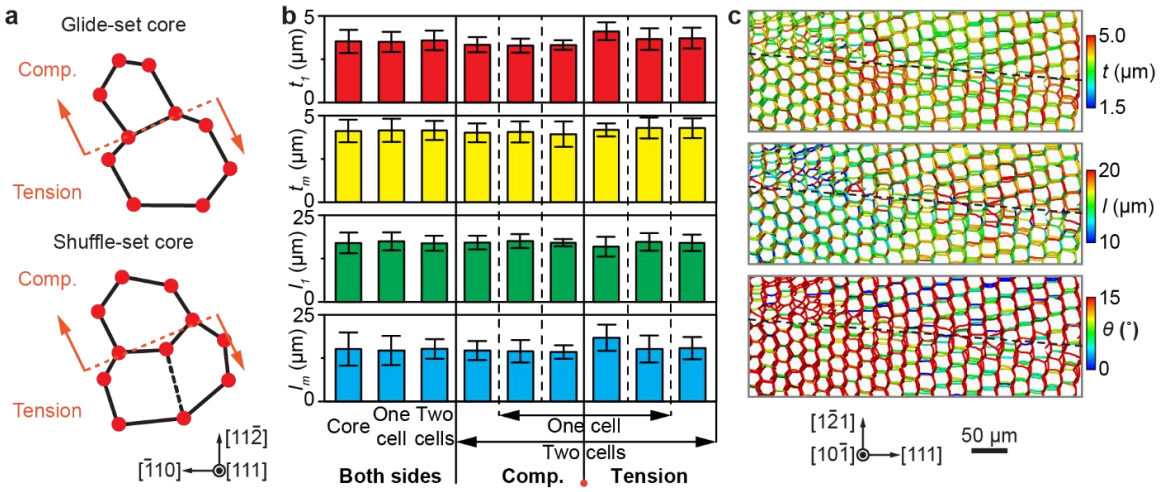


Figure 8.5. Quantitative analysis of the 60° dislocation. (**a**) Schematic illustrations of the compression and tension sides of the 60° dislocation. (**b**) Histograms of t_1, t_m, l_1, and l_m of dislocation cores and surrounding structures. (**c**) Distributions of the branch thickness, length, and θ. The dash line indicates the location of the 60° dislocation.

Table 8.2. Summary of dislocation core radius (r_0) and their ratio to the lattice constant (r_0/a) for diamond and silicon obtained from computational simulations.

Core type			r_0 (Å)	r_0/a
Diamond (IIa type, lattice constant $a = 3.57$ Å)[238]	Shuffle screw		4.3 1.7[239]	1.2 0.5
	60°	Glide-set	4.1 4.4[239]	1.2 1.2
		Shuffle-set	4.2	1.2
		30°	3.1	0.9

	Glide-set of partials	90° (SP)	3.0	0.8
		90° (DP)	3.3	0.9
	Shuffle-set of partials	30° (V)	6.0	1.7
		30° (I)	5.0	1.4
		30° (I')	5.5	1.5
		90° (V)	4.4	1.2
		90° (I)	4.1	1.2
		90° (I')	4.5	1.3
Silicon (lattice constant $a = 5.43$ Å)[240]	Both shuffle and glide screw		3.84 (1 burger's vector)[241]	0.7
	60° dislocation and 90° partial		≈5[242]	0.9

*The values of core radius without citation symbols are all from this reference[237].

8.3.3. Core structures in the screw dislocation

Detailed morphological (i.e., dislocation type, core morphologies, and connections) and quantitative analysis were also performed on the screw dislocation in the ossicle.

At first, different layers of crystallographic planes in the front and back of the screw dislocation core and the corresponding skeletons are shown in **Fig. 8.6a-f** where, other than the tetrahedron's N4 node, N-3 and N-5 nodes can be observed. This indicates significant reconstruction of the local diamond microlattice by the screw dislocation (**Fig. 8.6a-f**). By overlapping the skeletal lattices of different layers, three types of structures

can be identified: type I and type II screw dislocations separated by a transition region (**Fig. 8.6g**). Despite the void in the skeleton of the transition region, the structure of this transition region is actually occupied by a bulky solid which cannot be skeletonized correctly (**Fig. 8.6h**). In addition, based on the inclined direction of the branches, the slip plane is not $(11\bar{1})$ plane as shown later, which is found for screw dislocation in diamond crystals[239].

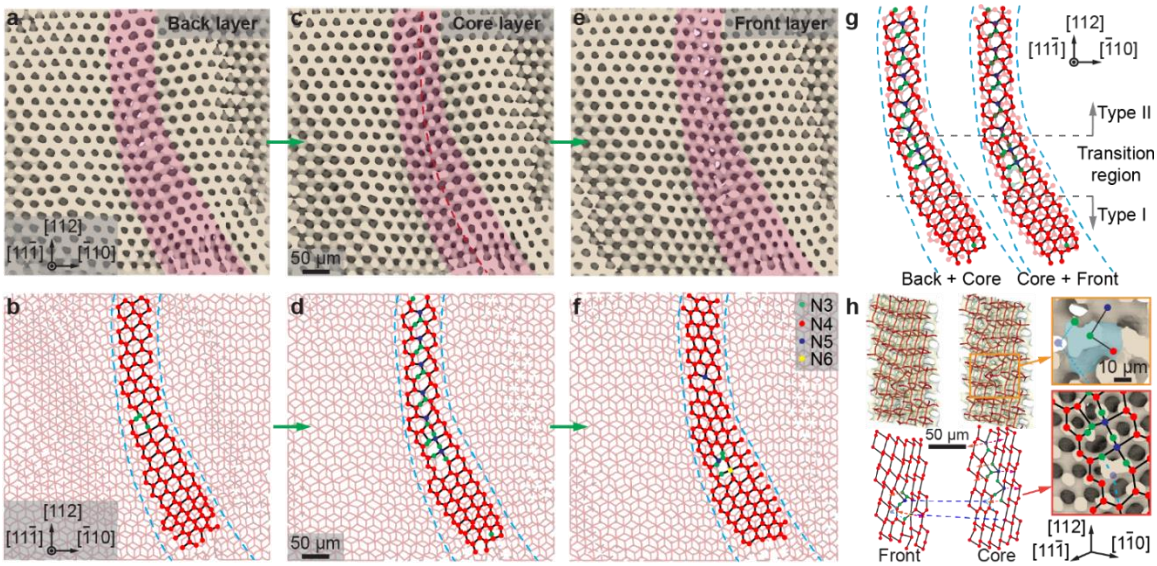


Figure 8.6. Core structure of the screw dislocation in the representative ossicle. (**a-e**) 3D volume rendering (**a,c,e**) and corresponding skeletal structure (**b,d,f**) of the back layer (**a,b**), core layer (**c,d**), and front layer (**e,f**), respectively, along $[11\bar{1}]$ direction. The skeletal connections and nodes are indicated by solid lines and dots with different color. The entire dislocation core region is enclosed by two cyan dash lines. (**g**) Overlaps of the skeletal structure of the back and core layers as well as the core and front layers. The back and front layers are transparent. Three regions of the screw dislocation, which are

type I, type II, and transition region, are identified. (**h**) 3D skeletal structure and volume rendering analysis of the transition region.

Furthermore, the skeletons on the left side (along the $[1\bar{1}0]$ direction) and on the right side (along the $[\bar{1}10]$ direction) of the screw dislocation core were analyzed (**Fig. 8.7a**). This reveals an upward trend on the left and a downward trend on the right side of the hexagonal pores, respectively, along the $[11\bar{1}]$ direction (**Fig. 8.7a,b**). **Fig. 8.7b** schematically shows this structure and demonstrates that both type I and type II screw dislocations have slip plane of $(1\bar{1}0)$. Specifically, the type I screw dislocation maintains N4 nodes without reconstructions; thus, it can be considered as a shuffle screw dislocation with dislocation line of $[\bar{1}\bar{1}\bar{2}]$ and with a slip plane of $(1\bar{1}0)$[239].

Thirdly, the skeletons of consecutive layers of $(11\bar{1})$ planes for the ossicle's diamond-TPMS microlattice in the vicinity of the screw dislocation were visualized for branch length and thickness analysis (**Fig. 8.7c,8.8,8.9**). The analysis found that, for type I screw dislocation, the distorted branches indicated by dark arrow heads are ca. 3 μm longer than other branches (**Fig. 8.7c**). While, for type II screw dislocation, the corresponding distorted branches at the core are relatively short compared to the distorted branches in the back layers due to the truncation by the N-3 nodes (**Fig. 8.7c**). In addition, in the front layers of the type II screw dislocation, the length is generally similar among branches in similar directions, despite the distorted structure which returns to the relatively regular hexagonal shape within about three layers (**Fig. 8.7c**). Thickness analysis was also performed which shows that the thickness of distorted branches around the screw dislocation core is similar to branches at other locations (**Fig. 8.8**). Moreover,

the skeletal lattice visualized along $[\bar{1}10]$ direction show that the branches connecting consecutive $(11\bar{1})$ planes around the screw dislocation core have no particular variations in length and thickness (**Fig. 8.9**). The suddenly increased thickness of the branches connecting the adjacent $(11\bar{1})$ planes on the left (or back) side of the type II screw dislocation is also observed (**Fig. 8.9**). I hypothesized that this is not a result of screw dislocation as the branches are away from the core where the lattice structure is not distorted.

Based on the morphological and quantitative analysis (**Fig. 8.7-8.9**), it can be found that the structural effect due to screw dislocation is within two cells around the cell containing the dislocation core. The radius of this region can be approximated as 58.4 μm, which is 1.7 times of the lattice constant of ossicle (**Fig. 8.7c**). Therefore, the ratio (r_0/a) of screw dislocation in ossicle is larger than that in the silicon and diamond crystal lattices (**Table 8.2**).

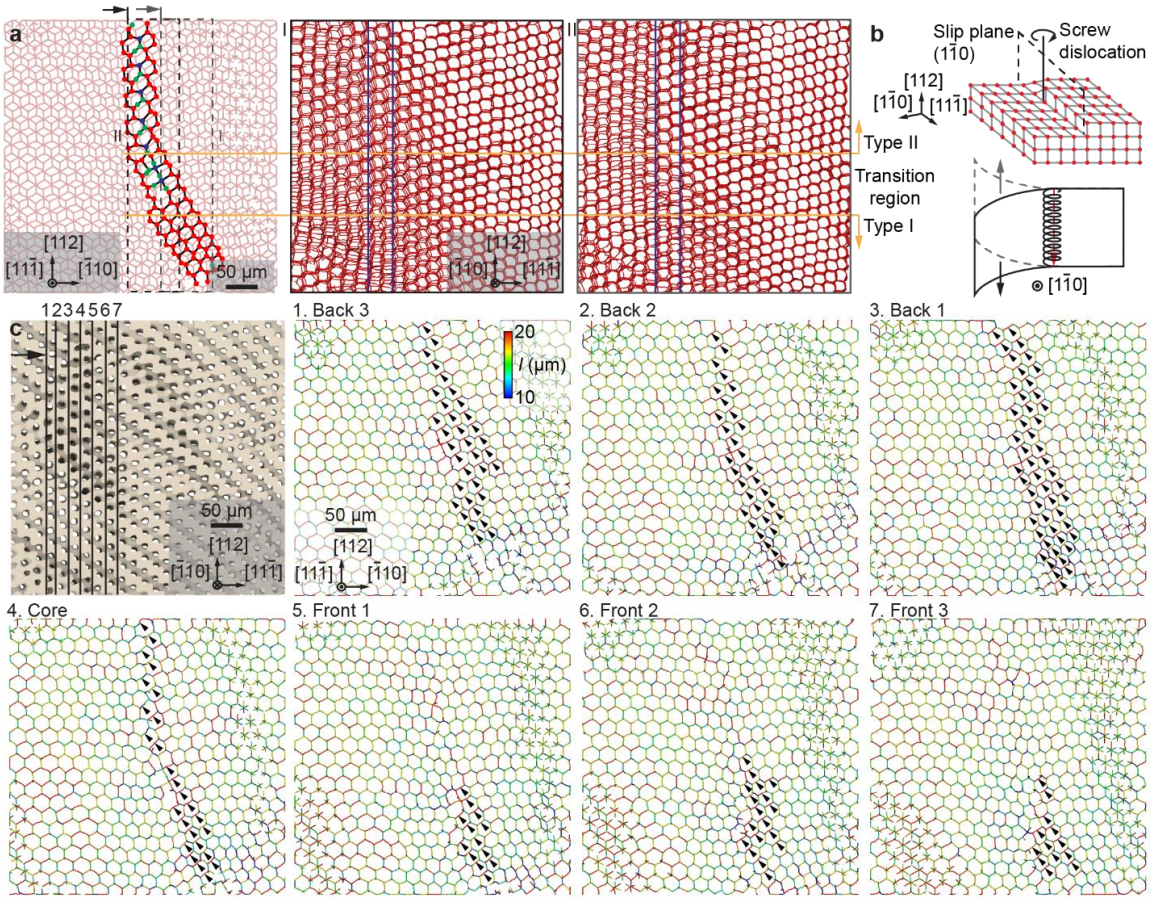


Figure 8.7. Identification of screw dislocation type and quantitative analysis of the core. (**a**) Skeletal structure of the screw dislocation viewed along $[11\bar{1}]$ and $[\bar{1}10]$ directions, respectively. Black and grey boxes on $(11\bar{1})$ plane indicate the region I and II shown on the right (different $(\bar{1}10)$ planes). Blue boxes roughly indicate the locations of the dislocation core. (**b**) Identifications of the screw dislocation type based on the observation of spiral direction, showing that the screw dislocation has a slip plane of $(\bar{1}10)$ and burger's vector along $[112]$ direction. The plane enclosed by solid black lines is in the front of the plane enclosed by gray dashed lines. (**c**) Consecutive layers around the screw dislocation core showing the distribution of the branch length. Dard arrows indicate the stretched branches due to the screw dislocation.

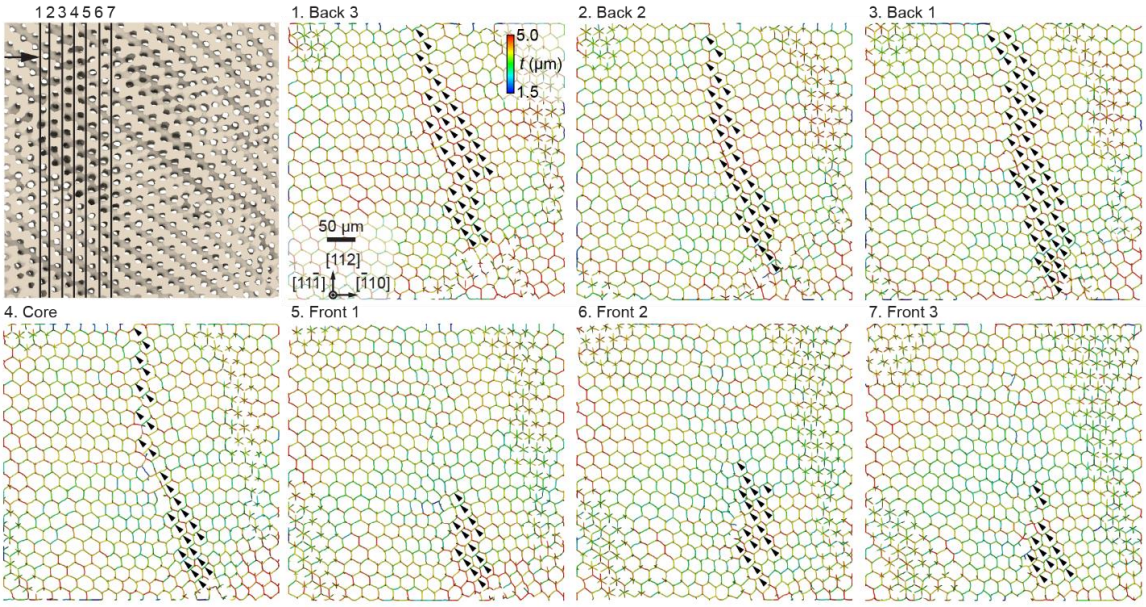


Figure 8.8. Branch thickness analysis of the screw dislocation core. Consecutive layers around the screw dislocation core showing the distribution of the branch thickness. Dard arrows indicate the stretched branches due to the screw dislocation.

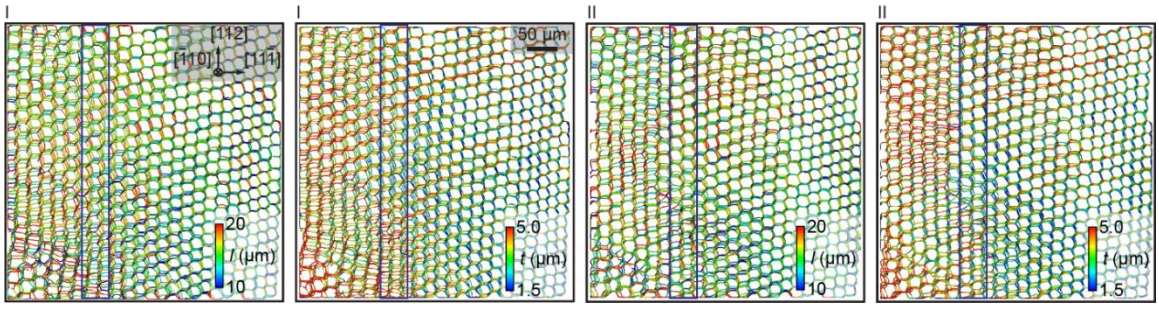


Figure 8.9. Branch length and thickness analysis on the $\{\bar{1}10\}$ planes. Skeletal structure of the screw dislocation with multiple layers viewed along $[\bar{1}10]$ direction. The skeletal branches are colored by either the length (l) or thickness (t). I and II indicate the regions shown in **Fig. 8.7a**. Blue boxes roughly indicate the locations of the dislocation core.

Since type II screw dislocation is uniquely found in ossicle's diamond-TPMS microlattice, it was then isolated for in-depth morphological and quantitative analysis. First of all, similar to the previous finding, the consecutive N3 and N5 nodes were found which are the signatures of the consecutive kink structures of the screw dislocation core (**Fig. 8.10a**)[4,243]. In addition, despite that the local dislocation line of each kink structure is along the [011] direction, the consecutive kink structures lead to the overall [112] dislocation line (**Fig. 8.10a**)[4]. Secondly, the kink structures, specifically the N3 and N5 nodal connections, are compared with those of the kink structure in the silicon (**Fig. 8.10a-d**)[243]. In both silicon and ossicle, the N-5 node of the kink structure is within one of the (111) or $(11\bar{1})$ planes, respectively, connecting to the adjacent layer (**Fig. 8.10a-d**). Furthermore, in silicon, there is only one N3 node within a (111) plane, connecting with the nodes on the same plane, leaving a large empty cell (**Fig. 8.10d**). While in the ossicle, each kink structure contains two connecting N3 nodes on the same $(11\bar{1})$ plane: one of the N-3 node is connecting to the nodes on the same $(11\bar{1})$ plane; another is connecting to a node on the adjacent $(11\bar{1})$ plane (**Fig. 8.10a-d**). This connection was confirmed by the 3D connection analysis (**Fig. 8.10e**). This provides structural and potential mechanical advantages by avoiding large spacing between connections like the one in **Fig. 8.10d** and shortening the stretched branches as indicated by the quantitative analysis shown in **Fig. 8.7c,8.10f**. Finally, the statistical structural analysis performed on the one or two cells surrounding the type II screw dislocation core show similar averaged values of branch thickness and length, including t_1, l_1, t_m, and l_m (**Fig. 8.10g**). Therefore, despite variations in some branches and connections due to the screw dislocation, the overall structure is maintained.

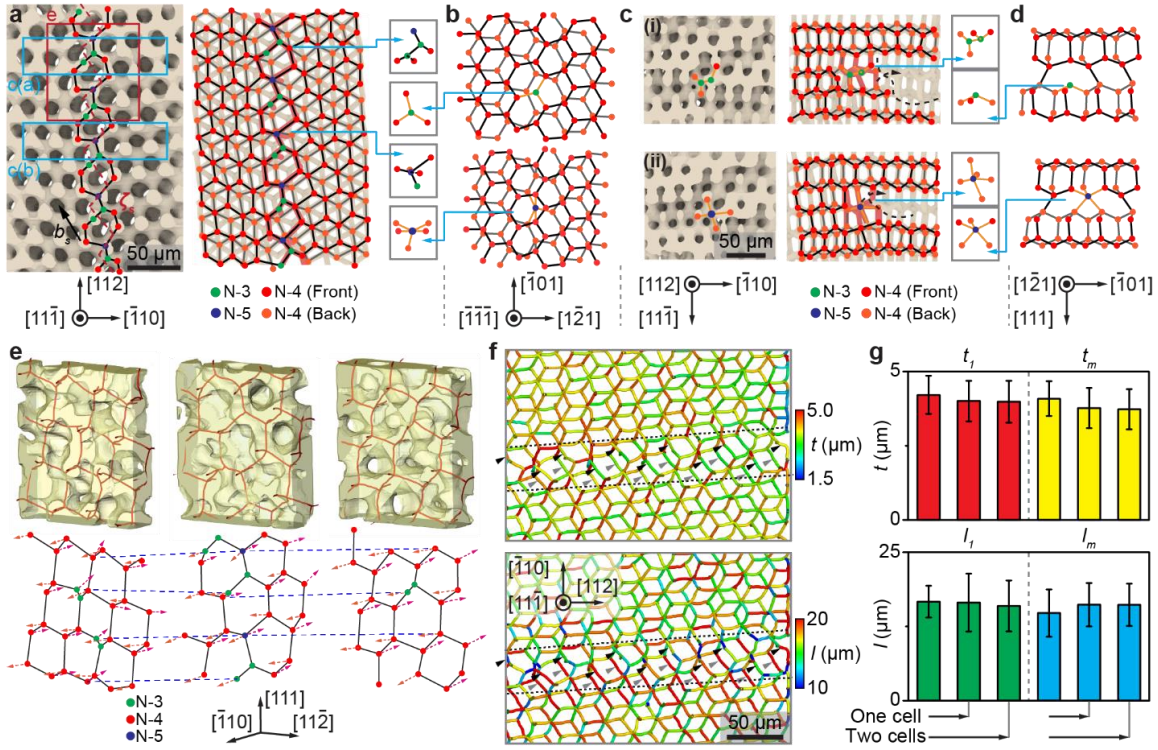


Figure 8.10. Morphological and quantitative analysis of type II screw dislocation. (**a**) 3D rendering and skeletal structure of the type II screw dislocation viewed along $[11\bar{1}]$ direction, showing consecutive N-3 and N-5 nodes. Connections of N-3 and N-5 nodes are shown on the right. (**b**) N-3 and N-5 nodes and connections in the kink structure of screw dislocation of silicon viewed along $[11\bar{1}]$ direction. (**c**) 3D rendering and skeletal structure of the type II screw dislocation with N-3 (**i**) and N-5 (**ii**) node viewed along [112] direction, showing a terrace surface with spiraling direction along $[\bar{1}\bar{1}\bar{2}]$ direction. (**d**) N-3 and N-5 nodes and connections in the kink structure of screw dislocation of silicon viewed along [112] direction. (**e**) 3D connections of the type II core. (**f**) Distributions of the branch thickness, length, and θ. (**g**) Histogram of the branch thickness, branch length, and θ surrounding the core structure. From left to right, the

histogram indicates θ for dislocation core, structure within one cell, and structure within two cells, respectively.

8.4. Discussions

Microscopic 60° and screw dislocations were found in the diamond-TPMS lattice of ossicle in starfish *P. nodosus*, which various types and core morphologies either similar or dissimilar to those found in the atomic crystals with diamond cubic lattice. In terms of the similarity, both ossicle and silicon/diamond crystals have: i) local 60° ($\boldsymbol{\xi_{60^\circ}} = [\bar{1}0\bar{1}]$, $\boldsymbol{b_{60^\circ}} = \frac{1}{2}[01\bar{1}]$) and shuffle-set screw ($\boldsymbol{b_s} = \boldsymbol{\xi_s} = \frac{1}{2}[011]$) dislocations; ii) 60° dislocation core of shuffle-set and glide-set; and iii) screw dislocation with kink structure[4]. In terms of the dissimilarity, the dislocation structures in ossicle possess: i) global 60° ($\boldsymbol{\xi} = [111]$, $\boldsymbol{b} = \frac{1}{2}[01\bar{1}]$) and shuffle-set screw ($\boldsymbol{b^s} = \boldsymbol{\xi^s} = \frac{1}{2}[112]$) dislocations due to the zig-zag forms of consecutive cores; ii) 60° dislocation cores with reconstructed morphologies (i.e., reinforced-shuffle and double-shuffle types); iii) screw dislocation with slip plane of $(\bar{1}10)$; and iv) consecutive kink structure in screw dislocation with reconnected kink cores. These particular core morphologies in 60° dislocation with additional "stitching" and reconnections in screw dislocation demonstrate that the ossicles tend to avoid large pores due to the structural defects. Further, quantitative analysis of the lattice structure around the dislocation cores show that ossicles tend to alleviate the structural variations due to i) 60° dislocation via blocking long-range structural distortion away from the core radius; and ii) screw dislocation via small affected region (< 2 unit cell size), core connections in kink structure, and maintaining the branch length and thickness and hexagonal connections.

Whether the dislocation structure is intentional left or a byproduct of the ossicle growth remains unknown. Our structural analysis implies that the ossicles tend to compensate the structural distortion via stitching the cores which would have generated large pores or reducing the effect of structural variations of branch length and thickness around the dislocation cores. Yet, the considerably higher density of dislocations in ossicles than in the diamond crystal lattice suggests that ossicles favor the existence of dislocation[4]. Therefore, we hypothesize that the ossicles prefer dislocations while suppress the large structural effects due to this type of defects, which improves significantly the dislocation density. In addition, this particular defect structure can provide mechanical benefits such as toughening and strengthening as the main regular lattice maintains the stiffness while the local heterogeneity redistributes the stress and hence improves strength and toughness[4,107].

Harnessing the unique structures and mechanical benefits of dislocations in architected lattice is another important goal of studying the dislocation structures in ossicles here. A recent work has already demonstrated that by introducing 5-7 defects found in graphene and beehives into the design of regular hexagonal lattice materials is able to provide 25-30% improvement in both strength and energy absorption capability[107]. This is because the structural heterogeneity in regular lattices deviates the originally regular stress distribution and crack path[106,107]. Therefore, introducing various types of dislocation defects into various architected lattice may be a promising strategy to further improve the mechanical performance. Here, a method as introduced in the Materials and Methods section was provided to generate the dislocations into the diamond lattices with 3D architecture (**Fig. 8.11**). This method is able to generate various

lattices with various types of dislocations and controllable dislocation density. We envision that using atomic simulations may provide another way to obtain stable dislocation core morphologies and hence different lattice connections for generating architected lattice materials[244].

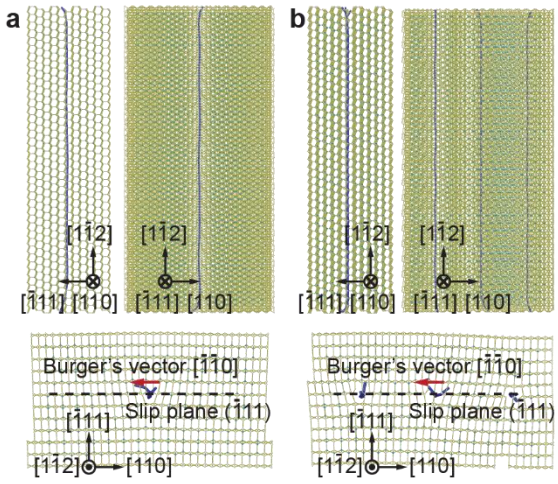


Figure 8.11. Demonstration of designing 3D architected lattice materials with dislocations. (**a,b**) Diamond lattices with one (**a**) and three (**b**) shuffle-set edge dislocations.

8.5. Conclusions

In this work, the in-depth qualitative and quantitative structural analysis were performed on the 60° and screw dislocations in ossicle. Unique core morphologies (i.e., reinforced-shuffle and double-shuffle core types in 60° dislocations, reconnections of kink structure in screw dislocation) and type (i.e., screw dislocation with slip plane of ($\bar{1}$10)) of the dislocations were observed. Based on this morphological exploration, one structural principle can be extracted: large void due to dislocation defect is usually

“stitched” by additional branch connection, closed by bulk solid, or branch reconnections. Furthermore, quantitative structural analysis around the dislocation core show that 60° and screw dislocations in ossicle have small core region (1~2 unit cell size of ossicle), which suppress the long-range structural variations despite of the dislocation defects. With the knowledge of high density of dislocations in ossicle, it is hypothesized that ossicles favor the existence of dislocations while, in the meantime, suppressing the structural variations due to defects. Finally, we envision the feasibility of introducing dislocations into architected lattices as demonstrated in the diamond lattices and harnessing the mechanical benefits such as strengthening and toughening.

Chapter 9 Mechanical properties of dual-scale crystallographic coalignment in starfish's ossicle stereom

This work generates the following regular research article: H. Chen, Z. Jia, Z. Deng, L. Li, On the mechanical properties of dual-scale microlattice of starfish ossicle: a computational study, In submission.

While artificial cellular solids, either stochastic foams or architected lattices, are typically made of polycrystalline or amorphous materials, echinoderms (e.g., sea urchins, starfish, and brittle stars) build their skeletons with porous, yet single-crystalline calcite. This type of biological cellular solid, known as stereom, also exhibits a vast diversity in pore morphology, ranging from random open-cell foams to fully periodic lattices. In particular, the skeletal elements (ossicles) of certain starfish species are composed of a diamond-triply periodic minimal surface (diamond-TPMS) microlattice, in which the crystallographic symmetries at both atomic and lattice levels are precisely aligned. Here we systematically investigate the mechanical performance of this unique dual-scale microlattice and discuss the synergistic effects of atomic- and lattice-scale crystallographic coalignment. Our theoretical and computational analysis suggests that the mechanical isotropy of ossicles is significantly enhanced due to the compensating mechanical anisotropy between the atomic and lattice level. Moreover, the observed 50 vol% relative density in the diamond-TPMS microlattice of ossicles may be the result of achieving overall mechanical isotropy, minimal surface curvature, and maximized surface area. Finally, we discuss the limitation and applicability of the analysis method reported here in studying other biological and synthetic lattice materials.

9.1. Introduction

Recent advancement of additive manufacturing has enabled the fabrication of 3D architected lattice materials from a variety of polymers, metals, ceramics/glass, or composites[8,9,245]. These architected lattices may exhibit some unusual mechanical properties, such as isotropic elastic stiffness approaching theoretical limits, negative Poisson's ratios, and etc[8,16,17,245–249]. The introduction of hierarchical designs further expands the material property space by tailoring mechanical behaviors at different length scales[7,11,12,250]. For example, one strategy to introduce structural hierarchy of architected lattices is to design the branches into cellular architectures at a smaller length scale[7,9,11,12,250]. Another is to engineer the material-level design of the branches, including core-shell composites, fiber- and particle-reinforced composites, high-entropy alloy with crystallographic texture, and etc[251–259]. However, single-crystalline constituent at atomic scale has rarely been taken into consideration for the mechanical design of hierarchical lattices.

Unlike artificial architected lattices that are typically composed of polycrystalline or amorphous constituents, the porous, biomineralized skeletal elements of many echinoderms (e.g., starfish, sea urchins, and brittle star) is composed of calcite that often diffracts as a single crystal[260–263]. This type of biological cellular solids, known as stereom, exhibits a vast diversity in pore morphology, ranging from random open-cell foams to fully periodic lattices[87]. While significant research efforts have been made to correlate the crystallographic orientation of calcite with the orientation of skeletal elements, such as the test (shell) plates and spines of sea urchins[260,262–264], how the

calcite's crystallographic orientations are aligned with the local pore morphology and organization in stereoms remains largely unknown[2,83,90,92].

Recently, our group has demonstrated that the skeletal elements (known as ossicles) of certain starfish species (e.g., *Protoreaster nodosus*) are composed of a diamond-triply periodic minimal surface (diamond-TPMS) microlattice (relative density, ~50vol%)[4]. In this natural architected microlattice, the crystallographic symmetries at both atomic (calcite, space group $R\bar{3}c$) and lattice (diamond, space group $Fd\bar{3}m$) levels are precisely aligned[4]. Specifically, the c-axis of calcite coincides with the [111] direction of the diamond-TPMS microlattice, which is also along the normal direction of the animal (e.g., from oral to aboral sides of starfish)[4]. Meanwhile, the $[0\bar{1}13]$, $[\bar{1}103]$ and $[10\bar{1}3]$ directions of calcite are aligned with the directions of non-[111] branches (i.e., $[1\bar{1}1]$, $[\bar{1}11]$ and $[11\bar{1}]$, respectively) of the tetrahedron in the diamond-TPMS lattice[4], through which the in-plane three-fold symmetry between calcite (plane perpendicular to c-axis or $[0001]$ direction) and diamond lattice ((111) plane) are precisely registered.

While our previous analysis suggests that this dual-scale crystallographic coalignment in ossicles provides a stiffness compensation for selected crystallographic directions[4], we lack a comprehensive 3D understanding of the mechanical properties of starfish ossicles. Here we develop a combined theoretical and computational methodology for predicting the full elastic properties of architected lattices with dual-scale crystallographic coalignment. This method is subsequently applied to obtain the 3D elastic properties of starfish ossicles. Furthermore, by analyzing the mechanical isotropy, strength, and structure of the dual-scale diamond-TPMS microlattice, we provide insights for the formation of starfish ossicles (e.g, why particular crystallographic coalignment and

relative density are selected). Finally, the limitation of this method and applicability to understanding the mechanics of other echinoderms' stereoms and developing dual-scale architected lattices are discussed.

9.2. Methods

Diamond-TPMS generation: The diamond-TPMS structure's iso-surface (U) is given by Eq. (9.2.1):

$$U = S_{x_0}S_{y_0}S_{z_0} + S_{x_0}C_{y_0}C_{z_0} + C_{x_0}S_{y_0}C_{z_0} + C_{x_0}C_{y_0}S_{z_0} - T \quad (9.2.1),$$

where $S_i = sin\ (k_i \cdot i)$, $C_i = cos\ (k_i \cdot i)$, and $i = x_0, y_0, or\ z_0$ represent three orthogonal directions of the Cartesian coordinates, corresponding to $[100]$, $[010]$, and $[001]$ directions of the diamond-TPMS microlattice, respectively. $k_i = 2\pi n_i/L_i$ is defined as the periodicity, where n_i and L_i represent the number of cells and the size of the diamond-TPMS structure along the x_0 , y_0 and z_0 directions, respectively. T is a geometric parameter that controls the relative density of the diamond-TPMS structure[100]. The solid region enclosed by $U < 0$ was chosen to generate a diamond-TPMS lattice, while various T was chosen (-0.5, -0.25, 0, 0.25, and 0.5) to produce microlattice with various relative densities $\bar{\rho}$ (30%, 40%, 50%, 60%, and 70%).

Structural analysis: Structural analyses, including 3D Fast Fourier Transform (3D-FFT) analysis, surface curvature analysis, and surface area analysis, were performed on representative cubic volumes of ossicles and the generated diamond-TPMS microlattices, respectively.

3D Fast Fourier Transform (3D-FFT) analysis was performed on the 3D binary data of cubic volumes of ossicles using the 3D-FFT module in Avizo 2019.2 (Thermo Fisher Scientific. MA, USA). The 3D logarithmic plot of the 3D-FFT data was used for visualization[4].

A customized Python script was developed to generate the binary image slices of the diamond-TPMS microlattice obtained from Eq. (1), which were subsequently fed to Avizo to generate corresponding Standard Triangle Language (STL) models. These STL models were used for surface curvature analysis and surface-area-to-volume ratio (SAV) calculations. The surface curvature analysis module in Avizo was used to obtain the principal curvatures, i.e., minimum and maximum curvatures (κ_1 and κ_2). The mean surface curvature, *H*, of each node was calculated using $H = (\kappa_1 + \kappa_2)/2$. The interfacial shape distribution (ISD) of κ_1 versus κ_2 was plotted using OriginPro 2016 (OriginLab. MA, USA). SAV is calculated by dividing the total surface area of a unit cell (*A*) of the diamond-TPMS microlattices by the total volume of the unit cell (i.e., the volume occupied by the unit cell, *V*) as:

$$SAV = \frac{A}{V} \qquad (9.2.2),$$

Therefore, SAV is dependent on the unit cell size and the unit for SAV is the inverse of the unit of length (i.e., μm^{-1}).

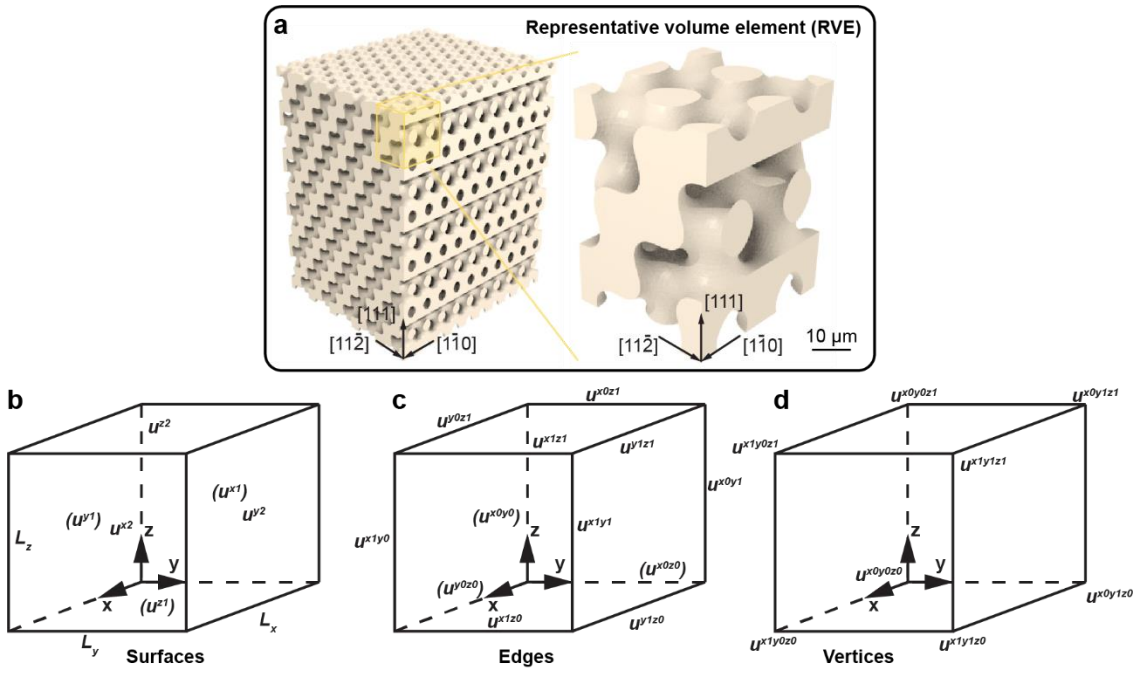


Figure 9.1. Simulation model and periodic boundary conditions. (**a**) Representative volume element (RVE) for mechanical simulations. (**b-d**) Nodal displacements of surfaces (**b**), edges (**c**), and vertices (**d**) in the RVE.

3D elastic property prediction workflow: The constituent solid calcite and various diamond-TPMS models were constructed for mechanical comparison (**Fig. 9.5a**). To predict the 3D elastic properties of these models, a four-step workflow was proposed (**Fig. 9.5b**): (1) configurations of material properties and periodic boundary conditions (PBCs) for FE simulations on all diamond-TPMS models with imposed compressive strain such as ε_{33} and shear strain such as γ_{23}, (2) computational simulations of the full stiffness matrix of the diamond-TPMS models, (3) transformations of the full stiffness matrix obtained from simulations to calculate elastic properties in any arbitrary 3D directions, and (4) visualization of the 3D elastic property based on the calculated directional elastic properties. The detailed modeling and workflow were introduced as follows.

Structural modeling: Four models were constructed for mechanical simulations, including the constituent solid calcite, diamond-TPMS microlattice with equivalent isotropic calcite (I-dTPMS), dual-scale diamond-TPMS microlattices (DS-dTPMS) as observed in starfish ossicles, and DS-dTPMS (180°) which is a modified DS-dTPMS with calcite rotated 180° about its c-axis (**Fig. 9.5a**). To build the DS-dTPMS, the diamond-TPMS microlattice generated using Eq. (9.2.1) was first rotated to a new coordinate system with three principal directions of $[1\bar{1}0]$, $[11\bar{2}]$, and $[111]$. These directions correspond to the $[1\bar{2}10]$, $[10\bar{1}0]$, and $[0001]$ directions of calcite as observed in the ossicles, respectively[199,265]. We further denote these three directions as 1, 2, and 3 directions. Therefore, DS-dTPMS (180°) has $[1\bar{1}0]$ and $[11\bar{2}]$ directions of the diamond-TPMS microlattice aligned with the $[\bar{1}2\bar{1}0]$ and $[\bar{1}010]$ directions of calcite, respectively. The representative volume elements (RVE) of diamond-TPMS microlattice based on these configurations measure 49.0 μm, 42.4 μm, and 60.0 μm along $[1\bar{1}0]$, $[11\bar{2}]$, and $[111]$ directions, respectively, where the branch length was set 15.0 μm, following the previous measurement of starfish ossicles (**Fig. 9.1a**)[4].

Finite element (FE) simulations: To obtain the full stiffness matrix of the diamond-TPMS microlattices, we utilized Abaqus/Standard 2016 (Dassault Systems, Vélizy-Villacoublay, France) to perform static mechanical simulations, including uniaxial and shear loadings, on the RVEs of diamond-TPMS microlattice with PBCs.

3D solid mesh and different material parameters were used in the simulations (**Fig. 9.5b**). The RVEs for I-dTPMS, DS-dTPMS, and DS-dTPMS (180°) all contained ca. 3 million quadratic tetrahedral elements (C3D10). To evaluate the effects of mechanical anisotropy at constituent material level, anisotropic and equivalent isotropic calcite

properties were used as material input. For DS-dTPMS and DS-dTPMS (180°), the full stiffness matrix of single-crystalline calcite was used:

$$C^{Calcite} = \begin{pmatrix} c_{11} & c_{12} & c_{13} & c_{14} & 0 & 0 \\ c_{12} & c_{11} & c_{13} & -c_{14} & 0 & 0 \\ c_{13} & c_{13} & c_{33} & 0 & 0 & 0 \\ c_{14} & -c_{14} & 0 & c_{44} & 0 & 0 \\ 0 & 0 & 0 & 0 & c_{44} & c_{14} \\ 0 & 0 & 0 & 0 & c_{14} & c_{66} \end{pmatrix} \quad (9.2.3).$$

Each stiffness coefficient $c_{MN}^{Calcite}$ ($M, N = 1 - 6$ in Voigt notations where $4 \rightarrow 23$, $5 \rightarrow 13$, and $6 \rightarrow 12$) is given in **Table 9.1**[199]. For I-dTPMS, the equivalent isotropic material properties of calcite (elastic modulus $E_{Equivalent}^{Calcite} = 109\ GPa$, Poisson's ratio $v_{Equivalent}^{Calcite} = 0.29$) was also used[199].

Mechanical loadings of compression in 1, 2, and 3 directions, and pure shear in 4, 5, and 6 directions with a strain of 0.1% were conducted on the RVEs (**Fig. 9.5b**). Subsequently, the obtained stress-strain relationships from the simulations were used to calculate all stiffness coefficients of the diamond-TPMS microlattices. Due to the trigonal symmetry, the stiffness matrices for I-dTPMS, DS-dTPMS, and DS-dTPMS (180°) in the orthogonal system with bases of $[1\bar{1}0]$, $[11\bar{2}]$, and $[111]$ share the same form as following:

$$C^{I/DS-dTPMS} = \begin{pmatrix} c_{11}^{I/DS-dTPMS} & c_{12}^{I/DS-dTPMS} & c_{13}^{I/DS-dTPMS} & c_{14}^{I/DS-dTPMS} & 0 & 0 \\ c_{12}^{I/DS-dTPMS} & c_{11}^{I/DS-dTPMS} & c_{13}^{I/DS-dTPMS} & -c_{14}^{I/DS-dTPMS} & 0 & 0 \\ c_{13}^{I/DS-dTPMS} & c_{13}^{I/DS-dTPMS} & c_{33}^{I/DS-dTPMS} & 0 & 0 & 0 \\ c_{14}^{I/DS-dTPMS} & -c_{14}^{I/DS-dTPMS} & 0 & c_{44}^{I/DS-dTPMS} & c_{44}^{I/DS-dTPMS} & c_{14}^{I/DS-dTPMS} \\ 0 & 0 & 0 & 0 & c_{14}^{I/DS-dTPMS} & c_{66}^{I/DS-dTPMS} \\ 0 & 0 & 0 & 0 & & \end{pmatrix} \quad (9.2.4).$$

PBCs were used in the simulations of diamond-TPMS microlattices with anisotropic and equivalent isotropic calcite properties, respectively, as shown in **Fig. 9.1b-d**. The PBCs

are imposed on the opposite surfaces, edges, and vertices, separately, where the equations of PBCs are shown as follow:

$$\begin{cases} \dfrac{u_n^{x2} - u_n^{x1}}{L_x} - H_{x,n} = 0 \\ \dfrac{u_n^{y2} - u_n^{y1}}{L_y} - H_{y,n} = 0 \\ \dfrac{u_n^{z2} - u_n^{z1}}{L_z} - H_{z,n} = 0 \end{cases} \quad (9.2.5),$$

$$\begin{cases} u_n^{x1y1} - u_n^{x0y0} - L_x H_{x,n} - L_y H_{y,n} = 0 \\ u_n^{x0y1} - u_n^{x1y0} - L_x H_{x,n} + L_y H_{y,n} = 0 \\ u_n^{x1z1} - u_n^{x0z0} - L_x H_{x,n} - L_z H_{z,n} = 0 \\ u_n^{x1z0} - u_n^{x0z1} - L_x H_{x,n} + L_z H_{z,n} = 0 \\ u_n^{y1z1} - u_n^{y0z0} - L_y H_{y,n} - L_z H_{z,n} = 0 \\ u_n^{y1z0} - u_n^{y0z1} - L_y H_{y,n} + L_z H_{z,n} = 0 \end{cases} \quad (9.2.6),$$

$$\begin{cases} u_n^{x1y1z1} - u_n^{x0y0z0} - L_x H_{x,n} - L_y H_{y,n} - L_z H_{z,n} = 0 \\ u_n^{x1y1z0} - u_n^{x0y0z1} - L_x H_{x,n} - L_y H_{y,n} + L_z H_{z,n} = 0 \\ u_n^{x1y0z0} - u_n^{x0y1z1} + L_x H_{x,n} - L_y H_{y,n} - L_z H_{z,n} = 0 \\ u_n^{x1y0z1} - u_n^{x0y1z0} - L_x H_{x,n} + L_y H_{y,n} - L_z H_{z,n} = 0 \end{cases} \quad (9.2.7),$$

where $H_{m,n}$ denotes the component of displacement gradient $\boldsymbol{H}$ in m row and n column (m,n denote the surface normal and displacement direction, respectively, $m,n = x,y,or\ z$). Examples of the imposed displacement gradients of uniaxial compression in 3 direction and pure shear in 4 direction were given by Eq. (9.2.8) and (9.2.9) (**Fig. 9.5b**):

$$\boldsymbol{H} = \begin{bmatrix} 0 & 0 & 0 \\ 0 & 0 & 0 \\ 0 & 0 & \varepsilon \end{bmatrix} \quad (9.2.8),$$

$$\boldsymbol{H} = \begin{bmatrix} 0 & 0 & 0 \\ 0 & 0 & \gamma \\ 0 & \gamma & 0 \end{bmatrix} \quad (9.2.9),$$

where ε denotes the uniaxial strain and γ denotes the shear strain.

Table 9.1 Anisotropic and the homogenized equivalent isotropic material properties of calcite.

Anisotropic elastic constants (GPa)						
c_{11}	c_{12}	c_{13}	c_{14}	c_{33}	c_{44}	c_{66}
165.1	62.7	58.9	17.3	105.1	39.3	50.5

Equivalent isotropic material properties	
$E^{Iso}_{Calcite}$ (GPa)	Poisson's ratio
109	0.29

3D transformation of stiffness matrix: After obtaining the stiffness matrices for diamond-TPMS microlattices, the matrices were transformed to calculate the elastic property values, i.e., elastic modulus ($E_{[hkl]}$), shear modulus ($G^{12}_{[hkl]}$), and Poisson's ratio ($v^{12}_{[hkl]}$), in any arbitrary directions $[hkl]$ in 3D (**Fig. 9.5b**). Here $[hkl]$ represents the direction in an orthogonal coordinate system in which 1, 2, and 3 directions defined above are considered as $[100]$, $[010]$, and $[001]$ directions, respectively. To calculate the properties, the stiffness matrix obtained from simulations was transformed to the direction $[hkl]$ using:

$$C' = NCN^T \qquad (9.2.10),$$

where C and C' are the original and transformed stiffness matrices, respectively, and N^T is the transpose of the transformation matrix N as:

$$N = \begin{bmatrix} R_{11}^2 & R_{12}^2 & R_{13}^2 & 2R_{12}R_{13} & 2R_{11}R_{13} & 2R_{11}R_{12} \\ R_{21}^2 & R_{22}^2 & R_{23}^2 & 2R_{22}R_{23} & 2R_{21}R_{23} & 2R_{21}R_{22} \\ R_{31}^2 & R_{32}^2 & R_{33}^2 & 2R_{32}R_{33} & 2R_{31}R_{33} & 2R_{31}R_{32} \\ R_{21}R_{31} & R_{22}R_{32} & R_{23}R_{33} & R_{22}R_{33}+R_{23}R_{32} & R_{21}R_{33}+R_{23}R_{31} & R_{22}R_{31}+R_{32}R \\ R_{11}R_{31} & R_{12}R_{32} & R_{13}R_{33} & R_{32}R_{13}+R_{12}R_{33} & R_{11}R_{33}+R_{13}R_{31} & R_{11}R_{32}+R_{12}R \\ R_{11}R_{21} & R_{22}R_{12} & R_{13}R_{23} & R_{12}R_{23}+R_{22}R_{13} & R_{13}R_{21}+R_{23}R_{11} & R_{12}R_{21}+R_{22}R \end{bmatrix}$$

(9.2.11).

The transformation of the full stiffness matrix yields the following equations for calculating the elastic modulus, shear modulus, and Poisson's ratio in arbitrary directions:

$$\begin{cases} E_{[hkl]} = \dfrac{1}{S'_{11}} \\ \bar{G}^{12}_{[hkl]} = \dfrac{1}{2\pi}\displaystyle\int_0^{2\pi} G^{12}_{[hkl],\theta}\, d\theta \\ \bar{v}^{12}_{[hkl]} = \dfrac{1}{2\pi}\displaystyle\int_0^{2\pi} v^{12}_{[hkl],\theta}\, d\theta \end{cases} \qquad (9.2.12),$$

Where $E_{[hkl]}$ is the elastic modulus, $\bar{G}^{12}_{[hkl]}$ and $\bar{v}^{12}_{[hkl]}$ are averaged shear modulus and averaged Poisson's ratio, respectively, over 360° of θ, θ is defined as the angle between y'' (i.e., the transformed 2 direction) and any arbitrary direction j on the $y'' - z''$ plane (i.e., the transformed 2-3 plane) as shown in **Fig. 9.2**, $S' = (C')^{-1}$ is the transformed compliant matrix. The maximum and minimum shear modulus and Poisson's ratio on the arbitrary plane (hkl) can also be obtained based on Eq. (9.2.12). These directional values of elastic properties can be visualized as 3D contours (**Fig. 9.5b**).

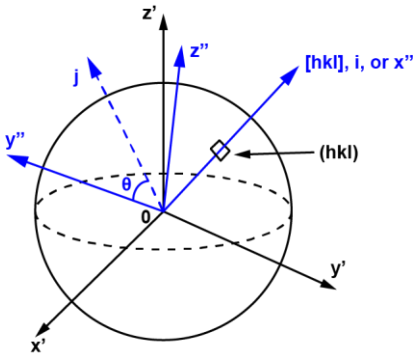


Figure 9.2. Schematics of the transformation of the stiffness matrix to find properties in any arbitrary orientation $[hkl]$.

9.3. Results

9.3.1. Dual-scale diamond-TPMS microlattice in ossicles

The skeletal system of the starfish *P. nodosus* consists of an assembly of calcite-based, millimeter-sized ossicles (**Fig. 9.3a**). The ossicles have a periodic lattice-like stereom structure which has been previously determined to be a diamond-TPMS microlattice with a relative density of ca. 50 vol% (**Fig. 9.3b-d**)[4]. **Fig. 9.3c,d** show a representative volume isolated from an ossicle and the corresponding 3D-FFT result, demonstrating the diamond-TPMS microlattice structure of "$Fd\bar{3}m$" symmetry (unit cell size of 34.6 ± 8.0 μm and branch length of 15.0 ± 3.4 μm). An RVE of diamond-TPMS microlattice with 50% relative density as shown in **Fig. 9.3e** can be used as an idealized model to represent the microlattice structure of ossicles. We also observed that the [111] direction of the diamond-TPMS microlattice in ossicles is usually aligned with the normal direction of the starfish, which is defined as the direction perpendicular to the plane formed by the five arms of the starfish (**Fig. 9.3b**)[4].

In addition to the lattice-level single-crystallinity, each ossicle is made of single-crystalline calcite at atomic-level[4]. This is evident from the epitaxial overgrowth experiment, where the overgrown calcite crystals all follow the same orientation as the underlying ossicle (**Fig. 9.3f**). This overgrowth experiment also reveals that the [111] direction of the diamond lattice is aligned with the c-axis of calcite as schematically shown in **Fig. 9.3g**. Furthermore, the three-fold symmetry of the basal plane of calcite is aligned with the three-fold symmetry of the diamond lattice: the non-[111] branches in the diamond lattice generally follow the direction of the intersected edges of two adjacent

$\{10\bar{1}4\}$ cleavage planes of calcite, i.e., the $\langle 4\bar{4}0\bar{1}\rangle$ directions[4] (**Fig. 9.3g** and **Fig. 9.4**). This results in the so-called dual-scale single-crystalline microlattice.

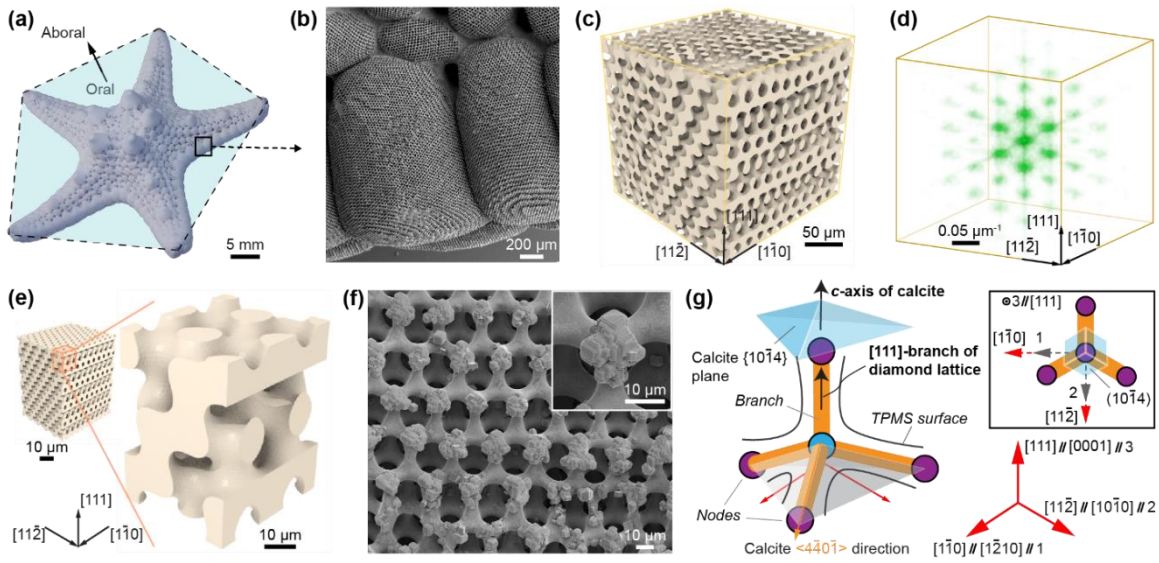


Figure 9.3. Dual-scale crystallographic coalignment in the ossicles of starfish *Protoreaster nodosus*. (**a**) The endoskeleton of starfish *P. nodosus*, showing radially-arranged arrays of ossicles and the normal direction (black solid arrow) from the oral to aboral sides. The cyan plane roughly indicates the plane of the starfish perpendicular to the normal direction. (**b**) SEM image of the ossicles where the exposed crystallographic planes of (111) are closely parallel to the plane of starfish. (**c**) A cubic volume of stereom in the ossicle. Here, the [111] direction is along the normal direction of the starfish's skeleton. (**d**) 3D-FFT pattern of the cubic volume of an ossicle with diffraction spots. (**e**) The RVE of diamond-TPMS microlattice as a model to represent the lattice-scale structure of ossicles. (**f**) Scanning electronic microscope (SEM) image of the calcite crystals overgrown on the underlying ossicle, showing the coalignment between crystallographic orientations of constituent calcite and the diamond-TPMS microlattice. (Image and experiment of

crystal overgrowth credit: Dr. Ting Yang) (**g**) Schematic of the dual-scale coalignment between atomic-scale crystallography of calcite and lattice-scale crystallography of diamond-TPMS microlattice in ossicles.

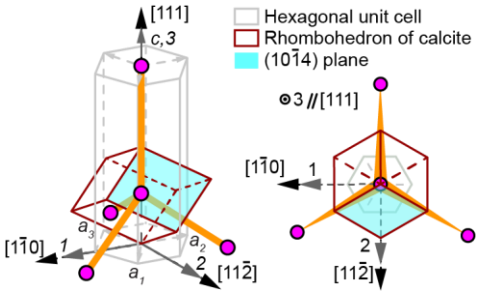


Figure 9.4. Detailed dual-scale coalignment in starfish ossicle.

9.3.2. 3D elastic properties

To evaluate the mechanical properties of the dual-scale microlattice in starfish ossicles, we built four models for mechanical modeling comparison as introduced in Methods: (1) the solid calcite, (2) I-dTPMS: a diamond-TPMS microlattice with equivalent isotropic calcite properties, (3) DS-dTPMS: a dual-scale diamond-TPMS microlattice as observed in ossicles, and (4) DS-dTPMS (180°): a modified DS-dTPMS microlattice with calcite rotated by 180° about its c-axis (**Fig. 9.5a**). The 3D elastic properties of these four models were then calculated using the four-step workflow described in Methods, including (1) the FE simulation configurations of material properties, PBCs, and mechanical loading, (2) calculation of the full stiffness matrices of all four models, (3) 3D transformation of the obtained stiffness matrices, and (4) visualization of the 3D elastic property contours (**Fig. 9.5b**).

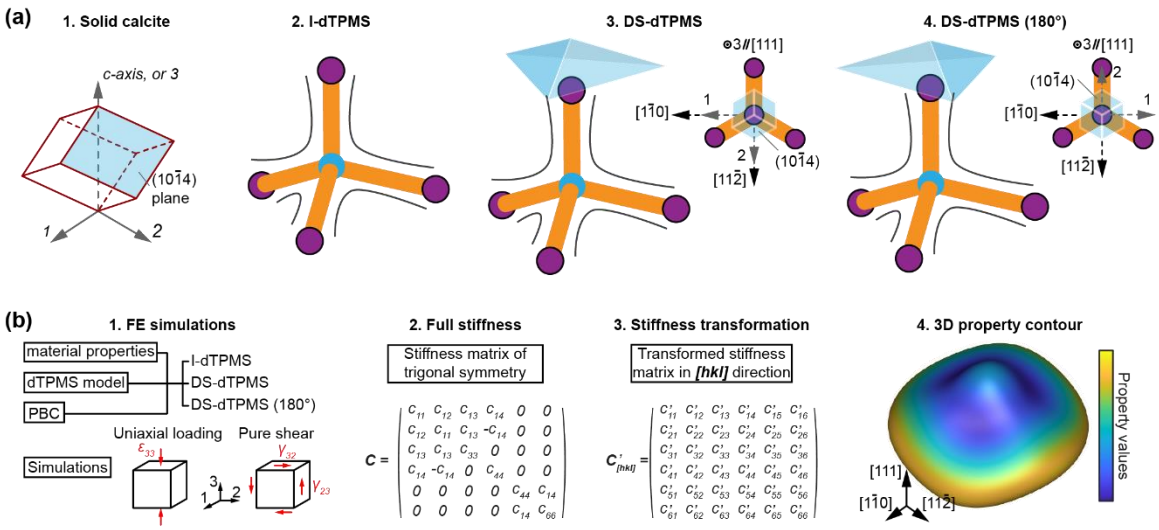


Figure 9.5. Introduction to models and methodology. (**a**) Schematic models of (1) single-crystalline solid calcite, (2) I-dTPMS, (3) DS-dTPMS, and (4) DS-dTPMS (180°). Here, DS-dTPMS represent an idealized model of ossicles. (**b**) Methodology of the elastic properties prediction, including (1) material properties and PBC configurations for FE simulations, (2) calculation of the full stiffness matrix of four models, (3) transformation of the full stiffness matrix to calculate elastic properties in any arbitrary $[hkl]$ directions, and (4) visualization of the 3D elastic property contour.

We first conducted detailed analysis of the mechanical properties of the DS-dTPMS in starfish ossicles in comparison to solid calcite and I-dTPMS microlattice. Representative 3D contours of elastic modulus ($E_{[hkl]}$), averaged shear modulus ($\bar{G}^{12}_{[hkl]}$), and averaged Poisson's ratio ($\bar{\nu}^{12}_{[hkl]}$) of the solid calcite, I-dTPMS microlattice, and DS-dTPMS microlattice at 50% relative density, were shown in **Fig. 9.6**. The maximum, and minimum shear modulus and Poisson's ratio contours (i.e., G_{max}, ν_{max}, G_{min}, and ν_{min}), respectively, as well as 2D visualizations of all elastic properties of all models were summarized in **Fig. 9.7-9.12**.

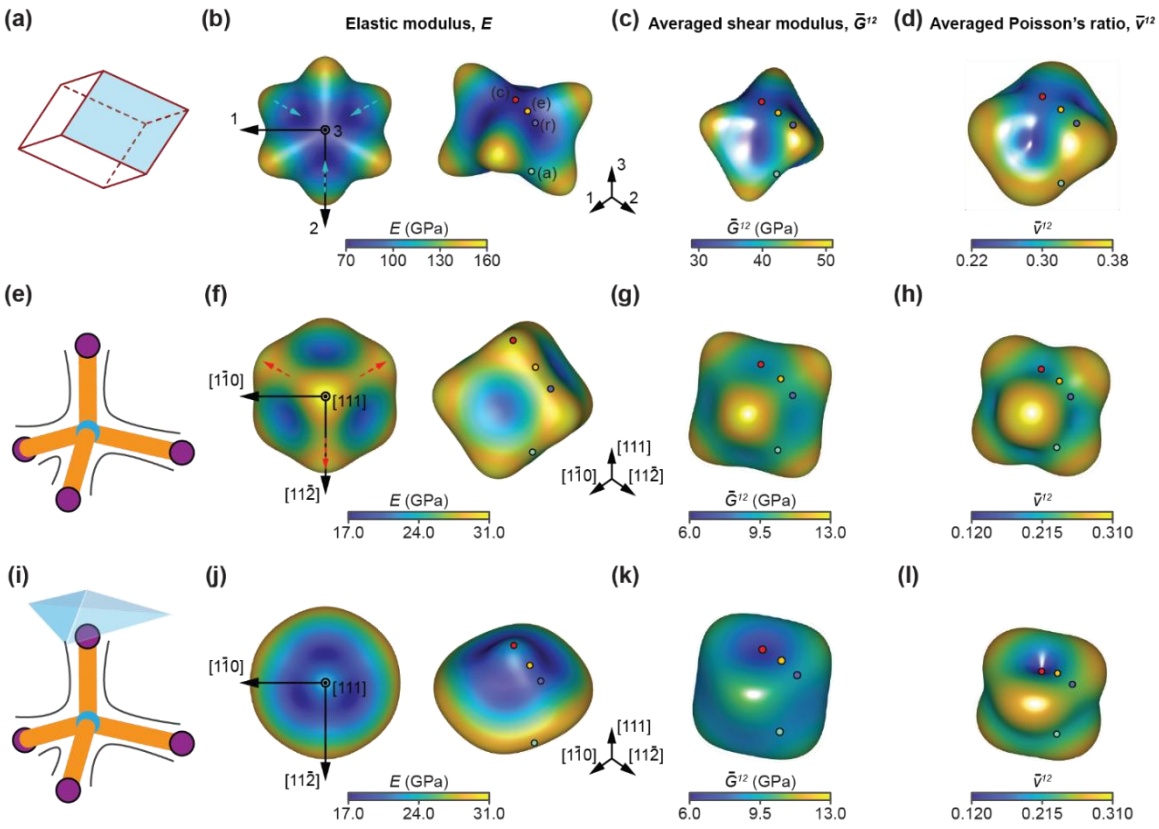


Figure 9.6. 3D elastic property contours of single-crystalline calcite, I-dTPMS, and DS-dTPMS. (**a**) Geometrical representation of the calcite's crystallographic symmetry. (**b-d**) 3D contours of elastic modulus $E_{[hkl]}$ (**b**), averaged shear modulus $\bar{G}^{12}_{[hkl]}$ (**c**), and averaged Poisson's ratio $\bar{\nu}^{12}_{[hkl]}$ (**d**) of calcite, respectively. The top view (-3 direction) of the 3D elastic modulus contour of calcite is shown, in which the cyan arrows indicate the most compliant directions of calcite. (**e**) Geometrical representation of crystallographic symmetry of I-dTPMS. (**f-h**) 3D contours of elastic modulus $E_{[hkl]}$ (**f**), averaged shear modulus $\bar{G}^{12}_{[hkl]}$ (**g**), and averaged Poisson's ratio $\bar{\nu}^{12}_{[hkl]}$ (**h**) of I-dTPMS, respectively. The $[\bar{1}\bar{1}\bar{1}]$ view of the 3D elastic modulus contour of I-dTPMS is shown, in which the red arrows indicate the stiffest directions of I-dTPMS. (**i**) Geometrical representation of the

resultant crystallographic symmetry of DS-dTPMS. (**j-l**) 3D contours of elastic modulus $E_{[hkl]}$ (**j**), averaged shear modulus $\bar{G}^{12}_{[hkl]}$ (**k**), and averaged Poisson's ratio $\bar{\nu}^{12}_{[hkl]}$ (**l**) of DS-dTPMS, respectively. The view along $[\bar{1}\bar{1}\bar{1}]$ direction of the 3D elastic modulus contour of DS-dTPMS is shown. Here, the red (c), yellow (e), blue (r), and green (a) dots on all 3D elastic property contours indicate the property values of the c-axis direction, plane normal of $(10\bar{1}8)$, plane normal of $(10\bar{1}4)$, and $[2\bar{1}\bar{1}0]$ direction (a_1-axis). Their values are summarized in **Table 9.3**.

For solid calcite, the elastic modulus contour exhibits a three-fold symmetry about its c-axis, resembling a 6-pointed star-like shape, agrees with the previous result (**Fig. 9.6a,b, Table 9.2**)[199]. For some characteristic planes of calcite, such as $(10\bar{1}4)$, $(10\bar{1}8)$, and (0001), the moduli are calculated as 72.4 GPa, 74.8 GPa and 74.6 GPa along their plane normals, respectively, which agree well with the previous values obtained from simulations and indentation experiments (**Table 9.3**)[4,118,266]. We also found that the maximum elastic moduli of 152.9 GPa are along $\langle 5\bar{5}01\rangle$ directions, while the minimum elastic moduli of 72.0 GPa are along $\langle 10\bar{1}\frac{23}{50}\rangle$ directions (**Fig. 9.6b**). Moreover, the 3D contours of $\bar{G}^{12}_{[hkl]}$ and $\bar{\nu}^{12}_{[hkl]}$ of calcite also show the trigonal symmetry where the directions with high $E_{[hkl]}$ has relatively low $\bar{G}^{12}_{[hkl]}$ and $\bar{\nu}^{12}_{[hkl]}$ (**Fig. 9.6b-d**).

For I-dTPMS microlattice, the elastic modulus contour exhibits a three-fold symmetry about the [111] direction due to the trigonal symmetry of the diamond-TPMS lattice and possesses a cube-like shape (**Fig. 9.6e,f, Table 9.2**)[267]. Furthermore, the calculated elastic moduli of $[1\bar{1}0]$, [111], and [100] directions are 27.2 GPa, 30.9 GPa, and 20.1 GPa, which match with the previously reported values[4,100]. Again, we found that the maximum elastic

moduli of 30.9 GPa are along ⟨111⟩ directions, while the minimum elastic moduli of 20.1 GPa are along ⟨100⟩ directions (**Fig. 9.6f**). Similarly, **Fig. 9.6g,h** show the 3D contours of $\bar{G}^{12}_{[hkl]}$ and $\bar{\nu}^{12}_{[hkl]}$ of I-dTPMS, further demonstrating that the directions with high $E_{[hkl]}$ has relatively low $\bar{G}^{12}_{[hkl]}$ and $\bar{\nu}^{12}_{[hkl]}$ (**Fig. 9.6g-h**).

For DS-dTMPS microlattice, its elastic modulus contour merges the morphological characteristics of the elastic modulus contours of calcite and I-dTPMS together, resulting in a "Saturn"-like geometry with trigonal symmetry (**Fig. 9.6i,j, Table 9.2**). In this case, the stiff [111] direction of the diamond-TPMS microlattice is coaligned with the compliant c-axis of calcite (**Fig. 9.6i,j**)[4]. In addition, the directions of minimum elastic modulus ($[0\bar{1}1\frac{23}{50}]$, $[\bar{1}10\frac{23}{50}]$, and $[10\bar{1}\frac{23}{50}]$ directions, respectively, cyan arrows in **Fig. 9.6b**) in calcite are approximately aligned (22.6° difference relative to c-axis) with the directions of the highest elastic modulus in I-dTPMS microlattice ($[1\bar{1}\bar{1}]$, $[\bar{1}1\bar{1}]$ and $[\bar{1}\bar{1}1]$ directions, red arrows in **Fig. 9.6f**). Therefore, the dual-scale coalignment in DS-dTPMS allows the elastic modulus compensation in 3D and results in a nearly transversely isotropic shape of its elastic modulus contour (**Fig. 9.6j**). This morphological combination can also be observed in the $\bar{G}^{12}_{[hkl]}$ and $\bar{\nu}^{12}_{[hkl]}$ contours (**Fig. 9.6k,l**).

Table 9.2. Summary of the coefficients of stiffness matrix of diamond-TPMS microlattice obtained from simulations. (Iso.: the diamond-TPMS microlattice with equivalent isotropic properties, isotropic diamond-TPMS; Ani.: the diamond-TPMS microlattice with anisotropic calcite properties, dual-scale diamond-TPMS)

Constant	T = -0.5	T = -0.25	T = 0	T = 0.25	T = 0.5

(GPa)	Iso.	Ani.	Iso.	Ani.	Iso.	Ani.	Iso.	Ani.	Iso.	Ani.
c_{11}	13.3	13.2	21.9	21.9	32.5	32.8	45.8	46.7	62.8	65.6
c_{12}	4.3	4.1	6.8	6.7	10.2	10.1	14.7	14.9	21.2	21.5
c_{13}	3.3	1.7	5.4	3.0	8.4	5.3	12.9	9.4	19.5	16.0
c_{14}	1.3	0.9	2.0	1.2	2.4	1.0	2.7	-0.03	2.4	-2.3
c_{33}	14.2	10.0	23.3	16.2	34.3	23.8	47.7	33.3	64.6	45.6
c_{44}	3.6	2.5	6.2	4.3	9.5	6.8	13.6	10.3	19.1	15.3
c_{66}	4.5	4.5	7.5	7.5	11.2	11.2	15.5	15.7	20.8	21.7

Table 9.3. Elastic moduli (E), averaged shear moduli (G^{12}), and averaged Poisson's ratios (v^{12}) of normal directions of selected crystallographic planes of solid calcite, I-dTPMS, and DS-dTPMS, respectively.

	Directions	E (GPa)	$\bar{G}^{12}$ (GPa)	$\bar{v}^{12}$ (GPa)
Solid calcite	[0001]	74.6	33.4	0.26
	$N_{(10\bar{1}8)}$	72.4	37.7	0.29
	$N_{(10\bar{1}4)}$	74.8	45.5	0.33
	$[2\bar{1}\bar{1}0]$	112.4	41.3	0.35
I-dTPMS	[0001]	30.9	8.9	0.20
	$N_{(10\bar{1}8)}$	27.9	9.8	0.23
	$N_{(10\bar{1}4)}$	27.7	9.8	0.23
	$[2\bar{1}\bar{1}0]$	27.2	10.0	0.23
Ds-dTPMS	[0001]	22.5	6.8	0.12
	$N_{(10\bar{1}8)}$	19.8	8.0	0.20

$N_{(10\bar{1}4)}$	19.6	9.2	0.24
$[2\bar{1}\bar{1}0]$	28.7	8.7	0.23

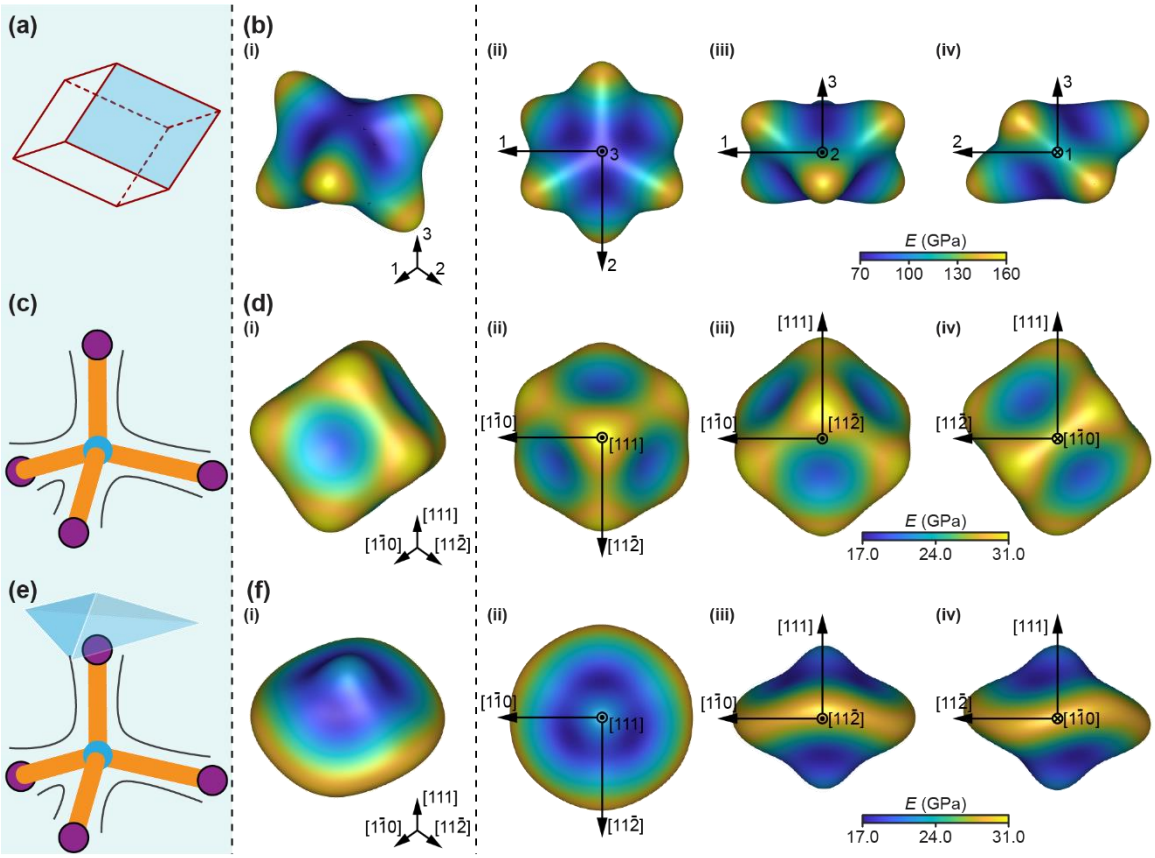


Figure 9.7. 3D elastic modulus contours and their 2D projection views of solid calcite, I-dTPMS, and DS-dTPMS. (**a,b**) Geometrical representation of the calcite's crystallography (**a**) and the 3D elastic modulus contour as well as its 2D visualizations (**b**). (**c,d**) Geometrical representation of crystallography of the I-dTPMS (**c**) and the corresponding 3D elastic modulus contour as well as the 2D visualizations (**d**). (**e,f**) Geometrical representation of the dual-scale coalignment of DS-dTPMS (**e**) and the 3D elastic modulus contour as well as the 2D visualizations (**f**).

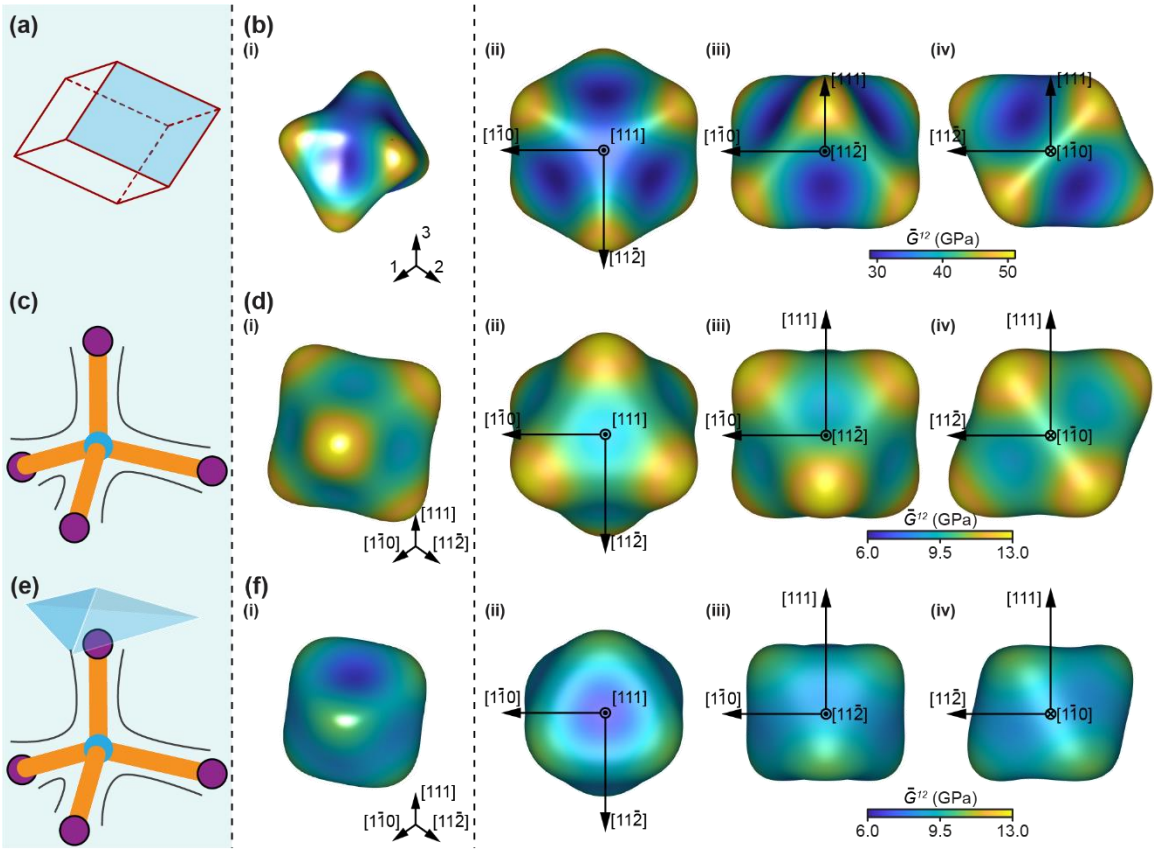


Figure 9.8. 3D averaged shear modulus contours and their 2D projection views of solid calcite, I-dTPMS, and DS-dTPMS. (**a,b**) Geometrical representation of the calcite's crystallography (**a**) and the 3D averaged shear modulus contour as well as its 2D visualizations (**b**). (**c,d**) Geometrical representation of crystallography of the I-dTPMS (**c**) and the corresponding 3D averaged shear modulus contour as well as the 2D visualizations (**d**). (**e,f**) Geometrical representation of the dual-scale coalignment of DS-dTPMS (**e**) and the 3D averaged shear modulus contour as well as the 2D visualizations (**f**).

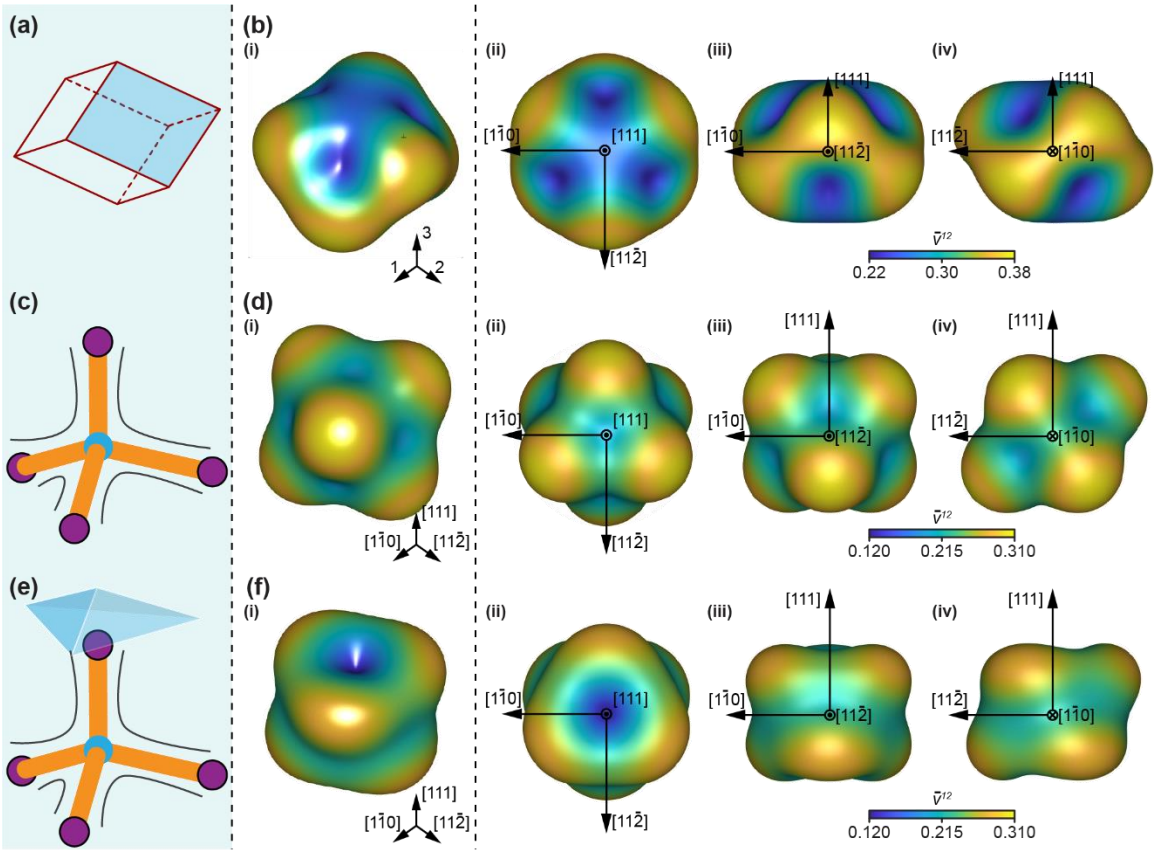


Figure 9.9. 3D averaged Poisson's ratio contours and their 2D projection views of solid calcite, I-dTPMS, and DS-dTPMS. (**a,b**) Geometrical representation of the calcite's crystallography (**a**) and the 3D averaged Poisson's ratio contour as well as its 2D visualizations (**b**). (**c,d**) Geometrical representation of crystallography of the I-dTPMS (**c**) and the corresponding 3D averaged Poisson's ratio contour as well as the 2D visualizations (**d**). (**e,f**) Geometrical representation of the dual-scale coalignment of DS-dTPMS (**e**) and the 3D averaged Poisson's ratio contour as well as the 2D visualizations (**f**).

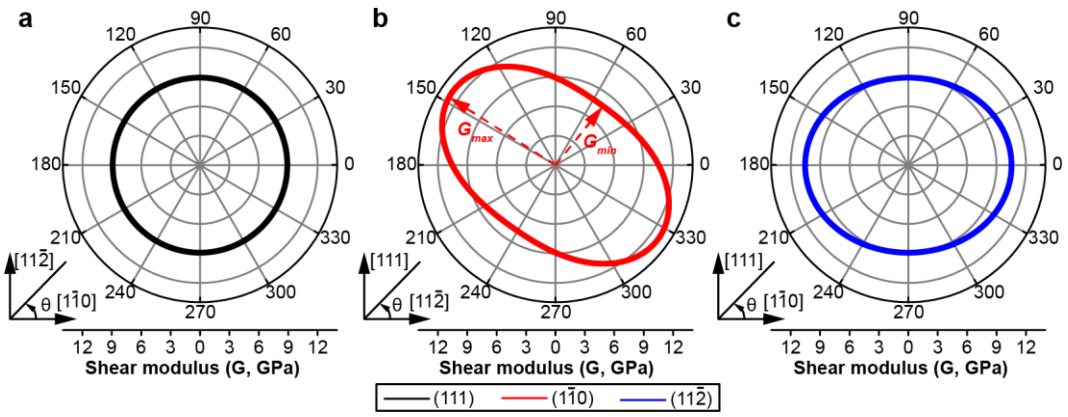


Figure 9.10. Shear modulus of three selected crystallographic planes of isotropic diamond-TPMS. (**a-c**) 2D shear modulus contours of the (111) (**a**), $(1\bar{1}0)$ (**b**), and $(11\bar{2})$ (**c**) planes, respectively. The minimum (G_{min}) and maximum (G_{max}) shear moduli on an arbitrary plane are defined in (**b**). The angle θ with respect to the 1 (or [110]), 2, and 3 directions are illustrated for each 2D contour.

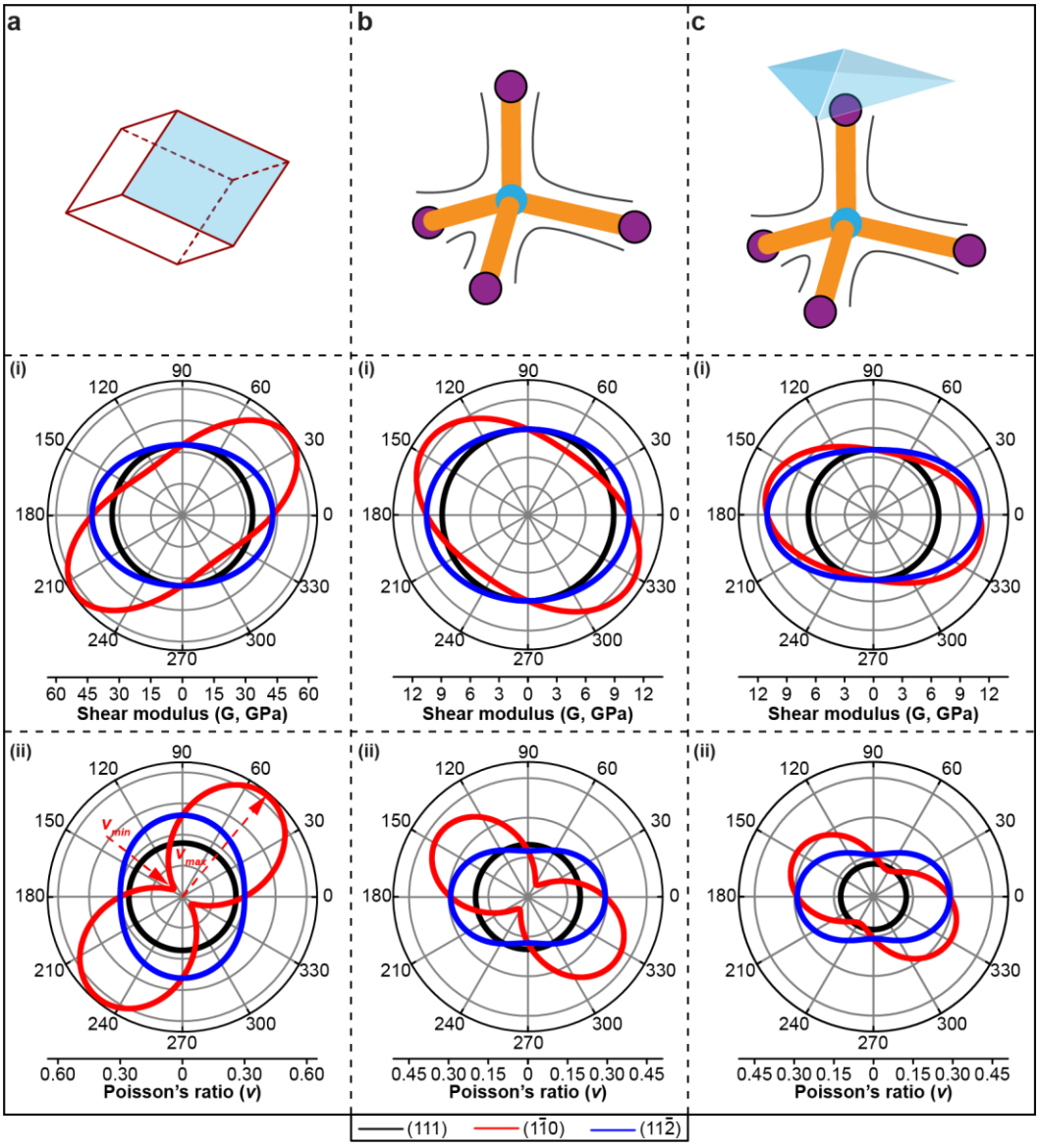


Figure 9.11. Shear moduli and Poisson's ratios on selected crystallographic planes. (**a**) Geometrical representation of the calcite's crystallography and corresponding shear modulus (i) and Poisson's ratio (ii) with respected to angle θ on the $(1\bar{1}0)$, $(11\bar{2})$, and (111) planes. (**b**) Geometrical representation of the crystallography of I-dTPMS and corresponding shear modulus (i) and Poisson's ratio (ii) with respected to angle θ on the $(1\bar{1}0)$, $(11\bar{2})$, and (111) planes. (**c**) Geometrical representation of the crystallography of

DS-dTPMS and corresponding shear modulus (i) and Poisson's ratio (ii) with respected to angle θ on the $(1\bar{1}0)$, $(11\bar{2})$, and (111) planes.

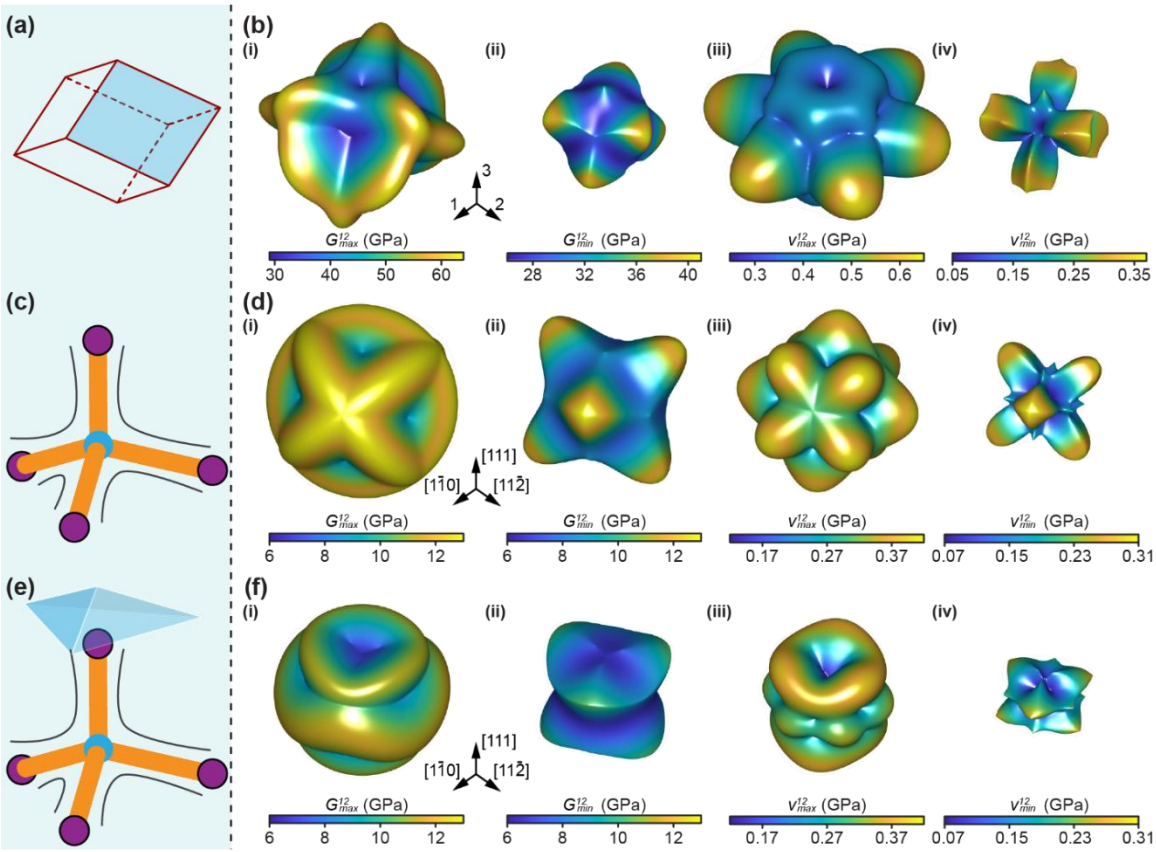


Figure 9.12. 3D maximum and minimum shear modulus and Poisson's ratio contours of solid calcite, I-dTPMS, and DS-dTPMS. (**a,b**) Geometrical representation of the calcite's crystallography (**a**) and the 3D contours of maximum (G^{12}_{max}, v^{12}_{max}) and minimum (G^{12}_{min}, v^{12}_{min}) shear moduli and Poisson's ratios (**b**). (**c,d**) Geometrical representation of the crystallography of the I-dTPMS (**c**) and the corresponding 3D contours of G^{12}_{max}, v^{12}_{max}, G^{12}_{min}, and v^{12}_{min} (**d**). (**e,f**) Geometrical representation of the dual-scale coalignment of DS-dTPMS (**e**) and the 3D contours of G_{max}, v_{max}, G_{min}, and v_{min} (**f**).

We also performed simulations to validate the calculated elastic modulus values at several orientation of the dual-scale diamond-TPMS. Limited by the fabrication of the dual-scale lattice with single-crystalline constituent, we validated the theoretical results of 3D elastic modulus surfaces (**Fig. 9.6**) via computational simulations. We performed compression and shear simulations (0.1% strain) on the RVE along different orientations, including 30°, 45°, 60°, 120°, 135°, and 150° rotation about [111] and $[1\bar{1}0]$ axes, respectively, to obtain the computational results of the elastic modulus (**Fig. 9.13** and **Table 9.3**). As shown in **Fig. 9.13**, by comparing the computational (red dots) and theoretical (black contour line) results of elastic moduli along the aforementioned directions, we found that they agree perfectly with each other. Therefore, our combined computational-theoretical method and the obtained 3D elastic property surfaces of dual-scale microlattice as shown in **Fig. 9.7-9.12** are trustworthy.

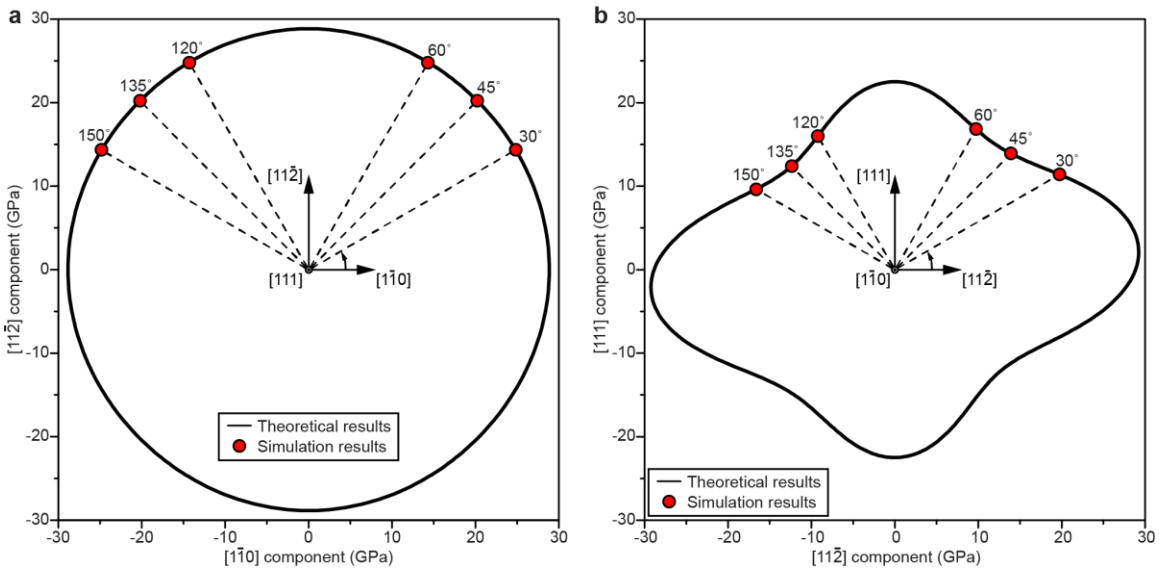


Figure 9.13. Validation of theoretical results via computational simulations. (**a**) 2D contour of theoretical elastic modulus and computational results indicated by red solid

circles on $[1\bar{1}0]$- $[11\bar{2}]$ plane of dual-scale diamond-TPMS. (**b**) 2D contour of theoretical elastic modulus and computational results indicated by red solid circles on $[11\bar{2}]$- [111] plane of dual-scale diamond-TPMS. The distance between origin (0,0) of the plot and the point on contour or red dot is the elastic modulus, while horizontal and vertical axes indicate the components of the elastic modulus along two orthogonal directions.

Table 9.4. Summary of the results to validate the theoretical calculation by computational simulations.

Rotational axis	Elastic modulus at different rotational angle (GPa)					
	30°	45°	60°	120°	135°	150°
$[1\bar{1}0]$-axis (computational)	22.79	19.67	19.43	18.45	17.49	19.18
$[1\bar{1}0]$-axis (theoretical)	22.79	19.66	19.43	18.46	17.52	19.24
[111]-axis (computational)	28.66	28.59	28.61	28.61	28.59	28.66
[111]-axis (theoretical)	28.66	28.60	28.66	28.66	28.60	28.66

9.3.3. Effect of relative density

We next explore how the relative density affects the structural-mechanical properties of the dual-scale microlattice, and whether the often-observed 50% relative density in ossicles possesses any special structural-mechanical significances.

For I-dTPMS, as the relative density increases, the faces of the cube-like shape of the elastic modulus contour become less concave, agreeing with previous results[267] (**Fig. 9.14a**). This leads to an increase in overall mechanical isotropy. For DS-dTPMS, the elastic modulus contour first becomes smoother and more isotropic up to 60% relative density, however, it starts to resemble the morphology of elastic modulus contour of calcite beyond 70% relative density (**Fig. 9.14b** and **Table 9.2**). This is expected since the increase of relative density of the microlattice results in the increased similarity of mechanical properties to its bulk constituent. The change in mechanical isotropy as a function of relative density can be more quantitatively represented by an universal anisotropic index calculated based on the full stiffness matrix (**Fig. 9.14c**)[268]. The higher the index, the lower the mechanical isotropy. The results reveal that the anisotropic indices of DS-dTPMS are always higher than those of the I-dTPMS, where their values are always smaller than that of calcite. The anisotropic indices closely approach to each other as the relative density reaches 60% (**Fig. 9.14c**). Furthermore, for DS-dTPMS, the anisotropic indices of 60% and 70% relative densities are similar, implying a minimal value in between as proposed above (**Fig. 9.14b,c**). Therefore, the dual-scale coalignment in ossicles improves the mechanical isotropy significantly compared to calcite, while the 50% relative density does not maximize the improvement.

Other than the mechanical isotropy, the distribution of elastic modulus values also depends on relative densities. As expected, the higher the relative densities, the larger the elastic modulus (**Fig. 9.14d**). In addition, all distributions show two peaks where one is at the lower end while another is at the higher end. Among them, the DS-dTPMS with 50%

relative density has elastic moduli ranged from 17 to 30 GPa with peaks at ca. 19 and 29 GPa.

Other than mechanical properties, we also investigated the effect of relative density on the structural characteristics of diamond-TPMS microlattice (**Fig. 9.14e-g**). First of all, the diamond-TPMS microlattice with 50% relative density yields the zero mean surface curvature ($H = 0$), while others result in the constant-mean-curvature surfaces (**Fig. 9.14e,9.15,** and **Table 9.5**)[269]. The increase of relative density changes H from positive to negative values, suggesting that the surfaces become less curved (**Fig. 9.14e**). Secondly, we found that SAV of the diamond-TPMS microlattice with relative density of 50% is maximal, regardless of the change of unit cell size (**Fig. 9.14f, Table 9.5,9.6**)[270]. Thirdly, we calculated the throat size (r_{throat}), which is defined as the smallest radius in the void phase, and the minimal solid branch thickness (r_{min}) of the diamond-TPMS microlattice (**Fig. 9.14g**). As expected, the increase of relative density yields lower r_{throat} and higher r_{min}, while at 50% relative density, $r_{throat} \approx r_{min}$. We previously have shown that the small throat size in natural ceramic foams such as sea urchin spines provides an efficient mechanism to locally jam the fractured fragments during deformation, leading to enhanced energy absorption capability[4,96]. Therefore, with the throat size comparable to the minimal branch size at 50% relative density, the structure may achieve efficient jamming for improved toughness.

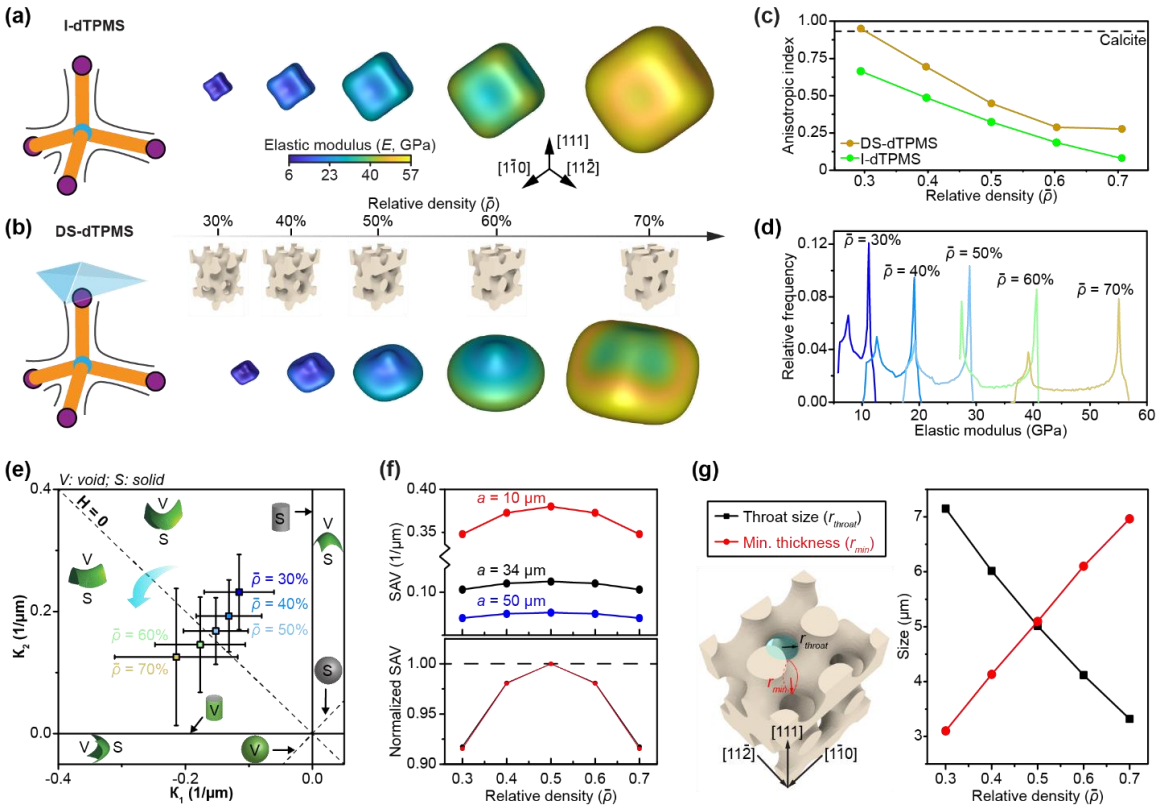


Figure 9.14. Effect of relative density on the mechanics and structure of DS-dTPMS. (**a,b**) Evolution of the 3D elastic modulus contours of the I-dTPMS (**a**) and DS-dTPMS (**b**) with various relative densities. (**c**) Universal anisotropic index of I-dTPMS, and DS-dTPMS with different relative densities, respectively. (**d**) Distribution of elastic modulus of DS-dTPMS with different relative densities. (**e**) Mean surface curvatures of the diamond-TPMS microlattice with 34 μm unit cell size and different relative densities. The standard deviations of principal curvatures κ_1 and κ_2 are used for error bars. (**f**) SAV (surface-area-to-volume ratio) and normalized SAV by the maximum value of various relative densities and unit cell sizes. (**g**) Throat size (r_{throat}) and minimal branch thickness (r_{min}) of diamond-TPMS microlattice with 34 μm unit cell size and different relative densities.

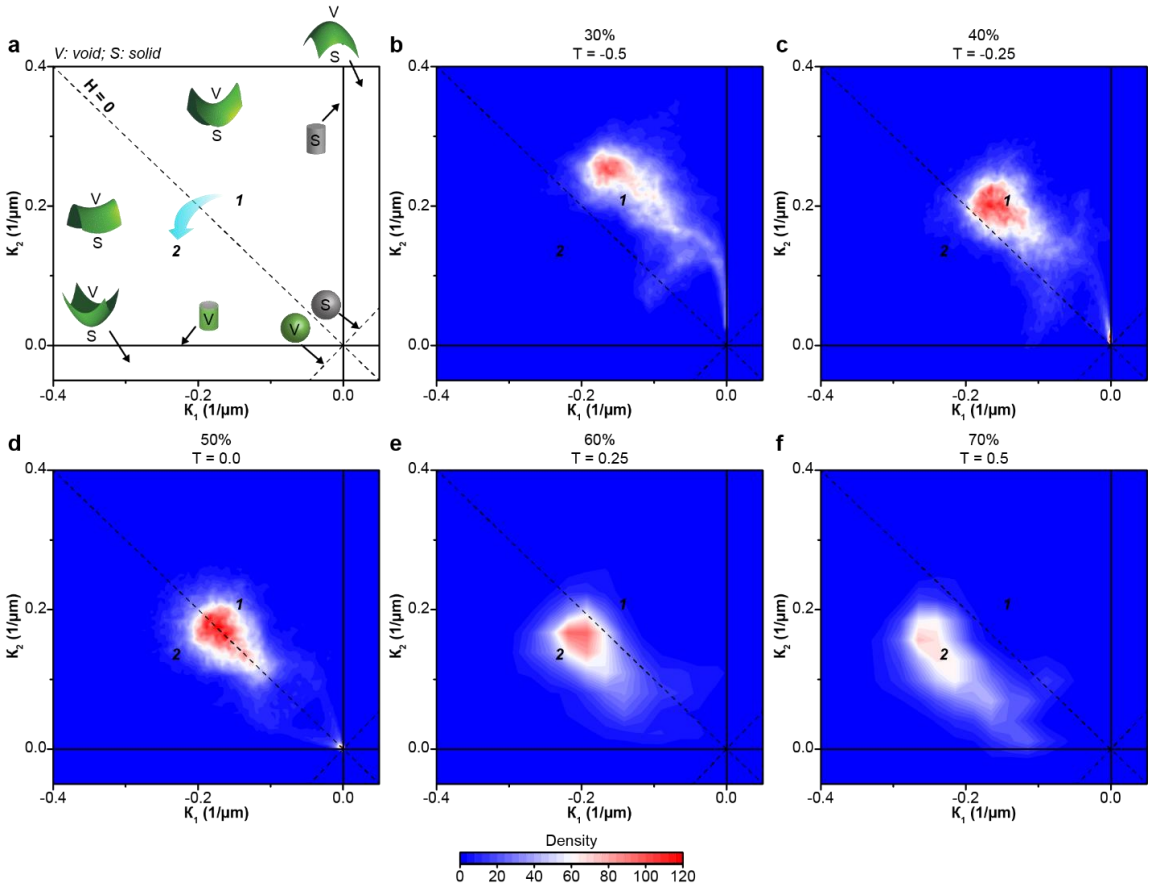


Figure 9.15. Surface curvature analysis. (**a**) Schematic of different types of surfaces in the interfacial shape distribution (ISD) plot. (**b-f**) ISD plots of the diamond-TPMS microlattice with relative density ranged from 30% to 70% and T value ranged from -0.5 to 0.5.

Table 9.5. Mean surface curvatures (*H*), surface area (SA), and surface-to-volume ratio (SAV) of diamond-TPMS microlattices with 34 μm unit cell size generated using different T values.

Constant T	Relative density	Mean curvature (H, μm^{-1})	Surface area (SA, μm^{2})	Surface-to-Volume ratio (SAV, μm^{-1})

-0.5	30%	0.048 ± 0.026	4051.9	0.103
-0.25	40%	0.022 ± 0.025	4331.9	0.110
0	50%	7.5e-6 ± 0.025	4416.3	0.112
0.25	60%	-0.023 ± 0.055	4331.8	0.110
0.5	70%	-0.051 ± 0.088	4051.9	0.103

Table 9.6. Surface area (SA) and surface-to-volume ratio (SAV) of diamond-TPMS microlattices with 10 μm and 50 μm unit cell size generated using different T values.

Constant T	Relative density	Unit cell size = 10 μm		Unit cell size = 50 μm	
		Surface area (SA, μm^2)	Surface-to-Volume ratio (SAV, μm^{-1})	Surface area (SA, μm^2)	Surface-to-Volume ratio (SAV, μm^{-1})
-0.5	30%	347.9	0.348	8762.9	0.070
-0.25	40%	372.6	0.373	9368.2	0.075
0	50%	380.1	0.380	9549.6	0.076
0.25	60%	372.6	0.373	9368.2	0.075
0.5	70%	347.9	0.348	8762.9	0.070

9.3.4. Effect of dual-scale coalignment

We next investigated the effects of the dual-scale coalignment on the mechanical properties. In starfish ossicles, the match of the two three-fold symmetries of calcite and diamond is achieved via a specific coalignment, i.e., $[0001]_{calcite}//[111]_{diamond}$ and $[4\bar{4}0\bar{1}]_{calcite}//[11\bar{1}]_{diamond}$. If we rotate calcite by 180° about c-axis while keeping the

diamond-TPMS lattice unchanged, we will obtain a new hypothetic dual-scale microlattice, i.e., DS-dTPMS (180°) (**Fig. 9.5,9.16**). In this DS-dTPMS (180°), both three-fold symmetries of calcite and diamond lattice are also precisely registered. However, in stark contrast to the increased mechanical isotropy due to 3D property compensation observed in DS-dTPMS, the DS-dTPMS (180°) microlattice has decreased mechanical isotropy (**Fig. 9.17b,9.18-9.22, Table 9.7**). This is because, for DS-dTPMS (180°), the misorientation angle between the stiffest directions of calcite ($[5\bar{5}01]$, $[05\bar{5}1]$, and $[\bar{5}051]$) and the stiffest directions of the diamond lattice ($[\bar{1}11]$, $[1\bar{1}1]$and $[11\bar{1}]$) is only 2.5° relative to c-axis. The increase in mechanical anisotropy for DS-dTPMS (180°) can be demonstrated by the 3D elastic modulus contour of DS-dTPMS (180°) which maintains 6-pointed star-like shape similar to that of calcite (**Fig. 9.17b**). Moreover, the isotropy improvement and reduction for DS-dTPMS and DS-dTPMS (180°), respectively, can be also visualized in the shear moduli distribution on a representative plane (**Fig. 9.17c,d**). Specifically, for DS-dTPMS, the highest shear modulus of calcite is approximately aligned with the lowest shear modulus of I-dTPMS, exhibiting the property compensation for improved mechanical isotropy (**Fig. 9.17c**). While for DS-dTPMS (180°), the closely aligned directions with highest shear moduli of both calcite and I-dTPMS increase and decrease the maximum and minimum shear moduli, respectively, compared to I-dTPMS, enhancing the mechanical anisotropy (**Fig. 9.17d**). We further calculated the universal anisotropic indices for the microlattices, which confirmed that the mechanical anisotropy of DS-dTPMS (180°) is higher than DS-dTPMS at relative density over 40% and nearly independent of the change of relative density (**Fig. 9.17e**).

So far, our analyses are primarily focused on elastic properties. For microlattice made of single-crystalline constituent, fracture behavior, particularly for those constituents that undergo cleavage fracture, is an important aspect to consider. For example, geological calcite is known to undergo easy fracture along cleavage planes, i.e., $(10\bar{1}4)$, $(\bar{1}104)$, and $(0\bar{1}14)$, although cleavage fracture is significantly suppressed in biogenic calcite such as echinoderm stereoms due to the incorporation of nanoscopic intracrystalline organic inclusions[271,272]. Here to demonstrate the effects of cleavage fracture behavior from the constituent crystal on the strength of dual-scale single-crystalline microlattices, we treat the biogenic calcite in ossicles as a geological calcite which undergoes cleavage fracture. Here we consider a compressive loading ($\sigma_{compression}^{[111]}$) along the [111] direction of the DS-dTPMS microlattice, which induces bending stress on the inclined (i.e., non-[111]) branches (denoted as $\sigma_{bending}^{non-[111]}$) (**Fig. 9.17f**). The branches are assumed as Euler-Bernoulli beams. The corresponding resolved normal stress on the cleavage planes of the calcite-based branches, denoted as the cleavage stress $\sigma_{tension}^{cleavage}$, can then be calculated. Here, we define the angle between the bending stress and the normal direction of the cleavage planes of calcite as α (**Fig. 9.17f**). Therefore, the cleavage stress is calculated as $\sigma_{tension}^{cleavage} = \sigma_{bending}^{non-[111]} \cdot (cos^2\alpha)$, where $cos^2\alpha$ is defined as the resolved stress factor (SF) [273]. Next, we introduce a dual-scale misorientation angle γ, which is the azimuthal angle between the original 1-axis and rotated 1'-axis with respect to c-axis of calcite (**Fig. 9.17f**). Therefore, $\gamma = 0°$ corresponds to the DS-dTPMS microlattice, while $\gamma = 180°$ corresponds to the DS-dTPMS (180°) microlattice (**Fig. 9.5a**). At a given γ, we can use SF as the measure of the resolved normal stress on different cleavage planes, and determine the maximum scenario of SF (or SF_{max}) (**Fig. 9.17g**). The increase of SF_{max} results in

increased maximum resolved $\sigma_{tension}^{cleavage}$, indicating lower strength of the dual-scale microlattice with given γ. We found that the DS-dTPMS has the highest $SF_{max} = 0.81$ among all γ, yet the DS-dTPMS (180°) has the smallest $SF_{max} = 0.32$ (**Fig. 9.17g**). Therefore, although DS-dTPMS results in the highest isotropy due to property compensation, it yields the lowest strength among all surveyed γ (**Fig. 9.17g**).

Table 9.7. Summary of the stiffness constants obtained from simulations (dual-scale diamond-TPMS with constituent calcite rotated 180° about the c-axis, or dual-scale diamond-TPMS (180°)).

Constant (GPa)	T = -0.5	T = -0.25	T = 0	T = 0.25	T = 0.5
c_{11}	14.5	24.1	36.2	51.5	71.3
c_{12}	5.1	8.0	11.8	16.8	23.7
c_{13}	4.1	6.7	10.1	14.9	21.5
c_{14}	1.4	2.3	3.6	5.1	7.2
c_{33}	11.6	18.5	26.8	36.7	49.0
c_{44}	3.3	5.7	8.9	12.9	17.9
c_{66}	4.6	7.9	12.1	17.1	23.5

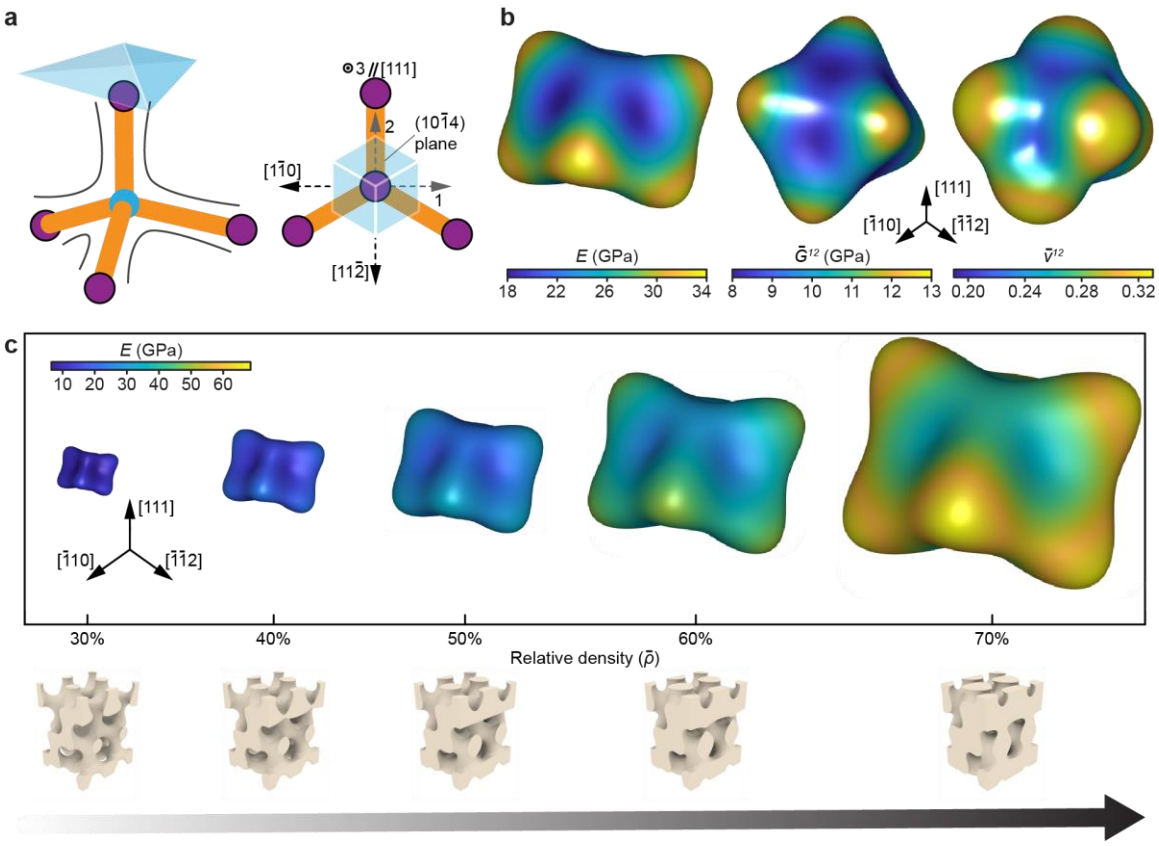


Figure 9.16. 3D elastic property contours and effect of relative density of DS-dTPMS (180°). (**a**) The dual-scale crystallography of DS-dTPMS (180°). (**b**) The 3D contours of elastic modulus, averaged shear modulus, and averaged Poisson's ratio of DS-dTPMS (180°). (**c**) 3D elastic modulus contours versus the relative density of DS-dTPMS (180°). The 3D volume rendering of the diamond-TPMS microlattice with different relative densities are shown at the bottom.

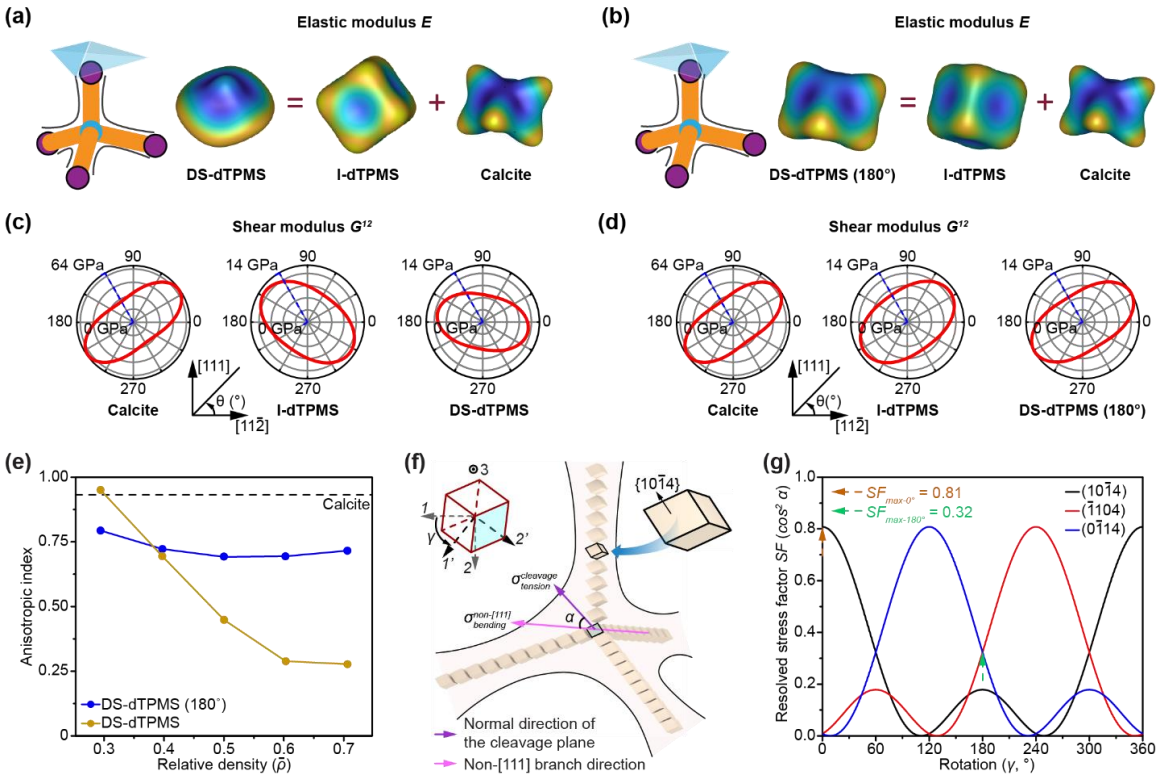


Figure 9.17. Effect of dual-scale coalignment. (**a**) Schematic representation of the property compensation of DS-dTPMS. (**b**) Schematic representation of the anisotropy enhancement of DS-dTPMS (180°). (**c,d**) Shear moduli on the $(1\bar{1}0)$ plane of DS-dTPMS (**c**) and DS-dTPMS (180°) (**d**), respectively. (**e**) Universal anisotropic index of DS-dTPMS and DS-dTPMS (180°) with different relative densities, respectively. (**f**) Schematic of the dual-scale crystallographic coalignment in ossicles. γ: misorientation angle of the single-crystalline calcite about its c-axis from 1-direction; α: angle between the normal direction of the cleavage plane (purple arrow) and the longitudinal direction of the non-[111] branch (pink arrow); $\sigma^{non-[111]}_{bending}$ denotes the bending stress on the non-[111] branch, while $\sigma^{cleavage}_{tension}$ denotes the normal resolved stress on the cleavage plane; cyan box: $(10\bar{1}4)$ plane. (**g**) Relationship between γ and resolved stress factor SF $((\cos\alpha)^2)$. Orange arrow

indicates $SF_{max-0^\circ} = 0.81$ which is the maximum SF_{max} for DS-dTPMS. Green arrow indicates $SF_{max-180^\circ} = 0.32$ which is the maximum SF_{max} for DS-dTPMS (180°).

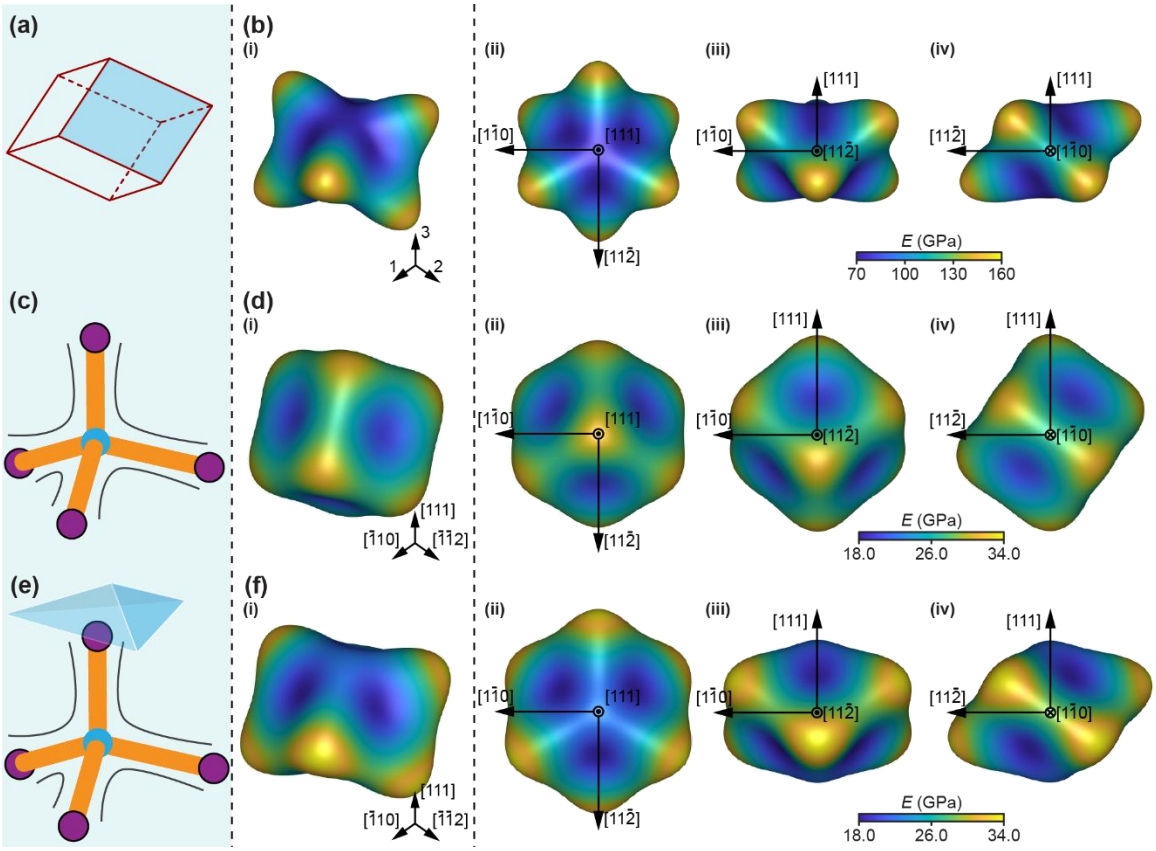


Figure 9.18. 3D elastic modulus contours and their 2D projection views of solid calcite, I-dTPMS, and DS-dTPMS (180°). (**a,b**) Geometrical representation of the calcite's crystallography (**a**) and the 3D elastic modulus contour as well as its 2D visualizations (**b**). (**c,d**) Geometrical representation of crystallography of the I-dTPMS (**c**) and the corresponding 3D elastic modulus contour as well as the 2D visualizations (**d**). (**e,f**) Geometrical representation of the dual-scale coalignment of DS-dTPMS (180°) (**e**) and the 3D elastic modulus contour as well as the 2D visualizations (**f**).

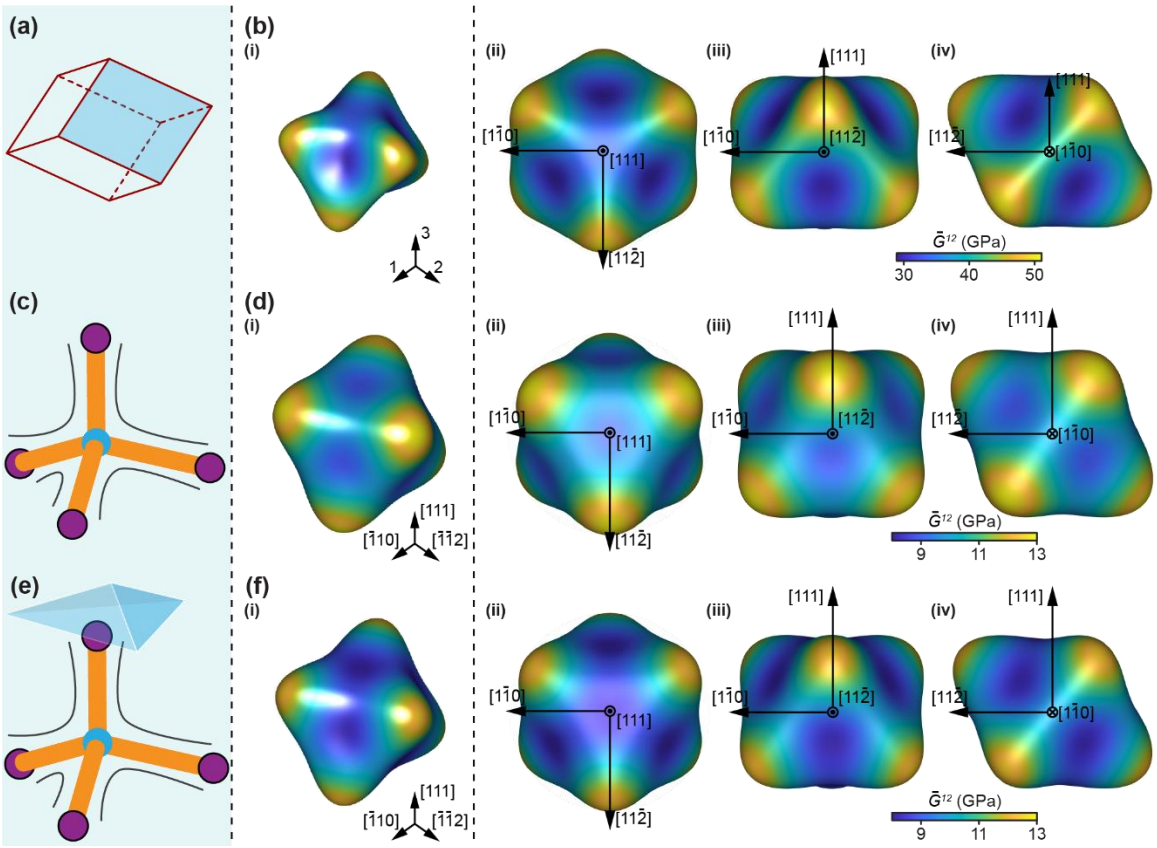


Figure 9.19. 3D averaged shear modulus contours and their 2D projection views of solid calcite, I-dTPMS, and DS-dTPMS (180°). (**a,b**) Geometrical representation of the calcite's crystallography (**a**) and the 3D averaged shear modulus contour as well as its 2D visualizations (**b**). (**c,d**) Geometrical representation of crystallography of the I-dTPMS (**c**) and the corresponding 3D averaged shear modulus contour as well as the 2D visualizations (**d**). (**e,f**) Geometrical representation of the dual-scale coalignment of DS-dTPMS (180°) (**e**) and the 3D averaged shear modulus contour as well as the 2D visualizations (**f**).

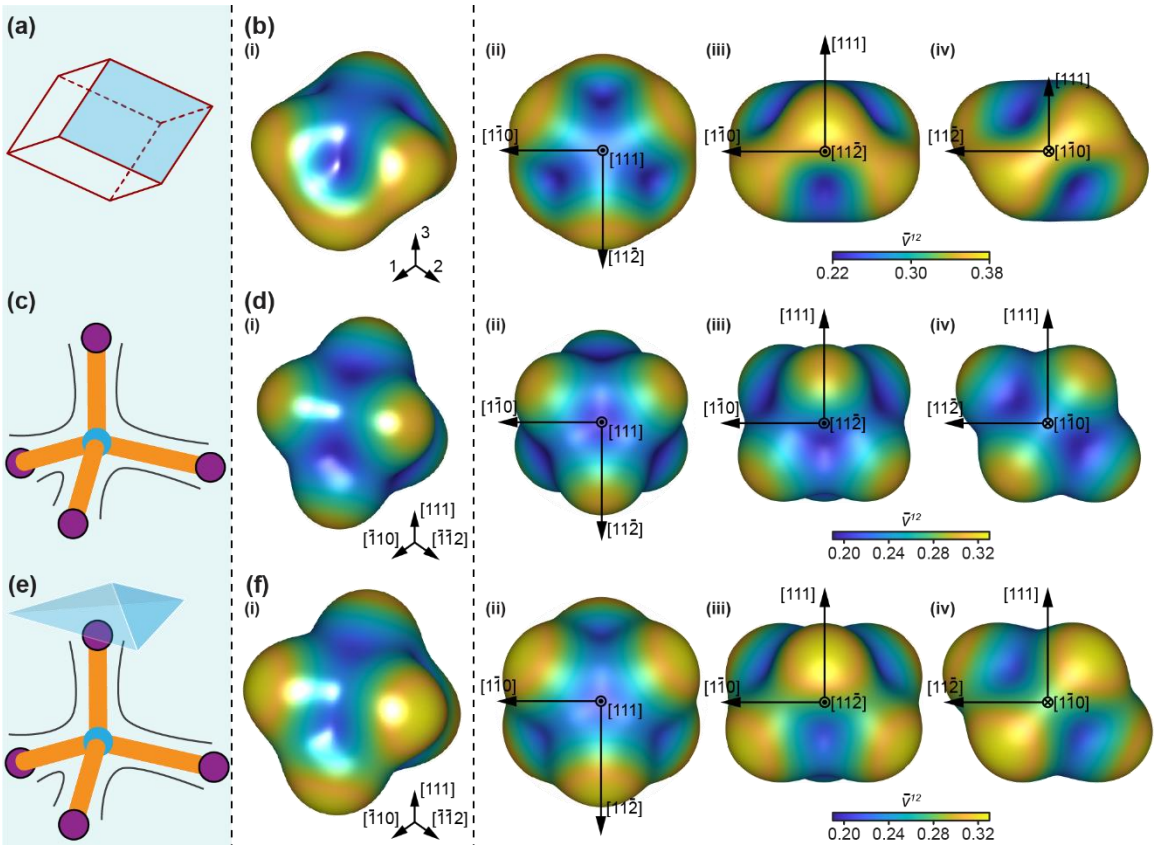


Figure 9.20. 3D averaged Poisson's ratio contours and their 2D projection views of solid calcite, I-dTPMS, and DS-dTPMS (180°). (**a,b**) Geometrical representation of the calcite's crystallography (**a**) and the 3D averaged Poisson's ratio contour as well as its 2D visualizations (**b**). (**c,d**) Geometrical representation of crystallography of the I-dTPMS (**c**) and the corresponding 3D averaged Poisson's ratio contour as well as the 2D visualizations (**d**). (**e,f**) Geometrical representation of the dual-scale coalignment of DS-dTPMS (180°) (**e**) and the 3D averaged Poisson's ratio contour as well as the 2D visualizations (**f**).

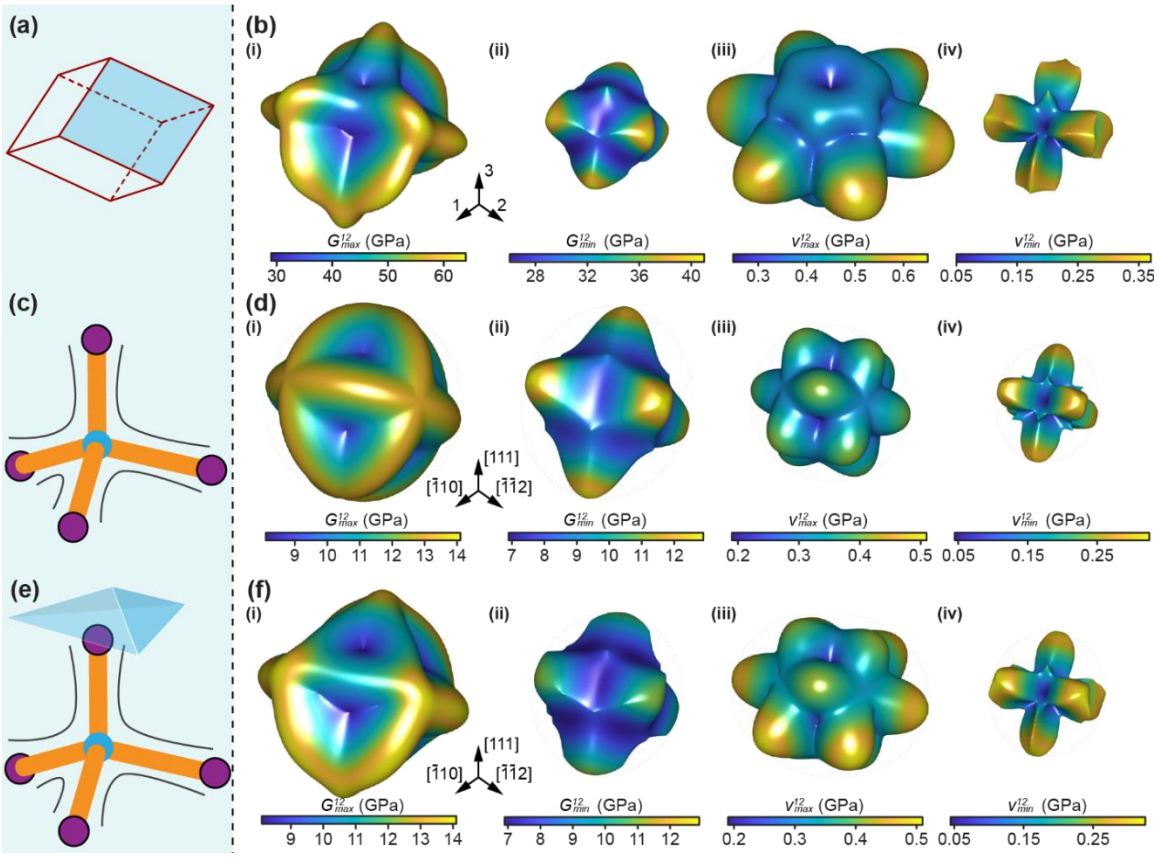


Figure 9.21. 3D maximum and minimum shear modulus and Poisson's ratio contours of solid calcite, I-dTPMS, and DS-dTPMS (180°). (**a,b**) Geometrical representation of the calcite's crystallography (**a**) and the 3D contours of maximum (G^{12}_{max}, v^{12}_{max}) and minimum (G^{12}_{min}, v^{12}_{min}) shear modulus and Poisson's ratio (**b**). (**c,d**) Geometrical representation of the crystallography of the I-dTPMS (**c**) and the corresponding 3D contours of G^{12}_{max}, v^{12}_{max}, G^{12}_{min}, and v^{12}_{min} (**d**). (**e,f**) Geometrical representation of the dual-scale coalignment of DS-dTPMS (180°) (**e**) and the 3D contours of G_{max}, v_{max}, G_{min}, and v_{min} (**f**).

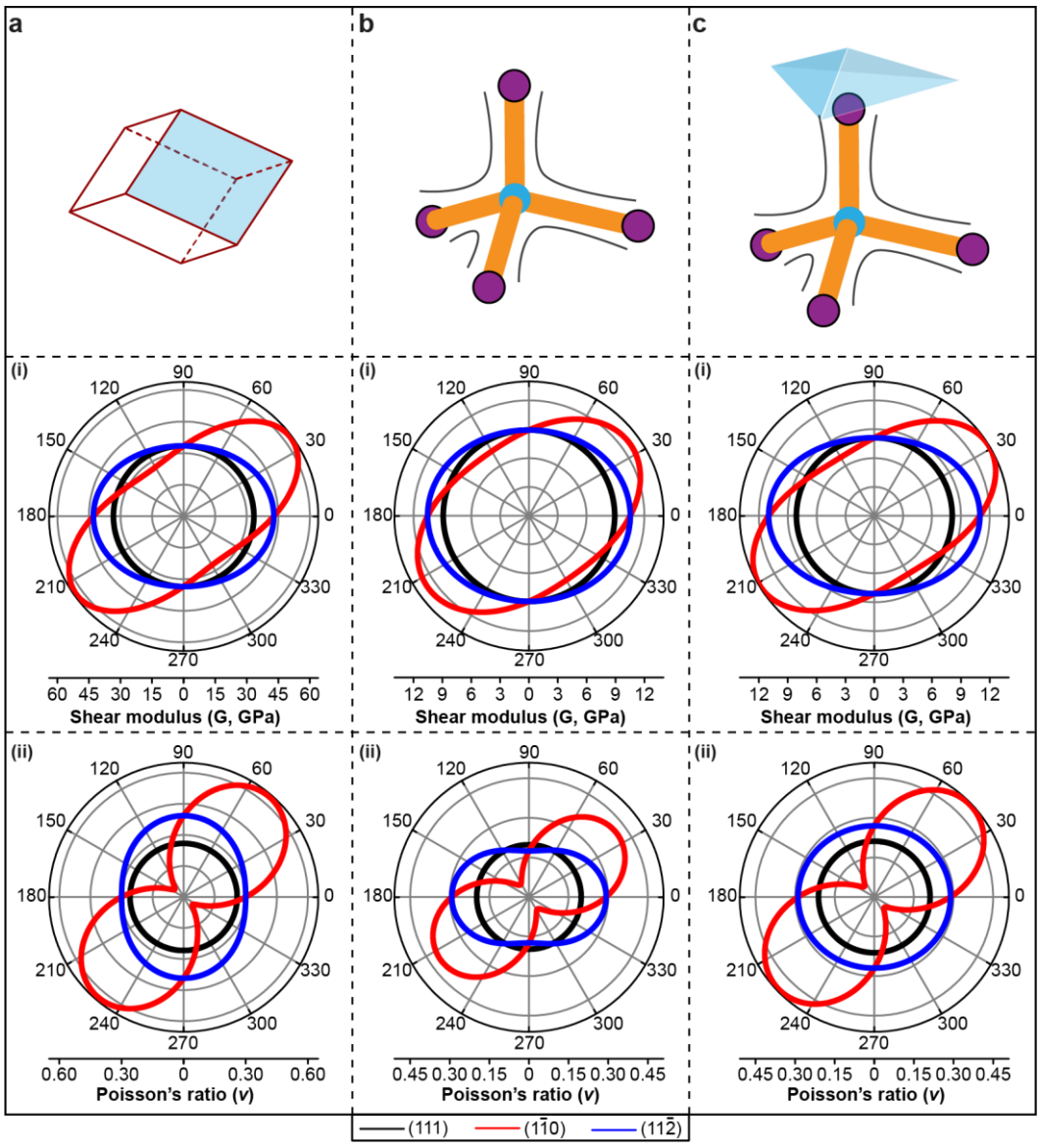


Figure 9.22. Shear moduli and Poisson's ratios on selected crystallographic planes. (**a**) Geometrical representation of the calcite's crystallography and corresponding shear modulus (i) and Poisson's ratio (ii) with respected to angle θ on the $(1\bar{1}0)$, $(11\bar{2})$, and (111) planes. (**b**) Geometrical representation of the crystallography of I-dTPMS and corresponding shear modulus (i) and Poisson's ratio (ii) with respected to angle θ on the $(1\bar{1}0)$, $(11\bar{2})$, and (111) planes. (**c**) Geometrical representation of the crystallography of

DS-dTPMS (180°) and corresponding shear modulus (i) and Poisson's ratio (ii) with respected to angle θ on the $(1\bar{1}0)$, $(11\bar{2})$, and (111) planes.

9.4. Discussions

The calcareous ossicles in the starfish *P. nodosus* possess a unique dual-scale single-crystalline nature. At atomic scale, it is a single-crystalline calcite, whereas at microlattice level, it is a diamond-TPMS lattice with a relative density of ~50%. In addition, we showed that the crystallographic symmetries at these two length scales are precisely registered following $[0001]_{\text{calcite}}//[111]_{\text{diamond}}$ and $[4\bar{4}0\bar{1}]_{\text{ calcite}}//\ [1\bar{1}\bar{1}]_{\text{ diamond}}$. The combined computational and theoretical methodology developed here allows us to investigate the mechanical properties this unique DS-dTPMS microlattice. Our results suggest that not only in specific crystal directions, but in 3D, the DS-dTPMS microlattice achieves enhanced mechanical isotropy by aligning the compliant and stiff directions from calcite and diamond-TPMS lattice together. Here we hypothesize that this enhanced mechanical isotropy in ossicles, particularly within the basal plane, i.e., the (0001) plane in calcite or (111) plane in diamond lattice, may be beneficial for the biomechanical performance of starfish. In the starfish endoskeletal system, the ossicles are arranged as a tessellated array, where the adjacent ossicles are connected by fibrous tissue[98]. During locomotion, the ossicles resist in-plane compressive and tensile loads resulted from the relative movements of ossicles and fibers in various directions, particularly within the basal plane[98,155]. The enhanced mechanical isotropy may reduce deformation mismatch among adjacent ossicles. Further analysis of the mechanical performance at the ossicles assembly level are needed to provide more insights in this regard[99,155].

We also note that despite the increase of mechanical isotropy for DS-dTPMS in ossicles due to 3D property compensation, the mechanical isotropy is not maximized at 50% relative density as observed in ossicles. Instead, the maximized isotropy is achieved when the relative density is within 60%-70%, beyond which the 3D modulus contour of DS-dTPMS approaches to that of calcite. Therefore, if maximizing mechanical isotropy is one of the driving forces of evolutionary selection for ossicles, other driving factors should also play roles in determining the microscopic structural characteristics of ossicles. For example, we show that 50% relative density in diamond-TPMS yields the zero mean surface curvature and highest SAV ratio. This minimal surface can avoid stress concentration to improve strength and damage tolerance compared to the sharp connection between branches[274,275]. In addition, it has been previously postulated that the minimal surface and highest SAV in echinoderm stereom provide maximum contact between the stroma within the void phase and mineralized phase, which maximize the biomineralization efficiency[110]. Another factor may be related to the damage tolerance of stereom by considering its jamming behavior. By having similar r_{throat} and r_{min} values in the diamond-TPMS microlattice at 50% relative density, the fractured fragments from the solid branches can be efficiently jammed in local by the small throat openings, leading to the formation of densified damage bands and contributing enhanced energy dissipation[4,96]. Therefore, the observed 50% relative density may be a compromised result considering mechanical properties (isotropy, stress distribution, damage tolerance via local jamming), light weight, and formation.

Regarding the particular dual-scale coalignment observed in ossicles (i.e., $[0001]_{\text{calcite}}//[111]_{\text{diamond}}$ and $[4\bar{4}0\bar{1}]_{\text{calcite}}//[1\bar{1}\bar{1}]_{\text{diamond}}$), our results indicate that other

alignments, particularly DS-dTPMS (180°) which is achieved by rotating the calcite about its c-axis by 180°, exhibits reduced mechanical isotropy. Note here that the DS-dTPMS (180°) microlattice still maintains a precise registration of two three-fold symmetries from atomic and microscopic scales. However, it is not appropriate to conclude that the particular crystallographic coalignment in ossicles is a result of maximizing mechanical isotropy. Other factors like particular growth or the biomineralization process may play a significant role here. On one hand, it is known that the growth of sea urchin larval spicules and calcareous sponges grow their spicules along specific crystallographic directions, namely, along their a^* axes[276–278], which is different from the DS-dTPMS microlattice here. On the other hand a diverse variety of stereom microstructures in echinoderm skeletal elements exists, which range from fully stochastic porous structure[87] to the highly regular microlattice as seen in the starfish ossicles here. Most of these structures all diffract as single crystals[260]. In these cases, the branches in stereom microscopically do not necessarily have to align with any specific crystallographic orientations of constituent calcite. This suggests that it is theoretically possible that echinoderms can produce the diamond microlattice with a different calcite orientation. Therefore, it is still an open question why this particular coalignment is achieved in the starfish ossicles.

Furthermore, other than the mechanical isotropy, the strength is another critical factor in designing dual-scale microlattices. Here, we proposed a dual-scale geometrical analysis method to study the effect of cleavage fracture behavior on strength of dual-scale microlattices. By varying the dual-scale misorientation angle (γ), we found that the external loading that induces cleavage fracture can be increased at $\gamma = 180°$ (DS-dTPMS (180°)) which improves the strength of dual-scale microlattices. This method can be

extended to predict the fracture behavior of other dual-scale microlattices with constituent experiencing easy cleavage fracture.

Finally, we envisioned the further applicability of the method: i) understanding of the mechanical properties of other echinoderm stereoms with dual-scale crystallographic coalignment; and ii) design of the dual-scale hierarchical lattice. Existing works provide some understanding of the lattice-scale microstructures of some echinoderm stereoms made of single-crystalline calcite. For example, the test plate of sea urchin has stereom similar to the primitive-TPMS microlattice[279], while the stereom in aboral sea urchin spine can be considered as a microlattice with transversely isotropic symmetry [92]. By understanding their coalignments with the calcite, the method here is able to predict the 3D mechanical properties of these stereoms. Moreover, it is not necessarily a crystallographic relationship between atomic-scale and lattice-scale architectures to design dual-scale lattice. The dual-scale coalignment may be utilized to design hierarchical lattice with crystallographic coalignment between any two distinct length-scales. Unlike the design for single-directional property of hierarchical lattices, we propose the design of dual-scale lattices for tailorable mechanical anisotropy and structural symmetry[7,11,12,267,280].

9.5. Conclusions

In this work, we investigated the mechanical properties of the dual-scale (i.e., atomic-scale and lattice-scale) crystallographic coalignment found in the ossicles of *P. nodosus*. We first utilized a combined theoretical and computational method to predict the structural symmetry and 3D elastic property contours of dual-scale diamond-TPMS microlattice in ossicles. The results demonstrate that the ossicles with 50% relative density possess

improved yet unmaximized mechanical isotropy among all surveyed relative density and dual-scale coalignment. Combining the structural analysis, we propose that the ossicles possess a trade-off between mechanical (i.e., mechanical isotropy, improved stiffness, strength, and toughness) and morphological advantages (i.e., zero mean curvature and highest surface-to-volume ratio). Finally, we envision that the method in this work can be adopted to understand other echinoderm stereoms made of single-crystalline calcite and design dual-scale microlattice for desired mechanical isotropy, strength and structural symmetry.

Chapter 10 Summary and future directions

10.1. Summary

In this dissertation, three model systems that represent three different classes of multiscale biomineralized lattices with high mineral contents (~ 99w.t.%), which are multiscale hierarchical structure in the Hexactinellid sponges, multiscale functionally graded structure in the sea urchin spine of *H. mammillatus*, and the dual-scale (microlattice- and atomic-scales) periodic structures in the ossicle of *P. nodosus*. The multiscale structures and the mechanical properties of each type of biomineralized lattices with multiscale structures were analyzed and correlated, which are summarized chapters by chapters.

Chapter 3: Compositional and mechanical analysis of biogenic silica in three species of Hexactinellid sponges

To observe whether compositional and mechanical gradients exist and the effect of humidity condition during experiments on the mechanical properties, the nanoscale structure and mechanics of the biogenic silica were explored for three different species of Hexactinellid sponges, including, *C. populiferum*, *H. sieboldin*, and *S. hawaiicus*, using Raman spectroscopy, EDS, and nanoindentations, respectively. The conclusions and contributions are summarized below:

- Via Raman spectroscopy and EDS measurements, other than hydrated silica (Si-O-H bond), organics, as indicated by the Amide I and C-H vibration peaks in Raman spectrum and the carbon element in the EDS spectrum, were found

within the biogenic silica of all species, which is consistent with the finding in the biogenic silica in species *E. aspergillum* and *M. chuni*;

- Via Raman and EDS scanning along the cross section of the spicules of each selected species as well as the correlation between the measured locations and values, the consistent distributions of compositions (i.e., Si-O-H, Si-O-Si, Amide I, and C-H) and elements (i.e., Si, O, and C) were demonstrated within the biogenic silica across the spicules;
- Via nanoindentation with Berkovich tip, I found that the consistent elastic modulus and hardness in the biogenic silica throughout the cross section of the spicules of the three selected species, which is a result of the consistent compositional and elemental distributions;
- In particular, the elastic modulus of ~35 GPa and hardness of ~3 GPa of biogenic silica were found, which are similar to those found in spicules of *E. aspergillum* and approximately half and 1/3 of those found in the synthetic silica, respectively;
- Immersing spicule samples for a week and performing nanoindentation in the 90% humidity do not have observable effect on the elastic modulus and hardness of the biogenic silica, which may be attributed to the originally highly saturated silica by hydration or the thin altered surface structure compared to the indentation depth (~180 nm);
- Via cube-corner indentation, the fracture toughness was found to be location dependent (lamellae region: ca. 0.3 $MPa \cdot m^{1/2}$; core: ca. 0.3 $MPa \cdot m^{1/2}$;

layering: ca. 0.45 $MPa \cdot m^{1/2}$); These results generally agree with the findings in the biogenic silica from *M. chuni*.

Chapter 4: The structural-mechanical understanding of the cellular dome in the sieve plate of glass sponge Euplectella aspergillum

Chapter 4 and 5 provides the first comprehensive investigation on the structure, formation, and mechanics of sieve plate, which is a biomineralized skeletal structure made of silica spicules and covering the osculum of glass sponge *E. aspergillum*. In particular, chapter 4 quantitatively studies three structural features (i.e., the dome structure, porous sieve plate branch, and cellular network) and their corresponding mechanical implications to the sieve plate and the skeleton of *E. aspergillum*. The structural characterizations reveal that the sieve plates possess Voronoi-like cellular dome with elliptical paraboloid shape and with porous branch of increased height along the dome thickness direction. The specific contributions are summarized below:

- Structural measurements revealed that, on average, the sieve plate's dome has an elliptical base (fitted results: long side of 15.9 ± 0.8 mm, short side of 13.2 ± 1.5 mm, and height of 5.6 ± 3.7 mm), a thickness of 0.9 ± 0.1 mm, and a relative density of 51.6% ± 8.3%;
- Measurement based on μ-CT scanning showed that the sieve plate branch is porous with relative density of 55.9% ± 6.7%, and has a rectangle-like cross section with height about 3 times of the width (measured results: length of 2.9 ± 0.7 mm, width of 0.3 ± 0.1 mm, and height of 0.9 ± 0.1 mm);

- The cellular structure of sieve plate has pore area of ca. 5~8 mm^2 with no particular trend from the periphery to the center, while the alignment of the pores (considered as elliptical pore) prefers ~30° and ~150° relative to the long side of the sieve plate;
- Voronoi analysis showed that the cellular pattern of sieve plates is Voronoi-like, which has 77.7% ± 3.0% similarity to the Voronoi tessellation generated based on the projected pore centers on the plane containing long and short sides (i.e., L-S plane).

With these structural findings, bio-inspired models were constructed to study the mechanical implications of each structural feature. The results show the following conclusions:

- Sieve plate's Voronoi-like cellular pattern exhibits anisotropic elastic modulus with stiff directions closer to the long side direction, which is attributed to the pore alignment along closer to the long side;
- Yet, in general, these patterns provide modulus similar to the regular honeycomb lattice and computer-generated Voronoi lattices;
- Dome structures were introduced to the cellular patterns, yielding sieve plate-like cellular domes, which show smaller height stiffness and similar long side stiffness compared to honeycomb lattice dome;
- The sieve plate branch, which is porous and has increased height, provides ca. 40% and 100% improvements in bending stiffness compared to solid branches with elliptical/rectangular and circular/cubic cross sections.

Therefore, the sieve plate, despite the irregularity, provides stiffness similar to the regular honeycomb lattice, which prevents the collapse of osculum and protects interior of sponge. Furthermore, the porous branch with increased height not only provides increased stiffness to the dome, but also maintains the large opening holes for sponge's current pumping mechanism.

Chapter 5: Microstructure-based study of the formation of the sieve plate in glass sponge Euplectella aspergillum

Next, the formation of the sieve plate is of interest, as it is the origin of the mechanical and biological functions of the sieve plate and can provide inspirations of cellular dome constructions. Therefore, chapter 5 explores the sieve plate formation based on the study of microscale structures. Below, the conclusions and contributions in the microstructural and formational understanding of the sieve plate are summarized:

- Microscale observations found that the sieve plate is completely spicule-based where synapticular bridging merges individual spicules together to form porous spicule bundles (or the sieve plate branch);
- Via the observations of the connection site of the cylindrical skeleton and sieve plate, the sieve plate can be considered as a continuation of the cylindrical skeleton
- The considerable amount of thin hexactines were discovered within the sieve plate and highly concentrated at the growth front of the sieve plate branch, which implies its function of assisting the anchoring of tissue and hence silica deposition, instead of providing mechanical stiffness;

- Moreover, bridging spicules were found in the sieve plate, demonstrating that spicules will grow at the later stage to intercept some existing pores to form final Voronoi-like tessellation;
- In addition, individual spicules were identified within the sieve plate nodes and branches, which show various types of spicules based on their locations and morphologies at the nodes and reveal the capability of sieve plate to grow long spicules spanning at least 12 nodes in the branches;
- Most of the spicules were ca. 15 μm in radius while those curved spicules located at the outer surface of the nodes are ca. 10 μm in radius. Combining with the SEM observations, I hypothesized that the outer spicules grow later on the existing inner spicules;
- The 2D schematics of the N-3 and N-4 nodes were proposed which are able to represent the 3D structure due to their similar structures along the dome thickness direction.

Based on these observations and quantitative analysis, the growth process of sieve plate was predicted:

- The sieve plate's spicule bundles start from both of the longitudinal and circumferential spicule bundles in the cylindrical skeleton;
- The sieve plate has an initial tessellation with long spicules radiating towards the center, while later the bridging spicule bundles close some existing pores which forms new sieve plate nodes and the final Voronoi-like tessellation;
- During the growth process, i) the hexactines assist tissue anchoring for silica deposition; ii) the inner spicules grow first which is followed by the growth of

the outer layers of spicules; and iii) The individual spicules can grow until reaching ca. 15 μm in radius.

This formation process may be related to the mechanical and biological functions of sieve plate: the accommodation of symbiotic shrimps when sponge is young and providing stiffness when mature. Furthermore, we also hypothesized some driving forces which control the formation of sieve plate. The implement of the hypothetical driving forces computationally may improve our understanding of sieve plate formation and provide bio-inspired strategy to build cellular domes with different functions at different construction stages.

Chapter 6: Multifunctional properties of the lightweight lattice-based skeleton of the sponge Euplectella aspergillum

Chapter 6 quantitatively investigate the macroscale structural-mechanical/functional relationship of the cylindrical lattice of the glass sponge *E. aspergillum*. The conclusions and contributions are summarized as follow:

- Detailed structural measurements were first made on the cylindrical lattice, which yields the aspect ratios of rectangular cells and beams (except the diagonals), and the extruded length of the ridge structure;
- Based on these measurements, parametric biomimetic modeling and mechanical simulations of double-diagonal cylindrical lattice with variations of rectangular cell aspect ratio and the diagonal aspect ratio was performed;
- Our parametric study found that the sponge skeleton-like double-diagonal cylindrical lattice tends to optimize for torsional rigidity, while its linear

behaviors (compressive modulus, torsional rigidity, and bending rigidity) are similar to the control model which has two intercepting diagonals in each rectangular cell;

- This finding indicates that the selection of double-diagonal configuration can provide both mechanical stiffness and large opening holes for the sponge's current pumping;
- The bio-inspired ridge structures were also designed for mechanical study which reveals that adding ridge inefficiently provide improvement to the longitudinal compressive modulus, torsional rigidity, and bending stiffness, while it significantly improves the radial compressive modulus;
- Furthermore, our fluid-structure coupled simulations found that the ridge structure can not only improve resistance to the radial loading due to the current flow but also provide improvement of permeability via the prevention of abrupt change of fluid cross section.

Chapter 7: Multiscale functionally graded lattice and mechanics of the sea urchin spone of the Heterocentrotus mammillatus

Chapter 7 studies the structure and mechanics of another type of multiscale biomineralized lattices: multiscale functionally graded structure in the sea urchin spine of *H. mammillatus*. Through the use of an optimized cellular network analysis workflow, the microscale to macroscale structures of a large-volume of sea urchin spine were analyzed quantitatively. The results reveal the new and important structural-mechanical findings on the sea urchin spine as follow:

- In microscale, the branch radius (ca. 5.5 vs 9.5 μm) and relative density (ca. 10% vs 40%) increase from the center to the edge of the spine;
- In the center region, the branch highly aligns towards or perpendicular to the longitudinal direction of the spine, which demonstrates a galleried type stereom;
- In the edge region, however, radially arranged porous septa and relatively thin interconnecting branches were found which shows a laminar type stereom;
- In addition to this multiscale structural gradient, it is found that the N-3 and N-4 nodes with maximal 3D spanning pre-dominantly construct the stereom of sea urchin spine which was deemed as a strategy for lightweight design;
- Furthermore, the mechanical gradient is found via computer simulations where the core region exhibits more anisotropic moduli and lower modulus values compared to those found in the edge region due to different branch alignment and relative density.

Chapter 8: Dislocation engineering in the biomineralized microlattice of the ossicle of starfish Protoreaster nodosus

Chapter 8 and 9 surveys the diamond-TPMS micro-lattice found in the ossicles of *P. nodosus* which represents the dual-scale (microlattice- and atomic-scales) periodic architectures. In particular, the core structures of microlattice dislocations and the mechanical properties of dual-scale crystallographic coalignments were studied in-depth.

Here, chapter 8 investigates the core structures of the dislocations in ossicles to provide insights of how ossicles “engineer” dislocations. This work emphasizes the i)

dissimilarity of the dislocation core structure and dislocation types compared to the dislocations found in the crystals with diamond cubic lattice, and ii) quantitative descriptions of the structure surrounding the core. The structural findings and my hypothetical mechanical implications are summarized below:

- Compared to those found in the diamond and silicon, unique dislocation core structures in the 60° and screw dislocations were found in the ossicle, which avoids large voids generated by structural defects via additional branch or bulk solids;
- This avoidance of large pore space may provide local stiffening and strengthening by increasing connectivity, which is also found in stereom in the sea urchin spine;
- The quantitative structural analysis demonstrates that the core sizes of the 60° and screw dislocations are limited to 1~2 unit cell size of diamond lattice of ossicle, which is similar to the dislocation core sizes found in diamond and silicon. Yet, unlike diamond and silicon, the structural distortion outside of the dislocation cores in ossicle is not observed, demonstrating ossicle's favor to suppress structural variations due to defects;
- This small confined region affected by structural defects enables ossicles to accommodate a significantly higher density of dislocations than diamond crystals, which provides effective mechanical benefits such as improved toughness and strength;
- Finally, method demonstrations were provided to model 3D architected lattice materials with inserted dislocations of controllable density.

Chapter 9: Mechanical properties of dual-scale crystallographic coalignment in starfish's ossicle stereom

As another unique structural aspect, chapter 9 explores the mechanical functions of the recently discovered dual-scale crystallographic coalignment in ossicles of *P. nodosus*, using a proposed combined theoretical and computational method. The conclusions are summarized as follow:

- The proposed method provides the calculation of 3D property surfaces of elastic modulus, shear modulus, and Poisson's ratio for dual-scale diamond-TPMS lattice (DS-dTPMS), diamond-TPMS with isotropic parent material (I-dTPMS), and the constituent calcite;
- The results show that, due to an 3D mechanical compensation mechanism, mechanical isotropy of DS-dTPMS, which is significantly higher than the constituent calcite, was found approaching to that of the I-dTPMS when diamond-TPMS lattice has 50% relative density;
- Similar analysis on the diamond-TPMS lattice with various relative density shows that increasing the relative density to the range of 60%~70% can further improve the mechanical isotropy; however, ossicle usually adopts the 50% relative density;
- The structural analysis reveals that, the ossicle, which is usually 50% relative density, is potentially a result of trade-offs among mechanics (e.g., improved damage tolerance) and morphological requirements (e.g., zero mean surface curvature and maximal surface-to-volume ratio);

- Moreover, the effect of dual-scale coalignment and cleavage fracture on the strength of dual-scale lattice were analyzed which shows the minimal strength for dual-scale coalignment in ossicle. This geometrical analysis-based method can be used to guide the design of strength of dual-scale lattices;
- Finally, we hypothesize that the proposed method and the dual-scale crystallographic coalignment concept can be extended to understand the mechanical properties for other echinoderm's stereom with similar structural concept and to the multiscale hierarchical lattice design (not limited to the single-crystalline constituent) for desired mechanical isotropy and structural symmetry.

In summary, this dissertation provides comprehensive and quantitative structural-mechanical explorations on biomineralized cellular lattices with three most representative multiscale hierarchical structures. This type of comprehensive and quantitative explorations of the biomineralized materials is always the first critical step to derive bio-inspired strategies and models, which bridges the biological materials and engineering materials.

10.2. Future directions

Some potential future works have been mentioned in the previous chapters. Here, these future works are summarized and further discussed in a broader sense.

Computational implementation of biomineralized lattice formation

In chapter 5, the formation process for sieve plate was proposed based on the microstructural study, including observations and quantitative analysis of the identified individual spicules. The hypothetical driving forces were proposed which are believed to form the Voronoi-like tessellation of sieve plate, despite of the lack of grain growth mechanism as found in shell prisms. Computationally implementing these hypothetical driving forces may provide a further understanding of the sieve plate formation and design sieve plate-like Voronoi-like lattice with sieve plate's mechanical and biological functions.

This type of research, which implements the hypothetical driving forces of the natural pattern formation computationally, is applicable not only to the sieve plate formation, but also to the formation of many biomineralized cellular materials. One example is the recently investigated diatom frustule's structure and hypothetical driving forces, which provides insights to the diatom's pattern formation[144]. If applying to ossicle's formation, the formation of microlattice dislocations may be understood and hence the design of architected lattices with ossicle-inspired structural defects for improved mechanical performances.

High-throughput 3D structural-mechanical analysis of biomineralized lattices

Chapter 7 demonstrates the capability of studying the long-range 3D cellular structure in sea urchin spines of *H. mammillatus* using μ-CT and automatic computer algorithm. Despite the large amount of work, only one large-volume spine sample of one species in class Echinodermata was analyzed thoroughly. The skeletal information and hence the mechanical implications hidden in an incredibly large group of echinoderms remain largely unknown. This hinders our comprehensive understanding of the general structural

motifs in the skeletons of this class of marine animals. Therefore, implementing an automatic or semi-automatic workflow to obtain and analyze extremely large amount of data is significant in the exploration of biomineralized skeletons. This work can provide two main contributions. One is the structural-functional explorations on a large number of skeleton samples of one species, which provides in-depth understanding of the structures and functions of different parts of the skeleton such as different types of ossicles in starfish *P. nodosus*[4]. Another is the understanding of wide-spread or unique structural motifs, formation, phylogeny, and mechanical implications in echinoderms by comparing among different species[281].

Defect engineering in 3D architected lattice design

Most of artificial architected lattices is regularly arranged in branch connections, while biomineralized cellular lattices usually contain structural irregularity such as the dislocations found in the ossicles of starfish *P. nodosus* studied in chapter 8. Unlike random cellular structure, this unique design strategy to include structural irregularity is a novel way to maintain the main regular structure for maintaining stiffness while locally redistributing stress and deviating crack path for improving strength and toughness. Recently, increasing number of research has been focusing on designing defects into architected lattice such as the grain boundaries and dislocation-like defects which indeed yield improvements in strength and toughness[106,107]. Therefore, the understanding of the structural design of microlattice dislocations in ossicles opens up a vast space of designing 3D architected lattices with various types and controllable density of dislocations. This line of research is feasible with the help of atomic lattice modeling and 3D printing as demonstrated in chapter 8.

REFERENCES

1. Weaver, J. C. Structure-Function Relationships in Biomineralized Composites: Analysis of the Architectural Complexities of Sponge Skeletal Systems. (2006).

2. Chen, H. *et al.* Quantitative 3D structural analysis of the cellular microstructure of sea urchin spines (II): Large-volume structural analysis. *Acta Biomater.* **107**, 218–231 (2020).

3. Gutiérrez, A., Guney, M. G., Fedder, G. K. & Dávila, L. P. The role of hierarchical design and morphology in the mechanical response of diatom-inspired structures: Via simulation. *Biomater. Sci.* **6**, 146–153 (2018).

4. Yang, T. *et al.* A damage-tolerant, dual-scale, single-crystalline microlattice in the knobby starfish, Protoreaster nodosus. *Science* **375**, 647–652 (2022).

5. Miserez, A. *et al.* Effects of laminate architecture on fracture resistance of sponge biosilica: Lessons from nature. *Adv. Funct. Mater.* **18**, 1241–1248 (2008).

6. Woesz, A. *et al.* Micromechanical properties of biological silica in skeletons of deep-sea sponges. *J. Mater. Res.* **21**, 2068–2078 (2006).

7. Meza, L. R. *et al.* Resilient 3D hierarchical architected metamaterials. *Proc. Natl. Acad. Sci.* **112**, 11502–11507 (2015).

8. Zheng, X. *et al.* Ultralight, ultrastiff mechanical metamaterials. *Science* **344**, 1373–1377 (2014).

9. Meza, L. R., Das, S. & Greer, J. R. Strong, lightweight, and recoverable three-dimensional ceramic nanolattices. *Science* **345**, 1322–1326 (2014).

10. Ai, L. & Gao, X. L. Metamaterials with negative Poisson's ratio and non-positive thermal expansion. *Compos. Struct.* **162**, 70–84 (2017).

11. Zheng, X. Y. *et al.* Multiscale metallic metamaterials. *Nat. Mater.* **15**, 1100–1106 (2016).

12. Zhang, L., Hu, Z., Wang, M. Y. & Feih, S. Hierarchical sheet triply periodic minimal surface lattices: Design, geometric and mechanical performance. *Mater. Des.* **209**, 109931 (2021).

13. Wen, X. *et al.* 3D-printed silica with nanoscale resolution. *Nat. Mater.* **20**, 1506–1511 (2021).

14. Eckel, Z. C. *et al.* Additive manufacturing of polymer-derived ceramics. *Science* **351**, 58–62 (2016).

15. Bauer, J. *et al.* Nanolattices: An Emerging Class of Mechanical Metamaterials.

Adv. Mater. **29**, 1701850 (2017).

16. Bauer, J., Schroer, A., Schwaiger, R. & Kraft, O. Approaching theoretical strength in glassy carbon nanolattices. *Nat. Mater.* **15**, 438–443 (2016).

17. Deshpande, V. S. S., Ashby, M. F. F. & Fleck, N. A. A. Foam topology: bending versus stretching dominated architectures. *Acta Mater.* **49**, 1035–1040 (2001).

18. Meza, L. R. *et al.* Reexamining the mechanical property space of three-dimensional lattice architectures. *Acta Mater.* **140**, 424–432 (2017).

19. Gibson, L. J. & Ashby, M. F. *Cellular solids: structure and properties*. (Cambridge university press, 1999).

20. RS Lokes. Materials with structural hierarchy. *Nature* **361:511**–**15**, 511–515 (1993).

21. Weaver, J. C. *et al.* Hierarchical assembly of the siliceous skeletal lattice of the hexactinellid sponge Euplectella aspergillum. *J. Struct. Biol.* **158**, 93–106 (2007).

22. Leys, S. P., Mackie, G. O. & Reiswig, H. M. The Biology of Glass Sponges. in *Advances in Marine Biology* vol. 52 1–145 (2007).

23. Wörheide, G. *et al. Deep Phylogeny and Evolution of Sponges (Phylum Porifera). Advances in Marine Biology* vol. 61 (2012).

24. Chu, J. W. F., Maldonado, M., Yahel, G. & Leys, S. P. Glass sponge reefs as a silicon sink. *Mar. Ecol. Prog. Ser.* **441**, 1–14 (2011).

25. Cha, J. N. *et al.* Silicatein filaments and subunits from a marine sponge direct the polymerization of silica and silicones in vitro. *Proc. Natl. Acad. Sci.* **96**, 361–365 (1999).

26. Lowenstam, H. A. Minerals Formed by Organisms. *Science* **211**, 1126–1131 (1981).

27. Schulze, F. E. Report on the Hexactinellida collected by H.M.S. '"Challenger"' during the years 1873–1876. *Zoology* **21**, 1–513 (1887).

28. Hooper, J. N. A. & Van Soest, R. W. M. *SYSTEMA PORIFERA. A Guide to Classification of Sponges*. vol. 1 (2002).

29. Jochum, K. P., Wang, X., Vennemann, T. W., Sinha, B. & Müller, W. E. G. Siliceous deep-sea sponge Monorhaphis chuni: A potential paleoclimate archive in ancient animals. *Chem. Geol.* **300**–**301**, 143–151 (2012).

30. Aizenberg, J. *et al.* Skeleton of *Euplectella* sp.: Structural Hierarchy from the Nanoscale to the Macroscale. *Science* **309**, 275–278 (2005).

31. Ehrlich, H. *et al.* Mineralization of the metre-long biosilica structures of glass sponges is templated on hydroxylated collagen. *Nat. Chem.* **2**, 1084–1088 (2010).

32. Perry, C. C. & Keeling-Tucker, T. Biosilicification: the role of the organic matrix in structure control. *JBIC J. Biol. Inorg. Chem.* **5**, 537–550 (2000).

33. Grant, N. *et al.* Effect of suspended sediments on the pumping rates of three species of glass sponge in situ. *Mar. Ecol. Prog. Ser.* **615**, 79–100 (2019).

34. Leys, S. P. *et al.* The Sponge Pump: The Role of Current Induced Flow in the Design of the Sponge Body Plan. *PLoS One* **6**, e27787 (2011).

35. Grant, N., Matveev, E., Kahn, A. S. & Leys, S. P. Suspended sediment causes feeding current arrests in situ in the glass sponge Aphrocallistes vastus. *Mar. Environ. Res.* **137**, 111–120 (2018).

36. Li, G. *et al.* Self-powered soft robot in the Mariana Trench. *Nature* **591**, 66–71 (2021).

37. Zhang, R. *et al.* Design and characterization of the carbon fiber tube reinforced polymer composite for full ocean depth submersibles. *Compos. Sci. Technol.* **217**, 109074 (2022).

38. Neilson, J. R., George, N. C., Murr, M. M., Seshadri, R. & Morse, D. E. Mesostructure from hydration gradients in demosponge biosilica. *Chem. - A Eur. J.* **20**, 4956–4965 (2014).

39. Weaver, J. C. *et al.* Nanostructural features of demosponge biosilica. *J. Struct. Biol.* **144**, 271–281 (2003).

40. Arasuna, A. *et al.* Structural characterization of the body frame and spicules of a glass sponge. *Minerals* **8**, (2018).

41. Weaver, J. C. *et al.* Unifying Design Strategies in Demosponge and Hexactinellid Skeletal Systems. *J. Adhes.* **86**, 72–95 (2010).

42. Schröder, H. C., Wang, X., Tremel, W., Ushijima, H. & Müller, W. E. G. Biofabrication of biosilica-glass by living organisms. *Nat. Prod. Rep.* **25**, 455 (2008).

43. Shimizu, K., Cha, J., Stucky, G. D. & Morse, D. E. Silicatein : Cathepsin L-like protein in sponge biosilica. *Proc. Natl. Acad. Sci.* **95**, 6234–6238 (1998).

44. Ehrlich, H. *et al.* A modern approach to demineralization of spicules in glass sponges (Porifera: Hexactinellida) for the purpose of extraction and examination of the protein matrix. *Russ. J. Mar. Biol.* **32**, 186–193 (2006).

45. Wysokowski, M., Jesionowski, T. & Ehrlich, H. Biosilica as a source for

inspiration in biological materials science. *American Mineralogist* vol. 103 665–691 (2018).

46. Voznesenskiy, S. S., Kul'chin, Y. N. & Galkina, A. N. Biomineralization: A natural mechanism of nanotechnologies. *Nanotechnologies Russ.* **6**, 43–78 (2011).

47. Aizenberg, J., Sundar, V. C., Yablon, A. D., Weaver, J. C. & Chen, G. Biological glass fibers: Correlation between optical and structural properties. *Proc. Natl. Acad. Sci.* **101**, 3358–3363 (2004).

48. Kul'chin, Y. N. *et al.* Spicules of glass sponges as a new type of self-organizing natural photonic crystal. *Opt. Spectrosc.* **107**, 442–447 (2009).

49. Levi, C., Barton, J. L., Guillemet, C., Le Bras, E. & Lehuede, P. A remarkably strong natural glassy rod: the anchoring spicule of theMonorhaphis sponge. *J. Mater. Sci. Lett.* **8**, 337–339 (1989).

50. Drozdov, A. L., Andreykin, N. A. & Dorofeev, A. G. Structure and physico-chemical properties of organosilicon crystal-like composite spicules of the glass sponge Hyalonema sieboldi. *Mater. Res. Bull.* **105**, 372–376 (2018).

51. Wiens, M. *et al.* The role of the silicatein-α interactor silintaphin-1 in biomimetic biomineralization. *Biomaterials* **30**, 1648–1656 (2009).

52. Weaver, J. C. & Morse, D. E. Molecular biology of demosponge axial filaments and their roles in biosilicification. *Microsc. Res. Tech.* **62**, 356–367 (2003).

53. Ehrlich, H. *et al.* Arrested in Glass: Actin within Sophisticated Architectures of Biosilica in Sponges. *Adv. Sci.* **9**, 1–10 (2022).

54. Müller, W. E. G. *et al.* Silicatein expression in the hexactinellid Crateromorpha meyeri: The lead marker gene restricted to siliceous sponges. *Cell Tissue Res.* **333**, 339–351 (2008).

55. Müller, W. E. G. *et al.* Identification of a silicatein(-related) protease in the giant spicules of the deep-sea hexactinellid Monorhaphis chuni. *J. Exp. Biol.* **211**, 300–309 (2008).

56. Ehrlich, H. *et al.* Nanostructural Organization of Naturally Occurring Composites—Part I: Silica-Collagen-Based Biocomposites. *J. Nanomater.* **2008**, 1–8 (2008).

57. Kulchin, Y. N. *et al.* Optical fibres based on natural biological minerals — sea sponge spicules. *Quantum Electron.* **38**, 51–55 (2008).

58. Monn, M. A., Weaver, J. C., Zhang, T., Aizenberg, J. & Kesari, H. New functional insights into the internal architecture of the laminated anchor spicules of Euplectella aspergillum. *Proc. Natl. Acad. Sci.* **112**, 4976–4981 (2015).

59. Wang, X. *et al.* Axial growth of hexactinellid spicules: Formation of cone-like structural units in the giant basal spicules of the hexactinellid Monorhaphis. *J. Struct. Biol.* **164**, 270–280 (2008).

60. Müller, W. E. G. *et al.* Formation of giant spicules in the deep-sea hexactinellid Monorhaphis chuni (Schulze 1904): Electron-microscopic and biochemical studies. *Cell Tissue Res.* **329**, 363–378 (2007).

61. Pisera, A. *et al.* Insights into the structure and morphogenesis of the giant basal spicule of the glass sponge Monorhaphis chuni. *Front. Zool.* **18**, 1–26 (2021).

62. Müller, W. E. G. *et al.* Bio-sintering processes in hexactinellid sponges: Fusion of bio-silica in giant basal spicules from Monorhaphis chuni. *J. Struct. Biol.* **168**, 548–561 (2009).

63. Sarikaya, M. *et al.* Biomimetic model of a sponge-spicular optical fiber—mechanical properties and structure. *J. Mater. Res.* **16**, 1420–1428 (2001).

64. Monn, M. A., Vijaykumar, K., Kochiyama, S. & Kesari, H. Lamellar architectures in stiff biomaterials may not always be templates for enhancing toughness in composites. *Nat. Commun.* **11**, 373 (2020).

65. Monn, M. A. & Kesari, H. Enhanced bending failure strain in biological glass fibers due to internal lamellar architecture. *J. Mech. Behav. Biomed. Mater.* **76**, 69–75 (2017).

66. Cook, J., Gordon, J. E., Evans, C. C. & Marsh, D. M. A mechanism for the control of crack propagation in all-brittle systems. *Proc. R. Soc. London. Ser. A. Math. Phys. Sci.* **282**, 508–520 (1964).

67. Morankar, S. K., Mistry, Y., Bhate, D., Penick, C. A. & Chawla, N. In situ investigations of failure mechanisms of silica fibers from the venus flower basket (Euplectella Aspergillum). *Acta Biomater.* **162**, 304–311 (2023).

68. Kochiyama, S., Fang, W., Monn, M. A. & Kesari, H. Sawtooth patterns in flexural force curves of structural biological materials are not signatures of toughness enhancement: Part I. *J. Mech. Behav. Biomed. Mater.* **119**, 104362 (2021).

69. Fang, W., Kochiyama, S. & Kesari, H. Sawtooth patterns in flexural force curves of structural biological materials are not signatures of toughness enhancement: Part II. *J. Mech. Behav. Biomed. Mater.* **124**, 104787 (2021).

70. Fernandes, M. C., Aizenberg, J., Weaver, J. C. & Bertoldi, K. Mechanically robust lattices inspired by deep-sea glass sponges. *Nat. Mater.* **20**, 237–241 (2021).

71. Chen, H., Jia, Z. & Li, L. Lightweight lattice-based skeleton of the sponge Euplectella aspergillum: On the multifunctional design. *J. Mech. Behav. Biomed. Mater.* **135**, 105448 (2022).

72. Saito, T., Uchida, I. & Takeda, M. Skeletal growth of the deep-sea hexactinellid sponge Euplectella oweni, and host selection by the symbiotic shrimp Spongicola japonica (Crustacea: Decapoda: Spongicolidae). *J. Zool.* **258**, 521–529 (2002).

73. Fernandes, M. C. *et al.* Mechanical and hydrodynamic analyses of helical strake-like ridges in a glass sponge. *J. R. Soc. Interface* **18**, 20210559 (2021).

74. Li, L., Guo, C., Chen, Y. & Chen, Y. Optimization design of lightweight structure inspired by glass sponges (Porifera, Hexacinellida) and its mechanical properties. *Bioinspiration and Biomimetics* **15**, 36006 (2020).

75. Falcucci, G. *et al.* Extreme flow simulations reveal skeletal adaptations of deep-sea sponges. *Nature* **595**, 537–541 (2021).

76. Gao, Y., Yang, J., Xiong, Y., Wang, M. & Peng, G. Experimental investigation of the effects of the coverage of helical strakes on the vortex-induced vibration response of a flexible riser. *Appl. Ocean Res.* **59**, 53–64 (2016).

77. Krastev, V. K., Amati, G., Succi, S. & Falcucci, G. On the effects of surface corrugation on the hydrodynamic performance of cylindrical rigid structures. *Eur. Phys. J. E* **41**, 95 (2018).

78. Ranjith, E. R., Sunil, A. S. & Pauly, L. Analysis of Flow over a Circular Cylinder Fitted with Helical Strakes. *Procedia Technol.* **24**, 452–460 (2016).

79. Schulze, F. E. On the Structure and Arrangement of the Soft Parts in Euplectella aspergillum. *Trans. R. Soc. Edinburgh* **29**, 661–673 (1880).

80. Großmann, J. N. Stereom differentiation in sea urchin spines under special consideration as a model for a new impact protective system. (Universität Tübingen, 2010).

81. Nebelsick, J. H., Dynowski, J. F., Grossmann, J. N. & Tötzke, C. Echinoderms: Hierarchically Organized Light Weight Skeletons. in *Evolution of lightweight structures* 141–155 (Springer, 2015).

82. Lowenstam, H. A. & Weiner, S. *On Biomineralization*. *Biological Materials Science* (Oxford University Press, 1989).

83. Yang, T., Wu, Z., Chen, H., Zhu, Y. & Li, L. Quantitative 3D structural analysis of the cellular microstructure of sea urchin spines (I): Methodology. *Acta Biomater.* **107**, 204–217 (2020).

84. Weber, J., Greer, R., Voight, B., White, E. & Roy, R. Unusual strength properties of echinoderm calcite related to structure. *J. Ultrastruct. Res.* **26**, 355–366 (1969).

85. Lauer, C., Sillmann, K., Haußmann, S. & Nickel, K. G. Strength, elasticity and the limits of energy dissipation in two related sea urchin spines with biomimetic

potential. *Bioinspir. Biomim.* **14**, 016018 (2018).

86. Seto, J. *et al.* Structure-property relationships of a biological mesocrystal in the adult sea urchin spine. *Proc. Natl. Acad. Sci.* **109**, 7126–7126 (2012).

87. Smith, A. B. Stereom microstructure of the echinoid test. *Spec. Pap. Palaeontol.* **25**, 1–81 (1980).

88. Lauer, C. *et al.* Morphology and porosity of the spines of the sea urchin Heterocentrotus mamillatus and their implications on the mechanical performance. *Zoomorphology* **137**, 139–154 (2018).

89. Grossmann, J. N. & Nebelsick, J. H. Comparative morphological and structural analysis of selected cidaroid and camarodont sea urchin spines. *Zoomorphology* **132**, 301–315 (2013).

90. Grun, T. B. & Nebelsick, J. H. Structural design of the echinoid's trabecular system. *PLoS One* **13**, e0204432 (2018).

91. Tsafnat, N., Fitz Gerald, J. D., Le, H. N. & Stachurski, Z. H. Micromechanics of Sea Urchin Spines. *PLoS One* **7**, e44140 (2012).

92. Chen, T. T. Microstructure and Micromechanics of the Sea Urchin , Colobocentrotus atratus. (2011).

93. Moureaux, C. *et al.* Structure, composition and mechanical relations to function in sea urchin spine. *J. Struct. Biol.* **170**, 41–49 (2010).

94. Presser, V., Gerlach, K., Vohrer, A., Nickel, K. G. & Dreher, W. F. Determination of the elastic modulus of highly porous samples by nanoindentation: A case study on sea urchin spines. *J. Mater. Sci.* **45**, 2408–2418 (2010).

95. Presser, V., Schultheiß, S., Berthold, C. & Nickel, K. G. Sea urchin spines as a model-system for permeable, light-weight ceramics with graceful failure behavior. Part I. Mechanical behavior of sea urchin spines under compression. *J. Bionic Eng.* **6**, 203–213 (2009).

96. Yang, T. *et al.* High strength and damage-tolerance in echinoderm stereom as a natural bicontinuous ceramic cellular solid. *Nat. Commun.* **13**, 6083 (2022).

97. Lauer, C., Schmier, S., Speck, T. & Nickel, K. G. Strength-size relationships in two porous biological materials. *Acta Biomater.* **77**, 322–332 (2018).

98. O'Neill, P. Structure and mechanics of starfish body wall. *J. Exp. Biol.* **147**, 53–89 (1989).

99. Tomholt, L. *et al.* The structural origins of brittle star arm kinematics: An integrated tomographic, additive manufacturing, and parametric modeling-based

approach. *J. Struct. Biol.* **211**, 107481 (2020).

100. Maskery, I. *et al.* Effective design and simulation of surface-based lattice structures featuring volume fraction and cell type grading. *Mater. Des.* **155**, 220–232 (2018).

101. Choy, S. Y., Sun, C. N., Leong, K. F. & Wei, J. Compressive properties of functionally graded lattice structures manufactured by selective laser melting. *Mater. Des.* **131**, 112–120 (2017).

102. Porz, L. *et al.* Dislocation-toughened ceramics. *Mater. Horizons* **8**, 1528–1537 (2021).

103. Humble, P. & Hannink, R. H. J. Plastic deformation of diamond at room temperature. *Nature* **273**, 37–39 (1978).

104. Nie, A. *et al.* Direct Observation of Room-Temperature Dislocation Plasticity in Diamond. *Matter* **2**, 1222–1232 (2020).

105. Nabarro, F. R. N. *Theory of crystal dislocations*. (Oxford University Press, 1967).

106. Pham, M.-S., Liu, C., Todd, I. & Lertthanasarn, J. Damage-tolerant architected materials inspired by crystal microstructure. *Nature* **565**, 305–311 (2019).

107. Yu, B. *et al.* The design of "Grain Boundary Engineered" architected cellular materials: The role of 5-7 defects in hexagonal honeycombs. *Acta Mater.* **243**, 118513 (2023).

108. Deng, Z. *et al.* Strategies for simultaneous strengthening and toughening via nanoscopic intracrystalline defects in a biogenic ceramic. *Nat. Commun.* **11**, 1–11 (2020).

109. Nissen, H.-U. Crystal Orientation and Plate Structure in Echinoid Skeletal Units. *Science* **166**, 1150–1152 (1969).

110. Donnay, G. & Pawson, D. L. X-ray Diffraction Studies of Echinoderm Plates. *Science* **166**, 1147–1150 (1969).

111. DeCarlo, T. M. Characterizing coral skeleton mineralogy with Raman spectroscopy. *Nat. Commun.* **9**, 9–11 (2018).

112. Loh, H.-C. *et al.* Nacre toughening due to cooperative plastic deformation of stacks of co-oriented aragonite platelets. *Commun. Mater.* **1**, 1–10 (2020).

113. Marin, F., Luquet, G., Marie, B. & Medakovic, D. Molluscan Shell Proteins: Primary Structure, Origin, and Evolution. *Curr. Top. Dev. Biol.* **80**, 209–276 (2007).

114. Fratzl, P. Small-angle scattering in materials science - a short review of applications in alloys, ceramics and composite materials. *J. Appl. Crystallogr.* **36**, 397–404 (2003).

115. Lenting, C. & Geisler, T. Corrosion of ternary borosilicate glass in acidic solution studied in operando by fluid-cell Raman spectroscopy. *npj Mater. Degrad.* **5**, 37 (2021).

116. SCHWAB, D. W. & SHORE, R. E. Mechanism of Internal Stratification of Siliceous Sponge Spicules. *Nature* **232**, 501–502 (1971).

117. Schröder, H. C. *et al.* Apposition of silica lamellae during growth of spicules in the demosponge Suberites domuncula: Biological/biochemical studies and chemical/biomimetical confirmation. *J. Struct. Biol.* **159**, 325–334 (2007).

118. Deng, Z., Chen, L. & Li, L. Comparative nanoindentation study of biogenic and geological calcite. *J. Mech. Behav. Biomed. Mater.* **137**, 105538 (2023).

119. Yang, T. *et al.* Mechanical design of the highly porous cuttlebone: A bioceramic hard buoyancy tank for cuttlefish. *Proc. Natl. Acad. Sci.* **117**, 23450–23459 (2020).

120. Lei, H. Y., Li, J. R., Xu, Z. J. & Wang, Q. H. Parametric design of Voronoi-based lattice porous structures. *Mater. Des.* **191**, 108607 (2020).

121. Wang, B. *et al.* Enhanced tunable fracture properties of the high stiffness hierarchical honeycombs with stochastic Voronoi substructures. *Results Phys.* **12**, 1190–1196 (2019).

122. Christodoulou, I. & Tan, P. J. Crack initiation and fracture toughness of random Voronoi honeycombs. *Eng. Fract. Mech.* **104**, 140–161 (2013).

123. Du, Y. *et al.* Mechanical properties of the hierarchical honeycombs with stochastic Voronoi sub-structures. *EPL (Europhysics Lett.)* **111**, 56007 (2015).

124. Zhu, H. X. *et al.* The elastic and geometrical properties of micro- and nano-structured hierarchical random irregular honeycombs. *J. Mater. Sci.* **49**, 5690–5702 (2014).

125. Liu, L., Li, D. & Dong, L. Mechanical properties of 2D hierarchical re-entrant cellular structures with Voronoi sub-structures. *EPL (Europhysics Lett.)* **123**, 16002 (2018).

126. Zhu, H. X. *et al.* The effects of regularity on the geometrical properties of Voronoi tessellations. *Phys. A Stat. Mech. its Appl.* **406**, 42–58 (2014).

127. Zhu, H. X., Thorpe, S. M. & Windle, A. H. The effect of cell irregularity on the high strain compression of 2D Voronoi honeycombs. *Int. J. Solids Struct.* **43**,

1061–1078 (2006).

128. Zhu, H. X., Hobdell, J. R. & Windle, A. H. Effects of cell irregularity on the elastic properties of 2D Voronoi honeycombs. *J. Mech. Phys. Solids* **49**, 857–870 (2001).

129. Dohrmann, M. *et al.* An integrative systematic framework helps to reconstruct skeletal evolution of glass sponges (Porifera, Hexactinellida). *Front. Zool.* **14**, 1–31 (2017).

130. Lancaster, L. C. *Concrete Vaulted Construction in Imperial Rome*. *Concrete Vaulted Construction in Imperial Rome: Innovations in Context* (Cambridge University Press, 2005).

131. Shen, X., Zhang, Q., Lee, D. S.-H., Cai, J. & Feng, J. Static Behavior of a Retractable Suspen-Dome Structure. *Symmetry (Basel).* **13**, 1105 (2021).

132. Chen, X. & Shen, S. Z. Complete load-deflection response and initial imperfection analysis of single-layer lattice dome. *Int. J. Sp. Struct.* **8**, 271–278 (1993).

133. Ma, J., Fan, F., Wu, C. & Zhi, X. Counter-intuitive collapse of single-layer reticulated domes subject to interior blast loading. *Thin-Walled Struct.* **96**, 130–138 (2015).

134. Yahyai, M. & Chahardoli, M. Seismic behavior of single layer schwedler domes. *Int. J. Sp. Struct.* **29**, 39–48 (2014).

135. Bayraktar, A., Hökelekli, E. & Yang, T. T. Y. Seismic failure behavior of masonry domes under strong ground motions. *Eng. Fail. Anal.* **142**, 106749 (2022).

136. Zhang, J. & Yanagimoto, J. Topology optimization of microlattice dome with enhanced stiffness and energy absorption for additive manufacturing. *Compos. Struct.* **255**, 112889 (2021).

137. Cheng, L. *et al.* The Twisting of Dome-Like Metamaterial from Brittle to Ductile. *Adv. Sci.* **8**, 1–9 (2021).

138. Aranguren Van Egmond, D. A. Designing for Disorder: The Mechanical Behaviour of Bioinspired, Stochastic Honeycomb Materials. (2018).

139. Berg, S. *et al.* ilastik: interactive machine learning for (bio)image analysis. *Nat. Methods* **16**, 1226–1232 (2019).

140. Perricone, V. *et al.* Hexagonal Voronoi pattern detected in the microstructural design of the echinoid skeleton. *J. R. Soc. Interface* **19**, (2022).

141. Simpson, T. L. *The cell biology of sponges*. (Springer Science & Business Media, 2012).

142. Morankar, S. *et al.* Tensile and fracture behavior of silica fibers from the Venus flower basket (Euplectella aspergillum). *Int. J. Solids Struct.* **253**, 111622 (2022).

143. Duboisset, J. *et al.* Amorphous-to-crystal transition in the layer-by-layer growth of bivalve shell prisms. *Acta Biomater.* **142**, 194–207 (2022).

144. Feofilova, M. *et al.* Geometrical frustration of phase-separated domains in Coscinodiscus diatom frustules. *Proc. Natl. Acad. Sci.* **119**, 1–6 (2022).

145. Easey, N. *et al.* Dome-shape auxetic cellular metamaterials: Manufacturing, modeling, and testing. *Front. Mater.* **6**, 1–13 (2019).

146. Dou, N. G., Jagt, R. A., Portela, C. M., Greer, J. R. & Minnich, A. J. Ultralow Thermal Conductivity and Mechanical Resilience of Architected Nanolattices. *Nano Lett.* **18**, 4755–4761 (2018).

147. Mirabolghasemi, A., Akbarzadeh, A. H., Rodrigue, D. & Therriault, D. Thermal conductivity of architected cellular metamaterials. *Acta Mater.* **174**, 61–80 (2019).

148. Xu, H., Farag, A. & Pasini, D. Multilevel hierarchy in bi-material lattices with high specific stiffness and unbounded thermal expansion. *Acta Mater.* **134**, 155–166 (2017).

149. Wang, Y. *et al.* Architected lattices with adaptive energy absorption. *Extrem. Mech. Lett.* **33**, 100557 (2019).

150. Kotz, F. *et al.* Three-dimensional printing of transparent fused silica glass. *Nature* **544**, 337–339 (2017).

151. Cui, H., Hensleigh, R., Chen, H. & Zheng, X. Additive Manufacturing and size-dependent mechanical properties of three-dimensional microarchitected, high-temperature ceramic metamaterials. *J. Mater. Res.* **33**, 360-371 (2018).

152. Osanov, M. & Guest, J. K. Topology Optimization for Architected Materials Design. *Annual Review of Materials Research* vol. 46 211–233 (2016).

153. Borrega, M. & Gibson, L. J. Mechanics of balsa (Ochroma pyramidale) wood. *Mech. Mater.* **84**, 75–90 (2015).

154. Blowes, L. M. *et al.* Body wall structure in the starfish Asterias rubens. *J. Anat.* **231**, 325–341 (2017).

155. Schwertmann, L., Focke, O. & Dirks, J. Morphology, shape variation and movement of skeletal elements in starfish (Asterias rubens). *J. Anat.* **234**, 656–667 (2019).

156. Cadman, J., Zhou, S., Chen, Y. & Li, Q. Cuttlebone: Characterisation, application and development of biomimetic materials. *J. Bionic Eng.* **9**, 367–376 (2012).

157. Denton, E. J., Gilpin-Brown, J. B. & Howarth, J. V. The Osmotic Mechanism of the Cuttlebone. *J. Mar. Biol. Assoc. United Kingdom* **41**, 351–363 (1961).

158. Aitken, Z. H., Luo, S., Reynolds, S. N., Thaulow, C. & Greer, J. R. Microstructure provides insights into evolutionary design and resilience of Coscinodiscus sp. frustule. *Proc. Natl. Acad. Sci. U. S. A.* **113**, 2017–2022 (2016).

159. Hamm, C. E. *et al.* Architecture and material properties of diatom shells provide effective mechanical protection. *Nature* **421**, 841–843 (2003).

160. Lu, J., Sun, C. & Wang, Q. J. Mechanical Simulation of a Diatom Frustule Structure. *J. Bionic Eng.* **12**, 98–108 (2015).

161. Biard, T. Diversity and ecology of Radiolaria in modern oceans. *Environ. Microbiol.* **24**, 2179–2200 (2022).

162. Nakamura, Y., Sandin, M. M., Suzuki, N., Tuji, A. & Not, F. Phylogenetic Revision of the Order Entactinaria—Paleozoic Relict Radiolaria (Rhizaria, SAR). *Protist* **171**, 125712 (2020).

163. Leys, S. P. *et al.* Models of flow through sponges must consider the sponge tissue. *Nature* **603**, E23–E25 (2022).

164. Mackie, G. O. & Singla, C. L. Studies on hexactinellid sponges. I. Histology of Rhabdocalyptus dawsoni (Lambe, 1873). *Philos. Trans. R. Soc. London. B, Biol. Sci.* **301**, 365–400 (1983).

165. Reiswig, H. Studies on hexactinellid sponges. III. The taxonomic status of hexactinellida within the porifera. *Philos. Trans. R. Soc. London. B, Biol. Sci.* **301**, 419–428 (1983).

166. Garson, G. D. Random forests. in *Data Analytics for the Social Sciences* vol. 45 215–290 (Routledge, 2021).

167. Fraser, D. B. Factors Influencing the Acoustic Properties of Vitreous Silica. *J. Appl. Phys.* **39**, 5868–5878 (1968).

168. Anderson, J. D. & Wendt, J. *Computational fluid dynamics*. vol. 206 (Springer, 1995).

169. Montazerian, H., Davoodi, E., Asadi-Eydivand, M., Kadkhodapour, J. & Solati-Hashjin, M. Porous scaffold internal architecture design based on minimal surfaces: A compromise between permeability and elastic properties. *Mater. Des.* **126**, 98–114 (2017).

170. Kestin, J., Sokolov, M. & Wakeham, W. A. Viscosity of liquid water in the range −8 °C to 150 °C. *J. Phys. Chem. Ref. Data* **7**, 941–948 (1978).

171. Fox, R. W., McDonald, A. T. & Mitchell, J. W. *Fox and McDonald's introduction to fluid mechanics*. (John Wiley & Sons, 2020).

172. Dong, L., Deshpande, V. & Wadley, H. Mechanical response of Ti–6Al–4V octet-truss lattice structures. *Int. J. Solids Struct.* **60**–**61**, 107–124 (2015).

173. Zhang, S. & Norato, J. A. Optimal Design of Panel Reinforcements with Ribs Made of Plates. *J. Mech. Des. Trans. ASME* **139**, 1–11 (2017).

174. Yahel, G., Whitney, F., Reiswig, H. M., Eerkes-Medrano, D. I. & Leys, S. P. In situ feeding and metabolism of glass sponges (Hexactinellida, Porifera) studied in a deep temperate fjord with a remotely operated submersible. *Limnol. Oceanogr.* **52**, 428–440 (2007).

175. Flores, E. I. S. & Friswell, M. I. Multi-scale finite element model for a new material inspired by the mechanics and structure of wood cell-walls. *J. Mech. Phys. Solids* **60**, 1296–1309 (2012).

176. Gibson, L. J. The hierarchical structure and mechanics of plant materials. *J. R. Soc. Interface* **9**, 2749–2766 (2012).

177. Nalla, R. K., Kinney, J. H. & Ritchie, R. O. Mechanistic fracture criteria for the failure of human cortical bone. *Nat. Mater.* **2**, 164–168 (2003).

178. Ritchie, R. O., Kinney, J. H., Kruzic, J. J. & Nalla, R. K. A fracture mechanics and mechanistic approach to the failure of cortical bone. *Fatigue Fract. Eng. Mater. Struct.* **28**, 345–371 (2005).

179. Keaveny, T. M., Morgan, E. F., Niebur, G. L. & Yeh, O. C. Biomechanics of trabecular bone. *Annu. Rev. Biomed. Eng.* **3**, 307–333 (2001).

180. Telford, M. Echinoderm spine structure, feeding and host relationships of 4 species of dissodactylus (Brachyura, Pinnotheridae). *Bull. Mar. Sci.* **32**, 584–594 (1982).

181. Grossmann, N. & Nebelsick, J. H. Stereom differentiation in spines of Plococidaris verticillata, Heterocentrotus mammillatus and other regular sea urchins. in *Proceedings of the 13th International Echinoderm Conference* (ed. Johnson, C.) 97–104 (2013).

182. Yang, T., Wu, Z., Chen, H., Zhu, Y. & Li, L. Quantitative 3D structural analysis of the cellular microstructures of sea urchin spines (I): Methodology. *Press*.

183. Nickel, K. G., Klang, K., Lauer, C. & Buck, G. Sea urchin spines as role models for biologic design and integrative structures. in *Highlights of applied mineralogy* (eds. Heuss-Aßbichler, S., Amthauer, G. & John, M.) 273–287 (De Gruyter, 2018). doi:10.1515/9783110497342-013.

184. Jensen, M. The ultrastructure of the echinoid skeleton. *Sarsia* **48**, 39–48 (1972).

185. Presser, V. *et al.* Lessons from Nature for the Construction of Ceramic Cellular Materials for Superior Energy Absorption. *Adv. Eng. Mater.* **13**, 1042–1049 (2011).

186. Schmier, S. *et al.* Developing the Experimental Basis for an Evaluation of Scaling Properties of Brittle and 'Quasi-Brittle' Biological Materials. in *Biomimetic Research for Architecture and Building Construction: Biological Design and Integrative Structures* (eds. Knippers, J., Nickel, K. & Speck, T.) vol. 9 277–294 (Springer International Publishing, 2016).

187. Toader, N., Sobek, W. & Nickel, K. G. Energy absorption in functionally graded concrete bioinspired by sea urchin spines. *J. Bionic Eng.* **14**, 369–378 (2017).

188. Carnevali, M. D. C., Bonasoro, F. & Melone, G. Microstructure and mechanical design in the lantern ossicles of the regular sea-urchin Paracentrotus lividusi A scanning electron microscope study. *J Ital. J. Zool.* **58**, 1–42 (1991).

189. Stock, S. R., Ignatiev, K. & De Carlo, F. Very high resolution synchrotron microCT of sea urchin ossicle structure. in *Proceedings of the 11th International Echinoderm Conference* (eds. Heinzeller, T. & Nebelsick, J. H.) 353–358 (CRC Press, 2004).

190. Grun, T. B. & Nebelsick, J. H. Structural design of the minute clypeasteroid echinoid Echinocyamus pusillus. *R. Soc. Open Sci.* **5**, 171323 (2018).

191. Schindelin, J. *et al.* Fiji: an open-source platform for biological-image analysis. *Nat. Methods* **9**, 676–682 (2012).

192. Gürsoy, D., De Carlo, F., Xiao, X. & Jacobsen, C. TomoPy: A framework for the analysis of synchrotron tomographic data. *J. Synchrotron Radiat.* **21**, 1188–1193 (2014).

193. Dowd, B. A. *et al.* Developments in synchrotron x-ray computed microtomography at the National Synchrotron Light Source. *Dev. X-Ray Tomogr. Ii* **3772**, 224–236 (1999).

194. Breiman, L. Random forests. *Mach. Learn.* **45**, 5–32 (2001).

195. Jang, W. Y., Kraynik, A. M. & Kyriakides, S. On the microstructure of open-cell foams and its effect on elastic properties. *Int. J. Solids Struct.* **45**, 1845–1875 (2008).

196. Liebscher, A. & Redenbach, C. Statistical analysis of the local strut thickness of open cell foams. *Image Anal. Stereol.* **32**, 1–12 (2013).

197. De Jaeger, P., T'Joen, C., Huisseune, H., Ameel, B. & De Paepe, M. An experimentally validated and parameterized periodic unit-cell reconstruction of open-cell foams. *J. Appl. Phys.* **109**, 103519 (2011).

198. Dassault Systèmes, D. S. *Abaqus analysis user's guide*. (2016).

199. Zhu, L.-F. F. *et al.* Ab initio study of single-crystalline and polycrystalline elastic properties of Mg-substituted calcite crystals. *J. Mech. Behav. Biomed. Mater.* **20**, 296–304 (2013).

200. Ebert, T. A. The non-periodic nature of growth rings in echinoid spines. in *Proceedings of the International Echinoderm Conference* (eds. Keegan, B. F. & O'Connor, B. D.) 261–267 (Rotterdam: A.A. Balkema, 1984).

201. Reznikov, N. *et al.* Inter-trabecular angle: A parameter of trabecular bone architecture in the human proximal femur that reveals underlying topological motifs. *Acta Biomater.* **44**, 65–72 (2016).

202. Gorzelak, P., Stolarski, J., Dubois, P., Kopp, C. & Meibom, A. 26Mg labeling of the sea urchin regenerating spine: Insights into echinoderm biomineralization process. *J. Struct. Biol.* **176**, 119–126 (2011).

203. Weber, J. N. The incorporation of magnesium into the skeletal calcites of echinoderms. *American Journal of Science* vol. 267 537–566 (1969).

204. Strathmann, R. R. The role of spines in preventing structural damage to echinoid tests. *Paleobiology* **7**, 400–406 (1981).

205. Gibson, L. J. Biomechanics of cellular solids. *J. Biomech.* **38**, 377–399 (2005).

206. Dawson, M. A. & Gibson, L. J. Optimization of cylindrical shells with compliant cores. *Int. J. Solids Struct.* **44**, 1145–1160 (2007).

207. Seidel, R. *et al.* Mechanical properties of stingray tesserae: High-resolution correlative analysis of mineral density and indentation moduli in tessellated cartilage. *Acta Biomater.* **96**, 421–435 (2019).

208. Quintana-Alonso, I. & Fleck, N. A. Fracture of Brittle Lattice Materials: A Review. in *Major Accomplishments in Composite Materials and Sandwich Structures* 799–816 (Springer Netherlands, 2009).

209. Quintana Alonso, I. & Fleck, N. A. Damage tolerance of an elastic-brittle diamond-celled honeycomb. *Scr. Mater.* **56**, 693–696 (2007).

210. Romijn, N. E. R. & Fleck, N. A. The fracture toughness of planar lattices: Imperfection sensitivity. *J. Mech. Phys. Solids* **55**, 2538–2564 (2007).

211. Montemayor, L. C., Wong, W. H., Zhang, Y.-W. & Greer, J. R. Insensitivity to Flaws Leads to Damage Tolerance in Brittle Architected Meta-Materials. *Sci. Rep.* **6**, 20570 (2016).

212. Blinn, J. F. A generalization of algebraic surface drawing. *J ACM Trans. Graph.* **1**,

235–256 (1982).

213. Storm, J. *et al.* Geometrical modelling of foam structures using implicit functions. *Int. J. Solids Struct.* **50**, 548–555 (2013).

214. Su, X., Kamat, S. & Heuer, A. H. The structure of sea urchin spines, large biogenic single crystals of calcite. *J. Mater. Sci.* **35**, 5545–5551 (2000).

215. Liontas, R. & Greer, J. R. 3D nano-architected metallic glass: Size effect suppresses catastrophic failure. *Acta Mater.* **133**, 393–407 (2017).

216. Fau, M. & Villier, L. Post-metamorphic ontogeny of Zoroaster fulgens Thomson, 1873 (Asteroidea, Forcipulatacea). *J. Anat.* **233**, 644–665 (2018).

217. Jin, H. *et al.* A starfish robot based on soft and smart modular structure (SMS) actuated by SMA wires. *Bioinspir. Biomim.* **11**, 056012 (2016).

218. Mao, S. *et al.* Gait study and pattern generation of a starfish-like soft robot with flexible rays actuated by SMAs. *J. Bionic Eng.* **11**, 400–411 (2014).

219. Bell, M. A., Weaver, J. C. & Wood, R. J. An Ambidextrous STarfish-Inspired Exploration and Reconnaissance Robot (The ASTER-bot). *Soft Robot.* **9**, 991–1000 (2022).

220. Jeong, H. & Kim, J. Echinoderm Inspired Variable Stiffness Soft Actuator with Connected Ossicle Structure. in *2019 International Conference on Robotics and Automation (ICRA)* vols 2019-May 7389–7394 (IEEE, 2019).

221. Grun, T. B. *et al.* The Skeleton of the Sand Dollar as a Biological Role Model for Segmented Shells in Building Construction: A Research Review. in 217–242 (2016).

222. ANKETELL, J. & LEARNER, R. C. M. Dissociation of dislocations in diamond. *Proc. R. Soc. London. A. Math. Phys. Sci.* **386**, 241–249 (1983).

223. Yao, N., Epstein, A. & Akey, A. Crystal growth via spiral motion in abalone shell nacre. *J. Mater. Res.* **21**, 1939–1946 (2006).

224. Yao, N., Epstein, A. K., Liu, W. W., Sauer, F. & Yang, N. Organic-inorganic interfaces and spiral growth in nacre. *J. R. Soc. Interface* **6**, 367–376 (2009).

225. Li, L. & Ortiz, C. A Natural 3D Interconnected Laminated Composite with Enhanced Damage Resistance. *Adv. Funct. Mater.* **25**, 3463–3471 (2015).

226. Wise, S. W. & DeVilliers, J. Scanning Electron Microscopy of Molluscan Shell Ultrastructures: Screw Dislocations in Pelecypod Nacre. *Trans. Am. Microsc. Soc.* **90**, 376 (1971).

227. Gim, J. *et al.* The mesoscale order of nacreous pearls. *Proc. Natl. Acad. Sci. U. S. A.* **118**, 1–18 (2021).

228. Jia, Z., Deng, Z. & Li, L. Biomineralized Materials as Model Systems for Structural Composites: 3D Architecture. *Adv. Mater.* **2106259**, 2106259 (2022).

229. Beliaev, M., Zöllner, D., Pacureanu, A., Zaslansky, P. & Zlotnikov, I. Dynamics of topological defects and structural synchronization in a forming periodic tissue. *Nat. Phys.* **17**, 410–415 (2021).

230. Gao, Y., Guo, Z., Song, Z. & Yao, H. Spiral interface: A reinforcing mechanism for laminated composite materials learned from nature. *J. Mech. Phys. Solids* **109**, 252–263 (2017).

231. Stukowski, A. Visualization and analysis of atomistic simulation data with OVITO–the Open Visualization Tool. *Model. Simul. Mater. Sci. Eng.* **18**, 015012 (2010).

232. Stukowski, A., Bulatov, V. V. & Arsenlis, A. Automated identification and indexing of dislocations in crystal interfaces. *Model. Simul. Mater. Sci. Eng.* **20**, 085007 (2012).

233. Hirel, P. Atomsk: A tool for manipulating and converting atomic data files. *Comput. Phys. Commun.* **197**, 212–219 (2015).

234. Blumenau, A. T., Frauenheim, T., Öberg, S., Willems, B. & Van Tendeloo, G. Dislocation structures in diamond: Density-functional based modelling and high-resolution electron microscopy. *Defect Diffus. Forum* **226**–**228**, 11–30 (2004).

235. Hornstra, J. Dislocations in the diamond lattice. *J. Phys. Chem. Solids* **5**, 129–141 (1958).

236. Pizzagalli, L., Godet, J., Guénolé, J. & Brochard, S. Dislocation cores in silicon: new aspects from numerical simulations. *J. Phys. Conf. Ser.* **281**, 012002 (2011).

237. Blumenau, A. T., Heggie, M. I., Fall, C. J., Jones, R. & Frauenheim, T. Dislocations in diamond: Core structures and energies. *Phys. Rev. B - Condens. Matter Mater. Phys.* **65**, 2052051–2052058 (2002).

238. Shikata, S. *et al.* Precise measurements of diamond lattice constant using Bond method. *Jpn. J. Appl. Phys.* **57**, 111301 (2018).

239. Blumenau, A. T. *et al.* Dislocations in diamond: Dissociation into partials and their glide motion. *Phys. Rev. B* **68**, 014115 (2003).

240. Okada, Y. & Tokumaru, Y. Precise determination of lattice parameter and thermal expansion coefficient of silicon between 300 and 1500 K. *J. Appl. Phys.* **56**, 314–320 (1984).

241. Rabier, J., Pizzagalli, L. & Demenet, J. L. Dislocations in Silicon at High Stress. in *Dislocations in Solids* vol. 16 47–108 (Elsevier, 2010).

242. Nandedkar, A. S. & Narayan, J. Atomic structure of dislocations in silicon, germanium and diamond. *Philos. Mag. A Phys. Condens. Matter, Struct. Defects Mech. Prop.* **61**, 873–891 (1990).

243. Pizzagalli, L., Pedersen, A., Arnaldsson, A., Jónsson, H. & Beauchamp, P. Theoretical study of kinks on screw dislocation in silicon. *Phys. Rev. B - Condens. Matter Mater. Phys.* **77**, 1–14 (2008).

244. Godet, J., Pizzagalli, L., Brochard, S. & Beauchamp, P. Theoretical study of dislocation nucleation from simple surface defects in semiconductors. *Phys. Rev. B - Condens. Matter Mater. Phys.* **70**, 1–11 (2004).

245. Schaedler, T. A. & Carter, W. B. Architected Cellular Materials. *Annu. Rev. Mater. Res.* **46**, 187–210 (2016).

246. Berger, J. B., Wadley, H. N. G. & McMeeking, R. M. Mechanical metamaterials at the theoretical limit of isotropic elastic stiffness. *Nature* **543**, 533–537 (2017).

247. Li, T., Hu, X., Chen, Y. & Wang, L. Harnessing out-of-plane deformation to design 3D architected lattice metamaterials with tunable Poisson's ratio. *Sci. Rep.* **7**, 1–10 (2017).

248. Zhakatayev, A., Kappassov, Z. & Varol, H. A. Analytical modeling and design of negative stiffness honeycombs. *Smart Mater. Struct.* **29**, (2020).

249. Ha, C. S., Lakes, R. S. & Plesha, M. E. Cubic negative stiffness lattice structure for energy absorption: Numerical and experimental studies. *Int. J. Solids Struct.* **178**–**179**, 127–135 (2019).

250. Chen, Y., Jia, Z. & Wang, L. Hierarchical honeycomb lattice metamaterials with improved thermal resistance and mechanical properties. *Compos. Struct.* **152**, 395–402 (2016).

251. Xiao, R. *et al.* Stereolithography (SLA) 3D printing of carbon fiber-graphene oxide (CF-GO) reinforced polymer lattices. *Nanotechnology* **32**, 235702 (2021).

252. Kenel, C., Casati, N. P. M. & Dunand, D. C. 3D ink-extrusion additive manufacturing of CoCrFeNi high-entropy alloy micro-lattices. *Nat. Commun.* **10**, 1–8 (2019).

253. Mueller, J., Raney, J. R., Shea, K. & Lewis, J. A. Architected Lattices with High Stiffness and Toughness via Multicore–Shell 3D Printing. *Adv. Mater.* **30**, 1–8 (2018).

254. Chortos, A. *et al.* Printing Reconfigurable Bundles of Dielectric Elastomer Fibers.

Adv. Funct. Mater. **31**, 1–10 (2021).

255. Cui, H. *et al.* Three-dimensional printing of piezoelectric materials with designed anisotropy and directional response. *Nat. Mater.* **18**, 234–241 (2019).

256. Raney, J. R. *et al.* Rotational 3D printing of damage-tolerant composites with programmable mechanics. *Proc. Natl. Acad. Sci.* **115**, 1198–1203 (2018).

257. Surjadi, J. U., Gao, L., Cao, K., Fan, R. & Lu, Y. Mechanical Enhancement of Core-Shell Microlattices through High-Entropy Alloy Coating. *Sci. Rep.* **8**, 1–10 (2018).

258. Feng, X. *et al.* Microalloyed medium-entropy alloy (MEA) composite nanolattices with ultrahigh toughness and cyclability. *Mater. Today* **42**, 10–16 (2021).

259. Zhang, X. *et al.* Three-Dimensional High-Entropy Alloy-Polymer Composite Nanolattices That Overcome the Strength-Recoverability Trade-off. *Nano Lett.* **18**, 4247–4256 (2018).

260. Donnay, G. & Pawson, D. L. X-ray Diffraction Studies of Echinoderm Plates. *Science (80-.).* **166**, 1147–1150 (1969).

261. Seto, J. *et al.* Structure-property relationships of a biological mesocrystal in the adult sea urchin spine. *Proc. Natl. Acad. Sci.* **109**, 3699–3704 (2012).

262. Okazaki, K., Dillaman, R. M. & Wilbur, K. M. Crystalline axes of the spine and test of the sea urchin Strongylocentrotus purpuratus: Determination by crystal etching and decoration. *Biol. Bull.* **161**, 402–415 (1981).

263. Raup, D. M. Crystallography of Echinoid Calcite. *J. Geol.* **67**, 661–674 (1959).

264. Paul, C. R. C. & Smith, A. B. The early radiation and phylogeny of echinoderms. *Biol. Rev.* **59**, 443–481 (1984).

265. Le Page, Y., Saxe, P. & Rodgers, J. R. Ab initio stiffness for low quartz and calcite. *Phys. Status Solidi Basic Res.* **229**, 1155–1161 (2002).

266. Kunitake, M. E., Mangano, L. M., Peloquin, J. M., Baker, S. P. & Estroff, L. A. Evaluation of strengthening mechanisms in calcite single crystals from mollusk shells. *Acta Biomater.* **9**, 5353–5359 (2013).

267. Khaleghi, S. *et al.* On the directional elastic modulus of the TPMS structures and a novel hybridization method to control anisotropy. *Mater. Des.* **210**, 110074 (2021).

268. Ranganathan, S. I. & Ostoja-Starzewski, M. Universal elastic anisotropy index. *Phys. Rev. Lett.* **101**, 3–6 (2008).

269. Meeks, W. H. & Tinaglia, G. Triply periodic constant mean curvature surfaces.

Adv. Math. (N. Y). **335**, 809–837 (2018).

270. Al-Ketan, O. & Abu Al-Rub, R. K. Multifunctional Mechanical Metamaterials Based on Triply Periodic Minimal Surface Lattices. *Adv. Eng. Mater.* **21**, 1–39 (2019).

271. Berman, A., Addadi, L. & Weiner, S. Interactions of sea-urchin skeleton macromolecules with growing calcite crystals- a study of intracrystalline proteins. *Nature* **331**, 546–548 (1988).

272. Beniash, E. Spiculogenesis in Sea Urchin Larva. (Weizmann Institute of Science, 1998).

273. Spencer, A. J. M. *Continuum Mechanics*. (Longman Group Limited, 1980).

274. Gabbrielli, R., Turner, I. G. & Bowen, C. R. Development of modelling methods for materials to be used as bone substitutes. *Key Eng. Mater.* **361-363 II**, 901–906 (2008).

275. Vijayavenkataraman, S., Zhang, L., Zhang, S., Fuh, J. Y. H. & Lu, W. F. Triply periodic minimal surfaces sheet scaffolds for tissue engineering applications: An optimization approach toward biomimetic scaffold design. *ACS Appl. Bio Mater.* **1**, 259–269 (2018).

276. Aizenberg, J. *et al.* Morphogenesis of calcitic sponge spicules: a role for specialized proteins interacting with growing crystals. *FASEB J.* **9**, 262–268 (1995).

277. Lowenstam, H. A. & Weiner, S. *On Biomineralization*. (Oxford University Press, 1989).

278. Beniash, E., Aizenberg, J., Addadi, L. & Weiner, S. Amorphous calcium carbonate transforms into calcite during sea urchin larval spicule growth. *Proc. R. Soc. B Biol. Sci.* **264**, 461–465 (1997).

279. Lai, M. *et al.* Profiting from nature: Macroporous copper with superior mechanical properties. *Chem. Commun.* **1**, 3547–3549 (2007).

280. Chen, Z. *et al.* On hybrid cellular materials based on triply periodic minimal surfaces with extreme mechanical properties. *Mater. Des.* **183**, 108109 (2019).

281. Tomholt, L., Baum, D., Wood, R. J. & Weaver, J. C. High-throughput segmentation, data visualization, and analysis of sea star skeletal networks. *J. Struct. Biol.* **215**, 107955 (2023).

©Anita Walz CC BY http://creativecommons.org/licenses/by/4.0
Office of Scholarly Communications, University Libraries, Virginia Tech